Technical Physics, Vol. 47, No. 5, 2002, pp. 513–522. Translated from Zhurnal Tekhnicheskoĭ Fiziki, Vol. 72, No. 5, 2002, pp. 1–9.

THEORETICAL AND MATHEMATICAL PHYSICS

Relations between Matrix Elements of the Nonlinear Boltzmann Collision Integral in the Axisymmetric Case

A. Ya. Énder* and I. A. Énder**

** Ioffe Physicotechnical Institute, Russian Academy of Sciences, Politechnicheskaya ul. 26, St. Petersburg, 194021 Russia*

*** St. Petersburg State University, Universitetskaya nab. 7/9, St. Petersburg, 199034 Russia*

Received June 13, 2001

Abstract—The properties of the nonlinear Boltzmann collision integral for the axisymmetric velocity distribution are studied. Expansions in spherical Hermitian polynomials orthogonal to the Maxwellian weighting function are employed. It is shown that the nonlinear matrix elements of the collision operator are related to each other by simple relations, which are valid for arbitrary cross sections of particle interaction even if a preferential direction exists. The relations are derived from the invariance of the collision operator under the choice of basis functions or, more precisely, under both temperature and the mean velocity of the Maxwellian weighting function. The recurrent relations found allow one to calculate the matrix elements at large values of indices. This makes it possible to construct exact solutions to complicated kinetic problems. © *2002 MAIK "Nauka/Interperiodica".*

INTRODUCTION

Polynomial expansions are widely used in the kinetic theory of gases. In the case of the linearized Boltzmann equation, such an expansion forms the basis for the well-known Chapman–Enskog method [1]. For the nonlinear case, this method was extended by Burnett [2] and Grad [3]. The complete system of the nonlinear moment equations with the Gred condition satisfied is equivalent to the nonlinear Boltzmann equation. As Kumar noted [4], the most compact expansion is that in spherical Hermitian polynomials, which are the product of spherical harmonics and Sonine polynomials.

The basic challenge impeding the development of the nonlinear moment method is the calculation of the interaction matrix corresponding to the moments of the nonlinear collision integral. In recent years, some progress has been made in both calculating isotropic matrix elements (MEs) and solving relaxation problems for an isotropic (in terms of velocities) distribution function (DF) [5–9]. In [5, 6], analytical formulas (including multiple summations) for nonlinear isotropic MEs have been derived. In [7–9], recurrent relations for calculating MEs have been found. These relations have made it possible to substantially advance into the range of large indices. For example, it would take 9×10^4 years for a computer to calculate the MEs for $N_0 = 128$, where N_0 is the number of DF expansion coefficients, with the formulas in [5], whereas the same computation using the recurrent relations lasts a half an hour. It was shown [9] that a change from $N_0 = 15$ to $N_0 = 128$ makes it possible to pass from 2–3 to 8–10 thermal velocities in the exact description of the DF.

We emphasize that these relations between the MEs are based on the invariance of the collision integral under choice of basis functions. The recurrent relations found in [7–9] turn out to be very simple. Each nonlinear ME is determined from those found previously with the help of four arithmetic operations, all nonlinear ME being determined via the given linear ones. In the case of cross sections that have an arbitrary angular dependence and a velocity dependence corresponding to power potentials, simple formulas for the linear MEs are available [8].

The relations between the MEs obtained in [8, 9] for an isotropic (in terms of velocities) DF have made a substantial improvement in calculating both the nonlinear MEs of the collision integral and the DF during isotropic relaxation. The aim of this paper is to derive similar recurrent relations in the axisymmetric case. Here, the DF will depend on two velocity variables. In the isotropic case, the invariance of the Maxwellian weighting function under temperature T was used. In the axisymmetric case, we will employ the invariances under both T and the mean velocity u of the Maxwellian weighting function to find relations between MEs.

Note that in the recurrent relation hierarchy, it is the construction of MEs in the axisymmetric case that is of vital importance. Switching to the three-dimensional case is rather simple.

1063-7842/02/4705-0513$22.00

1. TRANSFORMATION FROM BASIS (u_0, T_0) TO BASIS (u_1, T_1)

The functions H_j of form

$$H_j = Y^i_{lm}(\Theta, \varphi)c^l S^{(r)}_{l+1/2}(c^2)$$

will be referred to as real unnormalized spherical Hermitian polynomials. Here, j covers four indices: i, r, l, and m. The functions $Y^i_{lm}(\Theta, \varphi)$ ($i = 0, 1$) are real unnormalized spherical harmonics. These harmonics are defined as follows:

$$Y^0_{lm}(\Theta, \varphi) = P^m_l(\cos\Theta)\cos m\varphi \ (m = 0, 1, \ldots, l), \quad (1)$$

$$Y^1_{lm}(\Theta, \varphi) = P^m_l(\cos\Theta)\sin m\varphi \ (m = 0, 1, \ldots, l). \quad (2)$$

The functions $P^m_l(x)$ are associated Legendre polynomials. Sonine polynomials, in their turn, are defined as [1]

$$S^{(r)}_{l+1/2}(x) = \sum_{q=0}^{r} a^l_{q,r}x^q,$$
$$a^l_{q,r} = \frac{(-1)^q(2l+2r+1)!!}{(2l+2q+1)!!q!(2r-2q)!!}. \quad (3)$$

In the axisymmetric (with respect to velocities) case ($m = 0$ and $i = 0$), the spherical Hermitian polynomials depend only on two indices:

$$H_{r,l} = c^l P_l\cos\Theta S^r_{l+1/2}(c^2),$$
$$c^2 = \frac{m}{2kT}(v_x^2 + v_y^2 + (v_z - u)^2). \quad (4)$$

Here, Θ is the angle between the velocity vector $\mathbf{c}$ and the axis of symmetry z and $P_l\cos\Theta$ are the Legendre polynomials

$$P_l(x) = \sum_{k=0}^{[l/2]} b_{k,l}x^{l-2k}, \quad b_{k,l} = \frac{(-1)^k(2l-2k-1)!!}{(2k)!!(l-2k)!}. \quad (5)$$

The polynomials $H_{r,l}$ are orthogonal to the Maxwellian weighting function having the mean velocity u directed along the z axis and temperature T:

$$(H_{r_1,l_1}, H_{r_2,l_2}) = \int M(T, c)H_{r_1,l_1}(\mathbf{c})H_{r_2,l_2}(\mathbf{c})d^3v$$
$$= \delta_{r_1,r_2}\delta_{l_1,l_2}g_{r_1,l_1}, \quad (6)$$
$$M(T, c) = \left(\frac{m}{2kT}\right)^{3/2} e^{-c^2}.$$

The normalizing factor $g_{r,l}$ has the form

$$g_{r,l} = \frac{(2r+2l+1)!!}{(2r)!!2^l(2l+1)}. \quad (7)$$

In the case under consideration, the velocity $\mathbf{v}$ is defined by two variables, for instance, by $c = |\mathbf{c}|$ and the angle Θ.

We express the axisymmetric DF in the form of the expansion

$$f(c, \Theta) = M(T, c)\sum_{r,l} C_{r,l}H_{r,l}(c, \Theta). \quad (8)$$

With this approach, the Boltzmann equation for the DF $f(c, \Theta)$ turns to a set of related equations for the coefficients $C_{r,l}$:

$$\frac{D(n_0(z,t)C_{r,l})}{Dt} = n_0^2 \sum_{r_1,l_1,r_2,l_2} K^{r,l}_{r_1,l_1,r_2,l_2}C_{r_1,l_1}C_{r_2,l_2}. \quad (9)$$

Here, D/Dt is the differential operator representing the left-hand sides of the moment equations, which have been considered in detail in [2, 10]. In this paper, we will concentrate on constructing the MEs of the collision integral, assuming that the Boltzmann equation is spatially uniform. An axisymmetric ME has the form

$$K^{r,l}_{r_1,l_1,r_2,l_2} = \frac{1}{g_{r,l}}\int H_{r,l}\hat{I}(M, H_{r_1,l_1}, MH_{r_2,l_2})d^3v. \quad (10)$$

In the isotropic (in terms of velocities) case, the simple relations between the MEs were obtained [9] based on the invariance of the collision integral under basis. The bases considered differed in temperatures of the Maxwellian weighting functions, i.e., in units of measure for velocity. In the axisymmetric case, the bases differ not only in temperatures T of the Maxwellian weighting functions but also in their mean velocities u. As a rule, we will characterize the basis by indexed variables, e.g., u_0 and T_0, u_1 and T_1, etc.

Let us expand the DF in the basis (u_0, T_0). In this basis, the velocity coordinates c and Θ are denoted by c_0 and Θ_0, respectively. Then, expansion (8) takes the form

$$f(c_0, \Theta_0) = M(T_0, c_0)\sum_{r,l} C_{r,l}H_{r,l}(c_0, \Theta_0),$$
$$c_0^2 = \frac{m}{2kT_0}(v_x^2 + v_y^2 + (v_z - u_0)^2).$$

In going from one basis to another, it is convenient to use the α–u representation of the Boltzmann equation [11]. With this representation, an axisymmetric DF is expanded in terms of Maxwellian functions with arbitrary temperatures and mean velocities:

$$f(\mathbf{v}) = \int_{-\infty}^{\infty}\int_{0}^{\infty} M(u, \alpha, \mathbf{v})\varphi(\alpha, u)du d\alpha. \quad (11)$$

For the function $\varphi(\alpha, u)$, the equation equivalent to the Boltzmann equation has been derived [10]. If we pass to the variable $\hat{T} = 1/\alpha$ and denote the couple u

and $\tilde{T}$ by W, this equation in the spatially uniform case can be written in the form

$$\frac{\partial\varphi(W,t)}{\partial t} = n_0\int A(W, W_1, W_2)\varphi(W_1, t)\varphi(W_2, t)dW_1dW_2. \quad (12)$$

In going from α, u to u, $\tilde{T}$, the same notation φ holds for the DF. Then, instead of (11), we have

$$f(\mathbf{v}) = \int_{-\infty}^{\infty}\int_{0}^{\infty} M(u, \tilde{T}, \mathbf{v})\varphi(u, T)du d\tilde{T}. \quad (13)$$

The kernel $A(W, W_1, W_2)$ is the map of the collision integral of two Maxwellian functions $J^M(\mathbf{v}, W_1, W_2) = \hat{I}(M(W_1, \mathbf{v}), M(W_2, \mathbf{v}))$ into the u–T space:

$$J^M(\mathbf{v}, W_1, W_2) = \int_{-\infty}^{\infty}\int_{0}^{\infty} M(W, \mathbf{v})A(W, W_1, W_2)dW.$$

In the Appendix, it is shown that the biorthogonal system of the functions $h^L_{r',l'}$ and $h^R_{r,l}$ in the α–u representation corresponds to the system of the polynomials $H_{r,l}$ that is orthogonal to the Maxwellian weighting function. In the basis W_0, for the right and left systems of the functions $h^R_{r,l}$ and $h^L_{r,l}$, we have

$$h^R_{r,l}(W, W_0) = \tilde{T}_0^{r+l/2}\sum_{p=0}^{[\frac{l}{2}]}\frac{b_{p,l}}{2^{l-2p}}\delta^{(l-2p)}(u-u_0) \times\frac{\delta^{(r+p)}(\tilde{T}-\tilde{T}_0)}{r!}, \quad (14)$$

$$h^L_{r',l'}(W, W_0) = \sum_{q=0}^{r'}\frac{a^{l'}_{q,r'}}{g_{r',l'}}\left(1-\frac{\tilde{T}}{\tilde{T}_0}\right)^{r'-q} \times(u-u_0)^{l'+2q}\frac{1}{\tilde{T}_0^{q+l'/2}}, \quad (15)$$

respectively. Here, $b_{p,l}$ are the coefficients of Legendre polynomial (5); $a^{l'}_{q,r'}$, those of Sonine polynomial (3); and $g_{r',l'}$, normalizing factor (7). Using the expansion of the DF in the right functions $h^R_{r,l}$,

$$\varphi(W, z, t) = \sum_{r,l} C_{r,l}(z, t)h^R_{r,l}(W, W_0),$$

and integrating Eq. (12) with respect to W with $h^L_{r',l'}$, we arrive at a set of moment equations for $C_{r,l}$ that coincides with (9) and obtain the new representation

$$K^{r,l}_{r_1,l_1,r_2,l_2}(W_0) = \iiint h^L_{r,l}(W, W_0)A(W, W_1, W_2) \times h^R_{r_1,l_1}(W_1, W_0)h^R_{r_2,l_2}(W_2, W_0)dW_1dW_2dW \quad (16)$$

for coefficients $K^{r,l}_{r_1,l_1,r_2,l_2}$ (10).

After substituting expressions (14) and (15) into (16), the calculation of $K^{r,l}_{r_1,l_1,r_2,l_2}$ for a given kernel $A(W, W_1, W_2)$ is reduced to multiple integrations and differentiations. Thus, the algorithm for deriving direct formulas for the MEs can be constructed with the α–u representation. However, formulas obtained from (16) turn out to be so awkward that the calculation of the MEs for large values of indices is practically impossible.

We continue considering the transition from one basis to another. Let the initial basis be characterized by the mean velocity u_0 and temperature $\tilde{T}_0$ and the transition be performed to a new basis with the mean velocity u_1 and temperature $\tilde{T}_1$. We also assume that u_0 and u_1 are directed along the axis of symmetry z. The same DF $\varphi(W)$ can be expressed in two bases W_0 and W_1:

$$\varphi(W) = \sum_{k=0}^{\infty} C^0_k h^R_k(W, W_0) = \sum_{j=0}^{\infty} C^1_j h^R_j(W, W_1). \quad (17)$$

Here, each of the indices k and j denotes the couple of indices corresponding to the indices of the Hermitian polynomials in the axisymmetric case. From the definition of the functions h^R_j and h^L_j, it is clear that relations (17) are invariant under transformation from the α–u space to the v space. In this case, one has to replace each of the functions h^R_k and h^R_j with $M(W_0, v)H_k(\mathbf{c}_0)$ and $M(W_1, v)H_j(\mathbf{c}_1)$, respectively.

In order to find a relation between the vectors C^0 and C^1, we multiply both parts of (17) by $h^L_j(W, W_1)$ and integrate with respect to W. Then, using the orthonormality property of biorthogonal system (A21), we obtain

$$C^1_j = \sum_{k=0}^{\infty} D_{j,k}(W_1, W_0)C^0_k, \quad (18)$$

where elements $D(W_1, W_0)$ of the matrix of transition from one basis to another are expressed via the scalar product,

$$D_{j,k}(W_1, W_0) = \int_0^{\infty} h^L_j(W, W_1)h^R_k(W, W_0)dW = (h^L_j(W, W_1), h^R_k(W, W_0)), \quad (19)$$

and the basis elements (Hermitian polynomials) are transformed as follows:

$$h_j^R(W, W_1) = \sum_{k=0}^{\infty} D_{k,j}(W_0, W_1) h_k^R(W, W_0). \quad (20)$$

The inverse operator $\hat{D}^{-1}$ and its matrix elements have the form

$$\hat{D}^{-1}(W_1, W_0) = \hat{D}(W_0, W_1),$$

$$(\hat{D}^{-1}(W_1, W_0))_{ij} = D_{ij}(W_0, W_1).$$

The collision integral is invariant under basis. Therefore,

$$\sum_{k',j'} C_{k'}^1 C_{j'}^1 \sum_{i'} K_{k',j'}^{i'}(W_1) h_{i'}^R(W, W_1) = \sum_{k,j} C_k^0 C_j^0 \sum_i K_{k,j}^i(W_0) h_i^R(W, W_0). \quad (21)$$

Here, $K_{k,j}^i(W_0)$ and $K_{k',j'}^{i'}(W_1)$ are the MEs in the bases W_0 and W_1, respectively. If we express the coefficients C_k^0 and the functions $h_k^R(W,W_0)$ in terms of C_k^1 and $h_k^R(W,W_1)$, respectively [using (18) and (20)], and take into account the arbitrariness of the expansion coefficients $C_{k'}^1$ and $C_{j'}^1$ and also orthogonality properties (A21), we obtain from (21)

$$K_{k',j'}^{i'}(W_1) = \sum_i D_{i',i}(W_1, W_0) \times \sum_{k,j} K_{k,j}^i(W_0) D_{k,k'}(W_0, W_1) D_{j,j'}(W_0, W_1). \quad (22)$$

From the operator form of this formula, it follows that to each of the MEs in the new basis W_1, there corresponds the operator $\hat{\hat{K}}'$, which is related to the operator $\hat{\hat{K}}$ in the initial basis W_0 as follows:

$$\hat{\hat{K}}'(W_1) = \hat{D}(W_1, W_0)\hat{\hat{K}}(W_0)(\hat{D}(W_0, W_1), \hat{D}(W_0, W_1)). \quad (23)$$

Before proceeding further, we will dwell on the study of the D matrix.

2. THE TRANSITION MATRIX AND ITS DERIVATIVES

In order to calculate the transition matrix, we will use the definition of an ME of operator $\hat{D}$ (19), substitute the explicit form of the functions $h_{r,l}^R$ and $h_{r,l}^L$ [(14) and (15)], and perform integration with respect to u and $\tilde{T}$. Taking into account the properties of δ function derivatives, we find

$$D_{j',j}(W_1, W_0) = \frac{\tilde{T}_0^{r+l/2}}{\tilde{T}_1^{r'+l'/2}} \sum_{p=0}^{[\frac{l}{2}]} \sum_{q=0}^{r'} \frac{b_{p,l}\tilde{a}_{q,r'}^{l'}}{2^{l-2p}} \times \frac{(l'+2q)!(r'-q)!(u_0-u_1)^{l'-l+2\rho}(\tilde{T}_1-\tilde{T}_0)^{r'-r-\rho}}{(l'-l+2\rho)!(r'-r-\rho)!r!}, \quad (24)$$

where

$$\rho = p + q. \quad (25)$$

Using (24) and (25), we will prove the orthonormality of the Hermitian polynomials and calculate the first derivatives with respect to u and T for $W_1 = W_2$. From the form of expression (24), it is clear that at $W_1 = W_0$, the MEs $D_{j'j}(W_0, W_0)$ are nonzero if and only if

$$\rho = r' - r = (l - l')/2, \quad q = \rho - p \geq 0, \quad p \leq \rho. \quad (26)$$

As a result, the double sum in (24) is reduced to the sum over the single index p. Since $\rho < l/2$ (26), the upper limit in this sum equals ρ:

$$D_{j',j}(W_0, W_0) = \sum_{p=0}^{\rho} \tilde{a}_{\rho-p,r+\rho}^{l-2\rho} \frac{b_{p,l}}{2^{l-2p}} \times (r+\rho-p)!(l-2\rho+2p)!/r!. \quad (27)$$

Therefore, $D_{j',j}(W_0, W_0) = \tilde{a}_{0,r}^{l} b_{0,l} l!/2^l$ at $\rho = 0$. Using expressions (5) and (3) for $b_{p,l}$ and $a_{q,r}^l$, respectively, and taking into account (26), we come to

$$D_{r,l,r,l}(W_0, W_0) = 1 \quad (28)$$

at $\rho = 0$.

In the case of arbitrary ρ, using (27), (5), and (3), one can find

$$D_{j',j}(W_0, W_0) = \frac{(r+\rho)!(2l-4\rho+1)}{2^\rho r!} S, \quad (29)$$

where

$$S = \frac{1}{\rho!} \sum_{p=0}^{\rho} \binom{\rho}{p} (-1)^p Q_{\rho-1}(p),$$

$$Q_{\rho-1}(p) = \frac{(2l-2p-1)!!}{(2l-2p-2(\rho-1)-1)!!}.$$

Here, the expression $Q_{\rho-1}(p)$ at $\rho > 0$ is a $(\rho - 1)$th degree polynomial in p. For sums with binomial coeffi-

cients, it is well known [12, p. 608] that

$$\sum_{p=0}^{\rho}\binom{\rho}{p}(-1)^p p^t = 0 \tag{30}$$

for $t < \rho$. Hence, both the function S and expression (29) vanish at $\rho \neq 0$. Thus,

$$\begin{aligned} &D_{r',l',r,l}(W_0, W_0) \\ &= (h^L_{r,'l'}(W, W_0), h^R_{r,l}(W, W_0)) = \delta_{r,r'}\delta_{l,l'}, \end{aligned} \tag{31}$$

which was to be proved. This means that the matrix D is a unit matrix for $W_1 = W_0$. On the other hand, this property reflects the orthonormality of the biorthogonal system of the Hermitian polynomials in the u–T representation.

Now, let us calculate the derivatives of the D matrix. First, we will find the derivative $dD_{j',j}(W_1, W_0)/du_1$ for $W_1 = W_0$ using (24). It is clear that the first equality from (26) is replaced by

$$\rho = r' - r = (l - l' + 1)/2. \tag{32}$$

As a result, we have

$$\begin{aligned} &\frac{d}{du_1}(D_{r',l',r,l}(W_1, W_0))\big|_{W_1 = W_0} = -\frac{1}{\tilde{T}_0^{1/2}}\sum_{p=0}^{a}\frac{b_{p,l}}{2^{l-2p}} \\ &\times \tilde{a}^{l+1-2\rho}_{\rho-p,\rho+p}\frac{(l'+2\rho-2p)!(r'-\rho+p)!}{r!} = \frac{B}{\tilde{T}_0^{1/2}}, \end{aligned} \tag{33}$$

where

$$a = \min([l/2], \rho). \tag{34}$$

With expression (5) for $b_{p,l}$, expression (3) for $a^l_{q,r}$, and equality (32), we arrive at

$$B = -\frac{2r'!(2l-4\rho+3)}{2^\rho r!}S_1, \tag{35}$$

$$S_1 = \frac{1}{\rho!}\sum_{p=0}^{\rho}(-1)^{p+\rho}\binom{\rho}{p}Q_{\rho-2}(p)(l-2p+1), \tag{36}$$

where

$$Q_{\rho-2}(p) = \frac{(2l-2p-1)!!}{(2l-2p-2\rho+3)!!}. \tag{37}$$

In going from (33) to (36), $a = \rho$ is taken to be the upper limit. In the case $l' \neq 0$, this choice is evident from (32) and (34). For $l' = 0$, (32) and (34) yield $a = [l/2] = \rho - 1$ and l is an odd number. However, at $l' = 0$, $a = \rho$ can always be used as the upper limit of the sum in (36), since the corresponding term in (36) vanishes with $p = \rho = (l + 1)/2$.

Let us show that S_1 vanishes for $\rho > 1$. At $\rho = 2$, the function $Q_{\rho-2}(p) = 1$, i.e., is a zero-degree polynomial in p. At $\rho = 3$, the function $Q_{\rho-2}(p) = 2l - 2p - 1$ is a first-degree polynomial in p. At $\rho = 2 + k$, the function $Q_{\rho-2}(p)$ will be the kth-degree polynomial in p and the product $Q_{\rho-2}(p)(l - 2p + 1)$ in (36), a $(k + 1)$th-degree polynomial. Hence, for $\rho > 1$, the degree of the polynomial is always less than ρ, and according to (30), $S_1 = 0$. From (32), it follows that, for $\rho = 0$, only the equalities $r = r'$ and $l = l' - 1$ are possible, and for $\rho = 1$, $r = r' + 1$ and $l = l' + 1$.

At $\rho = 0$, sum (36) is reduced to the only term corresponding to $p = 0$, so that

$$S_1 = \frac{l+1}{(2l+1)(2l+3)}, \quad B = -\frac{2(l+1)}{(2l+1)}.$$

From (35)–(37), it follows that

$$S_1 = -\frac{2l}{(2l-1)(2l+1)}, \quad B = \frac{2l(r+1)}{(2l+1)} \tag{38}$$

at $\rho = 1$.

Substituting (38) into (33) yields

$$\begin{aligned} &\frac{d}{du_1}(D_{r',l',r,l}(W_1, W_0))\big|_{W_1 = W_0} = \frac{2}{\sqrt{\tilde{T}_0}}\frac{1}{(2l+1)} \\ &\times(-(l+1)\delta_{r',r}\delta_{l',l+1} + l(r+1)\delta_{r',r+1}\delta_{l',l-1}). \end{aligned} \tag{39}$$

The function $D_{r,l,r',l'}(W_0, W_1)$ at $\tilde{T}_1 = \tilde{T}_0$ is a polynomial in $(u_1 - u_0)$. The coefficients of this polynomial differ from those of $D_{r',l',r,l}(W_1, W_0)$ by the changes $r \longrightarrow r'$, $l \longrightarrow l'$, and $W_0 \longrightarrow W_1$. Finally, we have

$$\begin{aligned} &\frac{d}{du_1}(D_{r,l,r',l'}(W_0, W_1))\big|_{W_1 = W_0} = \frac{2}{\sqrt{\tilde{T}_0}}\frac{1}{(2l'+1)} \\ &\times((l'+1)\delta_{r,r'}\delta_{l,l'+1} - l'(r'+1)\delta_{r,r'+1}\delta_{l,l'-1}). \end{aligned} \tag{40}$$

Before differentiating this equation with respect to temperature, we will simplify the expression for transition matrix (24). First, we interchange the orders of summation in (24), taking into account (26):

$$\begin{aligned} D_{j',j}(W_1, W_0) &= \frac{(-1)^{l+r+r'}\tilde{T}_0^{r+l/2}}{r!\tilde{T}_1^{r'+l'/2}} \\ &\times\sum_{p=a}^{r'-r}\frac{(u_0-u_1)^{l'-l+2\rho}(\tilde{T}_1-\tilde{T}_0)^{r'-r-\rho}}{(l'-l+2\rho)!(r'-r-\rho)!} \\ &\times\sum_{p=0}^{b} b_{p,l}a^{l'}_{q,r'}(-1)^\rho(l'+2q)!(r'-q)!. \end{aligned} \tag{41}$$

Here, $a = \max(0, [(l - l')/2])$ and $b = \min(\rho, [l/2])$. Substituting expression (3) for $a^l_{q,r}$ and expression (5) for

$b_{p,l}$ into (41), we find after straightforward calculations

$$D_{j',j}(W_1, W_0) = \frac{(-1)^{r+r'} r'! \tilde{T}_0^{r+l/2} (2l'+1)}{2^{l-l'} r! \tilde{T}_1^{r'+l'/2}} \times \sum_{\rho=a}^{r'-r} \frac{(u_0-u_1)^{l'-l+2\rho} (\tilde{T}_1-\tilde{T}_0)^{r'-r-\rho} 2^\rho}{(l'-l+2\rho)!(r'-r-\rho)!\rho!} B^\rho_{l,l'}, \quad (42)$$

where

$$B^\rho_{l,l'} = \sum_{p=0}^{b} (-1)^p \binom{\rho}{p} \frac{(2l-2p-1)!!(l'+2\rho-2p)!}{(l-2p)!(2l'+2\rho-2p+1)!!}.$$

Let $u_1 = u_0$ in (42). Then, following the same reasoning as in proving (31), we obtain $B^\rho_{l,l'} = \delta_{\rho,0}\delta_{l,l'}/(2l+1)$ and (42) takes the form

$$D_{j',j}(W_1, W_0)\big|_{u_1=u_0} = \frac{(-1)^{r+r'} r'!}{r!} \frac{\tilde{T}_0^{r+l/2}}{\tilde{T}_1^{r'+l/2}} \frac{(\tilde{T}_1-\tilde{T}_0)^{r'-r}}{(r'-r)!} \delta_{l,l'}. \quad (43)$$

Note that this formula coincides with that for the isotropic case [9] up to the factor $(\tilde{T}_0/\tilde{T}_1)^{l/2}$. It is evident that differentiating (43) with respect to $\tilde{T}_1$ and putting $\tilde{T}_1 = \tilde{T}_0$ yields

$$\tilde{T}_0 \frac{d}{d\tilde{T}_1} (D_{r',l',r,l}(W_1, W_0))\big|_{W_1=W_0} = \delta_{l',l}(-(r'+l'/2)\delta_{r',r} + r'\delta_{r',r+1}). \quad (44)$$

Substituting the parameters r for r', l for l', and $\tilde{T}_0$ for $\tilde{T}_1$ in $D_{j',j}(W_1, W_0)|_{u_1=u_0}$, we get

$$\tilde{T}_0 \frac{d}{d\tilde{T}_1} (D_{r,l,r',l'}(W_0, W_1))\big|_{W_1=W_0} = \delta_{l',l}(r+l/2)\delta_{r',r} - r\delta_{r,r'+1}. \quad (45)$$

3. RELATIONS BETWEEN THE MATRIX ELEMENTS OF THE COLLISION INTEGRAL

Consider relation (23) once again. We will show that the relation between the MEs in a given basis, e.g., in W_0, can be found by differentiating these equality with respect to the basis parameters u and $\tilde{T}$. It is in the way that the relations between the MEs in the isotropic case have been deduced by differentiating with respect to temperature [9].

We will begin with the differentiation with respect to u. Let us differentiate (23) with respect to u_1 and set $u_1 = u_0$ and $\tilde{T}_1 = \tilde{T}_0$, i.e., $W_1 = W_0$. In the right-hand side of (23), $\hat{\hat{K}}$ is independent of u_1; hence, we have to differentiate only the operators $\hat{D}$. Obviously, the MEs of the matrix $K(W)$ do not depend on the velocity u if the cross section is independent of this velocity. As a rule, the cross section does not depend on the center-of-mass velocity of colliding particles, and hence, is independent of the reference frame velocity. Such a dependence may take place only in exotic cases when strong external electric and magnetic fields are present or at relativistic velocities of the particles. Thus, omitting such rare cases from consideration, we can argue that the derivative with respect to u_1 in (22) is equal to zero. Eventually, we have

$$0 = \left(\frac{d\hat{D}(W_1, W_0)}{du_1}\right)_{W_1=W_0} \hat{\hat{K}}(\hat{E}, \hat{E}) + \hat{E}\hat{\hat{K}}\left(\left(\frac{d\hat{D}(W_0, W_1)}{du_1}\right)_{W_1=W_0}, \hat{E}\right) + \hat{E}\hat{\hat{K}}\left(\hat{E}, \left(\frac{d\hat{D}(W_0, W_1)}{du_1}\right)_{W_1=W_0}\right). \quad (46)$$

Then, using derivatives (39) and (40) of the transition matrices with respect to the velocity (see the previous section) in the matrix form, we come to

$$0 = \sum_{r,l} K^{r,l}_{r_1',l_1',r_2',l_2'} \times \frac{2(-(l+1)\delta_{r',r}\delta_{l',l+1} + l(r+1)\delta_{r',r+1}\delta_{l',l-1})}{(2l+1)\sqrt{\tilde{T}_0}} + \sum_{r_1,l_1} K^{r',l'}_{r_1,l_1,r_2',l_2'} \times \frac{2((l_1'+1)\delta_{r_1,r_1'}\delta_{l_1,l_1'+1} - l_1'(r_1'+1)\delta_{r_1,r_1'+1}\delta_{l_1,l_1'-1})}{(2l_1'+1)\sqrt{\tilde{T}_0}} + \sum_{r_2,l_2} K^{r',l'}_{r_1',l_1',r_2,l_2} \times \frac{2((l_2'+1)\delta_{r_2,r_2'}\delta_{l_2,l_2'+1} - l_2'(r_2'+1)\delta_{r_2,r_2'+1}\delta_{l_2,l_2'-1})}{(2l_2'+1)\sqrt{\tilde{T}_0}}.$$

Performing summations with the Kronecker symbols, removing primes, and canceling by $2/\sqrt{\tilde{T}_0}$, we finally obtain

$$0 = -\frac{l}{2l-1} K^{r,l-1}_{r_1,l_1,r_2,l_2} + \frac{(l+1)r}{2l+3} K^{r-1,l+1}_{r_1,l_1,r_2,l_2} + \frac{l_1+1}{2l_1+1} K^{r,l}_{r_1,l_1+1,r_2,l_2} - \frac{l_1(r_1+1)}{2l_1+1} K^{r,l}_{r_1+1,l_1-1,r_2,l_2} + \frac{l_2+1}{2l_2+1} K^{r,l}_{r_1,l_1,r_2,l_2+1} - \frac{l_2(r_2+1)}{2l_2+1} K^{r,l}_{r_1,l_1,r_2+1,l_2-1}. \quad (47)$$

Here, we have omitted the argument of the ME, since this equality is valid in any given basis. We rewrite (47) in the more compact form

$$0 = \beta(l-1)K^{r,l-1}_{r_1,l_1,r_2,l_2} + \gamma(r-1,l+1)K^{r-1,l+1}_{r_1,l_1,r_2,l_2} - \beta(l_1)K^{r,l}_{r_1,l_1+1,r_2,l_2} - \gamma(r_1,l_1)K^{r,l}_{r_1+1,l_1-1,r_2,l_2} - \beta(l_2)K^{r,l}_{r_1,l_1,r_2,l_2+1} - \gamma(r_2,l_2)K_{r_1,l_1,r_2+1,l_2-1},$$

where

$$\beta(l) = -\frac{l+1}{2l+1}, \quad \gamma(r,l) = \frac{(r+1)l}{2l+1}.$$

These relations are supplemented by those between the MEs that result from the differentiation of (23) with respect to $\tilde{T}_1$ at $W_1 = W_0$. Applying the operator $d/d\tilde{T}_1$ to expression (23) in the matrix form at $W_1 = W_0$, taking into account that the operator $\hat{\hat{K}}$ in the right-hand side is independent of $\hat{T}_1$, and using derivatives (44) and (45) of the transition matrices with respect to temperature (see the previous section), we obtain

$$\tilde{T}\frac{d}{d\tilde{T}}K^{r,l}_{r_1,l_1,r_2,l_2}(\tilde{T}) = RK^{r,l}_{r_1,l_1,r_2,l_2}(\tilde{T}) + rK^{r-1,l}_{r_1,l_1,r_2,l_2}(\tilde{T}) - (r_1+1)K^{r,l}_{r_1+1,l_1,r_2,l_2}(\tilde{T}) - (r_2+1)K_{r_2+1,l_2,r_1,l_1}(\tilde{T}), \tag{48}$$

where

$$R = r_1 + r_2 - r + \frac{l_1 + l_2 - l}{2}. \tag{49}$$

In (48), T_0 is replaced by $\tilde{T}$, because this relation, like (47), is valid in any basis. Formulas (47) and (48) are the basic equations relating all the MEs in the axisymmetric case.

Equation (48) relates the MEs at fixed values l, l_1, and l_2. In the particular case $l = l_1 = l_2 = 0$, (48) and (49) yield the relation deduced in [8] for the isotropic case. Relations (47) and (48) obtained by us are valid for any kind of particle interaction.

As has been noted in [8, 9], for power interaction potentials, the cross section is factorized into an angular dependence and a power dependence on the relative velocity g. For the power dependence on g, the ME is proportional to T^μ irrespective of the form of the angular dependence, where μ is constant ($\mu = 0$ for Maxwellian molecules and $\mu = 0.5$ for solid spheres). Thus, in the case of power potentials (to be more precise, in the case of power dependence of the cross section on the velocity), (48) has the form

$$(R-\mu)K^{r,l}_{r_1,l_1,r_2,l_2}(\tilde{T}) + rK^{r-1,l}_{r_1,l_1,r_2,l_2}(\tilde{T}) - (r_1+1)K^{r,l}_{r_1+1,l_1,r_2,l_2}(\tilde{T}) - (r_2+1)K^{r,l}_{r_1,l_1,r_2+1,l_2}(\tilde{T}) = 0.$$

Analysis has shown that in the axisymmetric case, relations (47) and (48) constitute a complete set of equations relating the MEs. Higher order derivatives (including mixed) with respect to u and $\tilde{T}$ do not result in additional relations. A similar property for the isotropic case (upon differentiating with respect to $\tilde{T}$) was discussed in detail in [8, 9].

Thus, recurrent relations for the axisymmetric MEs $K^{r,l}_{r_1,l_1,r_2,l_2}$ have been obtained from the invariance of the collision integral under basis. These relations are always valid; in particular, they hold in the presence of a preferred spatial direction. Even in this case, using Eqs. (47) and (48) as recurrent relations, nonlinear MEs can be found from given isotropic and axisymmetric linear MEs. The use of these recurrent relations decreases the dimension of ME calculation by many orders of magnitude, making possible their application to solving problems requiring immense computational resources with the standard approach.

In the next paper, we will show that a series of additional relations between the MEs appears in the case of nondirectional particles, i.e., in the conventional kinetic theory of gases, where the collision integral has extra symmetry (Hecke theorem) [13]. This makes it possible to express any nonlinear ME via isotropic MEs through simple recurrent relations.

APPENDIX: AXISYMMETRIC HERMITIAN POLYNOMIALS IN α–u REPRESENTATION

For the axisymmetric case in the v space, the spherical Hermitian polynomials have the form of (4) and (5). In the basis (u_0,α_0), with regard for $c_0\cos\Theta = c_{0z}$, expressions (4) and (5) can be represented in the form

$$H_{r,l}(c_0, c_{0z}) = S^{(r)}_{l+1/2}(c_0^2)\sum_{k=0}^{[l/2]} b_{k,l}c_0^{2k}c_{0z}^{l-2k}. \tag{A1}$$

The distribution function $f(\mathbf{v})$ in the v space is related to its α–u representation by formula (11). In the α–u space, the expression $F(c_0^2)c_0^{2k}c_{0z}^j$, where $F(c_0^2)$ is an arbitrary function of the velocity magnitude c_0, is given by

$$\{\{F(c_0^2)c_0^{2k}c_{0z}^j\}_\alpha\}_u = \frac{(-1)^j e^{\alpha(u-u_0)^2}\delta^{(j)}(u-u_0)}{(2\alpha)^j\alpha^{3/2}\alpha_0^{-(k+j/2)}}\frac{d^k}{d\alpha^k}(\alpha^{3/2}\varphi(\alpha)). \tag{A2}$$

Here, $\delta^{(j)}(x)$ denotes the jth derivative of the δ function; double braces denote the representation of the function in the α–u space; and $\varphi(\alpha)$ is the α representation of the function $F(c_0^2)$:

$$F(c_0^2) = \int_0^\infty \left(\frac{\alpha}{\pi}\right)^{3/2} e^{-\frac{\alpha}{\alpha_0}c_0^2}\varphi(\alpha)d\alpha. \quad \text{(A3)}$$

Formula (A2) can easily be proven by substituting (A2) into (11) and integrating first with respect to u and then with respect to α by parts.

Two generalized functions are considered to be equal if their integration with an arbitrary finite function ψ yields the same result. Then, using the formula for the jth derivative of the product of two functions and the formula for a higher derivative of $e^{\alpha x^2}$ [14], one can show that the following equality is valid:

$$e^{\alpha(u-u_0)^2}\delta^{(j)}(u-u_0) = \sum_{p=0}^{[j/2]} q_{p,j}\alpha^p\delta^{(j-2p)}(u-u_0), \quad \text{(A4)}$$

$$q_{p,j} = \frac{j!}{p!(j-2p)!}.$$

Substituting (A4) into (A2), we find

$$\{\{F(c_0^2)c_0^{2k}c_{0z}^j\}_\alpha\}_u = \alpha_0^{k+j/2}\frac{(-1)^j}{(2\alpha)^j} \times \sum_{p=0}^{[j/2]} \frac{q_{p,j}\delta^{(j-2p)}(u-u_0)}{\alpha^{-p+3/2}}\frac{d^k}{d\alpha^k}(\alpha^{3/2}\varphi(\alpha)). \quad \text{(A5)}$$

Using (4) and (5), we have from (A5)

$$\{\{F(c_0^2)c_0^l P_l(\cos\Theta)\}_\alpha\}_u = \sum_{k=0}^{[l/2]} b_{k,l}\frac{(-1)^l\alpha_0^{l/2}}{(2\alpha)^{l-2k}} \times \sum_{p=0}^{\left[\frac{l}{2}-k\right]} \frac{q_{p,l-2k}\delta^{(l-2(k+p))}(u-u_0)}{\alpha^{-p+3/2}}\frac{d^k}{d\alpha^k}(\alpha^{3/2}\varphi(\alpha)). \quad \text{(A6)}$$

Substituting p for $k+p$ and interchanging the orders of summation, we obtain from (A6)

$$\{\{F(c_0^2)c_0^l P_l(\cos\Theta)\}_\alpha\}_u = \sum_{p=0}^{[l/2]} \frac{(-1)^l\delta^{(l-2p)}(u-u_0)\alpha_0^{l/2}}{2^l}A_{p,l}, \quad \text{(A7)}$$

where the function $A_{p,l}$ has the form

$$A_{p,l} = \sum_{k=0}^{p} \frac{b_{k,l}q_{p-k,l-2k}2^{2k}}{\alpha^{l-k-p+3/2}}\frac{d^k}{d\alpha^k}(\alpha^{3/2}\varphi(\alpha)). \quad \text{(A8)}$$

Let us substitute expression (5) for $b_{k,l}$ and expression (A4) for $q_{p,j}$ into (A8) and make use of the formula

$$\frac{(2m+2n-3)!!(-1)^n}{(2m-3)!!2^n\alpha^{m+n-1/2}} = \frac{d^n}{d\alpha^n}\left(\frac{1}{\alpha^{m-1/2}}\right).$$

Setting $n = p-k$ and $m = l-p+1$, we get

$$A_{p,l} = \frac{(-1)^p 2^p(2l-2p-1)!!\alpha^{p-1}}{p!(l-2p)!} \times \sum_{k=0}^{p}\binom{p}{k}\frac{d^{p-k}}{d\alpha^{p-k}}\left(\frac{1}{\alpha^{l-p+1/2}}\right)\frac{d^k}{d\alpha^k}(\alpha^{3/2}\varphi(\alpha)) \quad \text{(A9)}$$

$$= 2^{2p}b_{p,l}\alpha^{p-1}\frac{d^p}{d\alpha^p}\left(\frac{\varphi(\alpha)}{\alpha^{l-p-1}}\right).$$

Substituting (A9) into (A7), in the α–u representation, we finally find

$$\{\{F(c_0^2)c_0^l P_l(\cos\Theta)\}_\alpha\}_u = \alpha_0^{l/2}\sum_{p=0}^{[l/2]} b_{p,l} \times \frac{(-1)^l\delta^{(l-2p)}(u-u_0)\alpha^{p-1}}{2^{l-2p}}\frac{d^p}{d\alpha^p}\left(\frac{\varphi(\alpha)}{\alpha^{l-p-1}}\right). \quad \text{(A10)}$$

In the isotropic part of (A10), one may pass from the v space to the $\tilde{T}$, instead of α, space. In this case, the formula

$$F(c_0^2) = \int_0^\infty \left(\frac{1}{\tilde{T}\pi}\right)^{3/2} e^{-\frac{c_0^2}{\alpha_0\tilde{T}}}\tilde{\varphi}(\tilde{T})d\tilde{T}, \quad \left(\tilde{T} = \frac{1}{\alpha}\right) \quad \text{(A11)}$$

takes place instead of (A3).

It is clear that

$$\varphi(\alpha) = T^2\tilde{\varphi}(\tilde{T}). \quad \text{(A12)}$$

Let a function in the u–T representation be denoted as $\{\{\}_T\}_u$. Evidently,

$$\{\{\}_\alpha\}_u = \tilde{T}^2\{\{\}_T\}_u. \quad \text{(A13)}$$

It can be shown [15] that the equality

$$\alpha^{p-1}\frac{d^p}{d\alpha^p}\left(\frac{\varphi(\alpha)}{\alpha^{l-p-1}}\right) = \tilde{T}^2\frac{d^p}{d\tilde{T}^p}(\tilde{\varphi}(\tilde{T})\tilde{T}^l) \quad \text{(A14)}$$

is valid in the sense of generalized functions.

Taking into account (A13) and (A14) and canceling by $\tilde{T}^2$, we have the formula

$$\{\{F(c_0^2)c_0^l P_l(\cos\Theta)\}_u\}_T = \frac{(-1)^l}{\tilde{T}_0^{l/2}}\sum_{p=0}^{l[l/2]} b_{p,l}\frac{\delta^{(l-2p)}(u-u_0)}{2^{l-2p}}\frac{d^p}{d\tilde{T}^p}(\tilde{\varphi}(\tilde{T})\tilde{T}^l) \quad \text{(A15)}$$

in the u–T representation, along with α–u representation (A10).

Consider the product of Sonine polynomial (3) and the Maxwellian function as the function $F(c_0^2)$. As has been noted [16], a Sonine polynomial can be represented in the form

$$S_{l+1/2}^{(r)}(x) = \frac{1}{r!}\frac{d^r}{ds^r}\left(\left(\frac{1}{1-s}\right)^{l+3/2}\exp\left(-\frac{xs}{1-s}\right)\right)\Bigg|_{s=0}.$$

It is easy to see that after substituting y for $1 - s$ in this formula, the following relation is valid:

$$\left(\frac{\alpha_0}{\pi}\right)^{3/2} e^{-c_0^2} S_{l+1/2}^{(r)}(c_0^2) = \frac{(-1)^r}{r!}\tilde{T}_0^{l+r}\frac{d^r}{dy^r}\left(\frac{1}{y^l}\left(\frac{1}{\pi y}\right)^{3/2} e^{-(\mathbf{v}-\mathbf{u}_0)^2/y}\right)\Bigg|_{y=\tilde{T}_0}.$$

In the T space, we accordingly have

$$\tilde{s}_{r,l}^R(\tilde{T},\tilde{T}_0) = \{M(\tilde{T}_0,c_0)S_{l+1/2}^{(r)}(c_0^2)\} = \frac{\tilde{T}_0^{l+r}}{r!}\frac{\delta^{(r)}(\tilde{T}-\tilde{T}_0)}{\tilde{T}^l}. \quad \text{(A16)}$$

This can be shown by setting $\tilde{\varphi}(\tilde{T}) = \tilde{s}_{r,l}^R(\tilde{T}, \tilde{T}_0)$ in (A11) and using the properties of δ function derivatives.

After the substitution of (A16) into (A15), the $\tilde{T}$ dependence of the terms in (A15) takes the form

$$\frac{d^p}{d\tilde{T}^p}(\tilde{s}_{r,l}^R(\tilde{T},\tilde{T}_0)\tilde{T}^l) = \frac{\tilde{T}_0^{l+r}}{r!}\delta^{(p+r)}(\tilde{T}-\tilde{T}_0). \quad \text{(A17)}$$

Denoting the right map of the Hermitian polynomials in the u–T space by $h_{r,l}^R$, combining (A15)–(A17), and using (4), we finally have

$$h_{r,l}^R(W,W_0) = \{\{M(W_0,\mathbf{v})H_{r,l}(c_0^2,c_{0z})\}_u\}_T = \frac{(-1)^l\tilde{T}_0^{r+l/2}}{r!}\sum_{p=0}^{[l/2]}\frac{b_{p,l}}{2^{l-2p}}\delta^{(l-2p)}(u-u_0)\delta^{(p+r)}(\tilde{T}-\tilde{T}_0). \quad \text{(A18)}$$

Here, $b_{p,l}$ are coefficients of the Legendre polynomials (5). The Hermitian polynomials in the **v** space have orthogonal property (6). The functions h_i^R and H_i are related by the formula

$$M(W_0,\mathbf{v})H_i(\mathbf{c}_0) = \int M(W,\mathbf{v})h_i^R(W,W_0)dW. \quad \text{(A19)}$$

Let us substitute (A19) in (6) and interchange the orders of integration. Then, the inner integral with respect to **v** divided by the normalizing factor g_i will be referred to as the left mapping of the Hermitian polynomials into the u–$\tilde{T}$ space. We denote it by $h_i^L(W, W_0)$:

$$h_i^L(W,W_0) = \int M(W,\mathbf{v})H_i(\mathbf{c}_0)d^3(\mathbf{v}-\mathbf{u}_0)/g_i. \quad \text{(A20)}$$

Formulas (A19), (A20), and (6) specify the biorthonormality of the Hermitian polynomials in the u–T representation:

$$\int h_i^L(W,W_0)h_{i_1}^R(W,W_0)dW = \delta_{i,i_1}. \quad \text{(A21)}$$

The functions $h_i^L = h_{r,l}^L$ have the form

$$h_{r,l}^l(W,W_0) = \sum_{p=0}^{r}\frac{\tilde{a}_{p,r}^l\left(1-\frac{\tilde{T}}{\tilde{T}_0}\right)^{r-p}}{\tilde{T}_0^{p+l/2}}(u-u_0)^{l+2p}, \quad \text{(A22)}$$
$$\tilde{a}_{p,r}^l = a_{p,r}^l/g_{r,l}.$$

Here, $a_{p,r}^l$ are the coefficients of Sonine polynomial (3). At small values of the indices, the validity of formula (A22) can be verified by directly integrating formula (A20). In the general case, in order to prove the validity of (A22), it is sufficient to show that orthonormality condition (A21) is satisfied with such a definition of the left maps of the Hermitian polynomials. The proof is given in Section 2.

ACKNOWLEDGMENTS

This work was supported by the Russian Foundation for Basic Research (grants no. 00-02-16882 and 01-02-17903) and the Russian Federal Program “Integration” (grant no. AO 143).

REFERENCES

1. S. Chapman and T. G. Cowling, *Mathematical Theory of Non-Uniform Gases* (Cambridge Univ. Press, Cambridge, 1952; Inostrannaya Literatura, Moscow, 1960).
2. D. Burnett, Proc. London Math. Soc. **40**, 382 (1935).
3. H. Grad, Commun. Pure Appl. Math. **2**, 311 (1949).
4. K. Kumar, Ann. Phys. **37**, 113 (1966).
5. G. Turchetti and M. Paolilli, Phys. Lett. A **90**, 123 (1982).
6. A. Ya. Énder and I. A. Énder, Zh. Tekh. Fiz. **64** (10), 38 (1994) [Tech. Phys. **39**, 997 (1994)].
7. A. Ya. Énder and I. A. Énder, Zh. Tekh. Fiz. **68** (5), 18 (1998) [Tech. Phys. **43**, 493 (1998)].

8. A. Ya. Énder and I. A. Énder, Zh. Tekh. Fiz. **69** (6), 22 (1999) [Tech. Phys. **44**, 628 (1999)].
9. A. Ya. Enger and I. A. Enger, Phys. Fluids **9**, 2720 (1999).
10. L. Sirovich, Phys. Fluids **6**, 10 (1963).
11. I. A. Énder and A. Ya. Énder, Dokl. Akad. Nauk SSSR **193**, 61 (1970) [Sov. Phys. Dokl. **15**, 633 (1971)].
12. A. P. Prudnikov, Yu. A. Brychkov, and O. I. Marichev, *Integrals and Series* (Nauka, Moscow, 1981; Gordon and Breach, New York, 1986).
13. A. Ya. Énder, I. A. Énder, and M. B. Lyutenko, Preprint of the Ioffe Physicotechnical Institute, Russian Academy of Sciences, St. Petersburg, 2000, No. 1748.
14. I. S. Gradshteyn and I. M. Ryzhik, *Table of Integrals, Series, and Products* (Nauka, Moscow, 1963; Academic, New York, 1980).
15. A. Ya. Énder and I. A. Énder, Preprint of the Ioffe Physicotechnical Institute, Russian Academy of Sciences, St. Petersburg, 2000, No. 1747.
16. L. Waldmann, in *Handbuch der Physik*, Bd. 12: *Thermodynamik der Gase* (Springer-Verlag, Berlin, 1958; Moscow, 1970), p. 169.

Translated by M. Fofanov

Technical Physics, Vol. 47, No. 5, 2002, pp. 523–528. Translated from Zhurnal Tekhnicheskoĭ Fiziki, Vol. 72, No. 5, 2002, pp. 10–15.

THEORETICAL AND MATHEMATICAL PHYSICS

Effective Stopping of Relativistic Composite Heavy Ions Colliding with Atoms

V. I. Matveev

Pomor State University, Arkhangel'sk, 163006 Russia

e-mail: matveev.victor@pomorsu.ru

Received June 27, 2001; in final form, October 10, 2001

Abstract—A nonperturbative theory of energy loss by relativistic composite heavy highly charged ions colliding with atoms is developed. A simple formula for effective stopping is derived. By composite ions, we mean partially ionized atoms of heavy elements consisting of the ion core and several bound electrons that incompletely neutralize the ion core charge. Such ions, which have, as a rule, a high charge (for example, partly stripped uranium atoms), are used in many experiments performed with modern heavy ion accelerators. *© 2002 MAIK "Nauka/Interperiodica".*

INTRODUCTION

In calculations of ionization losses suffered by charged relativistic particles colliding with atoms, the particles are usually assumed to be point. To such objects, the perturbation theory is applied (see, e.g., [1–3]), which requires the inequality $Z/v \ll 1$ to be fulfilled (where Z is the charge of a projectile and v is the relative impact velocity). Hereafter, we use atomic units $\hbar = e = m_e = 1$, where $\hbar$ is the Planck constant and e and m_e are the charge and the mass of an electron, respectively. In recent experiments, the charges of the ions were so high that the Born approximation for them becomes, strictly speaking, invalid [4] even if $v \approx c$ (c is the speed of light, which equals ≈137 in terms of atomic units), because Z/v is often ≈1 (see [5–9] and Refs. therein). A nonperturbative theory of decelerating bare relativistic heavy ions by free electrons has recently been put forward [10]. In experiments, however, partly stripped ions are often used. In addition, when an ion moves in a medium, it acquires an equilibrium charge that is smaller than the charge of the bare ion core because of charge exchange processes and electron losses. When the impact parameter is small (large) or the momentum transfer is high (low), the ion behaves as a bare unscreened (screened) charge. In other words, it seems that an ion should be considered not as a point particle but as an extended composite particle of size comparable to the size of the electron shells occupied by electrons when the ion acquires the equilibrium (steady-state) charge. Such effects have been discussed in terms of the perturbation theory [11–14]. However, to adequately taking into account the presence of the electron coat of a relativistic heavy ion, a nonperturbative approach is needed.

In this work, we develop a nonperturbative theory of energy losses suffered by relativistic composite heavy highly charged ions colliding with atoms. A simple formula for effective stopping is derived.

1. INELASTIC CROSS SECTIONS

To calculate mean energy losses, we must know the cross sections of inelastic processes accompanying collisions between relativistic heavy ions with atoms. The application of the perturbation theory for describing collisions between highly charged ions and atoms, when $Z/v \sim 1$, is, strictly speaking, invalid because the Born approximation fails in this case. Since the domain of applicability of the Born approximation loses unitarity, the probability exceeds unity [15]. Note that if the charge of the ions is sufficiently high, the Born approximation remains invalid even for collision energies as high as desired. Nonperturbative approaches have been discussed in [16–19] (the sudden perturbation approximation), [20–22] (the eikonal approximation and its modifications), [23] (the numerical solution of the Dirac temporal equation), and [24, 25] (the exact solution of the Dirac equation in the ultrarelativistic limit). A nonperturbative approach that generalizes the Glauber approximation [26–29] for the case of inelastic relativistic ion–atom collisions has been suggested in [30–32]. According to [30, 31], the cross section of the transition of an N-electron atom from the state $|0\rangle$ (with an energy ε_0) to the state $|n\rangle$ (with an energy ε_n) when the atom meets a relativistic ion is given by

$$\sigma_n = \int d^2b \left| \left\langle n \left| \left[1 - \exp\left\{ -\frac{i}{v} \int dX U(X, \mathbf{b}; \{\mathbf{r}_a\}) \right\} \right] \right. \right. \times \gamma^{-N} S^{-2} \exp\left[i \sum_a \frac{x_a v}{c^2} (\varepsilon_n - \varepsilon_0) \right] \left. |0\rangle \right\rangle \right|^2, \quad (1)$$

1063-7842/02/4705-0523$22.00

where $\gamma = 1\sqrt{1 - v^2/c^2}$, $S^{-2} = \prod_{a=1}^{N} S_a^{-2}$, and S_a is the Lorentz transformation matrix for the wave function that acts on the bispinor indices of an atomic electron with a number a (related Dirac matrices are $\boldsymbol{\alpha}_a$). Note that $S_a^{-2} = \gamma(1 - \mathbf{v}\boldsymbol{\alpha}_a/c)$ [15]. The scattering potential $U = U(X, \mathbf{b}; \{\mathbf{r}_a\})$ is a function of the ion coordinate $\mathbf{R} = (X, \mathbf{b})$ and the positions of atomic electrons $\{\mathbf{r}_a\}$ ($a = 1, \ldots, N$), $\mathbf{r}_a = (x_a, y_a, z_a)$. The product d^2b in the integrand means that integration is over the impact parameter plane; specifically, in the polar coordinate system, $d^2b = bdbd\varphi$, where φ is the polar angle of the vector $\mathbf{b}$ in the impact parameter plane.

The designations X, $\mathbf{b}$, and $\mathbf{s}$ are explained in Fig. 1. The integrand in (1) is treated as the probability that an atom colliding with an impact parameter $\mathbf{b}$ passes from the state $|0\rangle$ to the state $|n\rangle$. In the ultrarelativistic limit, this probability thus represented is obviously coincident with the probability that is obtained upon using the exact expression for the transition amplitude in the ultrarelativistic case [24] and has a standard [26] nonrelativistic limit. For collisions between relativistic ions and nonrelativistic atoms, when $|0\rangle$ and $|n\rangle$ in (1) are double-component spinors, one can assume that $\gamma^{-N}S^{-2} = 1$ and $\exp[i\sum_a v x_a(\varepsilon_n - \varepsilon_0)/c^2] = 1$, so that formula (1) takes the simpler form

$$\sigma_n = \int d^2b \left| \left\langle n \left| 1 - \exp\left\{ -\frac{i}{v}\int dX U(X, \mathbf{b}; \{\mathbf{r}_a\}) \right\} \right| 0 \right\rangle \right|^2. \quad (2)$$

2. ENERGY LOSSES IN COLLISIONS WITH INDIVIDUAL ATOMS

Mean energy losses due to collisions are characterized by the effective stopping κ [26]. For simplicity, let us consider first the collision of a relativistic multiply charged ion with a hydrogen atom. As in [22], we divide the range $0 < b < \infty$ of the parameter b into three subranges:

$$\text{(A) } 0 < b < b_0; \text{ (B) } b_0 < b < b_1; \text{ (C) } b_1 < b < \infty, \quad (3)$$

which correspond to small, moderate, and large values of the impact parameters. We will calculate κ in each of them and find the effective stopping by adding the partial contributions. The exact values of the extremes of the subranges are of minor significance, since the dependence of κ on the parameters b_0 and b_1 turns out to be logarithmic in each of the subranges and we can correctly join together the contributions from adjacent subranges and, accordingly, find the dependence of κ on the joining parameters b_1 and b_0. (The domain of applicability for such an approach is discussed below in Section 3.)

(A) *The subrange of small impact parameters*, $0 < b < b_0$. In collisions with a small impact parameter or a high momentum transfer, atomic electrons can be assumed to be free and at rest prior to scattering [1] and the ion can be represented as a bare unscreened charge Z. Then, we can take advantage of the results obtained in [10]. According to numerical calculations [10], for $\gamma \le 10$ and the ion charges ≤ 92, energy losses can be expressed (with an accuracy of $\approx 1\%$) as

$$\kappa(b < b_0) = \frac{4\pi Z^2}{v^2}(L^{\text{pert}} + \Delta L_{\text{Bloch}} + \Delta L_{\text{Mott}}), \quad (4)$$

where

$$L^{\text{pert}} = \ln(b_0\gamma v\eta) - \frac{1}{2}\beta^2, \quad (5)$$

$\gamma = 1/\sqrt{1 - \beta^2}$, $\beta = v/c$, and $\eta = 1.781$, and the corrections ΔL_{Bloch} and ΔL_{Mott} are essentially nonzero [10] only if the impact parameter is small.

The Bloch correction [33] is given by

$$\Delta L_{\text{Bloch}} = -\text{Re}\,\psi\left(1 + i\frac{Z}{v}\right) + \psi(1), \quad (6)$$

where $\psi(z)$ is the logarithmic derivative of the gamma function [34].

If $\Delta L_{\text{Bloch}} = 0$ ($Z/v \ll 1$), the perturbation theory applies. The case $\Delta L_{\text{Bloch}} = \ln[v/(Z\eta)]$ corresponds to the classical collision conditions ($Z/v \gg 1$), since $\psi(1) = -\ln\eta$ and $\text{Re}\,\psi(1 + iZ/v) \longrightarrow -\ln(Z/v)$. The so-called Mott correction [35], ΔL_{Mott}, arises because of the difference between the Rutherford cross section and the exact cross section of quantum relativistic scattering [36] in the Coulomb field. The Mott correction value can be obtained only numerically; in applications, however, it is conveniently approximated (with

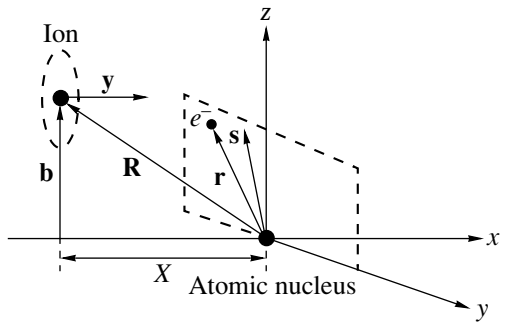

Fig. 1. Collision between an ion moving with a velocity $\mathbf{v}$ and a one-electron atom whose nucleus is placed at the origin. The x axis is aligned with the vector $\mathbf{v}$ and the plane yz is perpendicular to $\mathbf{v}$ and parallel to the impact parameter $\mathbf{b}$, so that the dashed rectangle lies in the impact parameter plane. Thus, the radius vector $\mathbf{R}$ of the ion is represented as $\mathbf{R} = (X, \mathbf{b})$, where X is the projection of $\mathbf{R}$ onto the x axis. The vector $\mathbf{r}$ is the radius vector of the atomic electron e^-, and the projection of $\mathbf{r}$ onto the impact parameter plane is represented by the vector $\mathbf{s}$.

an accuracy of ≈1% for the charge of the colliding ion $Z \le 92$ and $\gamma \le 10$) as [29, 37] $\Delta L_{\text{Mott}} = \ln f(Z, v)$, where

$$f(Z, v) = 1 + [0.222592\beta - 0.042948\beta^2 + (0.6016 + 5.15289\beta - 3.73293\beta^2)\alpha - (0.52308 + 5.71287\beta - 8.11358\beta^2)\alpha^2]^2, \quad \alpha = Z/c. \tag{7}$$

(B) *The subrange of moderate impact parameters*, $b_0 < b < b_1$. Let us restrict our consideration to collisions of an ion with light (the atomic nucleus charge $Z_a \ll Z$) nonrelativistic atoms. In this case, as in [11–14], we can neglect the excitation of the electronic shell of the ion and treat the striking composite ion as an extended charge. In this subrange, it is assumed that an atomic electron gains a momentum $\ll c$ as a result of the collisions, so that it can be viewed as nonrelativistic both before and after the collisions (the related values of b_0 and b_1 are evaluated in Section 3). Then, we can use formula (2) for the cross section with the potential in the Coulomb static form. Following [11–14, 38], we assume that the core of the striking ion has a charge Z and its N_i electrons are distributed around the core with a density

$$\rho(r) = -\frac{N_i}{4\pi\lambda^3}\frac{\lambda}{r}\exp\left[\frac{r}{\lambda}\right],$$

where λ is the screening parameter.

The Coulomb interaction of an ion located at a point **R** with an atomic electron located at a point **r** is described as

$$U(\mathbf{R}, \mathbf{r}) = -\frac{Z(1-\nu)}{|\mathbf{r}-\mathbf{R}|} - \frac{Z\nu}{|\mathbf{r}-\mathbf{R}|}\exp\left(-\frac{1}{\lambda}|\mathbf{r}-\mathbf{R}|\right),$$

where $\nu = N_i/Z$ is the relative number of electrons of the ion.

In calculating the eikonal phase, the coordinates of the electron and the ion are usually written in terms of the parameters **b** and **s**, where **b** is the impact parameter and **s** is the projection of the radius vector $\mathbf{r} = (x, \mathbf{s})$ of the atomic electron on the impact parameter plane $\mathbf{R} = (X, \mathbf{b})$. The standard expedient [16, 29] used for calculating the eikonal phase for the Coulomb potential is as follows: $U(\mathbf{R}, \mathbf{r}) = U((X, \mathbf{b}); (x, \mathbf{s}))$ is replaced by $U'((X, \mathbf{b}); (x, \mathbf{s})) = U((X, \mathbf{b}); (x, \mathbf{s})) - U((X, \mathbf{b}); (x, 0))$ and the prime in the integral of $U'dX$ is omitted. Integration yields

$$\frac{i}{v}\int_{-\infty}^{+\infty} U dX = 2i\frac{Z^*}{v}\ln\frac{|\mathbf{b}-\mathbf{s}|}{b} + 2i\nu\frac{Z}{v}\left[K_0\left(|\mathbf{b}-\mathbf{s}|\frac{1}{\lambda}\right) - K_0\left(\frac{b}{\lambda}\right)\right], \tag{8}$$

where $Z^* = Z(1-\nu)$ and $K_0(x)$ and $K_1(x)$ are the Macdonald functions.

A specific feature of collisions between multiply charged ions and atoms is that the inelastic cross sections are, as a rule, rather large and far exceed atomic sizes. With this in mind, we assume that $s/b \ll 1$. Then, expression (8) can be recast as

$$\frac{i}{v}\int_{-\infty}^{+\infty} U dX = i\mathbf{qs}, \tag{9}$$

where the vector

$$\mathbf{q} = \frac{2Z(1-\nu)}{vb}\left[1 + \frac{\nu}{1-\nu}\frac{b}{\lambda}K_1\left(\frac{b}{\lambda}\right)\right]\frac{\mathbf{b}}{b} \tag{10}$$

obviously has the meaning of the momentum gained by the atomic electron colliding with the ion at a given impact parameter **b** (in (9) **qs** is the scalar product). The limit values of **q** have the clear physical meaning: $\mathbf{q} \longrightarrow 2Z(1-\nu)\mathbf{b}/(vb^2)$ at $b \longrightarrow \infty$ corresponds to scattering by a screened ion of charge $Z(1-\nu)$, while $\mathbf{q} \longrightarrow 2Z\mathbf{b}/(vb^2)$ at $b \longrightarrow 0$ corresponds to scattering by a bare ion of charge Z. Note that the vector **q** can alternatively be represented through the effective impact-parameter-dependent ion charge $Z(b)$:

$$\mathbf{q} = \frac{\mathbf{b}}{b}\frac{2Z(b)}{vb}, \quad Z(b) = Z\left[1 - \nu\left(1 - \frac{b}{\lambda}K_1\left(\frac{b}{\lambda}\right)\right)\right].$$

Thus, inelastic cross section (2) for orthogonal $|n\rangle$ and $|0\rangle$ takes the form

$$\sigma_n = \int d^2b\left|\left\langle n\left|\exp\left(-\frac{i}{v}\int_{-\infty}^{+\infty} U dX\right)\right|0\right\rangle\right|^2 = \int d^2b|\langle n|\exp(-i\mathbf{qr})|0\rangle|^2 = \int d^2b|f_{0n}|^2,$$

where $f_{0n} = \langle n|\exp(-i\mathbf{qr})|0\rangle$ is the generalized form factor.

The effective stopping is given by

$$\kappa = \sum_n(\varepsilon_n - \varepsilon_0)\sigma_n = \sum_n(\varepsilon_n - \varepsilon_0)\int d^2b|f_{0n}|^2, \tag{11}$$

where $f = \exp(-i\mathbf{qr})$.

According to [26], one easily finds that

$$\sum_n(\varepsilon_n - \varepsilon_0)|f_{0n}|^2 = \frac{1}{2}(\nabla f\,\nabla f^+)_{00} = \frac{1}{2}q^2, \tag{12}$$

where $\nabla = \partial/\partial\mathbf{r}$; then, according to (10),

$$q^2 = \left(\frac{2Z(1-\nu)}{vb}\right)^2\left[1 + \frac{2\nu}{1-\nu}\frac{b}{\lambda}K_1\left(\frac{b}{\lambda}\right) + \frac{\nu^2}{(1-\nu)^2}\frac{b^2}{\lambda^2}K_1^2\left(\frac{b}{\lambda}\right)\right]. \tag{13}$$

Therefore, the effective stopping in the subrange $b_0 < b < b_1$ is represented as

$$\kappa(b_0 < b < b_1) = \frac{1}{2}\int_{b_0}^{b_1} q^2 2\pi b\,db = 4\pi\frac{Z^2(1-\nu)^2}{v^2}[I_1 + I_2 + I_3], \quad (14)$$

where

$$I_1 = \int_{b_0}^{b_1}\frac{db}{b} = \ln\frac{b_1}{b_0},$$

$$I_2 = \frac{2\nu}{1-\nu}\int_{b_0}^{b_1}\frac{b}{\lambda}K_1\left(\frac{b}{\lambda}\right)db = \frac{2\nu}{1-\nu}\left[K_0\left(\frac{b_1}{\lambda}\right) - K_0\left(\frac{b_0}{\lambda}\right)\right], \quad (15)$$

$$I_3 = \frac{\nu^2}{(1-\nu)^2}\int_{b_0}^{b_1}\frac{b}{\lambda^2}K_1^2\left(\frac{b}{\lambda}\right)db = \frac{\nu^2}{(1-\nu)^2} \times\left[-\frac{x^2}{2}\left\{\left[\frac{dK_1(x)}{dx}\right]^2 - K_1^2(x)\left(1+\frac{1}{x^2}\right)\right\}\right]\Bigg|_{b_0/\lambda}^{b_1/\lambda}.$$

We will also assume (see Section 3) that

$$\frac{b_0}{\lambda} \ll 1, \quad \frac{b_1}{\lambda} \gg 1. \quad (16)$$

The asymptotics of the Macdonald functions are as follows.

At small x,

$$K_0(x) \longrightarrow \ln\frac{2}{\eta x}, \quad \eta = 1.781; \quad K_1(x) \longrightarrow \frac{1}{x}$$

at large x,

$$K_\nu(x) \longrightarrow \sqrt{(\pi/2x)}\exp(-x).$$

Therefore, with conditions (16) met, we have

$$I_2 = \frac{2\nu}{(1-\nu)}\ln\frac{b_1}{b_0}, \quad I_3 = \frac{\nu^2}{(1-\nu)^2}\ln\frac{2\lambda}{\eta b_0}.$$

Substituting these values into formula (14), one finds the contribution to the effective stopping from the subrange of moderate impact parameters:

$$\kappa(b_0 < b < b_1) = 4\pi\frac{Z^2(1-\nu)^2}{v^2} \times\left[\ln\frac{b_1}{b_0} + \frac{2\nu}{1-\nu}\ln\frac{2\lambda}{\eta b_0} + \frac{v^2}{(1-\nu)^2}\ln\frac{2\lambda}{\eta b_0}\right] \quad (17)$$

$$= \frac{4\pi Z^2(1-\nu)^2}{v^2}\ln b_1 + \frac{4\pi Z^2}{v^2}\ln\left[\frac{1}{b_0}\left(\frac{2\lambda}{\eta}\right)^{\nu(2-\nu)}\right].$$

(C) *The subrange of large impact parameters,* $b_1 < b < \infty$. Here, ion–atom interaction can be considered in terms of the perturbation theory. At large impact parameters, the atom experiences the field of the screened ion; that is, the apparent charge of the ion equals $Z^* = Z(1-\nu)$. The related effective stopping is [22]

$$\kappa(b > b_1) = 4\pi\frac{(Z^*)^2}{v^2}\left\{\ln\frac{2v}{\eta I b_1\sqrt{1-\beta^2}} - \beta^2/2\right\}. \quad (18)$$

Following [1, Sec. 82], we have introduced the "mean atomic energy" I:

$$\ln I = \frac{\Sigma_n(\varepsilon_n - \varepsilon_0)|x_{0n}|^2\ln(\varepsilon_n - \varepsilon_0)}{\Sigma_n(\varepsilon_n - \varepsilon_0)|x_{0n}|^2}, \quad x_{0n} = \langle n|x|0\rangle. \quad (19)$$

The total stopping is obtained by adding the contributions from the three subranges:

$$\kappa = \kappa(b < b_0) + \kappa(b_0 < b < b_1) + \kappa(b > b_1).$$

Eventually,

$$\kappa = \frac{4\pi Z^2(1-\nu)^2}{v^2}\left(\ln\frac{2v}{\eta I\sqrt{1-\beta^2}} - \frac{\beta^2}{2}\right) + \frac{4\pi Z^2}{v^2}\left(\ln\frac{v\eta}{\sqrt{1-\beta^2}} - \frac{\beta^2}{2} + \ln\left[\left(\frac{2\lambda}{\eta}\right)^{\nu(2-\nu)}\right] + \Delta L_{\text{Bloch}} + \Delta L_{\text{Mott}}\right). \quad (20)$$

This formula can conventionally be generalized for collisions between heavy relativistic composite ions and complex atoms [26]: its left-hand side is multiplied by the number N_a of atomic electrons, and characteristics (19) are calculated for the complex atom. Moreover, it is easy to see that, within this approach, one can directly take into account the fact that the number N_i of ion electrons (and hence v) becomes dependent on the target parameters, ion charge, and relative impact velocity if capture and losses are included into consideration.

3. THE APPLICABILITY DOMAIN OF THE APPROACH

The extremes of subranges (3) and the validity of the approach need additional comments. The small parameter subrange $0 < b < b_0$ is the domain of applicability for the Lindhard–Sorensen approach [10], which is valid when the angular momentum $l_0 = v\gamma b_0 \gg 1$ (i.e., $b_0 \gg 1/(v\gamma)$). The subrange of moderate impact parameters $b_0 < b < b_1$ is the domain of applicability for the eikonal approximation, which is valid only if atomic electrons remain fixed for a collision time τ [26–30]

($\tau \approx b\sqrt{1-\beta^2}/v$ [29, 30]). In other words, the collision time must be much less than the characteristic atomic time ($\tau \ll 1$). In this case, the impact parameter is bounded from above: $b_1 \ll v/\sqrt{1-\beta^2}$. Moreover, the eikonal approximation in the form of (2) applies [29–31] if an atomic electron, having collided with a relativistic ion, remains nonrelativistic; i.e., its velocity increases by $\Delta v \ll c$ in the Coulomb field ($\Delta v \approx 2Z/(vb)$. From this condition, we find that the impact parameter is bounded from below as $b_0 \gg 2Z/(vc)$. Thus, the extremes of the subranges satisfy the following inequalities:

$$b_0 \gg 1/(v\gamma); \quad b_0 \gg 2Z/(vc); \quad b_1 \gg v\gamma. \qquad (21)$$

Since the correct joining implies that the extremes of the subranges are rejected from formula (20), we required that inequalities (16), which can now be recast in the more convenient form

$$1/(\gamma v) \ll \lambda \ll \gamma v; \quad \gamma = 1/\sqrt{1-\beta^2}, \qquad (22)$$

be satisfied.

It is easy to see that inequalities (21) and (22) are compatible and can be satisfied in many practical cases where collisions between heavy relativistic ions and nonrelativistic light ($Z_a \ll Z$) atoms are investigated (including the case $Z \le 92$ and $\gamma \le 10$ touched upon in this work). It should also be noted that, although inequality (22) holds in a wide range of the screening parameter λ, it does not allow one to directly pass to the limit $\lambda \longrightarrow 0$ or $\lambda \longrightarrow \infty$ in formula (20).

4. ESTIMATES

Thus, the total effective stopping κ of a composite ion with a charge $Z^* = Z(1-\nu)$ containing $N_i = \nu Z$ electrons and having a core charge Z can be found by formula (20). Note that the ion was considered as an extended charge. We introduce a correction for ion charge extent $\delta\kappa = \kappa - \kappa_{point}$ and a relative correction $\chi = (\kappa - \kappa_{point})/\kappa_{point}$, where κ_{point} is the effective stopping [3] of the point core with a charge Z^*:

$$\kappa_{point} = \frac{4\pi(Z^*)^2}{v^2}\left(\ln\frac{2v^2}{I(1-\beta^2)} - \beta^2 + \Delta L_{Bloch} + \Delta L_{Mott}\right). \qquad (23)$$

The behavior of the relative correction χ is shown in Fig. 2. The need for the nonperturbative computing method at large Z is illustrated in Fig. 3, where the values of $\delta\kappa/(\delta\kappa)_{Born}$ are plotted. Here, $(\delta\kappa)_{Born}$ is the value of $\delta\kappa$ calculated in the Born approximation [that is, with formulas (20) and (23) at $\Delta L_{Bloch} = 0$ and $\Delta L_{Mott} = 0$]. In the calculations, the screening parameter λ was calculated by the formula [12, 14]

$$\lambda = g\frac{\nu^{2/3}}{1-\nu/7}\frac{a}{Z^{1/3}}, \quad g = 0.3(3\pi^2/50)\Gamma(1/3) \approx 0.48,$$

where a is the Bohr radius (basically, a can be considered as the parameter taking into account the effective size of an ion in the presence of excited electronic shells).

In commonly encountered cases $Z \gg 1$ and $Z^* \gg 1$ ($\nu \ll 1$), we can leave only terms linear in ν; then,

$$\kappa = \frac{4\pi(Z^*)^2}{v^2}\left(\ln\frac{2v^2}{I(1-\beta^2)} - \beta^2 + \Delta L_{Bloch} + \Delta L_{Mott}\right)$$
$$+ \frac{8\pi(Z^*)^2}{v^2}\nu\left(\ln\frac{2v\lambda}{\eta\sqrt{1-\beta^2}} + \Delta L_{Bloch} + \Delta L_{Mott}\right. \qquad (24)$$
$$\left. - \frac{Z^*}{2}\frac{d}{dZ^*}(\Delta L_{Bloch} + \Delta L_{Mott})\right),$$

where ΔL_{Bloch} and ΔL_{Mott} and their derivatives are calculated, as in (23), for the point charge Z^*. Here, the first term is the effective stopping of a point ion of charge

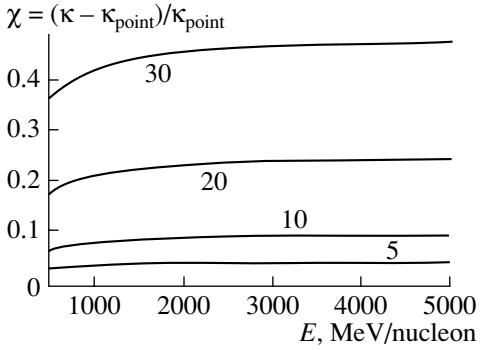

Fig. 2. Relative correction χ vs. striking ion energy for the ion core charge $Z = 92$. Figures at the curves stand for the number N_i of screening electrons.

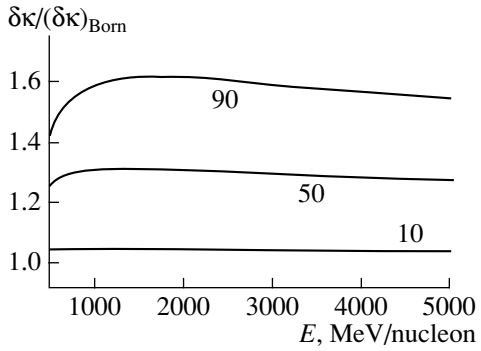

Fig. 3. $\delta\kappa/(\delta\kappa)_{Born}$ vs. striking ion energy for $\nu = 0.2$. Figures at the curves indicate the values of the ion core charge Z.

Z^*, while the second one is the correction for ion size finiteness. Thus, with the extent of an ion taken into account, the effective stopping κ of the ion rises noticeably compared with the stopping κ_{point} for a point ion of the same charge Z^*. The order of the energy loss can be estimated as $(\kappa - \kappa_{point})/\kappa_{point} \geq \nu$. For example, an atom of uranium with ten bound electrons experiences stopping about 10% stronger than a bare point core of charge 82 and of the same mass.

ACKNOWLEDGMENTS

The author thanks the Ministry of Education of the Russian Federation and the Russian Foundation for Basic Research for the financial support.

REFERENCES

1. V. B. Berestetskii, E. M. Lifshitz, and L. P. Pitaevskii, *Course of Theoretical Physics*, Vol. 4: *Quantum Electrodynamics* (Nauka, Moscow, 1989; Pergamon, New York, 1982).
2. P. Sigmund, Nucl. Instrum. Methods Phys. Res. B **135**, 1 (1998).
3. S. P. Ahlen, Rev. Mod. Phys. **52**, 121 (1980).
4. J. Eichler and W. E. Meyrhof, *Relativistic Atomic Collisions* (Academic, New York, 1995).
5. C. Scheidenberger, H. Geissel, Th. Stohlker, *et al.*, Nucl. Instrum. Methods Phys. Res. B **90**, 36 (1994).
6. C. Scheidenberger, H. Geissel, H. H. Mikelsen, *et al.*, Phys. Rev. Lett. **77**, 3987 (1996).
7. C. Scheidenberger and H. Geissel, Nucl. Instrum. Methods Phys. Res. B **135**, 25 (1998).
8. H. Weick, H. Geisel, and C. Scheidenberger, Nucl. Instrum. Methods Phys. Res. B **164**, 168 (2000).
9. E. E. Zhurkin and S. D. Bogdanov, Nucl. Instrum. Methods Phys. Res. B **164/165**, 230 (2000).
10. J. Lindhard and A. Sorensen, Phys. Rev. A **53**, 2443 (1996).
11. G. L. Yudin, Zh. Tekh. Fiz. **55**, 9 (1985) [Sov. Phys. Tech. Phys. **30**, 4 (1985)].
12. G. Maynard, D. Gardes, M. Chabot, *et al.*, Nucl. Instrum. Methods Phys. Res. B **146**, 88 (1998).
13. G. Maynard, K. Katsonis, G. Zwicknagel, *et al.*, Nucl. Instrum. Methods Phys. Res. A **415**, 687 (2000).
14. G. Maynard, M. Chabot, and D. Gardes, Nucl. Instrum. Methods Phys. Res. B **164/165**, 139 (2000).
15. J. Eichler, Phys. Rep. **193**, 167 (1990).
16. J. Eichler, Phys. Rev. A **15**, 1856 (1977).
17. A. Salop and J. H. Eichler, J. Phys. B **12**, 257 (1979).
18. G. L. Yudin, Zh. Éksp. Teor. Fiz. **80**, 1026 (1981) [Sov. Phys. JETP **53**, 523 (1981)].
19. V. I. Matveev and M. M. Musakhanov, Zh. Éksp. Teor. Fiz. **105**, 280 (1994) [JETP **78**, 149 (1994)].
20. J. H. McGuire, Phys. Rev. A **26**, 143 (1982).
21. D. S. F. Crothers and S. H. McCann, J. Phys. B **16**, 3229 (1983).
22. V. I. Matveev and S. G. Tolmanov, Zh. Éksp. Teor. Fiz. **107**, 1780 (1995) [JETP **80**, 989 (1995)].
23. U. Becker, N. Grun, W. Scheid, and G. Soff, Phys. Rev. Lett. **56**, 2016 (1986).
24. A. J. Baltz, Phys. Rev. Lett. **78**, 1231 (1997).
25. A. J. Baltz, Phys. Rev. A **61**, 042701 (2000).
26. L. D. Landau and E. M. Lifshitz, *Course of Theoretical Physics*, Vol. 3: *Quantum Mechanics: Non-Relativistic Theory* (Nauka, Moscow, 1989, 4th ed.; Pergamon, New York, 1977, 3rd ed.).
27. M. L. Goldberger and K. M. Watson, *Collision Theory* (Wiley, New York, 1964; Mir, Moscow, 1967).
28. N. F. Mott and H. S. W. Massey, *The Theory of Atomic Collisions* (Clarendon, Oxford, 1965; Mir, Moscow, 1969).
29. V. I. Matveev, Fiz. Élem. Chastits At. Yadra **26**, 780 (1995) [Phys. Part. Nucl. **26**, 329 (1995)].
30. V. I. Matveev and Kh. Yu. Rakhimov, Zh. Éksp. Teor. Fiz. **114**, 1646 (1998) [JETP **87**, 891 (1998)].
31. V. I. Matveev, Kh. Yu. Rakhimov, and D. U. Matrasulov, J. Phys. B **32**, 3849 (1999).
32. V. I. Matveev and D. U. Matrasulov, J. Phys. B **33**, 2721 (2000).
33. F. Bloch, Ann. Phys. (Leipzig) **16**, 285 (1933).
34. *Handbook of Mathematical Functions*, Ed. by M. Abramowitz and I. A. Stegun (National Bureau of Standards, Washington, 1964; Nauka, Moscow, 1979).
35. N. F. Mott, Proc. R. Soc. London, Ser. A **124**, 425 (1929).
36. J. A. Doggett and L. V. Spenser, Phys. Rev. **103**, 1597 (1956).
37. V. I. Matveev and S. G. Tolmanov, Zh. Tekh. Fiz. **68** (2), 9 (1998) [Tech. Phys. **43**, 138 (1998)].
38. W. Brandt and M. Kitagawa, Phys. Rev. B **25**, 5631 (1982).

Translated by V. Isaakyan

Technical Physics, Vol. 47, No. 5, 2002, pp. 529–534. Translated from Zhurnal Tekhnicheskoĭ Fiziki, Vol. 72, No. 5, 2002, pp. 16–21.

THEORETICAL AND MATHEMATICAL PHYSICS

Vibration of a Flexible Plate in Contact with the Free Surface of a Heavy Liquid

V. V. Alekseev, D. A. Indeĭtsev, and Yu. A. Mochalova

Institute of Problems in Machine Science, Russian Academy of Sciences, Vasil'evskiĭ ostrov, Bol'shoĭ pr. 61, St. Petersburg, 199178 Russia

Received August 1, 2001

Abstract—Free vibration of a flexible plate floating on the free surface of a perfect incompressible finite-depth heavy liquid are studied. The problem is solved in the shallow water approximation. Conditions for the existence of discrete frequencies below the waveguide cutoff frequency and associated localized (nonpropagating) liquid vibration modes in the plate–liquid system are determined. © *2002 MAIK "Nauka/Interperiodica".*

INTRODUCTION

In the last decade, a variety of works devoted to the dynamic contact interaction of thin flexible plates with the liquid surface has appeared. The need for solving such problems arises in the analysis of the dynamics of extended floating platforms (floating airfields). Constructions of this type have been examined, e.g., in [1–4]. Resonance structure–liquid interaction has received the bulk of attention. Another issue of interest is the localization of wave processes in the liquid near the contact with a floating construction [2]. The latter problem seems to be topical, since when the structure vibration is localized in the surrounding volume of the liquid, the vibration amplitude is maximal because of the lack of radiation into the environment. It has been shown [4] that such localized processes are absent for the case of a round floating plate: its vibration is accompanied by energy removal in the form of waves propagating over the liquid surface.

The problem of the existence of localized vibration modes in an infinite continuum in the presence of elastically deformable body has been the subject of much investigation [5–7]. It has been shown that the problem is reduced to the existence of a discrete real spectrum of vibration natural frequencies. This work is aimed at confirming the fact that a model of floating structures in the form of thin plates in contact with the liquid surface in a finite-depth flat-bottom channel results in practically unfeasible conditions for resonant vibration described above if the shallow water approximation is used. The effect of bottom relief, as well as the choice of another model of a floating structure, demands special attention.

STATEMENT OF THE PROBLEM

Let a flexible plate of infinite length and width $2a$ float on the surface of a channel of finite depth H. The channel is filled with a perfect incompressible heavy liquid. The statement of the problem is linear. Let the origin be at the bottom of the channel, and the y axis be directed along the plate length. The z axis is directed upward through the center of the plate (see the figure). We consider small-amplitude vibrations of the liquid and the plate. The motion of the plate is specified by the function $W(x, y, t)$ and is described by the equation

$$M\frac{\partial^2 W}{\partial t^2} + D\left(\frac{\partial^4 W}{\partial x^4} + \frac{\partial^4 W}{\partial x^2 \partial y^2} + \frac{\partial^4 W}{\partial y^4}\right) = P(x, y, t), \quad (1)$$

where $W(x, y, t)$ is the displacement of the plate surface from the equilibrium position, $M = \rho_0\delta$ is the mass of the plate per unit area, $D = E\delta^3/12$ is the modulus of rigidity, ρ_0 is the material density, δ is the plate thickness, E is Young's modulus, and P is the pressure the liquid exerts on the plate.

The boundary conditions to be met at the edges of the plate are the absence of the bending moment and

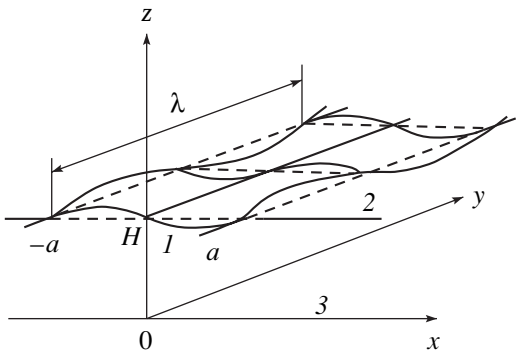

Flexible plate on the liquid surface: (*1*) plate; (*2*) free liquid surface; and (*3*) channel bottom. λ is the wavelength.

1063-7842/02/4705-0529$22.00 © 2002 MAIK "Nauka/Interperiodica"

shear force:

$$\frac{\partial^2 W}{\partial x^2} + \mu\frac{\partial^2 W}{\partial y^2} = 0, \quad x = \pm a,$$
$$\frac{\partial^3 W}{\partial x^3} + (2-\mu)\frac{\partial^3 W}{\partial x \partial y^2} = 0, \quad x = \pm a, \tag{2}$$

where μ is Poisson's ratio of the plate material.

The motion of the liquid is assumed to be potential, that is, defined by the velocity potential $\Phi(x, y, z, t)$ that satisfies the Laplace equation

$$\nabla^2\Phi = 0 \tag{3}$$

with the boundary conditions

$$\frac{\partial\Phi}{\partial z} = 0 \tag{4}$$

at the channel bottom ($z = 0$) and

$$\frac{\partial\Phi}{\partial z} = \frac{\partial W}{\partial t} \quad (|x| \le a), \quad \frac{\partial\Phi}{\partial z} = -\frac{1}{g}\frac{\partial^2\Phi}{\partial t^2} \quad (|x| > a), \tag{5}$$

on the free surface of the liquid ($z = H$), where g is the gravitational acceleration.

The pressure experienced by the plate is given by

$$P(x, y, t) = -\rho\frac{\partial\Phi}{\partial t}\bigg|_{z=H} - \rho g W, \tag{6}$$

where ρ is the density of the liquid.

A solution will be sought in the form of surface waves propagating along the y axis and decaying along the x axis; that is,

$$\Phi(x, y, z, t) \longrightarrow 0 \tag{7}$$

at $x \longrightarrow \pm\infty$.

To find the motion of the plate floating on the surface, it is necessary to know the distribution of the hydrodynamic pressure acting on the plate.

HYDRODYNAMIC FORCES ACTING ON THE PLATE

A solution to Eqs. (1)–(7) will be sought in the form of waves propagating along the y axis with a wave number m and an arbitrary frequency ω:

$$\Phi(x, y, z, t) = \mathrm{Re}\{\varphi(x, z)\exp[i(my - \omega t)]\},$$
$$W(x, y, t) = \mathrm{Re}\{w(x)\exp[i(my - \omega t)]\}. \tag{8}$$

Substituting (8) into Eqs. (1)–(7) yields the boundary-value problem for $\varphi(x, z)$ and $w(x)$:

$$\frac{\partial^2\varphi}{\partial x^2} + \frac{\partial^2\varphi}{\partial z^2} = m^2\varphi, \tag{9}$$

$$\frac{\partial\varphi}{\partial z} = 0, \quad z = 0, \tag{10}$$

$$\frac{\partial\varphi}{\partial z} = \phi(x) = \begin{cases} -i\omega w, & |x| \le a \\ \dfrac{\omega^2}{g}\varphi, & |x| > a \end{cases} \quad z = H, \tag{11}$$

$$D\left[\frac{\partial^4 w}{\partial x^4} - 2m^2\frac{\partial^2 w}{\partial x^2} + m^4 w\right] - M\omega^2 w = p(x). \tag{12}$$

Here, $\varphi \longrightarrow 0$ at $x \longrightarrow \infty$. The pressure $p(x)$ is given by

$$p(x) = \rho(i\omega\varphi - g w). \tag{13}$$

Boundary conditions (2) are written in the form

$$\frac{\partial^2 w}{\partial x^2} - \mu m^2 w = 0, \quad \frac{\partial^3 w}{\partial x^3} - (2-\mu)m^2\frac{\partial w}{\partial x} = 0, \quad x = \pm a. \tag{14}$$

Applying Fourier transformations to (9)–(11) with respect x, we obtain

$$\frac{\partial^2\varphi^F}{\partial z^2} - (k^2 + m^2)\varphi^F = 0,$$
$$\frac{\partial\varphi^F}{\partial z} = 0, \quad z = 0, \tag{15}$$
$$\frac{\partial\varphi^F}{\partial z} = \phi^F(k), \quad z = H,$$

where

$$\varphi^F(k, z) = \int_{-\infty}^{\infty}\varphi(x, z)\exp(-ikx)dx,$$
$$\phi^F(k) = \int_{-\infty}^{\infty}\phi(x)\exp(-ikx)dx. \tag{16}$$

The solution to boundary problem (15) has the form

$$\varphi^F(z) = \frac{\cosh(z(k^2 + m^2)^{1/2})}{(k^2 + m^2)^{1/2}\sinh(H(k^2 + m^2)^{1/2})}\phi^F(k).$$

The backward Fourier transformation of $\varphi^F(z)$ with respect to k at $z = H$ with the use of convolution yields

$$\varphi(x, m, H) = \int_{-\infty}^{\infty}\phi(\xi)G(|x - \xi|)d\xi, \tag{17}$$

where the function $G(x)$ has the form

$$G(x) = \frac{1}{2\pi}\int_{-\infty}^{\infty}\frac{\cosh(H(k^2 + m^2)^{1/2})}{(k^2 + m^2)^{1/2}\sinh(H(k^2 + m^2)^{1/2})} \times \exp(ikx)dk. \tag{18}$$

Let us substitute the function $\phi(x)$, defined by (11), into expression (17). Then, assuming that the liquid flow and the plate vibrations are symmetric about the y axis, we will come to the integral relationship

$$\varphi_{1,2}(x, m, H) = -i\omega\int_{-a}^{a} w(\xi, m)G(|x-\xi|)d\xi + \frac{\omega^2}{g}\int_{a}^{\infty}\varphi_2(\xi, m, H)[G(|x+\xi|) + G(|x-\xi|)]d\xi. \quad (19)$$

Here, the potential $\varphi(x, m, H)$ equals φ_1 for $|x| < a$ and φ_2 for $|x| > a$. Relationship (19) is an integral equation for the potential $\varphi_2(x, m, H)$ outside the plate. Having found $\varphi_2(x, m, H)$, one can determine the potential $\varphi_1(x, m, H)$ under the plate.

Now let us find the explicit form of the function $G(x)$, given by (18). We will integrate the right-hand side of (18) over the complex plane using the residue theorem. The integrand in (18) has first-order poles at points $k = \pm ik_n$ ($n = 0, 1, 2, \ldots$), where k_n satisfy the equality

$$k_n^2 = m^2 + \left(\frac{\pi n}{H}\right)^2. \quad (20)$$

After integration, we obtain

$$G(|x|) = \frac{\exp(-m|x|)}{2mH} + \sum_{n=1}^{\infty}\frac{\exp(-k_n|x|)}{k_nH}. \quad (21)$$

Thus, the boundary-value problem (9)–(14) has been reduced to the joint solution of integral equation (19) and differential equations (12)–(14), which relate the potential φ and the plate bend w. In the general case, these equations are solved only numerically. Therefore, we will assume that $mH \ll 1$; that is, we will take advantage of the shallow water approximation. In this case, the second term in (21) becomes negligibly small compared with the first one, since the quantities k_n [see (20)] tend to infinity for any n if $H \longrightarrow 0$. Then, the function $G(|x|)$ can be approximated as

$$G(|x|) \approx \frac{\exp(-m|x|)}{2mH}. \quad (22)$$

The same expression can be obtained from formula (18). At small H, the integrand is represented as $[H(k^2 + m^2)]^{-1}\exp(ikx)$. The integral of this function gives expression (22). Then, Eq. (19) with the function $G(|x|)$, defined by (22), takes the form

$$\varphi_{1,2}(x, m, H) = -\frac{i\omega}{2mH}\int_{-a}^{a} w(\xi, m)\exp[-m|x-\xi|]d\xi + \frac{\omega^2}{2mgH}\int_{a}^{\infty}\varphi_2(\xi, m, H) \times (\exp[-m|x+\xi|] + \exp[-m|x-\xi|])d\xi. \quad (23)$$

Let us find the potential $\varphi_2(x, m, H)$ outside the plate. Doubly differentiating Eq. (23), we reduce it to an equation for $\varphi_2(x, m, H)$ in the form

$$\frac{\partial^2\varphi_2}{\partial x^2} - \gamma^2\varphi_2 = 0, \quad \gamma^2 = m^2 - \frac{\omega^2}{gH}. \quad (24)$$

A solution to (24) that satisfied the condition $\varphi_2(x, m, H) \longrightarrow 0$ at $x \longrightarrow \infty$ is represented in the form

$$\varphi_2(x, m, H) = B\exp(-\gamma|x|), \quad |x| > a. \quad (25)$$

The constant B will be found below.

For waves not propagating along the coordinate x to exist, the condition $\gamma^2 > 0$ or

$$\omega < \omega_1, \quad \omega_1 = m\sqrt{gH} \quad (26)$$

must be met, where ω_1 is the waveguide cutoff frequency in the shallow water approximation.

If $\omega > \omega_1$, the solution will involve waves transferring the energy to infinity. In this case, the problem of finding a real discrete spectrum becomes radically different. Namely, it transforms to the problem of finding a discrete spectrum along the axis of the continuous one [8, 9]. Such a problem is beyond the scope of this work.

The constant B in (25) is found by substituting expression (25) into (23) at $x = a$:

$$B = -\frac{i\omega\exp(\gamma a)}{2H(m\sinh(am) + \gamma\cosh(am))} \times \int_{-a}^{a} w(\xi, m)\exp(m\xi)d\xi. \quad (27)$$

Now one can find the potential $\varphi_1(x, m, H)$ under the plate ($|x| < a$) from Eq. (23) using the value of $\varphi_2(x, m, H)$ ($|x| > a$). Substituting (25) into (23) yields

$$\varphi_1(x, m, H) = -\frac{i\omega}{2mH}\left[\int_{-a}^{a} w(\xi, m)\exp[-m|x-\xi|]d\xi + \Delta(m, \omega)Y(w)\cosh(mx)\right], \quad (28)$$

where

$$\Delta(m, \omega) = \frac{(m-\gamma)\exp(-am)}{m\sinh(am) + \gamma\cosh(am)},$$

$$Y(w) = \int_{-a}^{a} w(\xi, m)\exp(m\xi)d\xi.$$

Thus, relationship (28) defines the velocity potential through the plate bend in the range $|x| < a$. Substituting (28) into formula (13) for the pressure, one arrives at an expression for the pressure experienced by the plate on the side of the liquid:

$$p(x, m) = \frac{\rho\omega^2}{2mH}\left[\int_{-a}^{a} w(\xi, m)\exp[-m|x-\xi|]d\xi + \Delta(m, \omega)Y(w)\cosh(mx)\right] - \rho g w(x, m). \quad (29)$$

DISCRETE SPECTRUM OF VIBRATION NATURAL FREQUENCIES

Consider first the case of a wide plate, for which $ma \gg 1$. Expression (29) for the pressure can be simplified in this case. Applying the definition $\lim_{z\to\infty}[z\exp(-z|x|)] = 2\delta(x)$ for the delta function [10] to the integral in the first term of (29), we will obtain the approximate expression

$$\int_{-a}^{a} w(\xi, m)\exp[-m|x-\xi|]d\xi \approx \frac{2w(x, m)}{m}. \quad (30)$$

Substituting expression (29) for $p(x, m)$ into Eq. (12) in view of (30), we come to an equation for the free vibrations of the plate on the surface of the liquid:

$$D\frac{\partial^4 w}{\partial x^4} - N\frac{\partial^2 w}{\partial x^2} + (K - \omega^2 M_q)w = F(x). \quad (31)$$

Here,

$$N = 2m^2 D, \quad K = Dm^4 + \rho g, \quad M_q = M + \frac{\rho}{m^2 H},$$

$$F(x) = \frac{\rho\omega^2}{2mH}\Delta(m, \omega)Y(w)\cosh(mx).$$

A solution to (31) must satisfy boundary conditions (14). Equation (31) is similar to the differential equation for forced vibrations of a beam that lies on an elastic support with a stiffness coefficient K and is stretched by a force N. It is known that the spectrum of the natural frequencies for such a beam always lies above the cutoff frequency $\omega_2^2 = K/M_q$ [9]. Then, the spectrum of the natural frequencies of the plate lying on the surface of the liquid is above the value

$$\omega_2 = \left[\frac{Dm^4 + \rho g}{M + \rho/(m^2 H)}\right]^{1/2}. \quad (32)$$

On the other hand, the desired spectrum must lie below the waveguide cutoff frequency ω_1 (see (26)). Thus, the natural frequencies satisfy the inequalities

$$\omega_2 < \omega < \omega_1. \quad (33)$$

Inequalities (33) are the necessary condition for the existence of the spectrum of natural frequencies.

A solution to Eq. (31) for plate vibrations symmetric about $x = 0$ has the form

$$w(x, m) = C_1\cosh(\alpha_1 x) + C_2\cos(\alpha_2 x) - \frac{F(x)}{m^4 + \Omega^2}, \quad (34)$$

where

$$\alpha_1 = (m^2 + (m^4 + \Omega^2)^{1/2})^{1/2},$$
$$\alpha_2 = (-m^2 + (m^4 + \Omega^2)^{1/2})^{1/2},$$
$$\Omega^2 = (\omega^2 M_q - K)/D.$$

The substitution of solution (34) into boundary conditions (14) yields a set of equations for the unknown constants C_1 and C_2:

$$C_1(\alpha_1^2 - \mu m^2)\cosh(\alpha_1 a) - C_2(\alpha_2^2 + \mu m^2)\cos(\alpha_2 a) = A,$$
$$C_1(\alpha_1^3 - (2-\mu)m^2\alpha_1)\sinh(\alpha_1 a) + C_2(\alpha_2^3 + (2-\mu)m^2\alpha_2)\sin(\alpha_2 a) = -m\tanh(am)A, \quad (35)$$

where

$$A = \frac{m^2(1-\mu)F(a)}{m^4 + \Omega^2}.$$

This set of equations is homogeneous, since the right-hand side involved the integral $Y(w)$, which, in its turn, is expressed in terms of C_1 and C_2. In fact, having integrated (34) with respect of x from $-a$ to a, we express $Y(w)$ through C_1 and C_2. Substituting the expression found for $Y(w)$ into (35), we come to a homogeneous algebraic set of equations for C_1 and C_2. Equating its determinant to zero, we will find an equation for the natural frequencies of the starting problem. For a wide plate ($ma \gg 1$), the frequency equation is given by

$$\tan(\alpha_2 a) = -\frac{Q(\alpha_2^2 + \mu m^2)^2\alpha_1 + m^3(1-\mu)(\alpha_2^2 + \mu m^2)\alpha_1 + (1-\mu)^2 m^6}{Q(\alpha_1^2 - \mu m^2)^2\alpha_2 + m^3(1-\mu)(\alpha_1^2 - \mu m^2)\alpha_2 - (1-\mu)^2 m^4\alpha_1\alpha_2}, \quad (36)$$

where

$$Q = (m^4 + \Omega^2)^{1/2}\left[\frac{1}{4m} + \frac{mHD(m^4 + \Omega^2)(m+\gamma)}{\rho\omega^2(m-\gamma)}\right].$$

Equation (36) characterizes the discrete spectrum of the plate vibration natural frequencies. As follows from calculations, roots of Eq. (36) appear in a very narrow range of plate and channel parameters. Only a single

root has been found. This result agrees with that obtained in [11], where the only natural frequency close to the cutoff frequency ω_1 has been found by numerically analyzing the initial equations for wide floating plates. For vibrations asymmetric about $x = 0$, a frequency equation similar to (36) (here omitted) has no roots. It should be noted that, for a plate at the channel bottom, a range of parameters where a spectrum of eigenvalues may appear is rather wide and the number of eigenvalues may differ [12]. In what follows, we will consider reasons for such a substantial difference in the natural frequency spectra of plates located on the surface of the liquid and at the bottom of the channel. To this end, it is convenient to consider plate vibrations on the surface in the absence of flexural waves along the coordinate x.

PLATE VIBRATIONS WITHOUT FLEXURAL WAVES ALONG THE COORDINATE x

Consider a plate for which flexural waves along the coordinate x are absent. Let such a plate be called "rigid." This situation can be realized, e.g., if the plate has ribbed stiffeners running normal to the y axis. In this case, the plate vibration has a form of a flexural wave propagating only in the y direction. Equation (12) describing the propagation of such a wave is given by

$$(-M\omega^2 + Dm^4)w = \frac{1}{2a}\int_{-a}^{a} p(x, m, \omega)dx. \qquad (37)$$

Here, $p(x, m, \omega)$ is the pressure and w is a constant. The amplitude of the pressure $p(x, m)$ calculated by formula (29) is expressed as

$$p(x, m) = \frac{\rho\omega^2 w}{m^2 H}\left[1 - \frac{\gamma\cosh(mx)}{m\sinh(am) + \gamma\cosh(am)}\right] - \rho g w. \qquad (38)$$

Substituting expression (38) into (37) yields the frequency equation

$$Dm^4 + \rho g = \omega^2\left\{M + \frac{\rho}{m^2 H}\left[1 - \frac{\gamma\tanh(ma)}{ma(m\tanh(am) + \gamma)}\right]\right\}$$

or

$$\omega^2 = \frac{Dm^4 + \rho g}{M + M_a(\omega)}, \qquad (39)$$

where $M_a(\omega)$ is the associated mass of the liquid:

$$M_a(\omega) = \frac{\rho}{m^2 H}\left\{1 - \frac{\gamma\tanh(am)}{am[m\tanh(am) + \gamma]}\right\}.$$

Equation (39) is a transcendental equation for frequency ω. For given system parameters, its solution specifies the natural frequency of a localized vibration mode. Note that M_a depends on ω, since $\gamma^2 = m^2 - \omega^2/gH$. The maximal value of the associated mass is reached at large ma: $M_a \approx \rho/m^2 H$. Thus,

$$\omega_2 = \left[\frac{Dm^4 + \rho g}{M + \rho/(m^2 H)}\right]^{1/2} < \omega$$

and the range where the spectrum of vibration natural frequencies may exist must meet the inequalities

$$\omega_2 < \omega < \omega_1. \qquad (40)$$

Let us compare expression (39) for plate vibration frequency with the cutoff frequency of operator (31) (see (32)). It is easy to see that the frequencies coincide at large ma. Consequently, we can conclude that the range where the spectrum of vibration natural frequencies ω of a plate deformed along the coordinate x can exist is also defined by inequalities (40). In (40), the upper limit ω_1 specifies the waveguide cutoff frequency and the lower one ω_2, vibration frequency of the rigid plate. It is obvious that the inequality

$$\omega_2 > \omega_1,$$

may be satisfied for certain plate and channel parameters. In this case, the natural frequency spectrum for a plate deformed along the coordinate x does not exist. The condition $\omega_2 < \omega_1$, which is necessary for the spectrum to exist, can be represented as

$$\frac{Dm^2}{gHM} < 1$$

or

$$\frac{c^2}{12gH}\left(\frac{\delta}{H}\right)^2 (mH)^2 < 1,$$

where c is the velocity of sound in the plate.

Let us estimate the range of ω, varying according (40). Ignoring higher order infinitesimals, we have

$$\Delta = (\omega_1 - \omega_2)\sqrt{H/g} \approx \sqrt{\frac{\rho_0\delta}{\rho H}}(mH)^2.$$

Obviously, this quantity is small: $\Delta = O(m^2H^2)$. Hence, it becomes clear why the solution to (36) gives the only eigenvalue very close to the cutoff frequency ω_1. In turn, the solution to frequency equation (39) for vibrations of a plate undeformable along the x axis shows that this equation always has the single real root $\omega_* \approx \omega_1$. To this root, there corresponds a free vibration mode localized with respect to the x axis and propagating along the y axis with a wave number m.

Physically, this result means that a thin flexible plate on the liquid surface virtually copies the motion of the surface itself (by virtue of boundary conditions (5)).

This is because the force experienced by the plate on the side of the liquid, which depends on the product $-\rho g w$ and the inertial force $M_a \omega^2 w$, far exceeds elastic and inertial forces exerted by the plate itself. Thus, with a flexible thin-walled structure floating on the surface, the surface wave pattern remains almost unchanged.

REFERENCES

1. M. Kashiwagi, J. Mater. Sci. Technol., No. 3, 37 (1998).
2. M. Ohkusu and Y. Namba, in *Proceedings of the 13th International Workshop on Water Waves and Floating Body, 1998.*
3. J. W. Kim and R. C. Ertekin, J. Fluid Mech. **43**, 241 (1999).
4. G. Zilman and T. Miloh, in *Proceedings of the 14th International Workshop on Water Waves and Floating Body, 1999*, p. 179.
5. V. A. Babeshko, I. I. Vorovich, and I. F. Obraztsov, Izv. Akad. Nauk SSSR, Mekh. Tverd. Tela, No. 3, 74 (1990).
6. V. A. Babeshko, B. V. Glushkov, and N. F. Vinchenko, *Dynamics of Inhomogeneous Linearly Elastic Media* (Nauka, Moscow, 1989).
7. A. K. Abramyan, V. V. Alekseev, and D. A. Indeĭtsev, Zh. Tekh. Fiz. **68** (3), 15 (1998) [Tech. Phys. **43**, 278 (1998)].
8. D. Indeitsev and Yu. Mochalova, in *Proceedings of the 13th International Workshop on Water Waves and Floating Body, 1998.*
9. D. Indeitsev and Yu. Mochalova, in *Proceedings of the 15th International Workshop on Water Waves and Floating Body, 2000.*
10. W. Kecs and P. Teodorescu, *Introducere in teoria distributiilor cu aplicatii in tehnica* (Editura Tehnica, Bucharest, 1975; Mir, Moscow, 1978).
11. D. A. Azalinov, Akust. Zh. **47**, 558 (2001) [Acoust. Phys. **47**, 484 (2001)].
12. V. V. Alekseev, D. A. Indeĭtsev, and Yu. A. Mochalova, Zh. Tekh. Fiz. **69** (8), 37 (1999) [Tech. Phys. **44**, 903 (1999)].

Translated by V. Isaakyan

Technical Physics, Vol. 47, No. 5, 2002, pp. 535–538. Translated from Zhurnal Tekhnicheskoĭ Fiziki, Vol. 72, No. 5, 2002, pp. 22–25.

THEORETICAL AND MATHEMATICAL PHYSICS

Space Charge Limiting Current of an Electron Beam Transported in a Coaxial Drift Chamber

G. V. Sotnikov and T. Yu. Yatsenko

Institute for Electromagnetic Research, Kharkov, 61022 Ukraine

e-mail: sotnikov@kipt.kharkov.ua

Received September 20, 2001

Abstract—An expression for the space charge limiting current of an electron beam in a vacuum coaxial drift chamber is obtained in the strong field approximation. The expression is an analogue of the Bogdankevich–Rukhadze interpolation formula for a cylindrical drift chamber. The space charge limiting currents in the coaxial and cylindrical chambers are compared. The space charge limiting current in the vacuum coaxial chamber is numerically calculated and compared to analytical predictions. *© 2002 MAIK "Nauka/Interperiodica".*

To increase the power of relativistic vacuum microwave devices, it is necessary to solve the electron beam transport problem. At high currents, the space self-charge of an electron beam affects its motion significantly. There exists a threshold current above which the electrons of the beam are trapped in the drift chamber. The laminar motion of the electron flow fails, and a so-called virtual cathode forms. The threshold current for this phenomenon is usually estimated with the Bogdankevich–Rukhadze interpolation formula [1, 2] or with the more exact Genoni–Proctor formula [3]. In the works cited, electron beam transport through a cylindrical channel in a vacuum was considered. Approximate formulas derived in [1–3] are in good agreement with direct numerical simulations, especially at relativistic beam energies.

In recent years, considerable research has been concentrated on high-power microwave devices with a coaxial transport channel [4–8]. Currents injected into the interaction chamber of these devices have a limit, which is qualitatively similar to that imposed on electron beams injected into a cylindrical drift chamber. The problem of critical current is particularly significant for a coaxial ubitron [4, 5], which uses high-current beams with a significant azimuth velocity and a coaxial virtual cathode [8]. The effect of virtual cathode on transport in a coaxial has not been analyzed quantitatively although this is a key issue to be solved by a designer of any coaxial microwave device with external electron beam injection. Below, we will derive an expression for the space charge limiting current in a coaxial vacuum drift chamber following the formalism developed in [1].

In the strong magnetic field approximation, we can neglect the Larmor gyration and assume that the electrons move along the magnetic field lines. Then, the potential produced by a hollow electron beam in a coaxial can be found from the Poisson equation

$$\frac{1}{r}\frac{\partial}{\partial r}\left(r\frac{\partial\Phi}{\partial r}\right) = -\frac{4\pi}{v_\parallel}\begin{cases}0, & \rho < r < r_\mathrm{i}\\ j, & r_\mathrm{i} \le r < r_0\\ 0, & r_0 \le r \le R,\end{cases} \tag{1}$$

where ρ and R are the inner and outer radii of the coaxial, respectively; r_0 is the beam outer radius; r_i is the inner beam radius; j is the current density; and $v_\parallel$ is the beam longitudinal velocity.

Boundary conditions for Eq. (1) imply that the potential vanishes on the metallic surfaces of the coaxial cylinders and is continuous, along with its derivatives, at the inner and outer boundaries of the beam:

$$\Phi(\rho) = \Phi(R) = 0, \quad \Phi(r_\mathrm{i} - 0) = \Phi(r_\mathrm{i} + 0),$$

$$\Phi(r_0 - 0) = \Phi(r_0 + 0), \tag{2}$$

$$\left.\frac{\partial\Phi}{\partial r}\right|_{r = r_i - 0} = \left.\frac{\partial\Phi}{\partial r}\right|_{r = r_i + 0}, \quad \left.\frac{\partial\Phi}{\partial r}\right|_{r = r_0 - 0} = \left.\frac{\partial\Phi}{\partial r}\right|_{r = r_0 + 0}.$$

A solution to Eq. (1) subject to boundary conditions (2) for the current density constant across the beam has the form

$$\Phi^I(r) = \frac{I_0}{v_\parallel}\frac{\ln(r/\rho)}{\ln(R/\rho)}G, \tag{3}$$

$$\Phi^\mathrm{II}(r) = \frac{I_0}{v_\parallel}\left\{\frac{\ln(r/\rho)}{\ln(R/\rho)}G - \frac{r^2 - r_\mathrm{i}^2}{r_0^2 - r_\mathrm{i}^2} + \frac{2r_\mathrm{i}^2}{r_0^2 - r_\mathrm{i}^2}\ln\frac{r}{r_\mathrm{i}}\right\}, \tag{4}$$

$$\Phi^\mathrm{III}(r) = \frac{I_0}{v_\parallel}\frac{\ln(r/R)}{\ln(R/\rho)}\left[G - 2\ln\frac{R}{\rho}\right], \tag{5}$$

1063-7842/02/4705-0535$22.00

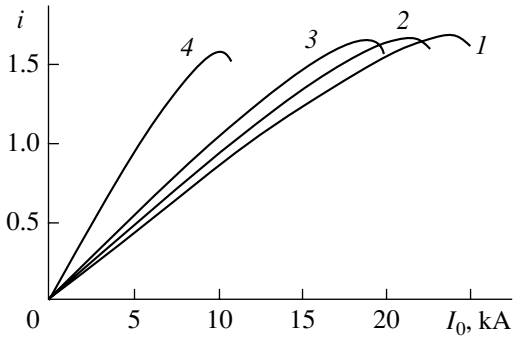

Fig. 1. Normalized current i of the electron beam in a coaxial drift chamber versus injection current for the transverse electron beam velocity β_w = 0.1 (*1*), 0.2 (*2*), 0.28 (*3*), and 0.5 (*4*). The drift chamber parameters are R = 15.2 cm, ρ = 6.7 cm, γ = 2, r_i = 9.2 cm, and r_0 = 12.6 cm.

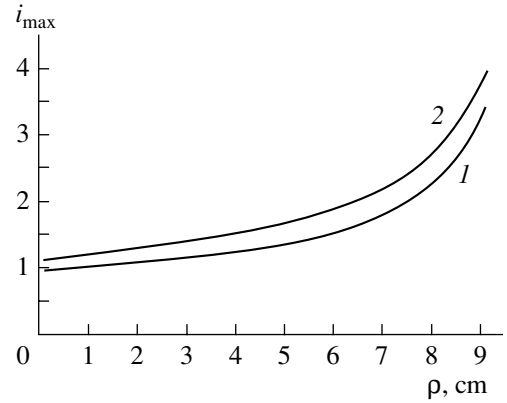

Fig. 2. Space charge limiting current $i_{max} = I_{max}/J_0$ of the electron beam in a coaxial versus radius ρ of the inner conductor. (*1*) Direct calculation and (*2*) approximate formula (11) with $\gamma = \gamma_\parallel = 2$. The remaining parameters are the same as in Fig. 1.

where

$$G = 1 + 2\ln\frac{R}{r_0} + 2\frac{r_i^2}{r_0^2 - r_i^2}\ln\frac{r_i}{r_0}. \quad (6)$$

Superscripts I, II, and III in expressions (3)–(5) refer to domains inside ($r < r_i$) in ($r_i < r < r_0$), and outside ($r > r_0$) the beam, respectively; $I_0 = \pi j[r_0^2 - r_i^2]$ is the beam total current.

In a cylindrical drift chamber, the potential well depth is maximum at the inner surface of the electron beam. In a coaxial drift chamber, the maximum is observed inside the electron beam. As follows from formula (4), its position is given by

$$r_{max} = r_i\left(1 + \frac{r_0^2 - r_i^2}{2r_i^2\ln(R/\rho)}G\right)^{1/2} \quad (7)$$

and its value is

$$\Phi_{max} = \frac{I_0}{v_\parallel\ln(R/\rho)}\left\{\left[\ln\left(\frac{r_{max}}{\rho}\right) - \frac{1}{2}\right]G + \frac{2r_i^2}{r_0^2 - r_i^2}\ln\frac{r_{max}}{r_i}\ln\frac{R}{\rho}\right\}. \quad (8)$$

To find the space charge limiting current of the electron beam, it is necessary to consider the potential dependence of $v_\parallel$ in expression (8) and maximize the current by differentiating with respect to beam potential [9]. This procedure must use the integrals of electron motion in the space charge field and in a strong magnetic field [1]:

$$v_\perp\left(1 - \frac{v_\parallel^2 + v_\perp^2}{c^2}\right)^{-1/2} = v_{\perp 0}\left(1 - \frac{v_{\perp 0}^2 + v_{\parallel 0}^2}{c^2}\right) \equiv v_{\perp 0}\gamma, \quad (9)$$

$$mc^2\left(1 - \frac{v_\parallel^2 + v_\perp^2}{c^2}\right)^{-1/2} + e\Phi = mc^2\gamma, \quad (10)$$

where $v_{\perp 0}$ and $v_{\parallel 0}$ are the transverse and longitudinal velocities of the electrons at the entrance to the drift chamber.

As a result, we obtain an expression for the space charge limiting current of an electron beam in a coaxial vacuum chamber:

$$I_{max}^{coax} = I_A\frac{\gamma}{\gamma_\parallel}(\gamma_\parallel^{2/3} - 1)^{3/2}\frac{\ln(R/\rho)}{\ln(r_{max}/\rho) - 1/2} \times\left\{G + \frac{2r_i^2}{r_0^2 - r_i^2}\frac{\ln(R/\rho)\ln[r_{max}/r_i]}{r_0^2 - r_i^2\ln(r_{max}/\rho) - 1/2}\right\}^{-1}, \quad (11)$$

where $\gamma_\parallel = (1 - v_{\parallel 0}^2/c^2)^{-1/2}$ and $I_A = mc^3/e \approx 17$ kA.

In the limit $\rho \longrightarrow 0$, expression (11) is reduced to the well-known Bogdankevich–Rukhadze interpolation formula [1]

$$J_0 = I_A\frac{\gamma}{\gamma_\parallel}(\gamma_\parallel^{2/3} - 1)^{3/2}G^{-1}. \quad (12)$$

For a thin beam ($a = r_0 - r_i \ll r_0$) away from the metallic walls ($a/r_0 \ll \min\{\ln(R/r_0), \ln(r_0/\rho)\}$), formula (11) yields an expression for the space charge limiting current of an electron beam in a coaxial:

$$I_{max}^{coax} = I_A\frac{\gamma}{\gamma_\parallel}(\gamma_\parallel^{2/3} - 1)^{3/2}\frac{1}{2\ln(R/r_0)}\frac{\ln(R/\rho)}{\ln(r_0/\rho)}; \quad (13)$$

i.e., the space charge limiting current of a thin electron beam in a coaxial is $\ln(R/\rho)/\ln(r_0/\rho)$ times that in a cylindrical drift chamber. To estimate the accuracy of approximate analytical expressions (11) and (13), we numerically solved Poisson equation (1) under bound-

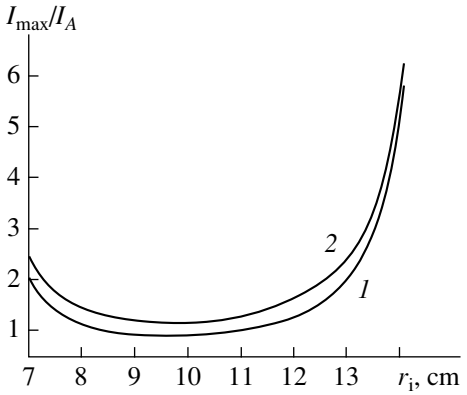

Fig. 3. Space charge limiting current of the electron beam versus beam position in the coaxial drift chamber. (*1*) Direct calculation and (*2*) approximate formula (11). The beam thickness is $a = 1$ cm and $\gamma = \gamma_{\|} = 2$. The remaining parameters are the same as in Fig. 1.

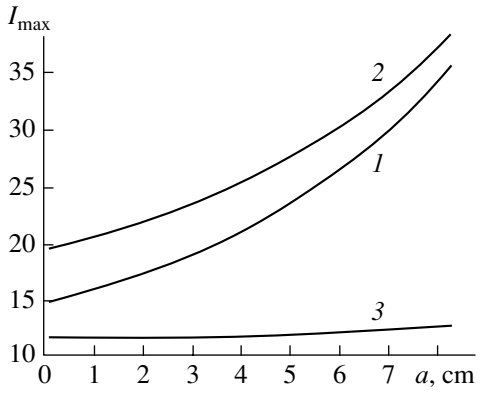

Fig. 4. Space charge limiting current of the electron beam versus beam thickness a. (*1*) Approximate formula (11), (*2*) direct calculation for the coaxial drift chamber, and (*3*) formula (12) for the cylindrical chamber. The beam average radius is $(r_i + r_0)/2 = 10.95$ cm and $\gamma = \gamma_{\|} = 2$. The remaining parameters are the same as in Fig. 1.

ary conditions (2) with regard for integrals of motion (9) and (10) using the Newton method of solution of nonlinear difference equations [10]. In the calculations, we used the parameters of the coaxial and an electron beam for a high-power coaxial ubitron under development [4]: $\rho = 6.7$ cm, $R = 15.2$ cm, and $\gamma = 2$. Figure 1 shows the dimensionless current $i = I/J_0$ versus injected current I_0 for different transverse beam velocities $\beta_w = v_{\perp 0}/c(\gamma_{\|} = \gamma/(1 + \beta_w^2\gamma^2))$ with $r_i = 9.2$ cm and $r_0 = 12.6$ cm. The current in the drift chamber was calculated as

$$I = I_0 \frac{2}{v_{\|0}(r_0^2 - r_i^2)} \int_{r_0}^{r_i} v_{\|}(r) r dr, \qquad (14)$$

where $v_{\|}(r)$ is a solution to system of equations (1), (2), (9), and (10).

Qualitatively, the dependence of the beam current in the coaxial drift chamber on the injection current is the same as that in the cylindrical drift chamber. The current first grows, reaching the maximum value I_{max} (the space charge limiting current), and then decreases with increasing injection current. Figure 1 shows the current fall only up to the point where the electron beam velocity vanishes at any cross section. Further calculations in the framework of this model are invalid. As follows from Fig. 1, the dimensionless current i is almost independent of $\gamma_{\|}$ (or of β_w). This indicates that the dependence of the space charge limiting current in the coaxial drift chamber on γ and $\gamma_{\|}$ is predicted by analytical expression (11) with a high accuracy and is the same as that for the cylindrical chamber. The table compares the space charge limiting current calculated directly I_{max}^{calc}, space charge limiting current in the coaxial drift chamber I_{max}^{coax} determined from formula (11), and space charge limiting current J_0 in the cylindrical chamber at the same electron beam radii, γ, and $\gamma_{\|}$. As follows from these data, the accuracy of approximate formula (11) significantly depends on the longitudinal energy $\gamma_{\|}$ of the electron beam. In particular, at $\gamma_{\|} = 2$ ($\beta_w = 0$), the difference between I_{max}^{calc} and I_{max}^{coax} is ≈18.2%. With $\gamma_{\|}$ decreasing to 1.41 ($\beta_w = 0.5$), this difference becomes ≈26.8%. It is natural to expect that, for $\gamma_{\|} \gg 1$, the difference between the results of the direct calculation and those given by approximate formula (11) will be much smaller. For example, at $\gamma = \gamma_{\|} = 10$, this difference is ≈3%. As follows from the last two columns of the table, the coaxial chamber can transport much higher currents than the cylindrical one.

Figure 2 shows the space charge limiting current I_{max}^{calc} versus radius of the inner conductor of the coaxial line at $\gamma = \gamma_{\|} = 2$ (curve *1*) and I_{max}^{coax} calculated from formula (11) (curve *2*). The results obtained by the direct calculation and by approximate formula (11) are seen to be in good agreement throughout the range of ρ. When the radius of the coaxial approaches the inner radius of the beam, the space charge limiting current in the coaxial grows significantly. This is because the

Table

β_w	I_{max}^{calc}, kA	I_{max}^{coax}, kA	J_0, kA
0	19.70	24.09	11.65
0.1	16.21	20.73	11.26
0.2	14.50	18.73	10.17
0.28	12.58	16.45	8.94
0.5	6.54	8.93	4.85

space charge of the electron beam near the metallic surface is screened. As a result, the potential well created by the electron beam smooths out, and, consequently, the decrease in the beam longitudinal velocity becomes smaller.

Figure 3 illustrates the space charge limiting current of the electron beam of a constant thickness $a = 1$ cm versus its position in the coaxial drift chamber. As follows from Fig. 3, the limiting current increases significantly as the inner boundary of the beam approaches the metallic walls of the coaxial line. Such behavior (like that shown in Fig. 2) is associated with a significant decrease in the potential well when the beam approaches the metallic surface. When the thin electron beam approaches the outer conductor of the coaxial line, the space charge limiting current tends to that in the cylindrical drift chamber. Curves *1* and *2* in Fig. 3 suggest that, as in Fig. 2, the direct calculations and the predictions are in good agreement.

Figure 4 plots the space charge limiting current in a vacuum against beam thickness for the constant beam average radius $r_{av} = (r_i + r_0)/2 = (\rho + R)/2$. When the beam thickness increases from 0.1 to 8.5 cm (the coaxial is totally filled), the space charge limiting current calculated directly (curve *2*) grows more than twofold. As in Figs. 2 and 3, the difference between the prediction (curve *1*) and direct calculation (curve *2*) is small. As the beam thickens, this difference decreases further. For comparison, Fig. 4 plots the space-charge limiting beam current in the cylindrical vacuum drift chamber calculated from formula (12). Curves *1* and *3* suggest that in the coaxial drift chamber, the limiting current is significantly higher than that in the cylindrical chamber. The ratio between the space-charge limiting currents in the coaxial and cylindrical drift chambers increases with growing beam thickness. This differs significantly from the situation with the thin beam (Fig. 3), where the limiting currents in the coaxial and cylindrical drift chambers increase to the same extent when the electron beam approaches the metallic surface.

Thus, asymptotic expression (11) obtained in this paper gives an estimate of the current in a coaxial vacuum drift chamber. It has been shown numerically that the accuracy of this formula is significantly improved when the longitudinal electron beam energy rises. In particular, at $\gamma_\parallel = \gamma = 2$, the discrepancy between the analytical formula and the direct calculation is less than 20%; at $\gamma_\parallel = \gamma = 10$, it is reduced to 3%.

ACKNOWLEDGMENTS

We are grateful to Yu.V. Tkach, who has drawn our attention to the problem.

REFERENCES

1. A. A. Rukhadze, L. S. Bogdankevich, S. E. Rosinskiĭ, and V. G. Rukhlin, *Physics of High-Current Relativistic Electron Beams* (Atomizdat, Moscow, 1990).
2. L. S. Bogdankevich and A. A. Rukhadze, Usp. Fiz. Nauk **103**, 609 (1971) [Sov. Phys. Usp. **14**, 163 (1971)].
3. L. E. Thode, B. B. Godfrey, and W. R. Shanahan, Phys. Fluids **22**, 747 (1979).
4. A. J. Balkcum, D. B. McDermott, R. M. Phylips, and N. C. Luhmann, IEEE Trans. Plasma Sci. **26**, 548 (1998).
5. H. P. Freud, R. H. Jackson, D. E. Pershing, and J. M. Taccetti, Phys. Plasmas **1**, 1046 (1994).
6. V. A. Balakirev, P. I. Markov, G. V. Sotnikov, and Yu. V. Tkach, Zarubezhn. Radioélektron., No. 12, 26 (1999).
7. G. V. Sotnikov, Fiz. Plazmy **27**, 509 (2001) [Plasma Phys. Rep. **27**, 480 (2001)].
8. M. Crawford, M. Kristiansen, and L. L. Hatfield, in *Proceedings of the 10th IEEE International Pulsed Power Conference, Albuquerque, New Mexico, 1995*, p. 682.
9. A. N. Lebedev and A. V. Shal'nov, *Foundations of Physics and Technology of Accelerators* (Énergoatomizdat, Moscow, 1991).
10. A. A. Samarskiĭ, *The Theory of Difference Schemes* (Nauka, Moscow, 1989).

Translated by A. Khzmalyan

Technical Physics, Vol. 47, No. 5, 2002, pp. 539–542. Translated from Zhurnal Tekhnicheskoĭ Fiziki, Vol. 72, No. 5, 2002, pp. 26–29.

GAS DISCHARGES, PLASMA

Unsteady Solution to the MHD Equations for Axisymmetric Plasma Configurations

N. D. Naumov

Received August 27, 2001

Abstract—A method for constructing an unsteady solution to the MHD equations is formulated on the basis of a self-similar extrapolation of the solution to the Shafranov equations. © *2002 MAIK "Nauka/Interperiodica".*

INTRODUCTION

In an ideal conducting fluid model, macroscopic plasma motions are described by the MHD equations [1]

$$\nabla \cdot \mathbf{B} = 0, \quad \frac{\partial \mathbf{B}}{\partial t} = \nabla \times [\mathbf{V} \times \mathbf{B}], \tag{1}$$

$$\frac{\partial \rho}{\partial t} + \nabla \cdot (\rho \mathbf{V}) = 0, \tag{2}$$

$$\frac{d\mathbf{V}}{dt} \equiv \frac{\partial \mathbf{V}}{\partial t} + (\mathbf{V} \cdot \nabla)\mathbf{V} = -\frac{1}{4\pi\rho}[\mathbf{B} \times \mathrm{rot}\mathbf{B}] - \frac{1}{\rho}\nabla p. \tag{3}$$

For a spatially bounded, axisymmetric plasma configuration, steady solutions to Eqs. (1)–(3) can be constructed by using the Shafranov equation for the magnetic surfaces [2]:

$$\nabla \cdot \left(\frac{\nabla \psi}{r^2}\right) = -16\pi^3 \frac{dP}{d\psi} - \frac{8\pi^2}{c^2 r^2}\frac{dJ^2}{d\psi}. \tag{4}$$

Analytic solutions to this equation were obtained in a number of papers [2–4].

As for the time-independent problem, the possibility of solving it on the basis of the self-similar approach was demonstrated earlier for unsteady plasma motions belonging to the class of such motions of continuous media whose velocities are proportional to the distance from the center of symmetry (see [5, 6] and the literature cited therein).

In the present paper, a method is proposed for constructing an unsteady solution to Eqs. (1)–(3) for an axisymmetric plasma configuration whose steady state is described by the solution to the Shafranov equation. The desired solution refers to the above-mentioned class of two-dimensional unsteady plasma motions.

SELF-SIMILAR EXTRAPOLATION

We denote by $a = a(t)$ and $b = b(t)$ the characteristic radial and axial dimensions of a moving plasmoid; to be specific, we set $a(0) = R$ and $b(0) = L$, where R and L are the corresponding dimensions of the plasma configuration in a steady state. We start by considering the class of nonrotating plasma motions, in which case the plasma density and the components of the plasma velocity have the form

$$\rho = \frac{LR^2}{ba^2}\varphi(\xi, \eta), \quad V_r = \dot{a}\xi, \quad V_\varphi = 0, \quad V_z = \dot{b}\eta. \tag{5}$$

Here, $\xi = r/a$ and $\eta = z/b$ are self-similar variables and the function φ is determined by the steady-state plasma density distribution, $\varphi(\chi, \zeta) = \rho(r, z)$, where $\chi = r/R$ and $\zeta = z/L$. We substitute the expressions for the velocity components into the condition for the magnetic field lines to be frozen in the plasma and obtain the equations

$$\frac{\partial B_r}{\partial t} = -\left(\frac{\dot{a}}{a} + \frac{\dot{b}}{b}\right)B_r - r\frac{\dot{a}}{a}\frac{\partial B_r}{\partial r} - z\frac{\dot{b}}{b}\frac{\partial B_r}{\partial z}, \tag{6}$$

$$\frac{\partial B_\varphi}{\partial t} = -\left(\frac{\dot{a}}{a} + \frac{\dot{b}}{b}\right)B_\varphi - r\frac{\dot{a}}{a}\frac{\partial B_\varphi}{\partial r} - z\frac{\dot{b}}{b}\frac{\partial B_\varphi}{\partial z}, \tag{7}$$

$$\frac{\partial B_z}{\partial t} = -2\frac{\dot{a}}{a} - B_z - r\frac{\dot{a}}{a}\frac{\partial B_z}{\partial r} - z\frac{\dot{b}}{b}\frac{\partial B_z}{\partial z}. \tag{8}$$

It is easy to see that the general solution to Eqs. (6)–(8) has the form

$$B_r = \frac{RL}{ab}f(\xi, \eta), \quad B_\varphi = \frac{RL}{ab}g(\xi, \eta), \quad B_z = \frac{R^2}{a^2}h(\xi, \eta), \tag{9}$$

where f, g, and h are certain functions.

Note that solutions (9) can be derived in a simpler way, i.e., from the following consequence of the frozen-in condition for the magnetic field lines:

$$\frac{d}{dt}\left(\frac{\mathbf{B} \cdot \nabla S}{\rho}\right) = 0, \tag{10}$$

where S is any quantity conserved during the plasma motion.

1063-7842/02/4705-0539$22.00

By successively setting S equal to ξ, φ, and η, we immediately obtain solutions (9) from expression (10).

On the other hand, the magnetic field components in an axisymmetric plasma configuration can be represented as

$$B_r = -\frac{1}{2\pi r}\frac{\partial\psi}{\partial z}, \quad B_\varphi = \frac{2J}{cr}, \quad B_z = \frac{1}{2\pi r}\frac{\partial\psi}{\partial r},$$

where ψ and J are, respectively, the magnetic flux and total current through a ring of radius r, perpendicular to the z-axis:

$$\psi = \int_0^r B_z 2\pi r dr, \quad J = \int_0^r j_z 2\pi r dr.$$

A comparison between the expressions for the radial and axial components of the magnetic field yields the following expressions for the functions f and h:

$$f = -\frac{1}{2\pi RL\xi}\frac{\partial\Psi}{\partial\eta}, \quad h = \frac{1}{2\pi r R^2\xi}\frac{\partial\Psi}{\partial\xi}, \qquad (11)$$

where the function Ψ satisfies the condition $\Psi(\xi, \eta) = \psi(r, z, t)$.

For the class of motions under consideration, the above expressions for B_φ give $b = L$, provided that the axial component of the current density is nonzero. In this case, it is only possible to speak of the solutions that describe plasma configurations with the time-dependent transverse dimension. The solutions describing plasma configurations whose longitudinal and transverse dimensions are both time-dependent are possible only when the current density distribution is purely azimuthal, i.e., when $J = 0$.

The formulas derived above imply that, for the class of motions under consideration, the desired solution to the MHD equations can be obtained by generalizing the solution to the Shafranov equation (4). For the function $\Psi(\chi, \zeta) = \psi(r, z)$, this equation can be written as

$$\frac{1}{R^2}\Gamma(\chi, \zeta) + \frac{1}{L^2}\Lambda(\chi, \zeta) = -16\pi^3\chi^2 R^2\frac{dP}{d\Psi} - \frac{8\pi^2}{c^2}\frac{dJ^2}{d\Psi}, \qquad (12)$$

where, for brevity, we introduce the notation

$$\Gamma(\chi, \zeta) = \frac{\partial^2\Psi}{\partial\chi^2} - \frac{1}{\chi}\frac{\partial\Psi}{\partial\chi}, \quad \Lambda(\chi, \xi) = \frac{\partial^2\Psi}{\partial\zeta^2}.$$

The solution to Eq. (12) enables us to specify the function Ψ in relationships (11). Clearly, this can be done under the assumption that the pressure of a moving plasma is a function of the magnetic flux, $p = P(\psi)$, as is the case in a steady state plasma.

In order to determine how the dimensions of the plasma configuration depend on time, we must insert expressions (5), (9), and (11) into the Euler equation (3). As a result, we obtain

$$\ddot{a}\xi = -\frac{A}{a\rho}\frac{\partial\Psi}{\partial\xi}, \quad \ddot{b}\eta = -\frac{A}{b\rho}\frac{\partial\Psi}{\partial\eta},$$

$$A = \frac{1}{16\pi^3 a^2\xi^2}\left[\frac{1}{a^2}\Gamma(\xi, \eta) + \frac{1}{b^2}\Lambda(\xi, \eta)\right] \qquad (13)$$

$$+ \frac{dP}{d\Psi} + \frac{1}{2\pi}\left(\frac{L}{abc\xi}\right)^2\frac{dJ^2}{d\Psi}.$$

We can readily see that, if the function $\Psi(\chi, \zeta)$ satisfies Eq. (12), then the solution to the ordinary differential equations (13) has the form

$$a = R(1 + ut), \quad b = L.$$

As was mentioned above, for a steady-state plasma configuration with a purely azimuthal distribution of the current density, a solution is possible in which the transverse and longitudinal dimensions of the plasmoid are both time-dependent:

$$a = R(1 + ut), \quad b = L(1 + wt),$$

where u and w are constants. Hence, we have shown that, using a self-similar extrapolation of the solution to the Shafranov equation, it is possible to construct an unsteady solution to the MHD equations that describes how the dimensions of an axisymmetric plasma configuration change with time.

TOROIDAL CONFIGURATION

As an illustration, let us consider the solution to the Shafranov equation in the case of a toroidal plasma configuration with an azimuthal distribution of the current density [3]:

$$\psi = \frac{1}{2}\psi_0\left[r^2z^2 + \frac{\alpha - 1}{4}(r^2 - R^2)^2\right], \qquad (14)$$

where R is the radius of the magnetic axis and ψ_0 and α are constants.

Expression (14) is a solution to the Shafranov equation (4) with $J = 0$:

$$16\pi^3\frac{dP}{d\psi} = -\alpha\psi_0. \qquad (15)$$

Assuming $\psi_0 = 8\pi^2 j_0/cR\alpha$, we can express the density of the current flowing in the plasma column as $j_\varphi = -j_0 r/R$. Near the magnetic axis, we have

$$\psi \approx \frac{1}{2}\psi_0 R^2[z^2 + (\alpha - 1)q^2], \qquad (16)$$

where $q = r - R$.

Setting $\alpha = \lambda^2 + 1$ and $\lambda = L/D$, we see that the cross section of the magnetic surface (16) is an ellipse with semiaxes L and D. The small parameter is the ratio of

the transverse dimension of the plasma column to the radius of the magnetic axis. In accordance with expression (15), the plasma pressure in a thin column is equal to

$$p = Q\left(1 - \frac{q^2}{D^2} - \frac{z^2}{L^2}\right), \quad (17)$$

where $Q = 2\pi j_0^2 L^2/\alpha c^2$. The magnetic field components are thus equal, within the same accuracy, to

$$B_r = -\frac{4\pi j_0}{\alpha c} z, \quad B_z = \frac{4\pi j_0 \lambda^2}{\alpha c} q. \quad (18)$$

As in the case of a straight plasma column with an elliptical cross section [4], the magnetic field (18) is a superposition of the external quadrupole confining field and the field of the plasma column:

$$\mathbf{B} = \mathbf{B}_0 + \mathbf{B}_1, \quad (19)$$

where

$$B_{0r} = kz, \quad B_{0z} = kq, \quad k = \frac{4\pi j_0 \lambda(\lambda - 1)}{c(\lambda + 1)(\lambda^2 + 1)},$$

$$B_{1r} = -\frac{4\pi j_0}{c(\lambda + 1)} z, \quad B_{1z} = \frac{4\pi \lambda j_0}{c(\lambda + 1)} q.$$

Now, we construct an unsteady solution for a toroidal plasma configuration, assuming that the pressure of a moving plasma satisfies the same condition as the pressure of an immobile plasma:

$$16\pi^3 \frac{dP}{d\psi} = -\mathrm{div}\frac{\nabla\psi}{r^2}.$$

In this case, from solution (14), we find

$$\Psi(\chi, \zeta) = \frac{1}{2}\psi_0 R^2\left[L^2\chi^2\zeta^2 + \frac{\alpha - 1}{4} R^2(\chi^2 - 1)^2\right].$$

Following the above procedure, we obtain an expression for the magnetic flux in a moving plasma:

$$\psi(r, z, t) = \Psi(\xi, \eta)$$
$$= \frac{1}{2}\psi_0 R^2\left[\left(\frac{Lrz}{ab}\right)^2 + \frac{\alpha - 1}{4} R^2\left(\frac{r^2}{a^2} - 1\right)^2\right].$$

Near the magnetic axis, the cross section of a magnetic surface in a moving plasma column

$$\psi \approx \frac{1}{2}\psi_0 R^2 L^2\left(\frac{z^2}{b^2} + \frac{q^2}{d^2}\right)$$

is an ellipse with semiaxes b and $d = aD/R$. The pressure of a moving plasma is described by an expression analogous to formula (17):

$$p = Q\frac{1 + \mu^2}{\alpha}\left(\frac{LD}{bd}\right)^2\left(1 - \frac{q^2}{d^2} - \frac{z^2}{b^2}\right). \quad (20)$$

In the unsteady solution, the current density in the plasma column is time-dependent:

$$j_\varphi = -j\frac{r}{a}, \quad j = j_0(1 + \mu^2)\frac{DL^2}{adb^2}, \quad (21)$$

where $\mu = b/d$ is the ratio of the semiaxes of the cross section of the column.

The magnetic field components are described by the expressions

$$B_r = -\frac{4\pi j_0 DL^2}{\alpha c d b^2} z, \quad B_Z = -\frac{4\pi j_0 DL^2}{\alpha c d^3} q, \quad (22)$$

which can be represented in a form analogous to expressions (19):

$$B_{0r} = \kappa z, \quad B_{0z} = \kappa q, \quad \kappa = \frac{4\pi j\mu(\mu - 1)}{c(\mu + 1)(\mu^2 + 1)},$$
$$B_{1r} = -\frac{4\pi j}{c(\mu + 1)} z, \quad B_{1z} = \frac{4\pi\mu j}{c(\mu + 1)} q. \quad (23)$$

Hence, the solution obtained describes the temporal behavior of the dimensions of a toroidal plasma column in which the pressure, current, and external quadrupole magnetic field evolve according to formulas (20), (21), and (23).

ROTATING PLASMA

Here, we consider a plasma configuration with a purely azimuthal current density distribution. In this case, condition (1) for the magnetic field lines to be frozen in a plasma rotating steadily with the velocity $\mathbf{V} = V_\varphi \mathbf{e}_\varphi$ has the form

$$\frac{\partial V_\varphi B_r}{\partial r} + \frac{\partial V_\varphi B_z}{\partial z} = 0. \quad (24)$$

It is easy to see that, if the plasma rotates as a solid body ($V_\varphi = \omega r$, where ω is a constant quantity), then condition (24) reduces to the condition $\nabla \cdot \mathbf{B} = 0$.

Unlike in the case of an immobile plasma, the equilibrium condition for an axisymmetric configuration of a rotating plasma contains the centrifugal term

$$\frac{1}{c} j_\varphi B_z = \frac{\partial p}{\partial r} - \rho\frac{V_\varphi^2}{r}.$$

A known solution to the equilibrium equation describing an immobile plasmoid can be readily generalized to a plasma configuration rotating as a single entity. To do this, we must choose the plasma density distribution to be

$$\rho = -\frac{\beta j_\varphi}{cr\omega^2}, \quad (25)$$

where β is a constant.

With this choice, the confinement of a rotating plasma is ensured by imposing an external uniform magnetic field $\mathbf{B}_{ext} = \beta \mathbf{e}_z$; the term describing the interaction of this field with the azimuthal current exactly cancels the centrifugal term.

Let us consider the time-dependent problem

$$\rho = \frac{LR^2}{ba^2}\varphi(\xi, \eta), \quad V_r = \dot{a}\xi,$$
$$V_\varphi = \Omega r, \quad V_z = \dot{b}\eta, \tag{26}$$

where $\Omega = \omega(R/a)^2$ is the angular velocity of plasma rotation.

In order to apply the results obtained in the previous section, we must take into account the fact that the magnetic flux density in a rotating plasma is equal to $\psi + \pi\beta r^2$, where ψ is the magnetic flux density in an immobile plasma. That is why, in the time-dependent problem, the magnetic field in expressions (9) and (11) should be calculated by making the replacement $\Psi(\xi, \eta) \longrightarrow \Psi(\xi, \eta) + \pi\beta R^2\xi^2$; in other words, the frozen-in condition for the magnetic field lines can be satisfied only if the external uniform magnetic field $\mathbf{B}_{ext} = \beta(R^2/a^2)\mathbf{e}_z$ is unsteady.

In this case, using formula (25), we obtain the following expression for the function φ in the time-dependent problem (26):

$$\varphi(\chi, \zeta) = \frac{\beta}{8\pi^2\omega^2\chi^2R^2}\left[\frac{1}{R^2}\Gamma(\chi, \zeta) + \frac{1}{L^2}\Lambda(\xi, \zeta)\right].$$

Then, we substitute expressions (9), (11), and (25) into the Euler equation (3) to arrive at the following equations for the dimensions of a rotating plasmoid:

$$\ddot{a} = \omega^2\frac{R^4}{a^3}\left(1 - \frac{L[b^2\Gamma(\xi, \eta) + a^2\Lambda(\xi, \eta)]}{b[L^2\Gamma](\xi, \eta) + R^2\Lambda(\xi, \eta)}\right) + \Omega^2 a,$$
$$\ddot{b} = 0.$$

As may be seen, these equations can be reduced to an ordinary differential equation describing the time evolution of the characteristic transverse dimension of the plasmoid only when the quantities Γ and Λ depend in a certain fashion on the self-similar variables: $\Gamma = C_1F(\xi, \eta)$ and $\Lambda = C_2F(\xi, \eta)$, where F is some function and the coefficients C_i are independent of the self-similar variables.

Thus, for the toroidal plasma configuration analyzed in the previous section, we have $\Gamma = \psi_0(\alpha - 1)R^4\xi^2$ and $\Lambda = \psi_0R^2L^2\xi^2$. Consequently, the time evolution of the radius of the magnetic axis of the toroidal configuration of a rotating plasma is described by the equation

$$\ddot{a} = \omega^2\frac{R^4}{a^3}\left[1 - \frac{b}{L}\left(1 - \frac{1}{\alpha}\right) - \frac{La^2}{\alpha bR^2}\right]. \tag{27}$$

The solution to Eq. (27) with $b = L$ can readily be reconstructed in the case of small oscillations about a steady state. We linearize this equation and obtain

$$a = R\left(1 + \frac{u}{\omega_r}\sin\omega_r t\right),$$

where $\omega_r = \omega\sqrt{2/\alpha}$.

For a thin plasma column, we have $d = Da/R$; consequently, the transverse dimension of the column changes in a similar fashion.

It should also be noted that the radial component of the plasma velocity can be represented as $V_r = \dot{a} + q\dot{d}/d$. This indicates that, to second order, the ratio q/d is a self-similar variable. We thus can conclude that the results obtained for a thin toroidal plasma column correspond to the solution to the MHD equations in the self-similar approximation. In my earlier paper [7], this approach was used to study the dynamics of an electron ring.

REFERENCES

1. L. D. Landau and E. M. Lifshitz, *Electrodynamics of Continuous Media* (Nauka, Moscow, 1982; Pergamon, New York, 1984).
2. V. D. Shafranov, Zh. Éksp. Teor. Fiz. **33**, 710 (1958) [Sov. Phys. Tech. Phys. **6**, 545 (1958)].
3. V. D. Shafranov, in *Reviews of Plasma Physics*, Ed. by M. A. Leontovich (Gosatomizdat, Moscow, 1963; Consultants Bureau, New York, 1966), Vol. 2.
4. L. E. Zakharov and V. D. Shafranov, in *Reviews of Plasma Physics*, Ed. by M. A. Leontovich and B. B. Kadomtsev (Énergoatomizdat, Moscow, 1982; Consultants Bureau, New York, 1986), Vol. 11.
5. L. I. Sedov, *Similarity and Dimensional Methods in Mechanics* (Nauka, Moscow, 1981; Academic, New York, 1959).
6. A. G. Kulikovskiĭ and G. A. Lyubimov, *Magnetohydrodynamics* (Fizmatgiz, Moscow, 1962; Addison-Wesley, Reading, 1965).
7. N. D. Naumov, Zh. Tekh. Fiz. **67** (7), 103 (1997) [Tech. Phys. **42**, 814 (1997)].

Translated by O. Khadin

Technical Physics, Vol. 47, No. 5, 2002, pp. 543–549. Translated from Zhurnal Tekhnicheskoĭ Fiziki, Vol. 72, No. 5, 2002, pp. 30–37.

SOLIDS

On the Role of Exchange Interaction in Magnetic Ordering and Conduction of Manganates

M. V. Krasin'kova

Ioffe Physicotechnical Institute, Russian Academy of Sciences, Politekhnicheskaya ul. 26, St. Petersburg, 194021 Russia

Received July 6, 2001

Abstract—A model of chemical bonds in manganates that allows for one-electron covalent σ bonding between manganese and oxygen ions is suggested. One-electron covalent bonding results in the strongly correlated state of electrons due to exchange interaction between the electrons when they are shared by the cation and anion orbitals. The correlated state shows up as the spatial ordering of electrons and the ordering of their spins, causing the spin-ordered electron lattice to form. In this model, electrical conduction in manganates takes place when the electron lattice (more precisely, its part) shifts from one site of localization to another. The conductivity of the material depends on the type of the spin order of electrons in the electron lattice and on the energy of localization, which is defined by the energy of one-electron σ bonding. The model also implies the strong cationic polarization of anions, which facilitates the 3*s*2*p* hybridization of anions and the transition of one of the pairs of 2*p* electrons from the singlet state to the triplet one. The 3*s*2*p* hybridization of anions favors the formation of the spin-polarized electron lattice (the electron spins are parallel) and the ferromagnetic ordering of manganese ions. Under these assumptions, the effect of giant magnetoresistance is explained by a change in the conduction mechanism when an external voltage is applied. In this case, the conduction mechanism typical of ionic crystals changes to that specified by the spin-polarized electron lattice. *© 2002 MAIK "Nauka/Interperiodica".*

INTRODUCTION

The electrical and magnetic properties of doped manganates have been the subject of extensive investigation in recent years, since these compounds are candidates for high-sensitivity magnetic detectors in resistive magnetic memory devices, magnetic read heads, and devices using spin-polarized transport [1].

Of particular interest are doped manganates where the transition to magnetic ordering is attended with the insulator–metal transition [2]. Such a correlation between the magnetic and transport properties in manganates has long been explained in terms of the theory of double (indirect) exchange [3]. This theory assumes that neighboring Mn^{3+} and Mn^{4+} ions exchange electrons through an O^{2-} oxygen ion in between.

However, recent experimental findings, such as the effect of increasing T_c in a magnetic field [4] or the effect of giant magnetoresistance [5]; the coexistence of charge ordering and ferromagnetism [6]; and ferromagnetic ordering in $CaCu_3MnO_{12}$ [7] and $Tl_2Mn_2O_7$ [8] compounds, where Mn^{3+} ions are absent, have thrown doubt on the double exchange mechanism as the mechanism governing the manganate behavior [9].

The discovery of local distortions in the doped manganate lattice [10] has been a breakthrough in the study of these compounds. It has been shown that the real lattice radically differs from the "averaged" lattice, which is determined by X-ray diffraction. These findings suggest an intimate correlation between the magnetic, transport, and structural properties. However, the question of how lattice local distortions may affect the electron lattice and magnetic ordering remains to be answered, and the nature of these distortions is still unclear.

In this work, we demonstrate that the interplay between the magnetic, transport, and structural properties can be understood by taking into consideration the strong covalence of manganese–oxygen bonds and treating it as the formation of one-electron σ bonds between ions of these elements. Such an approach has already been invoked for the explanation of antiferromagnetic ordering in manganates [11]. We will show that it also helps in explaining ferromagnetic ordering. Moreover, this work poses a more general problem, namely, to show (by an example of manganates) how the highly correlated state of electrons forming one-electron σ bonds may arise through electron exchange, this state being responsible for both magnetic ordering and high conductivity.

THE CONCEPT OF ONE-ELECTRON COVALENT σ BONDING IN MANGANATES

Chemically, manganates are intermediate between ionic and covalent crystals, as evidenced, for example, by the Polling electronegativity values (1.55 for Mn and 3.44 for O). The difference 1.9 means that bonds among

1063-7842/02/4705-0543$22.00

these elements are roughly 40% covalent and 60% ionic [12]. Recent high-resolution spectroscopy data [13] support the strong bond covalence in manganates. A high degree of covalence must show up largely in the behavior of valence electrons, since covalence means the sharing of these electrons by surrounding ions while ionicity means their localization on anions. The situation where valence electrons in a solid are localized on anions and, at the same time, shared by cations is difficult to imagine. For molecules, such bonding has been considered as the resonant state of structures with purely covalent and purely ionic bonds [12]. For ionic crystals, however, such a concept is hardly applicable. The formation of ordinary two-electron σ bonds in resonant structures, which is the basic idea in this concept, seems unlikely, because it requires considerable lattice strains. In our opinion, the most acceptable explanation of this situation is that each cation–anion pair shares only one electron, which would be localized on the anion in the case of purely ionic bonding.

Let us assume that ionic bonds, which specify the crystal structure of manganates, prevail at high temperatures (above T_c). As the temperatures lowers, additional covalent one-electron σ bonds between Mn and O ions appear. This effect causes a slight distortion of the crystal lattice and a reduction of the crystal symmetry, since a rise in the bond energy between the ions decreases the interionic spacing (it becomes smaller than the sum of the ionic radii).

We will consider one-electron covalent bonds in manganates as a set of localized bonds between neighboring ions. Below, it is shown that such a representation is valid because electrons occupying hybridized orbitals of the same ion interact with each other.

Let us also assume that manganese ions in the octahedral environment of oxygen ions produce covalent bonds with them through six equivalent hybridized $3d^2 4s 4p^3$ orbitals. The energy level of these orbitals is higher than that of d_{xy}, d_{yz}, and d_{xz} orbitals. This is because the higher energy 4*p* state is present and the *d* levels split in the high octahedral electric field. Therefore, one can assume that the energy gap between hybridized and unhybridized *d* orbitals is sufficiently large for the transition of a Mn^{3+} ion from the high-spin state ($t_{2g}^3 e_g^1$) to the low-spin one (t_{2g}^4) to be energetically favorable. Eventually, all hybridized orbitals of the Mn^{3+} ion will be unoccupied and accessible for covalent bonding. The possibility of the low-spin state for a Mn^{3+} ion in manganates was also discussed in [14].

An O^{2-} ion in manganates is also in the octahedral environment of the cations, two of which are manganese ions located on one of the octahedron axes. To produce one-electron covalent σ bonds with these cations, the O^{2-} ion may use its 2*p* orbital or two hybridized 3*s*2*p* orbitals facing Mn ions. The possibility of using the 2*p* orbital is beyond question and was considered in [11]. The possibility of 3*s*2*p* hybridization needs clarification.

Because of the great energy difference between the 2*p* and 3*s* levels for an oxygen atom, 3*s*2*p* hybridization is considered to be impossible. However, for an O^{2-} ion in the ionic crystal lattice, this hybridization seems to be likely for a number of reasons. First, the energy level of the 2*p* states in an O^{2-} ion comes closer to the 3*s* level, making the ion unstable. Second, the ion, being located between two Mn cations, which have the rather large charge and the relatively small ionic radius, will experience a high polarization due to the cations. The energy of polarization may partially compensate for the energy spent on the excitation of the two 2*p* electrons of the O^{2-} ion into the 3*s*2*p* state. Finally, the energy spent on hybridization will be compensated for by the energy gain due to the formation of stronger bonds between Mn and O ions.

Let us compare one-electron covalent bonds produced with the participation of the 2*p* and 3*s*2*p* orbitals of an O^{2-} ion (1*e*–σ and 1*e*–σ*, respectively). Since a 1*e*–σ bond involves shorter 2*p* orbitals, its energy is higher than that of a 1*e*–σ* bond, so that this bond is preferable for the stable state of the crystal. However, a 1*e*–σ bond may form if the cation and anion approach close enough for overlapping with the 2*p* orbital be possible. This depends on the deformability of the ionic sublattice and on the state of the electron shell of the cation. The nonspherical shape of the electron shell of a Mn^{3+} ion in the low-spin state makes its approach to the anion in the plane where a pair of t_{2g} electrons is located difficult, because the electrons of the anion repel strongly from this pair. Therefore, in this plane, overlapping with the more extended 3*s*2*p* orbital of the anion to produce 1*e*–σ* bonds remains possible, although the energy gain of the system is smaller in this case.

Another difference between 1*e*–σ and 1*e*–σ* bonds is the spin state of the anion electron pair, which forms these bonds. In the former case, the pair is in the singlet state, since it belongs to one *p* orbital (Pauli's exclusion principle). In the latter, the pair is in the triplet state, since the two *p* electrons must pass to two hybridized 3*s*2*p* orbitals and their spins must be parallel (the generalized Hund rule).

SPIN ORDERING OF ELECTRONS AND ELECTRONIC CRYSTALLIZATION

When the anion produces two one-electron σ bonds with two neighboring cations, the spin state of the anion electron pair, taking part in bonding, defines the orientation of the electron spins on the hybridized orbitals on the cations (Fig. 1). However, in the presence of six unoccupied hybridized orbitals, either cation can share six electrons, one from each of the six surrounding anions. The spin directions in these six electrons must coincide according to the Hund rule for the hybrid $d^2 sp^3$

orbitals of the cation. Hence, if all anions and all Mn ions are bonded by one-electron σ bonds, all electrons producing these bonds will be spin-ordered (Fig. 2).

It should be remembered that the Hund rule reflects the dependence of the electron system energy on the arrangement of the spins and that the presence of this dependence means the presence of an additional interaction known as exchange interaction. Then, one can argue that the spin ordering of electrons involved in covalent bonding results from two exchange interactions: between electrons on the anion orbitals and between the same electrons also occupying the cation orbitals.

In our case of one-electron bonding, the sign of the exchange interaction on the cation orbitals is always positive, while the exchange interaction between the electrons on the anion orbitals may be both positive (the triplet pair) and negative (the singlet pair) (Fig. 2), as has been discussed above.

If the exchange interaction on the anion and cation orbitals is positive, the spins of the electrons involved in one-electron σ bonding will be parallel; that is, 100% spin polarization of the electrons will take place. If the signs of the exchange interactions on the anion and cation orbitals are opposite, the electrons become spin-ordered so that the spins of the electrons on neighboring cations are antiparallel.

The exchange interaction leads not only to the spin ordering but also to the spatial ordering of the electrons involved in covalent bonds. This can be considered as the formation of the electron lattice (electron crystallization). Such ordering resembles the formation of a Wigner crystal [15]. The essential difference, however, is that a Wigner crystal arises as a result of the purely electrostatic repulsion between electrons in a uniform field of a positive charge. Therefore, it forms only at low temperatures, when the electrostatic repulsion energy exceeds the thermal energy of electrons.

In our case of electron lattice formation, the energy of purely electrostatic repulsion adds up to the energy of the exchange interaction between the electrons. That is why electronic crystallization is observed at high temperatures, such as T_c.

The participation of electrons in covalent bonding causes the localization of the electron lattice. The energy of localization depends on the energy of a one-electron σ bond and may vary with the overlap between the hybridized orbitals of the anion and cation.

Thus, the electrons involved in one-electron covalent bonds between the ions are in the strongly correlated state; i.e., they produce the localized spin-ordered electron lattice.

The magnetic ordering of the cations having their own magnetic moment due to unpaired t_{2g} electrons will then be set up through the purely magnetic interaction of these magnetic moments with the magnetic moment of the spin-ordered electron lattice. Then, all the cations will be ordered ferromagnetically if the sublattice is 100% spin-polarized (the spins are parallel).

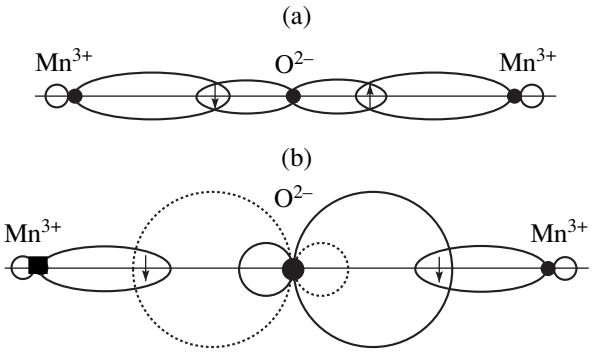

Fig. 1. Production of one-electron covalent bonds between Mn^{3+} and O^{2-} ions. (a) $1e$–σ and (b) $1e$–σ* bonds. Shown are free d^2sp^3 hybridized orbitals for two Mn^{3+} ions and (a) the p orbital of O^{2-} occupied by the singlet electron pair and (b) two $3s2p$ hybridized orbitals of O^{2-} occupied by the triplet electron pair.

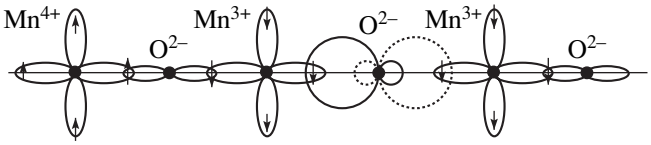

Fig. 2. Electron spin ordering on hybridized orbitals of (●) Mn^{3+} and (■) Mn^{4+} ions upon forming $1e$–σ and $1e$–σ* bonds through intermediate O^{2-} ions (singlet and triplet pairs). For simplicity, only four of six hybridized orbitals for each of the cations and only three anions are shown.

THE FEASIBILITY OF CONDUCTION IN A SYSTEM OF STRONGLY CORRELATED ELECTRONS

Now consider the feasibility of conduction in a system of strongly correlated electrons. It appears that in the presence of the strong repulsion between spin-polarized electrons (one orbital cannot be occupied by two electrons with parallel spins), the only possible mechanism of conduction is the successive displacement of the entire electron lattice from one site of localization to another. However, such a collective displacement is possible if the transition of each of the electrons to a hybridized orbital of a neighboring cation is not forbidden by the spin direction on this orbital and if the energy of electron lattice localization is not too large. The first condition is met if the electron lattice is spin-ordered (the spins of all the electrons are parallel). The second one can be fulfilled by decreasing the overlap between the anion and cation hybridized orbitals, i.e., by increasing the spacing between the Mn^{3+} and O^{2-} ions (for example, when the crystal lattice is locally distorted).

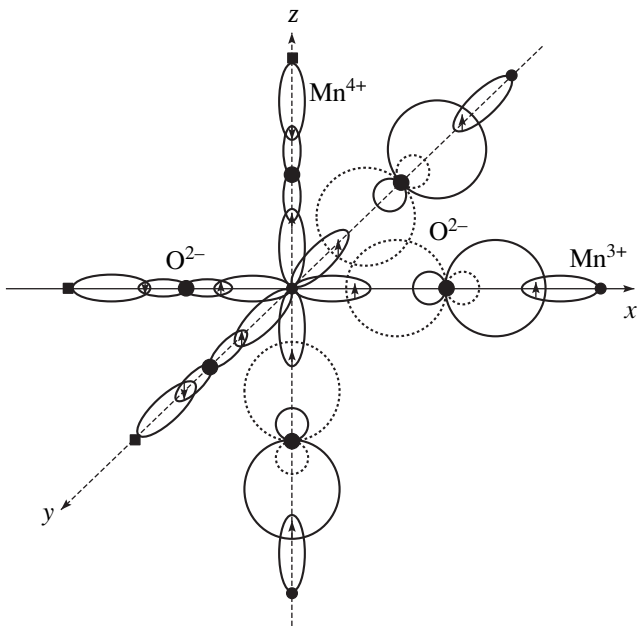

Fig. 3. Coordination polyhedron for the Mn^{3+} ion in $A_{0.67}B_{0.33}MnO_3$. Three pairs of $1e$–σ bonds with neighboring Mn^{4+} ions and three pairs of $1e$–σ* bonds with neighboring Mn^{3+} ions through O^{2-} intermediates are shown.

Note, however, that these conditions are nearly incompatible, since the loosening of covalent bonds, which provide spin ordering, would break the ordering. Yet, both conditions can be satisfied if various parts of the spin-polarized lattice are responsible for spin ordering and conduction. This can be achieved if one part of the spin-polarized lattice remains three-dimensional and localized and the other has a lower dimension and a small energy of localization.

Below, we will show how these functions can be divided between the parts of the spin-polarized electron lattice in doped manganates.

MAGNETIC ORDERING AND CONDUCTION IN DOPED AND UNDOPED MANGANATES

Consider how our model explains magnetic ordering and conduction in doped and undoped manganates. The experimentally observed perovskite-like cubic lattice of $CaMnO_3$ with an interionic distance smaller than the sum of the ion radii and with antiferromagnetic ordering of the Mn^{4+} ions [2] agrees well with the idea that each of the Mn^{4+} ions produces six equivalent one-electron σ bonds with the participation of singlet electron pairs of the anions. The anion electrons involved in covalent bonds and at the same time occupying the hybridized orbitals of the cations turn out to be mutually ordered. Then, their state can be considered as an electron lattice. In this case, the electron lattice consists of electronic tetrahedra surrounding the Mn^{4+} ions. In each of the tetrahedra, the spins are parallel to each other and antiparallel to the spins in a neighboring tetrahedron. The different orientation of the electron spins on the orbitals of neighboring cations forbids electron exchange between the cations and explains the absence of conduction. This is consistent with experimental data for $CaMnO_3$ [2] obtained at temperatures lower than T_N.

As for $LaMnO_3$, the electron shell of the Mn^{3+} ions is not spherical in the low-spin state, as was noted above. Therefore, only $1e$–σ* bonds may form in the plane where the pair of t_{2g} electrons is located. This must cause ferromagnetic ordering between adjacent cations. In the direction normal to this plane, the possibility for the formation of stronger $1e$–σ bonds, causing antiferromagnetic ordering between adjacent cations, persists.

The orientational ordering of the spherically asymmetric Mn^{3+} ions provides the ferromagnetic ordering of all the Mn^{3+} ions in the plane of paired t_{2g} electrons, with antiferromagnetic ordering between such planes. Such a pattern of magnetic ordering has been observed in experiments [2]. The orientational ordering of the Mn^{3+} ions decreases the lattice strain energy when covalent bonds of various length ($1e$–σ and $1e$–σ*) are produced and, therefore, is energetically favorable.

In this case, the spin-ordered electron lattice consists of electronic octahedra surrounding the Mn^{3+} ions. In each of the octahedra lying in the plane of Mn^{3+} orientational ordering (the plane of paired t_{2g} electrons), the spins are parallel to each other and antiparallel to the spins in the electronic octahedra lying in adjacent planes. Below T_N, $LaMnO_3$ is an insulator [2]. This is presumably associated both with a high energy of electron lattice localization in the plane of ferromagnetic ordering when the lattice distortions are absent and with the antiferromagnetic order between the planes.

In doped manganates where both Mn^{3+} and Mn^{4+} ions are present, either ion individually will tend to produce the same bonds with the anions as in undoped compounds. Regarding the bonding between the Mn^{3+} and Mn^{4+} ions through an intermediate anion, it appears that a $1e$–σ bond will form between them, since it is energetically more favorable. As a result, the Mn^{3+} and Mn^{4+} ions will be antiferromagnetically ordered relative to each other. Since a Mn^{3+} ion cannot produce six $1e$–σ bonds because of the presence of the paired t_{2g} electrons, this and neighboring Mn^{3+} ions must produce a $1e$–σ* bond through an intermediate anion. In this case, the order of these ions relative to each other will be ferromagnetic. The doped manganate of composition $A_{0.67}B_{0.33}MnO_3$ is unique in that it admits the charge order of the Mn^{3+} and Mn^{4+} ions such that each of the Mn^{4+} ions is surrounded by six Mn^{3+} ions, while each of the Mn^{3+} ions has three Mn^{4+} and three Mn^{3+} neighbors. In the latter case, cations with the same

degree of oxidation turn out to be the nearest neighbors (Figs. 3, 4). Such charge ordering produces $1e$–σ^* bonds between all the Mn^{3+} ions through intermediate O^{2-} ions and $1e$–σ bonds between all the Mn^{3+} and Mn^{4+} ions. Figure 4 shows two sublattices formed by the Mn^{3+} and Mn^{4+} ions ordered. Here, the electron lattice consists of two sublattices with oppositely directed spins. One includes electronic octahedra around the Mn^{4+} ions; the other, around the Mn^{3+} ions. Such a separation of the electron sublattices is convenient for determining the magnetic order of the cation magnetic moments, which results from the magnetic spin–spin interaction between the electronic lattice and unpaired t_{2g} electrons. In the manganate considered, ordering between the Mn^{3+} ions and between the Mn^{4+} ions is ferromagnetic, while that between Mn^{3+} and Mn^{4+} ions is antiferromagnetic.

To explain the phenomenon of conduction in the electronic lattice, it would be convenient to subdivide the whole lattice into the sublattice formed by the electrons of the anion triplet pairs and the sublattice formed by the electrons of the singlet pairs. In these pairs, the energies of electron localization, which depend on the energy of the $1e$–σ^* and $1e$–σ bonds, differ. Therefore, such a division into the two sublattices allows one to find the weaker localized part of the spin-polarized lattice (the spins are parallel). As follows from Figs. 3 and 4, the triplet sublattice is a part of the spin-polarized lattice and is quasi-one-dimensional in each of the MnO_2 planes. It is located between the Mn^{3+} ions and forms parallel stripes separated by the stripes of the singlet pairs between the Mn^{4+} ions (Fig. 5). Since the production of short $1e$–σ bonds between the Mn^{3+} and Mn^{4+} ions is accompanied by an increase in the spacing between the Mn^{3+} ions (Fig. 5), a decrease in the overlap between the orbitals of the Mn^{3+} and O^{2-} ions, and a decrease in the $1e$–σ^* bond energy, one can assume that, in the manganate considered, the triplet pair sublattice is localized weaker than in $LaMnO_3$. The singlet pair sublattice remains fixed, making no contribution to conduction. At the same time, it sustains the spin order because half the electrons of this lattice and the electrons of the triplet pairs occupy the orbitals of the same Mn^{3+} ions (Fig. 3).

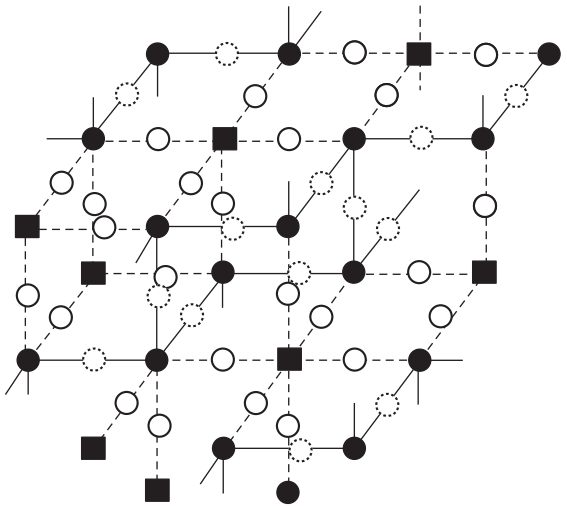

Fig. 4. Ordering of (●) Mn^{3+} and (■) Mn^{4+} ions, as well as of $1e$–σ bonds formed by singlet pairs (dashed lines) and $1e$–σ^* bonds formed by triplet pairs (solid lines), in $A_{0.67}B_{0.33}MnO_3$. Dotted circles, O^{2-} ions in the state of $3s2p$ hybridization. Lattice local distortions are not shown.

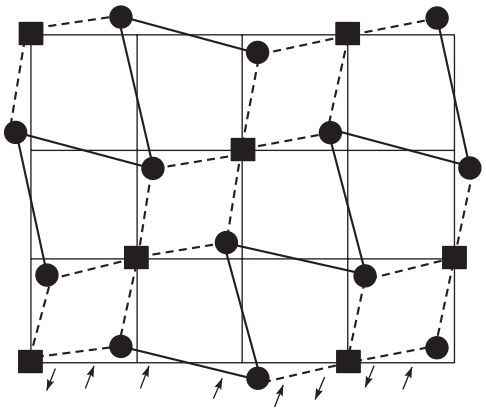

Fig. 5. Projection of the strained (distorted) crystal lattice onto the MnO_2 plane. $1e$–σ and $1e$–σ^* bonds produced by the singlet and triplet electron pairs are shown. O^{2-} ions producing these bonds are omitted. Designations are the same as in Fig. 4.

FERROMAGNETIC FLUCTUATIONS AND THE EFFECT OF AN APPLIED MAGNETIC FIELD ON T_c

As follows from the above consideration, T_c can be viewed as the temperature of formation of the spin-ordered electron lattice, including the spin-polarized sublattice of the triplet pairs. Above this temperature, the electrons are not spin-ordered and are localized on the anions. Although the anions, which are polarized by the Mn ions, may be in the state of $3s2p$ hybridization, the static overlap of these hybridized orbitals with those of the cations is absent. Only dynamic overlapping due to lattice thermal oscillation is possible. It does not order all valence electrons in the crystal in terms of the spin but may show up as ferromagnetic fluctuations, which have been observed experimentally [16]. As the temperature drops, approaching T_c, the system as if paves the way to the formation of the spin-polarized lattice. In other words, the spins of all the electrons of the triplet pairs gradually acquire the same orientation as the $1e$–σ^* bonds are produced between a Mn^{3+} ion and surrounding O^{2-} ions. It is obvious that the application of a magnetic field, orienting the spins of the triplet pair electrons in the same direction, may accelerate the formation of the spin-polarized electronic sublattice and

thereby raise T_c. For the same reason, T_c must increase with magnetic field as well [17].

In terms of our model, the effect of giant magnetoresistance arises because of the conduction mechanism change-over during the formation of the electron lattice: thermally activated conduction, typical of states with ionic bonds, changes to metallic conduction, which is associated with the spin-polarized electron sublattice of triplet pairs. The formation of the pairs is facilitated by the application of a magnetic field.

CONCLUSION

Thus, the nature of the strongly correlated state of electrons in manganates can be understood by taking into consideration the strong covalence of chemical bonds between the manganese and oxygen ions. The covalence shows up through the formation of one-electron σ bonds between these ions. The bonds are produced when the free d^2sp^3 hybridized orbitals of the manganese ions and the anion orbitals overlap. In this case, each of the anions produces two one-electron σ bonds with two neighboring Mn ions. It is assumed that, in manganates, Mn^{3+} ions are in the low-spin state. Also, the Mn ions are assumed to polarize the anion located between them, facilitating its 3*s*2*p* hybridization and the transition of its electron pair from the singlet to triplet state. In one-electron covalent bonds between the manganese and oxygen ions, the electrons of both the singlet and triplet pairs take place, hence, different spin orders of the electrons on the orbitals of adjacent cations. The correlated state of electrons forming one-electron σ bonds is due to the exchange interaction between the electrons that simultaneously occupy the hybridized orbitals of the cations and *p*- or 3*s*2*p* hybridized orbitals of the anions. It is this exchange interaction that causes the spin and spatial order of the electrons, which is the prerequisite for the formation of the spin-ordered electron lattice. The conductivity due to this electron lattice depends on the type of spin ordering; dimension of the lattice; and the energy of localization, which, in turn, depends on the energy of one-electron σ bonding.

The chemical bond model suggested in this work has turned out to be useful for the explanation of high-temperature conductivity in cuprates. In [18], an attempt was made to describe Cu–O ionic bonds, which are more covalent than Mn–O bonds in manganates, through the resonance state of ionic and ordinary two-electron σ bonds (by analogy with molecular bonds [12]). Although such a treatment of covalence has led to the idea of additional π bonding between the Cu and O ions, which made it possible to explain high-temperature conductivity on the qualitative basis, many assumptions of the model remained questionable.

The concept of one-electron σ bonding, put forward to accommodate bond covalence, has clarified the behavior of correlated electrons in cuprate superconductors. It can be assumed that one-electron σ bonds are also produced in the CuO_2 plane. The anions are also polarized by the cations. However, in the superconductivity effect, the polarization of the anions in the highly asymmetric electric field normal to the CuO_2 plane plays a crucial part. The polarization favors the 3*s*2*p* hybridization of the anion and the transition of its electron pair to the 3*s*2*p* orbital facing the large positive charge. The singlet pairs occupying the 3*s*2*p* orbitals of the anions produce the localized electron lattice. The displacement of this lattice, i.e., the collective displacement of the singlet pairs, can occur when the 3*s*2*p* orbitals of the anions overlap with the free hybridized orbitals of the Cu^{3+} ions via π bonds to form delocalized π orbitals. Thus, it turns out that the essence of the pairing mechanism in high-temperature superconductors is exchange interaction between electrons occupying the anion hybridized orbital polarized by the highly symmetric crystal field. In this model, superconductivity is provided by the displacement of the electron-pair lattice through the delocalized π orbitals belonging to the Cu^{3+} and O^{2-} chains in the CuO_2 plane.

After this article was written, Kagan and Kugel' published a work [Usp. Fiz. Nauk 171, 577 (2001)] where the problem of small-scale phase layering in manganates is discussed at length in terms of the instability of uniform magnetic or charge ordering.

REFERENCES

1. G. Prinz and K. Hathaway, Phys. Today **48**, 24 (1995); J. L. Simonds, Phys. Today **48**, 26 (1995); G. Prinz, Phys. Today **48**, 58 (1995).
2. G. H. Jonker and J. H. van Santen, Physica (Amsterdam) **16**, 337 (1950); E. O. Wollen and W. C. Koehler, Phys. Rev. **100**, 545 (1955); R. H. Heffner, L. P. Le, M. F. Hundley, *et al.*, Phys. Rev. Lett. **77**, 1869 (1996); J. M. D. Coey, M. Viret, and S. von Molnar, Adv. Phys. **48**, 167 (1999).
3. C. Zener, Phys. Rev. **82**, 403 (1951); P. W. Anderson and H. Hasegawa, Phys. Rev. **100**, 675 (1955).
4. J. Fontcuberta, B. Martinez, A. Seffar, *et al.*, Phys. Rev. Lett. **76**, 1122 (1996).
5. R. von Helmolt, J. Wecker, B. Holzapfel, *et al.*, Phys. Rev. Lett. **71**, 2331 (1993); S. Jin, T. H. Tiefel, M. McCormack, *et al.*, Science **264**, 413 (1994); K. Chahera, T. Ohno, M. Kasai, and Y. Kozono, Appl. Phys. Lett. **63**, 1990 (1993).
6. C. H. Chen and S.-W. Cheong, Phys. Rev. Lett. **76**, 4042 (1996); P. G. Radaelli, D. E. Cox, L. Capogne, *et al.*, Phys. Rev. B **59**, 14440 (1999).
7. Z. Zeng, M. Creenblatt, M. A. Subramanian, and M. Croft, Phys. Rev. Lett. **82**, 3164 (1999).
8. Y. Shimakawa, Y. Kubo, and T. Manako, Nature **379**, 53 (1996).
9. A. J. Millis, P. B. Littlewood, and B. I. Shraiman, Phys. Rev. Lett. **74**, 5144 (1995).
10. D. Louca, T. Egami, E. L. Brosha, *et al.*, Phys. Rev. B **56**, R8475 (1997); S. J. L. Billinge, R. G. DiFrancesco,

G. H. Kwei, *et al.*, Phys. Rev. Lett. **77**, 715 (1996); D. Louca and T. Egami, Phys. Rev. B **59**, 6193 (1999).

11. J. B. Goodenough, Phys. Rev. **100**, 564 (1955).
12. L. Pauling, *The Nature of the Chemical Bond and the Structure of Molecules and Crystals* (Cornell Univ. Press, Ithaca, 1940, 2nd ed.).
13. T. A. Tyson, Q. Qian, C.-C. Kao, *et al.*, Phys. Rev. B **60**, 4665 (1999).
14. T. H. Geballe and B. Y. Moyzhes, J. Electroceram. **4**, 289 (2000).
15. E. Wigner, Phys. Rev. **46**, 1002 (1934).
16. J. W. Lynn, R. W. Erwin, J. A. Borchers, *et al.*, Phys. Rev. Lett. **76**, 4046 (1996).
17. A. Urushibara, Y. Moritomo, T. Arima, *et al.*, Phys. Rev. B **51**, 14103 (1995).
18. M. V. Krasin'kova, Pis'ma Zh. Tekh. Fiz. **23** (17), 57 (1997) [Tech. Phys. Lett. **23**, 681 (1997)]; M. V. Krasin'kova, Zh. Tekh. Fiz. **68** (11), 82 (1998) [Tech. Phys. **43**, 1347 (1998)].

Translated by V. Isaakyan

Technical Physics, Vol. 47, No. 5, 2002, pp. 550–554. Translated from Zhurnal Tekhnicheskoĭ Fiziki, Vol. 72, No. 5, 2002, pp. 38–41.

SOLIDS

Physicochemical Interaction at the Contact of Higher Manganese Silicide with Chromium

L. I. Petrova*, L. D. Dudkin*, M. I. Fedorov, F. Yu. Solomkin**, V. K. Zaĭtsev**, and I. S. Eremin****

** Baikov Institute of Metallurgy, Russian Academy of Sciences, Leninskiĭ pr. 49, Moscow, 117334 Russia*

*** Ioffe Physicotechnical Institute, Russian Academy of Sciences, Politekhnicheskaya ul. 26, St. Petersburg, 194021 Russia*

e-mail: M.Fedorov@pop.ioffe.rssi.ru

Received July 18, 2001; in final form, November 16, 2001

Abstract—Diffusion processes taking place at the contact of higher manganese silicide $MnSi_{1.71–1.75}$ with chromium at elevated temperatures are considered. The microstructures of cast and annealed samples show a diffusion region that evolves at the HMS/Cr interface during the HMS melt crystallization on chromium flakes. As the temperature and time of annealing of HMS/Cr samples increase, the diffusion region grows thicker and new phases appear. It is shown that the diffusion is of reaction character. The diffusion coefficients of magnesium, chromium, and silicon in the solid solution based on manganese and chromium monosilicides and in the solid solution based on the Cr_3Si compound are calculated. It is also shown that, when the temperature of the HMS used as a thermoelement positive leg is optimal, the depletion time of a 10-μm-thick chromium layer exceeds 15000 h. Intermetallic phases forming in the diffusion region between the HMS and Cr are of metallic conduction and exhibit a high thermal conductivity, which minimizes energy losses in the contact layers of thermoelements. © *2002 MAIK "Nauka/Interperiodica"*.

Higher manganese silicide (HMS) $MnSi_{1.71–1.75}$ is a promising *p*-type material with a maximal thermoelectric figure of merit $ZT = 0.7$. Low vapor pressure, high chemical stability, no need for protection in open air at high temperatures, low production cost, as well as the availability and nontoxicity of the constituents, all makes HMS a candidate for the positive leg of thermogenerators [1].

In the design of thermoelectric devices, much attention is given to the production of contacts that retain their parameters at high temperatures and withstand temperature cycling. One of the most appropriate contact materials is nickel. Under certain conditions, nickel can also be used as the passive leg of a thermoelement [2]. Diffusion in the HMS/Ni contact were studied in [3]. It was established that, due to reaction diffusion, a diffusion region consisting of Mn–Ni–Si intermetallic layers forms between the contacting materials [4]. Different partial diffusion coefficients of the components and the brittleness of phases arising at the nickel boundaries cause cracking and void formation. The use of chromium as an antidiffusion interlayer between HMS and nickel was studied in [5]. It was demonstrated that the presence of a Cr interlayer suppresses the diffusion of Ni in HMS. The formation of a chromium–nickel solid solution and the penetration of Cr from the interlayer into HMS were also observed. In this study, we analyze diffusion processes that take place at HMS/Cr contact at high temperatures.

In our experiments, HMS/Cr contacts were prepared by vacuum casting: quartz ampules containing electrolytic chromium flakes were filled with molten HMS. Then, the samples were placed in argon-filled quartz ampules and heat-treated at temperatures from 1073 to 1173 K for 5 to 25 h. The samples were examined by electron probe X-ray analysis and structural analysis. The radiation intensities from Cr, Mn, and Si versus the depth of penetration into the HMS/Cr contact region were taken by a Cameca MS-46 microanalyzer with a spatial resolution of about 1 μm in the continuous record mode. To derive the concentrations of the components from the intensities, the latter were corrected for radiation absorption, atomic number of the element, and fluorescence with the technique presented in [6].

The microstructure of the as-cast and annealed samples shows a diffusion region that appears at the HMS/Cr interface even at the stage of the HMS crystallization on the Cr flakes (Fig. 1a). As the annealing temperature and time increase, the diffusion region thickens (Figs. 1b, 1c) and layers of new phases appear. The diffusion region consists largely of two layers of different color and structure. The space in between is a two-phase zone consisting of a layer adjacent to the chromium and new-phase inclusions. Such a structure arises when the components of the initial diffusion pair diffuse through the first single-phase region; cross the two-phase zone, which connects these two phases in the

1063-7842/02/4705-0550$22.00 © 2002 MAIK "Nauka/Interperiodica"

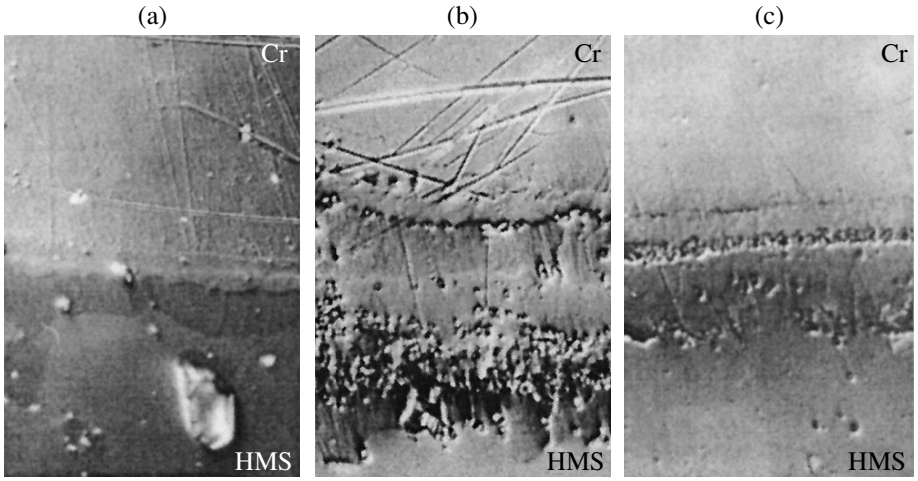

Fig. 1. Micrographs of the (a) as-prepared HMS/Cr contact (×625), (b) contact annealed at 1073 K for 25 h (×400), and (c) contact annealed at 1173 K for 5 h (×400).

ternary phase diagram; and then, crossing the ternary region, reach the other single-phase region [7].

The stepwise change in the Cr, Mn, and Si concentrations that was observed in the diffusion region implies the reaction character of the diffusion. Figure 2 shows the distribution of the Mn, Cr, and Si concentrations near the HMS/Cr contact in the as-cast and heat-treated samples. In the former, the transition region between the HMS and Cr contains new-phase nuclei (Fig. 2a). After the annealing, these phases thicken and phases of another composition appear (Figs. 2b, 2c). The compositions and thicknesses Δx of the phases formed by the reaction diffusion at the HMS/chromium contact were determined from the concentration profiles of the components. After the vacuum casting, two layers were observed in the diffusion region: a layer of the MnSi–CrSi solid solution and a narrow layer of a chromium-based solid solution. After the thermal treatment, a solid solution based on Cr_3Si and a phase based on the Mn_5Si_3 compound appeared. The compositions and thicknesses of the layers formed in the reaction diffusion region of the samples after annealing at 1073 K for 25 h are listed in Table 1. To determine the thicknesses of the layers grown in the diffusion region after the thermal treatment, the thickness of the diffusion region grown at the stage of sample preparation was subtracted from the diffusion region after the treatment.

A comparison of the X-ray electron probe data with the isothermal section of the equilibrium phase diagram for the ternary Cr–Mn–Si system [4, 8] shows that the compositions of the phases and the order of their arrangement between the HMS and Cr in the diffusion region correlate well with the phase equilibria in the Cr–Mn–Si system (Fig. 3). The dashed curve indicates the diffusion path of the components of the initial diffusion pair HMS/Cr, and the dots mark the homogeneity region for Mn_5Si_3, which has not yet been studied in detail.

Based on the experimental data obtained and employing the technique described in [9], we calculated the diffusion coefficients D of manganese, chromium, and silicon in the two thickest phases, namely, in the MnSi–CrSi solid solution and in the solid solution based on the Cr_3Si compound (Table 2). The diffusion

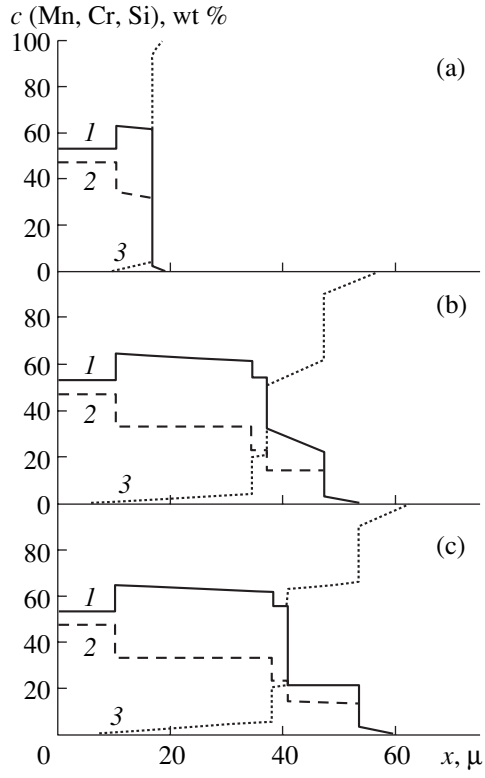

Fig. 2. Concentration profiles of (*1*) Mn, (*2*) Si, and (*3*) Cr in the HMS/Cr contact region of the (a) as-prepared sample, (b) after annealing at 1073 K for 25 h, and (c) after annealing at 1173 K for 5 h.

Table 1. Mn, Cr, and Si content in the layers of the diffusion region at the HMS/Cr contact and the thickness of the layers after annealing at 1073 K for 25 h

Phase composition	Concentration, wt %			Δx, μm
	Mn	Cr	Si	
HMS($MnSi_{1.75}$)	52.8	–	47.2	100
$Mn_{1-p}Cr_pSi$	65.1–61.8	6.1–4.7	33.3–33.5	18
$Mn_{5-y}Cr_ySi_{3+}$	55.5	21.0	23.5	2.6
$Cr_{3-q}Mn_qSi$	36.1	45.5	18.4	
$Cr_{3-q}Mn_qSi$	33.6–23.5	51.3–62.6	15.1–13.9	10.2
Cr(Mn, Si)	3.4–0	92.3–100	4.3–0	5.8

coefficients were calculated by the formula $D = k^2c/2\Delta c$, where k is the rate constant of phase growth, c is the mean of two extreme phase concentrations in the concentration profiles of components, and Δc is the concentration extent of a phase. For a parabolic dependence of the phase layer thickness on the diffusion time (τ), the rate constant is expressed in the form $k = \Delta x/\tau^{1/2}$ [10]. The data presented above indicate that, in the ($Mn_{1-p}Cr_pSi$) solid solution, the silicon has a maximal diffusion mobility, and the chromium, minimal. In the Cr_3Si-based solid solution, the diffusion coefficient of Cr increases. The diffusion coefficients of the components in all of the phases increase with annealing temperature.

The solid-phase growth of the phase layers at the HMS/Cr contact involves the following transformations: HMS decomposition,

$$4MnSi_{1.75} = 4MnSi + 3Si_{dif},$$

and the interaction between diffusing silicon and chromium atoms,

$$3Si_{dif} + 9Cr = 3Cr_3Si.$$

In addition, the interdiffusion of Cr and Mn atoms leads to the partial substitution of Cr for Mn with the formation of a $Mn_{1-p}Cr_pSi$ layer and of Mn for Cr with the formation of a $Cr_{3-q}Mn_qSi$ layer. It is evident that the HMS side of the diffusion layer must grow faster, since the decomposition of $MnSi_{1.75}$ yields four "molecules" of MnSi whereas only three molecules of Cr_3Si appear at the Cr interface.

As the intermediate phases grow in the diffusion region, the components that have initially been brought into contact come to an end. In this connection, it is of interest to determine the time taken for the chromium

Table 2. Diffusion coefficients of Mn, Cr, and Si in the reaction diffusion phases at the HMS/Cr contact at (a, b) 1073 and (c, d) 1173 K

Component	Δx, μm	τ, h	c, %	Δc, %	k^2, cm^2/s	D, cm^2/s
			(a) $Mn_{1-p}Cr_pSi$			
Mn	18	25	63.45	3.3	3.7×10^{-11}	3.6×10^{-10}
Cr	18	25	3.15	3.1		1.9×10^{-11}
Si	18	25	33.4	0.2		3.1×10^{-9}
			(b) $Cr_{3-q}Mn_qSi$			
Mn	10.2	25	28.3	9.6	1.2×10^{-11}	1.3×10^{-11}
Cr	10.2	25	56.45	11.3		2.9×10^{-11}
Si	10.2	25	14.5	1.2		7.0×10^{-11}
			(c) $Mn_{1-p}Cr_pSi$			
Mn	21.8	5	63.0	2.9	2.6×10^{-10}	2.8×10^{-9}
Cr	21.8	5	3.6	3.4		1.4×10^{-10}
Si	21.8	5	33.5	0.5		8.7×10^{-9}
			(d) $Cr_{3-q}Mn_qSi$			
Mn	12.8	5	21.5	1.2	9.1×10^{-11}	8.2×10^{-10}
Cr	12.8	5	64.15	3.1		9.4×10^{-10}
Si	12.8	5	14.4	1.8		3.6×10^{-10}

Table 3. Kinetic parameters of reaction diffusion at the HMS/Cr contact with $x_{Cr(0)} = 10$ μm

T, K	τ, h	$\Delta x_{Cr(1)}$, μm	$\Delta x_{Cr(2)}$, μm	K_1^2, cm²/s	K_2^2, cm²/s	K^2, cm²/s	t_{Cr}, h
1173	5	0.9	7.1	1×10^{-11}	5×10^{-11}	6×10^{-11}	4.6
1073	25	0.6	4.4	1.3×10^{-12}	4.9×10^{-12}	6.2×10^{-12}	44.8
873	–	–	–	5.1×10^{-15}	13.1×10^{-15}	1.8×10^{-14}	15260
773	–	–	–	1.1×10^{-16}	1.8×10^{-16}	2.9×10^{-16}	960000

antidiffusion interlayer at the HMS/Cr–Ni contact to be fully exhausted, since this layer has a much smaller initial thickness than the HMS and Ni layers [5].

We based our calculations on the experimentally verified assumption that both the growth and the depletion of the phases are a parabolic function of time [11]. Given the initial thickness $x(0)$ of each of the starting components, the variation of the thickness can be found from the expression $x(\tau) = x(0) - K\tau^{1/2}$, where K is the depletion constant. If we assume that $x(\tau) = 0$ at $\tau = t$, the depletion time $t = x(0)^2/K^2$. During the interdiffusion at the HMS/Cr contact, the chromium is mainly spent on the growth of the two intermediate phases: $Mn_{1-p}Cr_pSi$ (phase 1) and $Cr_{3-q}Mn_qSi$ (phase 2); therefore, the Cr depletion time is defined as $t_{Cr} = x_{Cr}(0)^2/(K_1^2 + K_2^2)$, where K_1 and K_2 are the depletion constants of the chromium spent on the related phases. The kinetic parameters of the reaction diffusion at the HMS/Cr contact were determined under the assumption that one phase does not affect diffusion in the order. Employing the technique used in [12], we believed that a decrease in the thickness of the initial Cr layer (Δx_{Cr}) is related to the thickness of the resulting compound (d) as follows: for the $Mn_{1-p}Cr_pSi$ layer, $\Delta x_{Cr(1)} = d_1 p V_{Cr}/V_1$; for the $Cr_{3-q}Mn_qSi$ (2) layer, $\Delta x_{Cr(2)} = d_2(1 - q)V_{Cr}/V_2$. Here, V are the molar volumes of the corresponding components, which were calculated from the room-temperature X-ray data for the size of the atoms in accordance with their coordination numbers [13]. The calculations were carried out for the phases with the highest Cr content. These phases were found from the concentration profiles of the components in the diffusion region of the HMS/Cr contact; the chromium depletion constants, from the equations $K_1^2 = d_1\Delta x_{Cr(1)}/\tau$ and $K_2^2 = d_2\Delta x_{Cr(2)}/\tau$, where τ is the diffusion time at a given temperature. The results of calculations are listed in Table 3.

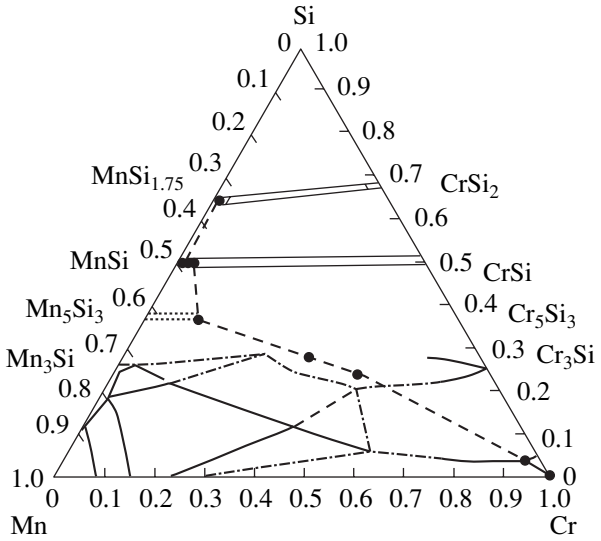

Fig. 3. Phase diagram of the Cr–Mn–Si system at 1273 K [6]. The dashed curve passes through the phase compositions (circles) of the layers in the diffusion region between HMS and Cr after annealing at 1073 K.

From the data obtained at 1073 and 1173 K, we derived the activation energies of chromium "depletion" in the two phases mentioned above: $Q_1 = 217.5$ kJ/mol and $Q_2 = 240$ kJ/mol. Using these values, we calculate the constants and times of depletion for a 10-μm-thick Cr layer at lower temperatures. It is seen from the table that the decrease in the operating temperature of the contact extends considerably the chromium layer lifetime and, thus, the service time of the contact.

Note also that the intermetallic phases forming in the diffusion region between the HMS and Cr has metallic conduction and a high thermal conductivity [13], which minimizes energy losses in thermoelement contacting layers.

The results presented above indicate that chromium is a candidate for antidiffusion interlayers in thermoelectric devices.

REFERENCES

1. L. D. Dudkin and L. I. Petrova, Perspekt. Mater., No. 5, 15 (1996).
2. M. I. Fedorov, V. K. Zaĭtsev, F. Yu. Solomkin, *et al.*, Pis'ma Zh. Tekh. Fiz. **23** (15), 64 (1997) [Tech. Phys. Lett. **23**, 602 (1997)].
3. L. I. Petrova, L. D. Dudkin, and V. S. Khlomov, Neorg. Mater. **31**, 1216 (1995).

4. E. I. Gladyshevskiĭ, *Crystal Chemistry of Silicides and Germanides* (Metallurgiya, Moscow, 1971).
5. L. I. Petrova, L. D. Dudkin, V. S. Khlomov, *et al.*, Zh. Tekh. Fiz. **70** (5), 119 (2000) [Tech. Phys. **45**, 641 (2000)].
6. V. I. Rydnik and I. B. Borovskiĭ, Zavod. Lab., No. 8, 955 (1967).
7. J. B. Clark, Trans. Metall. Soc. AIME **227**, 1250 (1963).
8. N. Kh. Abrikosov, E. I. Elagina, and L. I. Ledenkova, Izv. Akad. Nauk SSSR, Neorg. Mater. **7**, 870 (1971).
9. B. N. Arzamasov, Metalloved. Term. Obrab. Met., No. 3, 49 (1967).
10. Ya. I. Frenkel' and M. I. Sergeev, Zh. Éksp. Teor. Fiz. **9**, 189 (1939).
11. K. P. Gurov, B. A. Kartashkin, and Yu. É. Ugaste, *Interdiffusion in Multiphase Metallic Systems* (Nauka, Moscow, 1981).
12. V. I. Dybkov, Poroshk. Metall., No. 1, 66 (1990).
13. P. V. Gel'd and F. A. Sidorenko, *Silicides of Period IV Transition Metals* (Metallurgiya, Moscow, 1971).

Translated by A. Sidorova-Biryukova

Technical Physics, Vol. 47, No. 5, 2002, pp. 555–560. Translated from Zhurnal Tekhnicheskoĭ Fiziki, Vol. 72, No. 5, 2002, pp. 42–47.

SOLIDS

Effect of an External Magnetic Field on the Orientational Phase Diagrams of (011) Crystalline Garnet Ferrite Plates with Combined Anisotropy

R. M. Vakhitov, V. V. Grinevich†, and M. M. Vakhitova

Bashkortostan State University, ul. Frunze 32, Ufa, 450074 Bashkortostan, Russia

e-mail: VakhitovRM@bsu.bashedu.ru

Received September 3, 2001

Abstract—The effect of an external magnetic field on uniform magnetic states in (011) crystalline garnet ferrite plates with combined anisotropy is theoretically studied. Under the action of the field, the magnetic symmetry of the crystals is reduced and the pattern of spin-reorientation phase transitions, which depends significantly on the magnetic field strength and direction, changes. Curves of critical fields are found, and the general law of magnetization reversal in the (011) plates due to rotation is derived. *© 2002 MAIK "Nauka/Interperiodica".*

INTRODUCTION

As is known, epitaxial garnet ferrite single crystals, used in many magnetic electron devices, exhibit both induced uniaxial (IUA) and natural cubic (CA) anisotropies [1, 2]. Such a combination affects considerably the properties of the material, including its behavior in an external magnetic field. Studying the processes of magnetization and magnetization reversal in the crystals, one extracts much information on some magnetic characteristics that are of practical value. In this respect, it is of interest to study the effect of an external magnetic field on the equilibrium directions of the magnetization vector M in the (011) crystals with the combined anisotropy. Earlier [3–5], similar studies were performed on magnets in the form of (001) and (111) plates. In this work, we concentrate on magnetization reversal that is due to magnetic moment coherent rotation. Note also that in the magnets under study, IUA has two, perpendicular and rhombic, components. The latter improves the dynamic properties of the material, hence, increasing interest in it.

UNIFORM MAGNETIC STATES IN THE ABSENCE OF FIELD

Let us consider first the energy density of a uniformly magnetized (011) plate with combined anisotropy subjected to a magnetic field H. In the coordinate systems with the axis $Oz \parallel [011]$, the axis $Ox \parallel [100]$, and the axis $Oy \parallel [01\bar{1}]$, the energy density has the form

$$\begin{aligned} E &= K_u \sin^2\Theta + K_r \sin^2\Theta \sin^2\varphi \\ &+ K_1\Big[\sin^4\Theta\Big(\cos^2\varphi\sin^2\varphi + \frac{1}{4}\sin^4\varphi\Big) \\ &+ \sin^2\Theta\cos^2\Theta\Big(\cos^2\varphi - \frac{1}{2}\sin^2\varphi\Big) + \frac{1}{4}\cos^4\Theta\Big] \\ &+ \frac{1}{4}K_2[\sin^2\Theta\cos^4\Theta\cos^2\varphi - 2\sin^4\Theta\cos^2\Theta\sin^2\varphi \\ &\times \cos^2\varphi + \sin^6\Theta\sin^4\varphi\cos^2\varphi] - (\mathbf{MH}), \end{aligned} \quad (1)$$

where K_u and K_r are the constants of uniaxial and rhombic anisotropies, respectively; K_1 and K_2 are the first and second constants of CA; Θ and φ are the polar and azimuth angles of the magnetization vector $\mathbf{M}$; and $(\mathbf{MH})$ is the scalar product of the vectors. Taking into account the finiteness of the plate leads merely to the renormalization of the constant $K_u \longrightarrow K_u - 2\pi M_s^2$, where M_s is the saturation magnetization.

The equilibrium directions of the magnetization $\mathbf{M}$ in the crystal are found from the minimum of (1), i.e., from solutions of the equations

$$\frac{\partial E}{\partial \varphi} = 0, \quad \frac{\partial E}{\partial \Theta} = 0 \quad (2)$$

subject to

$$\frac{\partial^2 E}{\partial \varphi^2} > 0, \quad \frac{\partial^2 E}{\partial \Theta^2} > 0, \quad \frac{\partial^2 E}{\partial \varphi^2}\frac{\partial^2 E}{\partial \Theta^2} - \left(\frac{\partial^2 E}{\partial \varphi \partial \Theta}\right)^2 > 0. \quad (3)$$

It follows from the above equations [6] that nine magnetic phases may exist in the (011) plate if $H = 0$.

† Deceased.

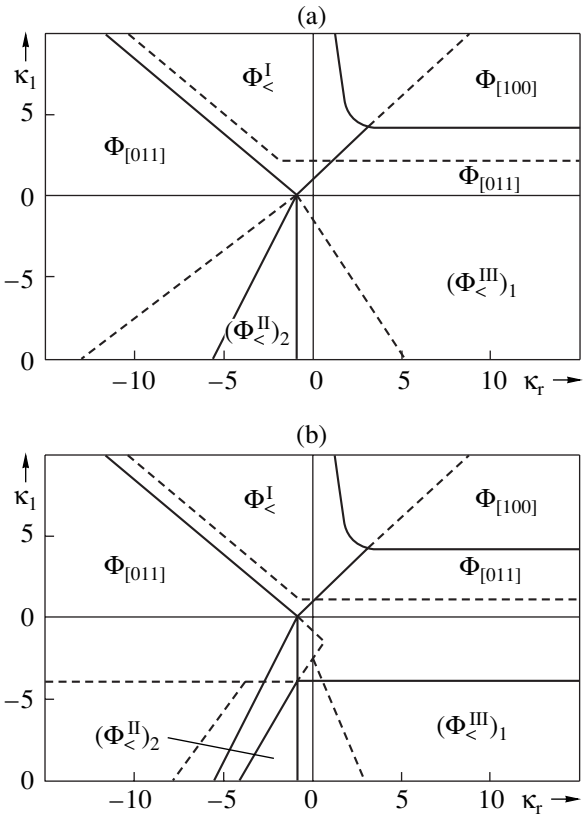

Fig. 1. Phase diagram for uniform magnetic states of the (011) plate in the absence of the field for $K_u > 0$. (a, b) $\kappa_2 = 4$. Continuous curves, SRPTs; dashed curves, boundaries of the domains of existence for metastable phases.

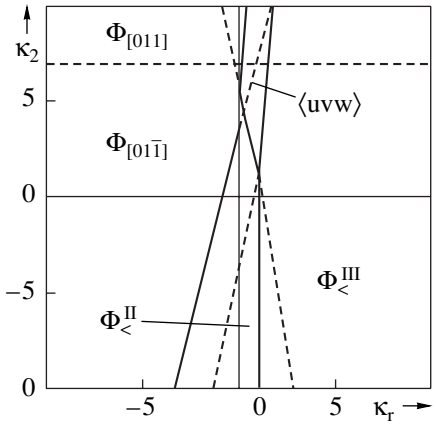

Fig. 2. The same as in Fig. 1 for $K_u < 0$ and $\kappa_1 = -1.5$.

Three of them are symmetrical and six, disymmetrical [7] (Figs. 1, 2). Of the latter six, five are angular. In them, the magnetization **M** varies in certain planes of symmetry of a cube, depending on the parameters κ_1, κ_2, and κ_r, where $\kappa_1 = K_1/|K_u|$, $\kappa_2 = K_2/|K_u|$, and $\kappa_r = K_r/|K_u|$. The sixth phase is of the general type. The parameters of these phases are listed in the table. The degree of their degeneracy depends mostly on the symmetry of the plate (group D_{2h}) [7, 8]. Specifically, the high-symmetry phases are doubly degenerate; the angular ones, quadruply degenerate; and the phase of the general type, octuply degenerate. The angular phases $(\Phi^{II}_{<})_{1,2}$ and $(\Phi^{III}_{<})_{1,2}$ have the same group of symmetry. Their presence is due to the fact that CA is taken into account ($K_2 \neq 0$). In fact, the asymptotic behavior ($K_2 \longrightarrow 0$) of the phases $(\Phi^{III}_{<})_{1,2}$ implies that the phase $(\Phi^{III}_{<})_1$ continuously turns to the angular phase $\Phi^{III}_{<}$, which was studied earlier in [9, 10] and takes place at $K_2 = 0$, and that the second solution of Eqs. (2) and (3), which corresponds to the phase $(\Phi^{III}_{<})_2$, loses its meaning. It becomes meaningful only if $K_2 = 0$, i.e., when the contribution of easy CA axes like [011] to the spectrum of uniform magnetic state of the plate is included. This follows, for example, from the coincidence of the domains of stability in terms of K_1 and K_2 for the phases $(\Phi^{III}_{<})_2$ and $\langle 011 \rangle$ [11]. The occurrence of the phase [uvw], whose domain of existence is shown in the coordinates (κ_r, κ_2) in the phase diagram (Fig. 2), is explained by the same reason.

Another feature of the orientational phase diagram for the (011) plate is the presence of the quintuple point (Fig. 1). This is consistent with the Gibbs phase rule, which states that a given thermodynamic system is in equilibrium under the action of three internal fields associated with three anisotropies with different symmetries: uniaxial, rhombic, and cubic [6].

MAGNETIC PHASE DIAGRAMS IN THE PRESENCE OF AN EXTERNAL FIELD

In order to study the effect of a magnetic field on the ground state of the crystal, it is necessary to take into account Zeeman interaction ($H \neq 0$, whose contribution to (1) depends on the orientation of **H** with respect to the crystallographic planes. Let us consider three typical orientations of the field: **H** ∥ [011], **H** ∥ [100], and **H** ∥ $[01\bar{1}]$.

(1) **H** ∥ [011]. In this case, the magnetic symmetry of the crystal is reduced to C_{2v} in the group D_{2h}. Because of the loss of the symmetry element σ [$\sigma_h(m)$ is the mirror reflection plane coincident with the plane (011)], the angular phases $\Phi^{I}_{<}$ and $\Phi^{III}_{<}$ split into two states: stable, where the magnetization **M** makes an acute angle Θ with the field, and metastable, where $\pi/2 < \Theta < \pi$. Their domains of existence are no longer coincident: the energetically less favorable phase $(\Phi^{1}_{<})^{z}_{2}$ is bounded by curve *1* in Fig. 3a, while the stable phase $(\Phi^{1}_{<})^{z}_{1}$ occupies the space bounded by curves *2* and *3*. The latter merges with the phase $\Phi_{[01\bar{1}]}$, which is skewed in the presence of the field (being symmetri-

Magnetic phases in the (011) plate in the absence of the field ($H = 0$)

Phases	Magnetization orientation	Domain of existence
$\Phi_{[011]}$	$\vartheta = 0; \pi$; $\mathbf{M} \parallel [011]$	$K_1 > -2(2K_u + K_1)$, $K_1 < K_u + K_r$
$\Phi_{[100]}$	$\vartheta = \pi/2$; $\varphi = 0, \pi$; $\mathbf{M} \parallel [100]$	$K_1 > K_u$, $K_1 < -K_r$
$\Phi_{[01\bar{1}]}$	$\vartheta = \pi/2$; $\varphi = \pi/2, 3\pi/2$; $\mathbf{M} \parallel [01\bar{1}]$	$K_1 < -(K_u + K_r)$, $K_1 > 2K_r - K_2/2$
$\Phi^{I}_{<}$	$\sin\varphi = \{[K_1 - (K_u + K_r)]/2K_1\}^{1/2}$, $\vartheta = \pi/2, 3\pi/2$; $\mathbf{M} \parallel [0uv]$	$K_1 > -(K_u + K_r)$, $K_1 > K_u + K_r$ $4K_1^3 + 2K_1^2(K_u - K_r) + K_2(K_u + K_r)^2 > 0$
$(\Phi^{II}_{<})_1$	$\vartheta = \pi/2$, $\sin\vartheta = \pm\sqrt{\frac{A_1 + B_1}{3K_2}}$, $\mathbf{M} \parallel [uv\bar{v}]$	
$(\Phi^{II}_{<})_2$	$\vartheta = \pi/2$, $\sin\vartheta = \pm\sqrt{\frac{A_1 - B_1}{3K_2}}$, $\mathbf{M} \parallel [uv\bar{v}]$	
$(\Phi^{III}_{<})_1$	$\sin\vartheta = \pm\sqrt{\frac{A_1 + B_1}{3K_2}}$, $\vartheta = 0, \pi$, $\mathbf{M} \parallel [uvv]$	
$(\Phi^{III}_{<})_2$	$\sin\vartheta = \pm\sqrt{\frac{A_1 - B_1}{3K_2}}$, $\vartheta = 0, \pi$, $\mathbf{M} \parallel [uvv]$	
$\Phi^{IV}_{<}$	$\mathbf{M} \parallel [uvv]$	

Note: $A_1 = K_2 - 3K_1$, $B_1 = \sqrt{A_1^2 + 12K_2(K_1 + K_2)}$, $A_1 = K_2 + 3K_1$, $B_1 = \sqrt{A_2^2 - 3K_2(K_u + 2K_1 + K_2)}$. Empty rows in the right-hand column mean that the domain of existence (stability) cannot be expressed through simple formulas; they are found from general conditions (3).

cal in its absence), to form the single angular phase $(\Phi^{I}_{[01\bar{1}]})^z_1$ with $\varphi = \pi/2$ or $3\pi/2$. Its domain of existence is bounded by the line of spin-reorientation phase transition (SRPT) of the second kind: $(\Phi^{I}_{[01\bar{1}]})^z_1 \longleftrightarrow (\Phi^{II}_{<})^z$ (curve *4*). Thus, the SRPT of the second kind $\Phi_{[01\bar{1}]} \longleftrightarrow \Phi^{I}_{<}$ (Fig. 3b) breaks, and the point *A* becomes quadruple rather than quintuple. In the presence of the field, the domains of existence of the stable phase $(\Phi^{III}_{<})^z_1$ and the metastable phase $(\Phi^{III}_{<})^z_2$ also diverge (their boundaries are depicted by curves *5*, *6* and *7*, *8* in the phase diagram).

The angular phases $(\Phi^{II}_{<})_{1,2}$ transform into the phases of the general type $(\Phi^{II}_{<})^z$, remaining degenerate, since $\mathbf{H} \parallel 2_z$ does not change their group of symmetry in our case. As the reduced field $h = M_s H/|K_u|$ grows, the line of the SRPT of the first kind, $(\Phi^{II}_{<})^z \longleftrightarrow (\Phi^{III}_{<})^z_1$, shifts toward smaller κ_r (curve *9* in Fig. 3a). For the same reason, the phase $\Phi_{[100]}$, which transforms into the angular phase $(\Phi_{[100]})^z_<$ of type [uvv], also remains degenerate. The domain of its existence is bounded by curve *10* in Fig. 3a and disappears from the phase diagram as *h* increases. Accordingly, the lines of the SRPTs of the first kind $(\Phi_{[100]})^z_< \longleftrightarrow \Phi_{[011]}$ (curve *11*) and $(\Phi_{[100]})^z_< \longleftrightarrow (\Phi^{I}_{[01\bar{1}]})^z_1$ (curve *12*) shift toward larger κ_1 and κ_2.

The degeneracy of the phase $\Phi_{[011]}$ is removed. It splits into two energetically nonequivalent symmetrical phases: stable with $\mathbf{M} \parallel [011]$, which displaces the rest of the phases with increasing *h*, and metastable with ($\mathbf{M} \parallel [0\bar{1}\bar{1}]$). The domain of existence of the latter is limited by the following inequality for the reduced field (Fig. 4):

$$h_{0z} \geq -2\,\mathrm{sgn}\,K_u - \kappa_1 - \frac{\kappa_2}{2}. \qquad (4)$$

Such a reduced field has the meaning of the coercive force. As follows from (4), it involves also the first and second CA constants.

(2) $\mathbf{H} \parallel [100]$. In this case, the degeneracy of the phases $(\Phi^{II}_{<})_{1,2}$ and $(\Phi^{III}_{<})_{1,2}$ is partially removed. Remaining angular with $\Theta = \pi/2$ ($\mathbf{M} \parallel [vu\bar{u}]$) and $\varphi = 0$ and π ($\mathbf{M} \parallel [vuu]$), respectively, they split into two doubly degenerate phases (stable and metastable), each having its own domain of existence. While the domain of existence of the metastable phase $(\Phi^{III}_{<})^x_2$ is bounded by curve *1* in Fig. 5, the phase $(\Phi^{III}_{<})^x_1$ occupies the

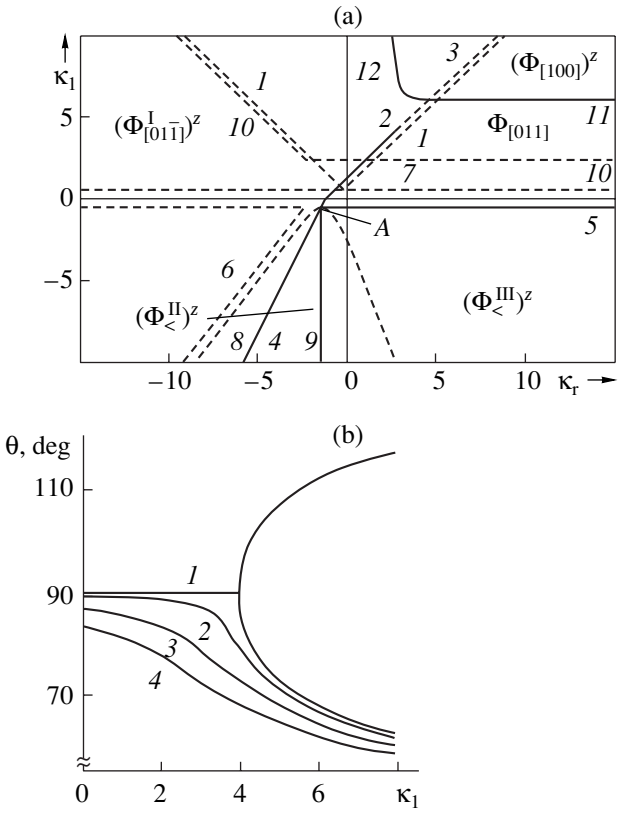

Fig. 3. (a) Phase diagram for uniform magnetic states of the (011) plate in the field **H** ∥ [011] for $K_u > 0$, $\kappa_2 = -4$, and $h = 0.5$; (b) SRPT of the second kind in the absence of the field ($\kappa_r = -5$) for $h = 0$ (*1*), 0.1 (*2*), 0.5 (*3*), and 10 (*4*). Figures at the curves correspond to Fig. 1.

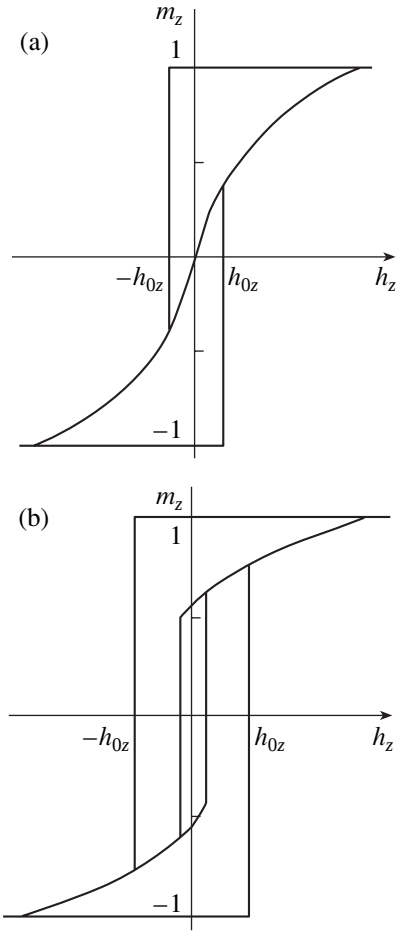

Fig. 4. Magnetization curves for $h = h_z$, $\kappa_2 = -4$, and $K_u > 0$. (a) $\kappa_1 = 2$ and $\kappa_r = -2$; (b) $\kappa_1 = 1$ and $\kappa_r = -3$.

entire space between curves *10* and *5* (the latter is the line of the SRPT of the first kind, $(\Phi^{III}_<)^x_1 \longleftrightarrow \Phi_{[100]}$). The metastable phase $(\Phi^{II}_<)^x_2$, lying below curve *12*, is displaced downward, i.e., toward smaller (negative) κ_1, as the reduced field grows. Simultaneously, the other phase $(\Phi^{II}_<)^x_1$ of the "doublet" merges with the skewed phase $\Phi_{[01\bar{1}]}$ to form the angular phase $(\Phi^{II}_{[01\bar{1}]})^x$. Its domain of existence lies to the left of and below curves *9* and *11*. Here, curve *9* corresponds to the SRTP of the second kind between the phases $(\Phi^{II}_{[01\bar{1}]})^x$ and $(\Phi^{I}_<)^x$, where the latter is a phase of the general type that is quadruply degenerate as before. It should be noted that the transformation of the angular phase $\Phi^I_<$ into the phase of the general type $(\Phi^I_<)^x$ can be explained by the fact that the vector **M** of the phase $\Phi^I_<$ lies in the plane (001) in the absence of the field. The field **H** ∥ [100] as if "extracts" spins from the plane (001), causing the phase of type [uvw] to form. At the same time, the vector **M** in the angular phases $(\Phi^{II}_<)_{1,2}$ and $(\Phi^{III}_<)_{1,2}$ lies in the plane (011) or $(01\bar{1})$. In this case, **H** ∥ [100] also lies in these planes, so that the phases do not transform when the field is applied.

The domain of existence of the phase $(\Phi^I_<)^x$, which is bounded by curves *6* and *8* [SRPT of the first kind $(\Phi^I_<)^x \longleftrightarrow (\Phi^{III}_<)^x_1$], is the same as in the case of the zero field (Fig. 1b). However, the region where it is energetically more favorable shrinks because the domain of existence of the more favorable symmetrical phase $(\Phi_{[100]})_1$ with **M** ∥ [100] expands. This phase arises when the doubly degenerate phase $\Phi_{[100]}$ splits into two magnetic states (doublet): $(\Phi_{[100]})_1$ with **M** ∥ [100] ($\varphi = 0$) and $(\Phi_{[100]})_2$ with **M** ∥ $[\bar{1}00]$ ($\varphi = \pi$). In this case, curve *3* in Fig. 5 bounds the stability domain of the phase $(\Phi_{[100]})_1$ and curve *4*, of the phase $(\Phi_{[100]})_2$. Also, we observe the SRPT of the first kind from $(\Phi_{[100]})_2$ to $(\Phi^{III}_<)^x$ (curve *5*) and from $(\Phi_{[100]})_1$ to $(\Phi^I_<)^x$ (curve *7*). The symmetrical phase $\Phi_{[011]}$ transforms into the angu-

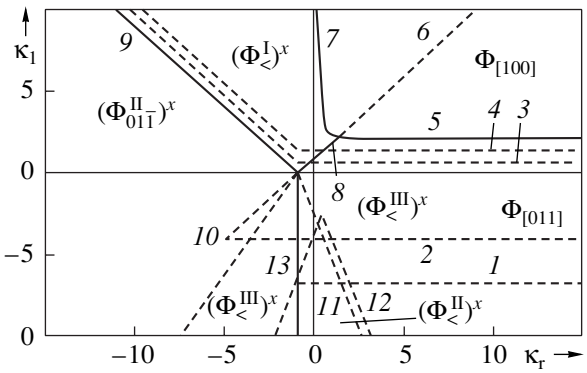

Fig. 5. Phase diagram for uniform magnetic states of the (011) plate in the field **H** || [100] for $K_u > 0$, $\kappa_2 = 4$, and $h = 0.5$. Dashed curves correspond to Fig. 1.

lar phase of type [uvv], which merges with $(\Phi_<^{III})^x$. Since **H** ⊥ [011], the degeneracy of the phases is retained. However, the SRPT of the second type $\Phi_{[011]} \longleftrightarrow \Phi_<^{III}$, taking place in the absence of the field, disappears.

(3) **H** || [$01\bar{1}$]. In this case, the field affects the original phase diagrams similarly to the case **H** || [011]. This follows from the symmetry of the (011) crystalline plate. Here, the equilibrium orientation of the vector **M** is specified by CA and IUA, both having perpendicular and rhombic components. The CA and IUA easy axes are mutually perpendicular and coincide with the directions [011] and [$01\bar{1}$], which are equivalent for CA. Therefore, the case **H** || [$01\bar{1}$] has the same effect as the case **H** || [011].

CRITICAL FIELD CURVES

To investigate the effect of a magnetic field on the ground state of the crystal throughout the field range, consider the curves of critical fields, which are determined from conditions (2) and (3) in view of (1) when the inequalities are replaced by equalities. For the plane $h_x h_z$, where $h_x = H_x M_s/|K_u|$ and $h_z = H_z M_s/|K_u|$, we come to the parametric equation

$$\begin{aligned} h_x &= P_1\cos\Theta - P_2\sin\Theta, \\ h_z &= -P_1\sin\Theta - P_2\cos\Theta, \end{aligned} \tag{5}$$

where

$$P_1 = \sin 2\Theta\left[\operatorname{sgn}K_u + \frac{1-3\sin^2\Theta}{4}(2\kappa_1 + \kappa_2\cos^2\Theta)\right],$$

$$P_2 = 2\operatorname{sgn}K_u\cos 2\Theta + \kappa_1[\sin^2\Theta(2\sin^2\Theta - 9\cos^2\Theta) \tag{6}$$

$$+ \cos^4\Theta] + \frac{\kappa_2}{2}\cos^2\Theta[\cos^4\Theta + \sin^2\Theta(6 - 17\cos^2\Theta)].$$

Figures 6a–6c show the associated curves. As the parameter κ_1 decreases (IUA begins to play a leading part), the domain of existence of the four states contracts and eventually (at $\kappa_1 = 1$) shrinks to a point. In the plane $h_y h_z$ ($h_y = H_y M_s/|K_u|$), the curves have a similar shape but are rotated by 90° with respect to the above case. Thus, we can argue that the magnetization of cubic crystals with IUA generally proceeds in a similar way [3–5]. Yet, the plate under study shows a number of specific features. For example, in the plane $h_x h_y$ (Fig. 6d), where conditions (2) and (3) yield the parametric equation

$$\begin{aligned} h_x &= -P_3\cos\Theta - P_4\sin\Theta, \\ h_y &= -P_3\sin\Theta + P_4\cos\Theta, \end{aligned} \tag{7}$$

with

$$P_1 = 2\kappa_r\cos 2\varphi + \kappa_1[2\cos^4\varphi - 9\sin^2\varphi\cos^2\varphi + \sin^4\varphi]$$

$$+ \frac{\kappa_2\sin^2\varphi}{2}(\sin^4\varphi - 11\sin^2\varphi\cos^2\varphi + 6\cos^4\varphi), \tag{8}$$

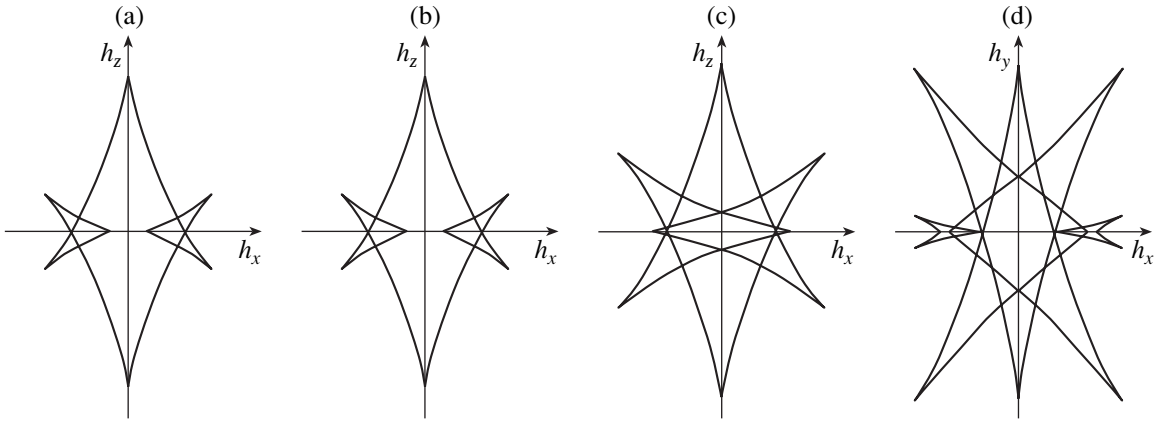

Fig. 6. Critical field curves for $K_u > 0$, $\kappa_2 = 1$, $\kappa_r = 1$, and $\kappa_1 = -0.8$ (a), 1 (b), and 2 (c). (d) $K_u < 0$, $\kappa_1 = -1$, and $\kappa_2 = -50$.

$$P_4 = \sin 2\varphi\left[\kappa_r + \frac{3\cos^2\varphi - 1}{4}(2\kappa_1 + \kappa_2 \sin^2\varphi)\right],$$

there appear two regions where six magnetic phases may coexist if the second constant of CA far exceeds (in magnitude) the constant of uniaxial anisotropy ($K_u < 0$). The presence of such regions, which correspond to hysteresis loops, indicates the complicated mechanism of magnetization reversal in the magnet under study.

CONCLUSION

Thus, the effect of a magnetic field on the ground state of the (011) plate shows up as a reduction of its magnetic symmetry. Because of this, the degeneracy of magnetic phases is partially or completely removed. As a result, the original phase diagram of the (011) plate changes significantly: some phases totally disappear, while others transform changing symmetry. The effect of the field on SRPTs is similar. The process of magnetization reversal in such crystals becomes more complicated: the process is governed not only by the strength and orientation of the magnetic field but also by the constants of CA and IUA (the latter is characterized by two parameters). The results obtained bridge the gap in the analysis of the (011) plates. Moreover, they indicate features of magnetization reversal in combined-anisotropy crystals, which is of interest for applications.

ACKNOWLEDGMENTS

This work was supported by the Ministry of Education of the Russian Federation (grant no. E00-3.4-342).

REFERENCES

1. V. V. Randoshkin and A. Ya. Chervonenkis, *Applied Magnetooptics* (Moscow, 1990).
2. S. Chikasumi, *The Physics of Ferromagnetism: Magnetic Characteristics and Engineering Applications* (Syokabo, Tokyo, 1984; Mir, Moscow, 1987).
3. A. I. Mitsek, N. P. Kolmakova, and D. I. Sirota, Metallofizika **4** (4), 26 (1982).
4. R. M. Vakhitov and V. Ye. Kucherov, J. Magn. Magn. Mater. **215–216**, 56 (2000).
5. V. V. Grinevich and R. M. Vakhitov, Fiz. Tverd. Tela (St. Petersburg) **38**, 3409 (1996) [Phys. Solid State **38**, 1859 (1996)].
6. R. M. Vakhitov, Fiz. Met. Metalloved. **80** (6), 16 (2000).
7. Yu. M. Gufan, *Structural Phase Transitions* (Moscow, 1982).
8. Yu. A. Izyumov and V. N. Syromyatnikov, *Phase Transitions and Crystal Symmetry* (Nauka, Moscow, 1984).
9. V. D. Buchel'nikov and V. G. Shavrov, Fiz. Tverd. Tela (Leningrad) **23**, 1296 (1981) [Sov. Phys. Solid State **23**, 760 (1981)].
10. R. M. Sabitov, R. M. Vakhitov, and E. G. Shanina, Mikroélektronika **18**, 266 (1989).
11. K. P. Belov, A. K. Zvezdin, A. M. Kadomtseva, and R. Z. Levitin, *Orientational Transitions in Rare-Earth Magnetics* (Moscow, 1979).

Translated by V. Isaakyan

Technical Physics, Vol. 47, No. 5, 2002, pp. 561–568. Translated from Zhurnal Tekhnicheskoĭ Fiziki, Vol. 72, No. 5, 2002, pp. 48–55.

SOLIDS

Fast Crystallization of Structural Steel during Laser Processing of the Surface

P. K. Galenko[1, 2], E. V. Kharanzhevskiĭ[1], and D. A. Danilov[1]

[1]*Udmurt State University, Universitetskaya ul. 1, Izhevsk, 426034 Russia*

[2]*German Aerospace Center, Institute for Space Simulation, Cologne 51170, Germany*

e-mail: Ddanilov@uni.udm.ru

Received September 6, 2001

Abstract—The size, shape, and structure of the molten zone appearing on the surface of Fe–C multicomponent alloy upon laser recrystallization are studied. The laser scan rate varies between 0.01 to 0.167 m/s. A set of equations for the temperature and concentration fields is derived within a model of locally nonequilibrium crystallization. The use of the hypothesis for marginal stability, as applied to crystal growth, makes it possible to find the characteristic size of the crystal structure. The mathematical simulation of recrystallization upon laser processing is in good agreement with experimental data. The results of the simulation can be used for predicting the mechanical properties in the molten zone as a function of the energy parameters of the radiation and thermophysical properties of the alloy. © *2002 MAIK "Nauka/Interperiodica".*

INTRODUCTION

Fast crystallization from melts due to fluxes of energetic particles, such as laser or electron beams, opens up vast possibilities of obtaining new structural states of alloys that qualitatively differ from those observed after conventional metallurgical processes. Specifically, it has been shown that fast crystallization during laser processing may lead to the formation of cellular, ribbon-like, and chemically inhomogeneous microstructures, as well as to the "freezing" of new metastable precipitates [1, 2]. It is well known that the mechanical properties to a great extent depend on the crystal structure parameters and that the capability of alloys to retain their properties at high temperatures is specified by the structure dispersity and the rate of secondary recrystallization. Therefore, the study of the alloy structure after laser processing is a topical problem of crystallization physics and materials science.

In metallurgy, the laser recrystallization of Fe–C alloys through surface melting is usually used for material hardening. However, unlike hardening without melting, this method has not found wide application and is applied, as a rule, for increasing the penetration depth of the laser beam [3]. This is because when the beam scan rate V_b is low, the microhardness of the molten zone after solidification is reduced. However, the effect of the molten zone on the mechanical properties still remains unclear. The very existence of the terms "shallow molten zone" and "deep molten zone" (see, e.g., [3, 4]), which have been introduced for the cases when the microhardness values greatly differ while the values of V_b remain the same, suggests that the problem of structure formation and mechanical properties upon the laser recrystallization of structural steels has not received due attention. The use of laser radiation in studying the crystallization processes provides a possibility for directly and reliably determining the rate of solidification (or the interface velocity) V_s. Different values of V_s can then be correlated with the type and characteristic size of the forming structure, and experimental dependences can be contrasted with model curves. Over two last decades, a breakthrough in understanding the factors that govern the structure of the material after fast crystallization has been achieved [5–7]. It has been established that the velocity of the crystallization front and the temperature gradient at the front are of crucial importance [1, 5–8].

In this work, we report experiments on the study and simulation of austenitic growth in the molten zone of structural steel with 0.5 wt % C during fast laser recrystallization. The alloys studied contained reducing agents (Mn and Si) and other alloying elements (Ni, Cr, P, and S), since we were interested in simulating the structure of Fe-based multicomponent alloys, which are of practical importance (for example, the Si addition improves the mechanical properties and corrosion resistance of Fe–C alloys).

Experience in simulating the crystallization (structure formation) of Fe-based multicomponent alloys [9, 10] convincingly suggests that carbon has a decisive effect on the final structure. Therefore, we can apply pseudobinary models of fast crystallization to simulating multicomponent systems.

To simulate the recrystallization, we will use the model of locally nonequilibrium solidification [11, 12], which was applied to simulate fast crystallization by quenching from the liquid state during the spinning of thin ribbons [13, 14]. A feature of the model is that it

1063-7842/02/4705-0561$22.00

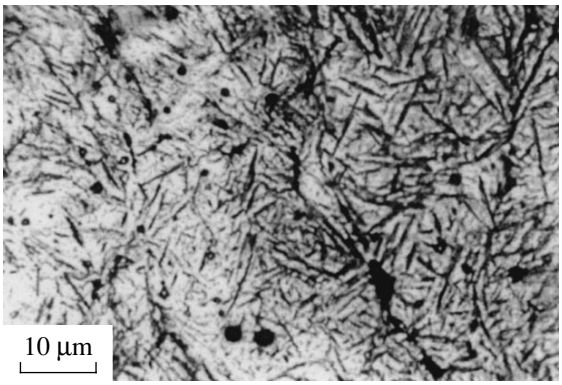

Fig. 1. Image of the longitudinal section obtained in a metallographic microscope. Etching in an HF-based solution.

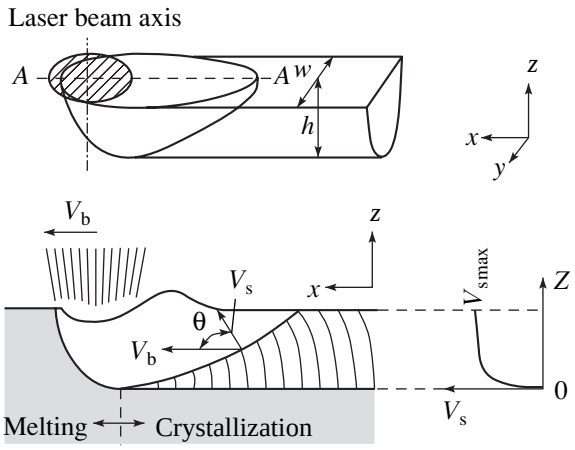

Fig. 2. Shape of the molten zone under laser heating [17]. In the central plane *XZ* of the molten track, the rate of solidification V_s depends on the laser beam velocity V_b and angle Θ. *w* and *h* are the width and depth of the zone, respectively.

includes the finiteness of the impurity diffusion rate both at the interface and in the bulk of the existing phases during fast solidification. The use of the hypothesis for marginal stability within the model of locally nonequilibrium solidification allows the determination of the characteristic size of the grains [15, 16]. In this work, the calculated value of the grain size is compared with the size of austenite grains found experimentally. The effect of the grain size on the yield point and hardness of laser-recrystallized structural steel is estimated.

Table 1. Concentrations of the components in the alloy, equilibrium distribution coefficient k_e, and slope of the equilibrium liquidus line m_e

Chemical element	Content, at. %	k_e	m_e, K/at. %
C	2.29	0.35	–14
Mn	0.71	0.8	–2.4
Si	0.62	0.6	–8.5
S	0.003	–	–
P	0.004	–	–
Cr	0.21	0.4	–5.8
Ni	0.26	0.5	–2.6

1. EXPERIMENT

Specimens used were made of structural steel with 0.5 wt % C. The concentrations of the components in the alloy, distribution coefficients, and slopes of the liquidus line are listed in Table 1. Carbon has the highest concentration, the maximal absolute value of the liquidus slope, and the least distribution coefficient. Clearly, this alloying element can be thought of as having a decisive effect on the structure formation during crystallization, since it is to the greatest extent responsible for the concentration supercooling at the crystallization front, which causes the morphological instability of the front and specifies the characteristic scale of the crystal structure. Therefore, the structural steel will be considered as a pseudobinary alloy where the formation of the crystal structure is governed by thermal processes upon laser processing and carbon redistribution in the molten (recrystallized) zone.

After melting in an induction furnace, the structural steel under study (Table 1) was cast into shells measuring $11 \times 11 \times 50$ mm. The castings were cut into specimens of size $8 \times 8 \times 22$ mm in order to remove chemical inhomogeneities due to the contact with the mold surface. As follows from metallographic studies, the cast macrostructure represents a ferrite–pearlite mixture at this stage.

Prior to laser processing, the specimens were covered by a 15-μm-thick Al_2O_3 absorbing coating to effectively absorb the laser radiation and provide similar surface conditions on the specimens. Experiments were carried out with a Lantan-3M cw CO_2 laser with a rated power of 1.0 kW. The laser beam scan rate was varied from 0.01 to 0.167 m/s. The beam was focused to a spot of diameter 0.2–2.0 mm, which corresponds to a power density between 3.2×10^{10} and 3.2×10^8 W/m^2. To suppress oxidation in the molten zone, helium was continuously delivered to the surface during the processing.

The microstructure of the specimens was examined on longitudinal microsections passing through the center of the laser beam path. The microsections exhibited the homogeneous phase (martensite) without traces of the dendritic microstructure even at large depths (Fig. 1). The further examination of the microstructure was performed on cleavages by SEM (REM-100U microscope). The specimens were cleaved both longitudinally and transversely relative to the beam path. The cleavage surface bends around the lateral surface of dendrites (so-called interdendritic fracture). Therefore, using SEM data, one can directly measure the characteristic size of the structure and the local rate of solidification V_s. The longitudinal cleavages were used

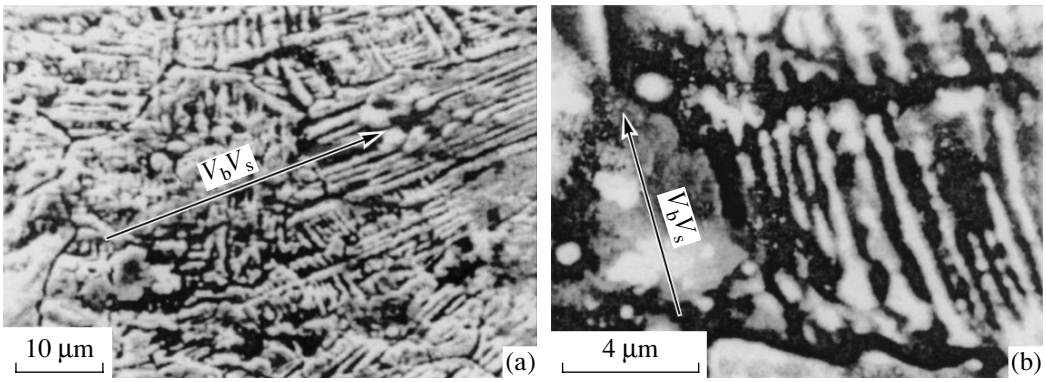

Fig. 3. Central dendrites lying in the surface plane of the specimens at $w/h > 10$. SEM micrographs of the surface were obtained for $\Theta = 0$. $V_b = 0.010$ (a) and 0.092 m/s (b).

for a more detailed investigation into the structure and shape of the molten zone in the section *YZ* (Fig. 2).

2. EXPERIMENTAL RESULTS

In this section, we report the SEM results for the fracture surface, microhardness, and the geometry of the molten zone. The depth, *h*, and width, *w*, of the molten track vs. laser power density *E* and beam scan rate V_b are listed in Table 2. Note that tracks with a depth of less than 20 μm are unstable by depth (the depth varies within ±2.5 μm) because of the initial chemical inhomogeneity of the specimens.

The local rate of solidification V_s is determined by measuring the orientational angle of the microstructure in the longitudinal section relative to the laser beam velocity vector and is given by

$$V_s = V_b \cos\Theta, \quad (1)$$

where Θ is the angle between the structure growth direction and the scan rate V_b (see Fig. 2).

A typical shape of the molten zone during thermal laser treatment is depicted in Fig. 2. Along the axis 0*Z*, the velocity V_s increases from zero (at the bottom of the zone) to the maximal value (on the surface), the latter being defined by the energy parameters of the laser beam. At the bottom, the velocity V_s sharply grows and then becomes fixed ($V_s \approx$ const) at angles $\Theta = 60°$–$85°$. Such behavior was observed throughout the range of V_b for $w/h < 10$ (where *w* and *h* are the width and the depth of the molten zone, respectively). If the width-to-height ratio is large ($w/h > 10$), the shape of the zone changes, which shows up in a considerable decrease in the angle Θ (hence, an increase in V_s). Closer to the surface, $\Theta \longrightarrow 0$ and, as follows from (1), the rate of solidification approaches the scan velocity: $V_s \approx V_b$. Under these conditions, we are dealing with the "shallow molten zone" [3, 4]. Thus, near the surface of the laser track, the growth proceeds parallel to the surface plane, which is clearly seen in Fig. 3. For $w/h < 10$, no central dendrites lying in the surface plane were revealed and the growth proceeded as shown in Fig. 2, which is supported by the SEM micrographs taken from the longitudinal and transverse cleavages of the specimens (Fig. 4).

The crystallization from the laser-produced melt results in the formation of γ-Fe austenite throughout the range of V_b considered. It solidifies in the form of dendrites or cells. Upon the further cooling of the austenite, it undergoes γ–α allotropic transformation by the martensitic mechanism, with the starting grain shape and sizes retained. This allows the examination of the austenitic growth morphology at low temperatures. Figure 4a shows the dendritic grain structure that forms as a result of the competing growth of dendrite ensembles in the direction specified by heat-and-mass transfer processes [18]. At the low value of $V_b = 0.01$ m/s, the growth direction of the dendrite ensemble is substantially affected by the surface energy anisotropy. That is why the growth directions of the ensembles in Fig. 4a diverge. The dendritic growth proceeds in a clearly defined crystallographic direction (for example, in ⟨100⟩ for the cubic lattice). This must be taken into account in calculating the local rate of solidification. If the crystallographic orientation is taken into consider-

Table 2. Experimental values of the melting depth *h* and molten zone width *w* vs. power density *E* and beam scan rate V_b

E, W/m^2	V_b, m/s	h, μm	w, μm
3.2×10^8	0.01	140	1400
8.8×10^8	0.01	220	900
6.3×10^9	0.042	52	160
7.2×10^9	0.092	5…10	100
9.6×10^9	0.092	28	90
3.2×10^{10}	0.142	38	80
3.2×10^{10}	0.167	25	75

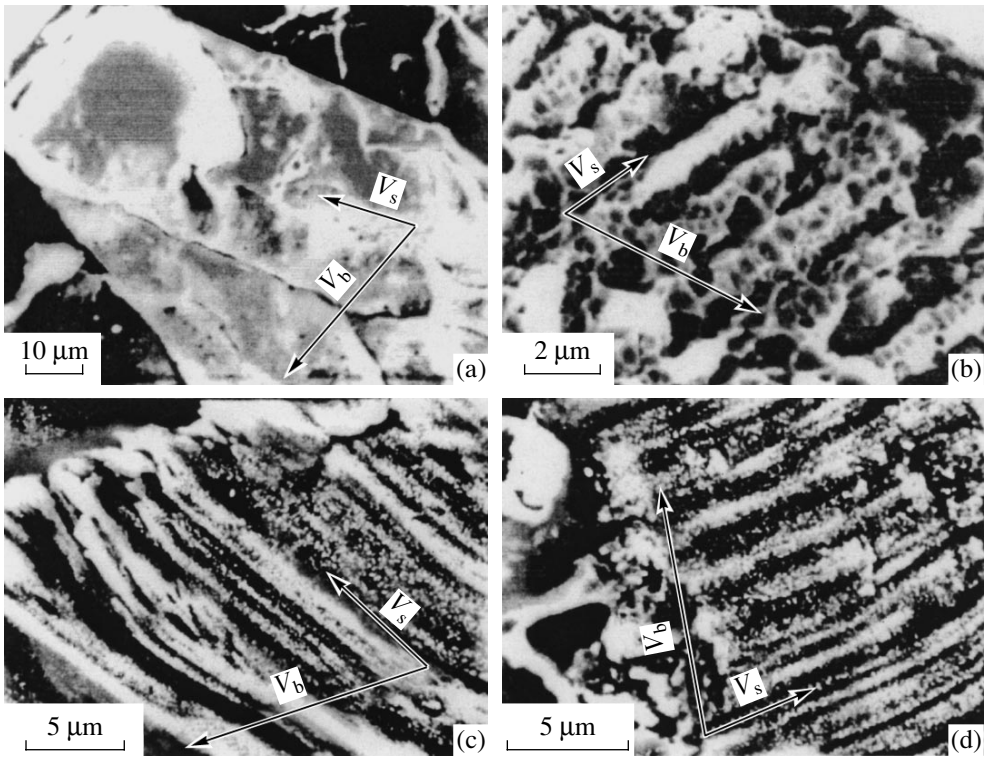

Fig. 4. SEM micrographs of austenite grains taken from the specimens cleaved in the longitudinal direction through the molten zone. The velocity vectors of the beam, V_b, and crystallization front, V_s, lie in the figure plane and are indicated by arrows. (a) Dendritic–granular structure, (b) dendritic structure, and (c, d) cellular structure. V_b = 0.01 (a), 0.042 (b), 0.092 (c), and 0.142 m/s (d).

ation, the rate of solidification V_{hkl} is given by

$$V_{hkl} = V_b \cos\Theta / \cos\varphi, \tag{2}$$

where *hkl* are Miller indices and φ is the angle between the dendritic growth direction and the normal to the interface.

At $V_b \geq 0.042$ m/s (Figs. 4b–4d), the surface energy anisotropy does not affect the grain growth direction and the growth is controlled only by heat-and-mass transfer processes.

3. SIMULATION

3.1. Temperature Field

The experimental methods currently available do not provide a possibility of directly observing the thermal field distribution within the laser action area. Therefore, we performed the numerical simulation of the temperature field in the specimen in order to estimate the temperature gradient at the crystallization front, since this gradient has a strong effect on structure formation.

When simulating heat transfer, we ignored convective transport in the melt. Also, the thermophysical parameters were assumed to be temperature-independent and the same in the liquid and solid phases. It should be noted that the characteristic scales of change of the temperature field and mass transfer differ by more than twofold. Therefore, the temperature field was simulated irrespectively of the carbon concentration gradient at the crystallization front and the carbon concentration was assumed to be uniform and equal to its initial concentration in the specimen. It was also assumed that the structure forms under the combined action of the temperature and concentration gradients (see Section 3.2). In this case, the temperature field $T(x, y, z, t)$ in the specimen is given by

$$c_p \frac{\partial T}{\partial t} = \lambda \nabla^2 T + \Delta H \frac{\partial g}{\partial t}, \tag{3}$$

where c_p is the specific heat at constant pressure, λ is the thermal conductivity, ΔH is the latent heat of phase transition, and g is the fraction of the solid phase.

The velocity of the crystallization front V_s, the melting point of the pure material T_m, as well as the temperature T_1 and the impurity concentration C_1 at the crystallization front, are related as

$$V_s = \mu(T_m + m_e C_1 - T_1). \tag{4}$$

Equation (3) was numerically solved with a uniform spatial grid having a constant time step. The finite-dif-

ference approximation of Eq. (3) has the form

$$\frac{T_{ijk}^{n+1} - T_{ijk}^{n}}{\tau} = \frac{\lambda}{c_p}\left(\frac{T_{i+1jk}^{n} - 2T_{ijk}^{n} + T_{i-1jk}^{n}}{h_x^2} + \frac{T_{ij+1k}^{n} - 2T_{ijk}^{n} + T_{ij-1k}^{n}}{h_y^2} + \frac{T_{ijk+1}^{n} - 2T_{ijk}^{n} + T_{ijk-1}^{n}}{h_z^2}\right) + \frac{\Delta H}{c_p}\frac{g_{ijk}^{n+1} - g_{ijk}^{n}}{\tau}$$

and describes a change in the temperature T_{ijk}^{n} at a point with the coordinates (ih_x, jh_y, kh_z) at a time instant $n\tau$ (where n is the number of iterations with a time step τ). The rate of change of the solid phase fraction in a solidifying or melting mesh is given by

$$\frac{g_{ijk}^{n+1} - g_{ijk}^{n}}{\tau} = \frac{V_{ijk}^{n}}{(h_x h_y h_z)^{1/3}}, \qquad (5)$$

$$V_{ijk}^{n} = \mu(T_m + m_e C_1 - T_{ijk}^{n}),$$

where V_{ijk}^{n} is the crystallization front velocity corresponding to Eqs. (1) and (4).

As was noted above, the carbon concentration at the interface was taken to be equal to its initial concentration; that is, $C_1 = C_0$. According Eqs. (4) and (5), the sign of the velocity defines the direction of the phase transition. Positive velocity values correspond to crystallization; negative ones, to melting.

The distribution of the laser power density over the beam cross section was assumed to be Gaussian:

$$q(\rho) = E\exp\left(-4\frac{\rho^2}{r^2}\right),$$

where r is the radius of the laser beam cross section and ρ is a distance from the beam axis in the radial direction.

The heat balance in the laser action area on the surface was defined in the form

$$-\lambda\frac{\partial T}{\partial n} = R(1-A)q(\rho).$$

The fraction of the laser beam energy absorbed by the specimen depends on the absorption coefficient R of laser radiation and the loss factor A, which combines the evaporation loss and plasma formation loss. In the simulation, we took $R = 0.8$ [3]. The value of A was selected in such a way that the molten zone depth agreed with the experimental value. The thermophysical parameters of the Fe–C system that were employed in the simulation are given in Table 3.

The results of the numerical simulation for various scan rates of the laser beam are summarized in Table 4. As the scan rate and the beam power increase, so does the mean value of the temperature gradient G at the crystallization front, while the depth of the molten zone h_{sim} decreases. The substantial change in the temperature gradient G at the crystallization front indicates that, with different scan rates, the microstructure of the material forms under considerably differing conditions (different rates) of heat removal into the bulk of the specimen. The coefficient A, taking into account the evaporation loss and plasma formation loss, grows with the power density E of the radiation source and can be approximated by the expression

$$A(E) = 0.82(1 - \exp(-1.14\times10^{-9}E)). \qquad (6)$$

Note that the refinement of the temperature distribution under laser processing requires a detailed investigation into mechanisms of evaporation and plasma formation in the laser action area on the surface. Appropriate studies of these surface processes may change quantitatively the boundary condition for heat fluxes.

3.2. Characteristic Size of the Microstructure

The characteristic size of the steel structure was determined by the approach in [19, 20], which generalizes the one put forward in [15, 16] for fast crystal growth when impurity transfer in the diffusion field is far from local equilibrium. This approach solves the problem of heat-and-mass transfer during crystallization using an additional condition that the characteristic size of a structure is selected morphologically. One of such conditions is the hypothesis for marginal stability [21], according to which the selected scale of a structure equals the least wavelength of Mullins–Sekerka morphological (in)stability. Thus, the structural scale selected is related to the state of marginal stability, the "demarcation line" between the stable and unstable states of a growing crystal, and equals the critical wavelength of a perturbation imposed on the interface.

Using this hypothesis, one can estimate the characteristic size of a structure forming during laser recrys-

Table 3. Physical parameters of the Fe–C system

Parameter	Value	Refs.
C_0, at. %	2.29	This work
m_e, K/at. %	–14	[6]
T_m, K	1811	[6]
ΔH, J/m^3	1.93×10^9	[6]
λ, W/K m	35	[6]
c_p, J/K m^3	5.74×10^6	[6]
D, m^2/s	2×10^{-8}	[6]
μ, m/s K	0.1	This work
V_D, m/s	17	[14]

Table 4. Results of the simulation of the temperature field upon laser processing

V_b, m/s	E, W/m^2	A	h_{sim}, m	h_{exp}, m	G, K/m
0.010	3.2×10^{8}	0.25	1.35×10^{-4}	1.4×10^{-4}	3.0×10^{6}
0.042	6.3×10^{9}	0.78	5.1×10^{-5}	5.2×10^{-5}	1.2×10^{7}
0.092	9.6×10^{9}	0.83	2.7×10^{-5}	2.8×10^{-5}	1.7×10^{7}
0.142	3.2×10^{10}	0.84	3.6×10^{-5}	3.8×10^{-5}	2.0×10^{7}

tallization [6, 7]. High velocities of the laser beam cause relatively high velocities of the crystallization front. Under these conditions, effects associated with the relaxation of the diffusion flux of an impurity in the melt may play a major part [11, 12]. The model of locally nonequilibrium crystallization that has been constructed in view of this circumstance [12] provides good agreement with experimental data in a wide range of growth rates [15, 16].

Taking into account the effects of the impurity diffusion flux relaxation leads to the hyperbolic equation for mass transfer in the melt:

$$\frac{\partial C}{\partial t} + \tau_D \frac{\partial^2 C}{\partial t^2} = D\nabla^2 C, \tag{7}$$

where C is the impurity concentration, τ_D is the time of diffusion relaxation, and D is the diffusion coefficient of the impurity.

Equation (7) includes the diffusion rate $V_D = (D/\tau_D)^{1/2}$, which is the maximal rate of propagation of concentration perturbations.

The morphological stability of a flat interface in the concentration field described by (7) with regard for the hypothesis for marginal stability has been analyzed in [15]. In this case, the characteristic size d of the structure can be found from the relationship

$$d = \left(\frac{\Gamma/\sigma}{mG_C\xi_C - \frac{1}{2}(G_L\xi_L + G_S\xi_S)}\right)^{1/2}, \tag{8}$$

where $\sigma = (4\pi^2)^{-1}$ is the stability parameter;

$$G_C = -\frac{(1-k)V_sC_0}{kD(1-V_s^2/V_D^2)} \tag{9}$$

Table 5. Calculated characteristic size of the structure

V_b, m/s	V_s, m/s	G, K/m	d_{sim}, m	d_{exp}, m
0.010	0.01	3.0×10^{6}	8.7×10^{-7}	10×10^{-7}
0.042	0.0144	1.2×10^{7}	9.9×10^{-7}	7.4×10^{-7}
0.092	0.0315	1.7×10^{7}	5.3×10^{-7}	3.9×10^{-7}
0.142	0.06	2.0×10^{7}	3.4×10^{-7}	3.0×10^{-7}

is the impurity concentration gradient [12]; C_0 is the impurity concentration away from the crystallization front (equal the initial concentration); and G_L and G_S are the temperatures gradients on the sides of the melt and solid phase, respectively (the mean temperature gradient G is given by $G = (G_L + G_S)/2$).

The stability functions ξ have the form

$$\xi_L = 1 - \frac{1}{\sqrt{1+\frac{1}{\sigma P_T^2}}}, \quad \xi_s = 1 + \frac{1}{\sqrt{1+\frac{1}{\sigma P_T^2}}},$$
$$\xi_C = 1 + \frac{2k}{1-2k-\sqrt{1+\frac{1-V^2/V_D^2}{\sigma P_C^2}}} \tag{10}$$

and depend on the thermal, $P_T = V_s d/2a$, and concentration, $P_C = V_s d/2D$, Peclet numbers ($a = \lambda/c_p$ is the thermal diffusivity).

The nonequilibrium distribution coefficient of the impurity with regard for the effect of diffusion flux relaxation is given by [22]

$$k(V_s) = \begin{cases} \dfrac{k_e(1-V_s^2/V_D^2) + V_s/V_D}{(1-V_s^2/V_D^2) + V_s/V_D}, & V_s < V_D \\ 1, & V_s \geq V_D, \end{cases} \tag{11}$$

where k_e is the equilibrium distribution coefficient.

The slope of the liquidus line in the kinetic phase diagram in view of the relaxation effect is found from the relationship [23]

$$m(V_s) = \begin{cases} \dfrac{m_e}{1-k_e}(1-k+\ln(k/k_e) + (1-k)^2 V_s/V_D), \\ \qquad\qquad V_s < V_D \\ \dfrac{m_e \ln(1/k_e)}{1-k_e}, \quad V_s \geq V_D, \end{cases} \tag{12}$$

where m_e is the slope of the liquidus in the equilibrium phase diagram of the pseudobinary alloy.

It should be noted that Eq. (8) holds if the rate of solidification is less than the diffusion rate, that is, if $V_s < V_D$. When the crystallization front moves with a

velocity exceeding the diffusion rate, the concentration profile ahead of the front degrades and the destabilizing force due to the impurity concentration gradient disappears. Since the crystallization during laser processing occurs under the positive temperature gradient, the forces causing the morphological instability of the flat interface are absent when $V_s \geq V_D$.

Using the set of equations (8)–(12), we calculated the characteristic sizes of the crystal structure. The velocity V_s of the crystallization front was determined from the micrographs according to (1); the concentration gradient, from the rate of solidification with (9); and the temperature gradients G, G_L, and G_s were found by numerically simulating the temperature field (Section 3.1). Table 5 compares the characteristic sizes d_{sim} of the structure with experimental data d_{exp}. Good agreement between the analytical and experimental results is obvious. Thus, the model of locally nonequilibrium solidification in combination with the hypothesis for marginal stability can be used for estimating the characteristic size of a structure forming during laser recrystallization.

CONCLUSIONS

We considered the formation of the microstructure of structural steel with 0.5 wt % C during the laser processing of the material surface. Using the model of locally nonequilibrium solidification [12], we derived a set of equations for the temperature and concentration fields in the pseudobinary approximation. This approximation is applicable to steel, since carbon plays a major part in diffusion and structure formation processes. The use of the hypothesis for marginal stability within the model of locally nonequilibrium solidification allows the determination of the characteristic size of the grains [15, 16]. The analytical results agree well with experimental data. The conclusions drawn are as follows.

(1) The austenite phase has a dendritic–granular, purely dendritic, or cellular structure when the laser beam scan rate is $V_b = 0.01$–0.167 m/s.

(2) The characteristic size d of the structure calculated in the pseudobinary approximation agrees well with the experimental data (Fig. 5). This suggests that carbon is the basic structure-forming alloying element in the steel.

(3) The effect of improved mechanical properties in the shallow molten zone is explained. The primary reasons for this effect are a change in the shape of the zone and a decrease in the angle Θ down to zero on the surface. As a result, the rate of solidification V_s grows. Eventually, the size d of the structure decreases and the microhardness rises in accordance with the qualitative dependence of the mechanical properties on the grain size [24–27].

(4) The models used in this work for simulating the temperature field and characteristic structure size in the laser action area make it possible to predict the mechanical properties of structural steels vs. energy parameters of laser processing and thermophysical properties of the alloy. Our approach to predicting steel characteristics may be useful for the further development of the laser-assisted hardening technology.

ACKNOWLEDGMENTS

We thank S.R. Anisimov, S.P. Kuz'kina, L.Yu. Styrova, and M.N. Korolev for the assistance in conducting the experiments.

We are indebted to M.D. Krivilev for the valuable discussions.

This work was financially supported by the Ministry of Education of the Russian Federation under the project "Computer-Aided Simulation of Structure Formation during Laser and Electron Recrystallization of Alloys" (grant no. 97-24-7.1-9).

REFERENCES

1. W. J. Boettinger, D. Shechtman, R. J. Schaefer, and F. S. Biancaniello, Metall. Trans. A **15**, 55 (1984).
2. S. C. Gill and W. Kurz, Acta Metall. Mater. **41**, 3563 (1993).
3. *Laser Technique and Technology*, Vol. 6: *Foundations of Laser Thermostrengthening of Alloys: Textbook for Institutes of Higher Education*, Ed. by A. G. Grigor'yants and A. N. Safonov (Vysshaya Shkola, Moscow, 1988).
4. V. D. Sadovskiĭ *et al.*, *Laser Heating and Structure of Steel: Atlas of Microstructures* (Ural. Otd. Akad. Nauk SSSR, Sverdlovsk, 1989).
5. W. J. Boettinger, S. R. Coriell, *et al.*, Acta Mater. **48**, 43 (2000).
6. W. Kurz and D. J. Fisher, *Fundamentals of Solidification* (Trans Tech Publications, Aedermannsdorf, 1992, 3rd ed.).
7. R. Trivedi and W. Kurz, Acta Metall. **34**, 1663 (1986).
8. Q. Y. Pan, W. D. Huang, *et al.*, J. Cryst. Growth **181**, 109 (1997).
9. M. S. F. Lima and H. Goldenstein, J. Cryst. Growth **208**, 709 (2000).
10. J. E. Gould, Weld. J. (Miami) **73**, 91-s (1994).
11. P. K. Galenko, Kristallografiya **38**, 238 (1993) [Crystallogr. Rep. **38**, 836 (1993)].
12. P. Galenko and S. Sobolev, Phys. Rev. E **55**, 343 (1997).
13. P. K. Galenko, M. D. Krivilev, V. I. Lad'yanov, and M. V. Osetrov, Kristallografiya **46**, 354 (2001) [Crystallogr. Rep. **46**, 310 (2001)]; Available from VINITI, No. 827-V00 (1999).
14. P. K. Galenko and M. D. Krivilyov, Modell. Simul. Mater. Sci. Eng. **8**, 81 (2000).
15. P. K. Galenko and D. A. Danilov, Phys. Lett. A **235**, 271 (1997).
16. P. K. Galenko and D. A. Danilov, J. Cryst. Growth **197**, 992 (1999).

17. M. Gremaud, M. Carrard, and W. Kurz, Acta Metall. Mater. **38**, 2587 (1990).
18. P. K. Galenko and V. A. Zhuravlev, *Physics of Dendrites* (World Sci., Singapore, 1994).
19. J. Lipton, W. Kurz, and R. Trivedi, Acta Metall. **35**, 957 (1987).
20. W. J. Boettinger, S. R. Coriell, and R. Trivedi, *Rapid Solidification Processing: Principles and Technologies IV*, Ed. by R. Mehrabian and P. A. Parrish (Claitor's, Baton Rouge, 1988), p. 13.
21. J. S. Langer and H. Müller-Krumbhaar, Acta Metall. **26**, 1681 (1978).
22. S. L. Sobolev, Phys. Lett. A **199**, 383 (1995).
23. P. Galenko, Phys. Rev. B **65**, 144103 (2002).
24. E. O. Hall, Proc. Phys. Soc. London, Sect. B **381**, 64 (1951).
25. N. I. Petch, J. Iron Steel Inst., London **25**, 174 (1953).
26. D. Tabor, *The Hardness of Metals* (Oxford Univ. Press, London, 1951).
27. A. I. Gusev, Usp. Fiz. Nauk **168**, 55 (1998) [Phys. Usp. **41**, 49 (1998)].

Translated by V. Isaakyan

Technical Physics, Vol. 47, No. 5, 2002, pp. 569–573. Translated from Zhurnal Tekhnicheskoĭ Fiziki, Vol. 72, No. 5, 2002, pp. 56–60.

SOLID-STATE ELECTRONICS

Formation of Defects in the Oxide Layer of Ion-Irradiated Si/SiO_2 Structures

A. P. Baraban and L. V. Miloglyadova

Research Institute of Physics, St. Petersburg State University, Ul'yanovskaya ul. 1, St. Petersburg, 198904 Russia

Received January 18, 2001; in final form, October 9, 2001

Abstract—Electroluminescence and high-frequency voltage–capacitance methods are used to study Si/SiO_2 structures obtained by thermal oxidation of KÉF-5 (100)Si wafers at 950°C in wet oxygen (oxide thickness 250 nm). The structures are irradiated by 130-keV argon ions with doses in the range of 10^{13}–3.2×10^{17} cm^{-2}. A correlation between the origin, properties, and formation mechanism of implantation-induced defects in the oxide layer is established, and a model of defect formation is proposed. *© 2002 MAIK "Nauka/Interperiodica".*

The properties of Si/SiO_2 structures, a building block of modern micro- and solid-state electronics, are of great scientific and applied interest. Radiation-induced effects in these structures have been studied over many years for different purposes. These effects are caused, in particular, by ion implantation (II). By varying implantation parameters, one can form local areas with specified properties in Si/SiO_2 structures. Such an approach has found wide application in different fields of science and technology. On the other hand, II-induced electrically active defects in Si/SiO_2 structures may adversely affect the performance of related devices. Therefore, the study of the postimplantation behavior of the Si/SiO_2 structures is of interest for predicting the performance of the devices under irradiation. In spite of extensive research in this field, the properties and origin of radiation-induced defects in such structures, as well as mechanisms of their formation, remain unclear.

The aim of this study was to find a correlation between the origin, properties, and formation mechanisms of defects generated in the oxide layer of Si/SiO_2 structures by Ar ion implantation.

Si/SiO_2 structures were obtained by thermal oxidation of KÉF-5 (100)Si wafers at 950°C in wet oxygen.[1] The oxide layer thickness was 250 nm. Ar ions were implanted at doses $D = 10^{13}$–3.2×10^{17} cm^{-2} in an Eaton Nova 4206 implanter. The samples were cooled and the ion beam density was low in order to avoid target overheating. The ion energy, 130 keV, was selected such that the maximum concentration of ions implanted was at the center of the oxide layer. Rapid thermal annealing (RTA) at 500, 700, and 900°C was performed with a halogen lamp for 10 s in nitrogen. The strength of the electric field applied to the structures was below the breakdown value for the oxide layer. Near-UV irradiation was provided with a DRL-250 mercury lamp ($h\nu$ = 4–6 eV).

In the experiments, we used the electroluminescence (EL) method in the 250–800 nm spectral range [1, 2] and electrophysical diagnostic methods based on taking high-frequency *C–V* characteristics, in particular, the depth profiling technique [1, 3–6]. All measurements were carried out at 293 K in an electrolyte–insulator–semiconductor system [1].

Earlier, characteristic emission bands at energies 1.9, 2.3, 2.7, 3.3, 3.8, and 4.6 eV were revealed in the EL spectrum of as-prepared Si/SiO_2 structures produced under different oxidation conditions [1]. The bands were assigned to various defects in the oxide layer and at the Si/SiO_2 interface. The EL band at 1.9 eV was excited by thermalized electrons; the others, by electrons heated by the electric field in the oxide layer (particularly, the EL band at 2.7 eV was excited in fields greater than or equal to the critical field E^* that initiates the process of impact ionization in the SiO_2 matrix) [1].

The EL spectra of the ion-irradiated structures closely resemble those of the as-prepared structures and contain three clearly defined EL bands: at 1.9 eV (650 nm), at 2.7 eV (460 nm), and at 4.4 eV (280 nm) (Fig. 1) [2]. The EL bands at 1.9 and 2.7 eV have the same energy position and are fitted by the same Gaussian distributions (0.12 ± 0.05 and 0.35 ± 0.05 eV, respectively) as in the starting structures. However, in the structures irradiated, the EL band at 2.7 eV is excited in fields lower than E^* and its intensity is considerably higher. The UV region of the EL spectrum has one distinct band at 4.4 eV, which can adequately be fitted by the Gaussian distribution with a variance of 0.4 ± 0.1 eV.

[1] KÉF-5 means phosphorus-doped silicon with a resistivity of 5 Ω cm.

1063-7842/02/4705-0569$22.00 © 2002 MAIK "Nauka/Interperiodica"

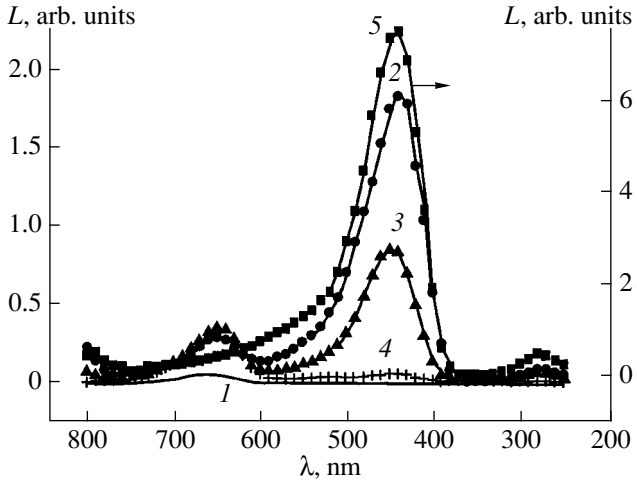

Fig. 1. EL spectra from Ar-irradiated structures. (*1*) As-prepared; $D = 10^{13}$ (*2*), 10^{14} (*3*), 10^{16} (*4*), and 3.2×10^{17} cm^{-2} (*5*).

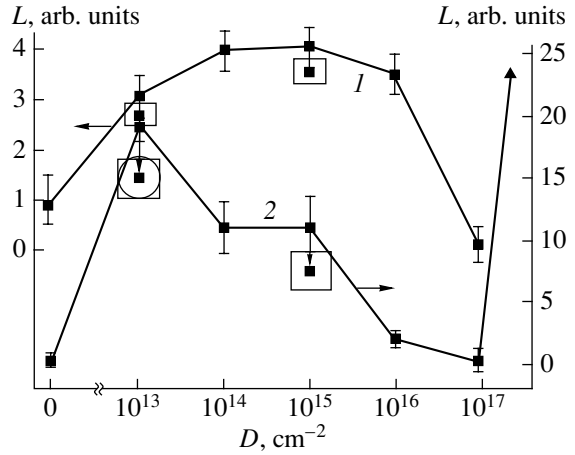

Fig. 2. Intensities of the EL bands in the spectra from the ion-irradiated structures as functions of the implant dose. The EL band position is (*1*) 1.9 and (*2*) 2.7 eV. (□) Near-UV irradiation; (○) near-UV irradiation with the electric field applied.

It was found that the intensity of the EL band at 1.9 eV grows as the implant dose increases to 10^{14} cm^{-2}, remains invariable up to 10^{15} cm^{-2}, and then drops (Fig. 2). In the structures irradiated, the EL band at 2.7 eV appears starting from a dose of 10^{13} cm^{-2}. At a dose of 10^{17} cm^{-2}, the intensity of this band decreases and then abruptly rises at a dose of 3.2×10^{17} cm^{-2} (Fig. 2). The dose dependence of the intensity of the 4.4-eV band is identical with that of the band at 2.7 eV. The ratio of the intensities of these bands remains constant.

The emission centers were located from the intensity of the EL bands at 1.9, 2.7, and 4.4 eV vs. oxide thickness dependence by layer-by-layer etching the oxide. It was found that the centers responsible for the 1.9-eV band are localized in the outer region of the oxide, as in the case of the as-prepared structures. The area of center localization expands with implant dose. The centers responsible for the EL bands at 2.7 and 4.4 eV concentrate at a distance of 30–140 nm from the Si/SiO_2 interface. As the implant dose rises, the emission center distribution broadens and its maximum shifts toward the interface.

High-temperature RTA, near-UV irradiation with and without a negative bias applied to the field electrode (the negatively biased field electrode prevents electron injection from the Si into the SiO_2), and the action of the field all decreased the intensity of all the EL bands.

From the *C–V* characteristics, it was found that the ion implantation raises the density of states at the Si/SiO_2 interface and modifies the charge state of the oxide [3]. From the curves $V_{fb}(d_{ox})$ (Fig. 3), we determined the true values of charges in the oxide layer that are induced by the ion implantation and the values of their centroids [4–6]. As the dose grows, so does the negative charge in the outer SiO_2 layer. At the dose $D = 10^{13}$ cm^{-2}, a positive charge forms (with the centroid at $X_{21} = 35 \pm 10$ nm measured from the Si/SiO_2 interface), which does not vary with implant dose (Figs. 3, 4) [4, 5]. Starting with $D = 10^{14}$ cm^{-2}, a negative charge (with the centroid at $X_{32} = 8 \pm 7$ nm) forms, along with the positive one, its amount increasing with the dose (Figs. 3, 4) [4, 6]. High-temperature RTA causes these charges (Fig. 4) and the density of surface states to decrease monotonically. The positions of the centroids for the positive and negative charges in the outer layer of the SiO_2 do not change, whereas near the Si/SiO_2 interface the position of the negative charge centroid shifts to greater values (remaining smaller than that of the positive charge).

The electric field applied to the as-prepared Si/SiO_2 structures and to those irradiated with $D = 10^{13}$ cm^{-2} modifies the charge state of the oxide insignificantly. At $D = 10^{14}$ cm^{-2} or higher, the field leads to the formation of a considerable positive charge in the SiO_2 near the interface. The centroid of this positive charge always coincides with that of the implantation-induced negative charge forming near the Si/SiO_2 interface. The amount of the field-induced positive charge varies in proportion with implantation-induced negative charge for all implant doses and RTA temperatures (Fig. 5) [6]. As the implant dose rises, so does the density of electron traps in the outer layer of the SiO_2, which are filled by the electric field.

The near-UV irradiation of the ion-irradiated Si/SiO_2 structures caused a negative charge to form in the SiO_2 (which is approximately twice as large as the positive charge forming as a result of ion implantation [5]) with the centroid coincident with that of the positive charge (Fig. 3). The near-UV irradiation with the negatively biased field electrode, preventing electron

injection from the Si into the SiO_2, does not modify the charge state of the ion-bombarded structures [5] (Fig. 3). The near-UV irradiation also decreases the negative charge amount and the electronic traps density in the outer region of the SiO_2.

The coincidence of the centroid positions for the negative charge in the SiO_2 near the Si/SiO_2 interface and for the positive charge arising in the electric field, as well as the fact that the amount of the positive charge is linearly dependent on that of the negative charge for all implantation doses and RTA temperatures (Fig. 5), suggests that the centers responsible for the negative charge are hole traps, which are filled in the electric field by hole injection from the Si into the SiO_2.

The coincidence of the centroid positions for the positive charge forming in the SiO_2 by the ion implantation and for the negative charge due to the near-UV irradiation, as well as the fact that the amount of this negative charge is twice as large as the amount of the positive charge, indicate that both charges are produced by the same amphoteric centers.

Earlier, the band at 1.9 eV, the negatively charged centers, and the electronic traps in the outer layer of the oxide have been shown to be related to hydrogenous complexes in the SiO_2 (in particular, silanol groups) [1] (Fig. 6). We found that the ion implantation modifies such complexes, whereas the postimplantation RTA, near-UV irradiation, and exposure to the electric field decrease their concentration in the outer layer of the SiO_2.

Based on our results and published data [7], we suppose that the bands at 2.7 and 4.4 eV are caused by defects like silicon atoms coordinated with two oxygen atoms (O_2=Si:), which are excited by hot electrons with an energy of ≈5 eV [2]. Ion implantation causes such defects through breaking two Si–O bonds in a silicon–oxygen tetrahedron. From the aforesaid, it follows that most emission centers responsible for the EL bands at 2.7 and 4.4 eV in the ion-irradiated Si/SiO_2 structures are concentrated within a distance of 30–140 nm from the interface (Fig. 6). With an increase in the dose of Ar ions, the concentration of defects like O_2=Si: in the SiO_2 first increases, then decreases, and increases again because of restructuring in the oxide layer. It was found that the postimplantation RTA, near-UV irradiation, and exposure to the electric field decrease the concentration of the emission centers responsible for the EL bands at 2.7 and 4.4 eV. This is because unsaturated silicon bonds are completed by neighboring uncoordinated Si atoms, O atoms, or diffusing H atoms (the hydrogen in the oxide layer appears as a product of silanol dissociation under the field). Or, alternatively, the actions listed above may decrease the probability of electron heating up to energies exciting the emission centers revealed (due to the restructuring in the oxide layer).

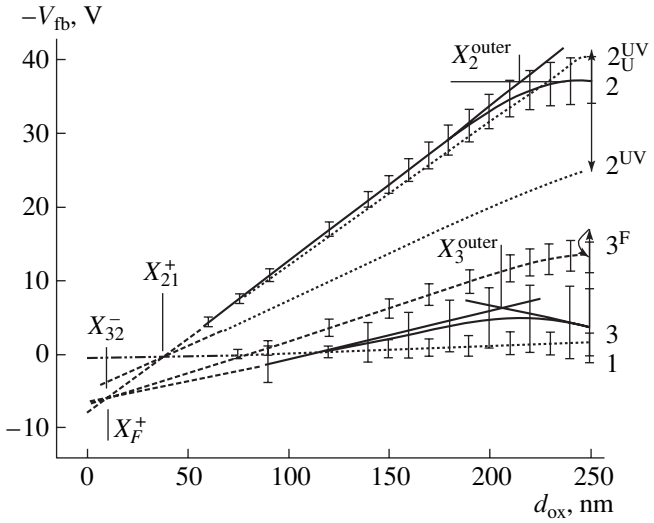

Fig. 3. Flat-band potential as a function of the oxide thickness for the (*1*) as-prepared and (*2*, *3*) ion-irradiated structures. $D = 10^{13}$ (*2*) and 10^{14} cm^{-2} (*3*). 2^{UV}, after near-UV irradiation for 10 s; 2_U^{UV}, after near-UV irradiation with the negatively biased field electrode; and 3^F, after the field action.

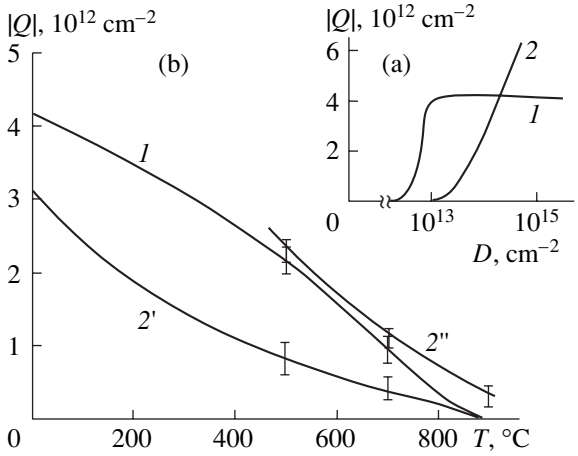

Fig. 4. Amounts of charges formed by the ion implantation in the oxide layer of the Si/SiO_2 structures near the interface as a function of the (a) implant dose and (b) RTA temperature: (*1*) positive charge; (*2*) negative charge. $D = 10^{14}$ (*2'*) and 10^{15} cm^{-2} (*2''*).

Thus, we can conclude that the ion implantation changes essentially the properties of the Si/SiO_2 structures and that these changes take place beyond the region of implanted argon location. The embedded ions lose their energy in the solid mainly by interacting with its atomic and electronic subsystems, generating electron–hole pairs and producing structure defects, respectively, in the SiO_2 matrix. Furthermore, the energy sufficient for individual surface atoms to leave the SiO_2 for the environment is transferred to them either directly by

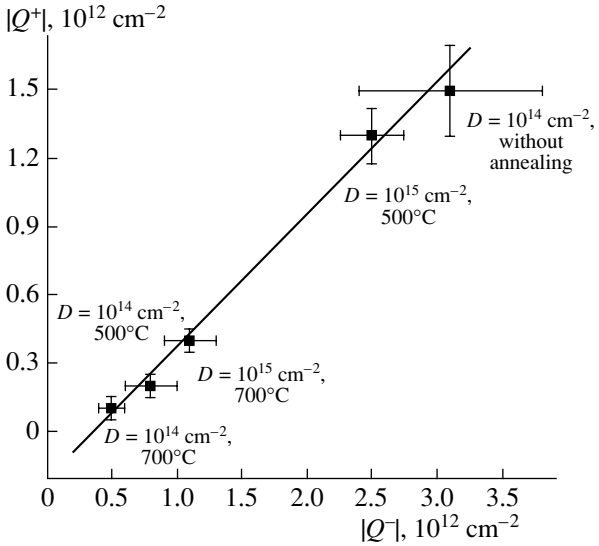

Fig. 5. Positive charge formed under the electric field in the oxide layer near the interface as a function of the negative charge formed in the same region of the oxide by the ion implantation.

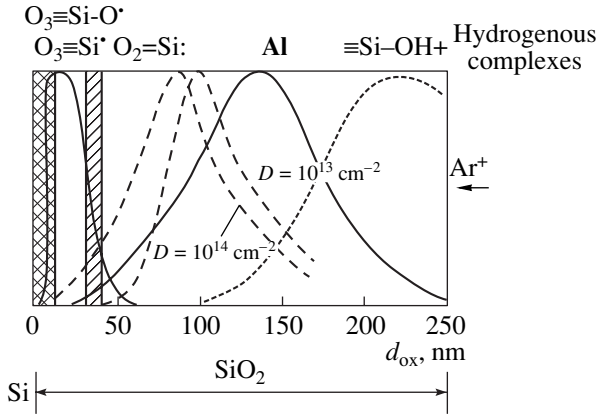

Fig. 6. Spatial distribution of the defects formed in the oxide layer of the Ar-irradiated Si/SiO_2 structures.

the bombarding ions or indirectly by the entire excited system of the material irradiated. This results in the sputtering of the SiO_2 outer layer, which shows up as a noticeable decrease in the oxide layer thickness at Ar ion doses $D \geq 10^{16}$ cm^{-2}. At the given implantation energy (E = 130 keV), the interaction with both the electronic and atomic subsystems causes energy dissipation in the outer part of the oxide layer in the Si/SiO_2 structures. The disorder of the oxide outer layer in this case is such that the hydrogenous complexes concentration increases in this region. It shows up in the increase in the concentration of the centers responsible for the EL band at 1.9 eV, as well as of the negatively charged centers and the electronic traps in the outer layer of the SiO_2. In the bulk of the oxide layer, the most likely process of energy dissipation for the embedded argon atoms is the interaction with the atomic subsystem. As a consequence, the greatest amount of dangling Si–O bonds is observed near the maximum of the Ar distribution and the Si and O atoms shift deeper into the oxide. According to estimates, the O and Si atoms are displaced from the Ar distribution maximum by distances of 80–170 and 30–70 nm, respectively. A considerable portion of the O atoms reaches the coesite (which is denser than SiO_2 layer, located at a distance of 0–10 nm from the interface [1]), and the silicon substrate. Because of retardation in these denser materials, the O atoms travel distances lesser than those calculated for SiO_2. As a result, two spatially separated nonstoichiometric SiO_x regions with $x > 2$ and $x < 2$ form in the oxide of the Si/SiO_2 structures. The oxygen-depleted region ($x < 2$) lies farther from the silicon surface, because the silicon atoms are displaced by a smaller distance than the oxygen atoms, and contains defects such as silicon atoms coordinated with two oxygen atoms. These defects are responsible for the emission bands at 2.7 and 4.4 eV. Thus, the EL data suggest that during the implantation, the $SiO_{x<2}$ layer forms in the SiO_2 at a distance of 30–140 nm from the interface, while the $SiO_{x>2}$ layer arises closer to the interface.

We assume that the electrically active centers are also related to the formation of these nonstoichiometric regions and associated defects. For the oxygen-depleted region, where the centroid of the implantation-induced positive charge is situated, the most likely defects are silicon atoms coordinated with three oxygen atoms ($O_3{\equiv}Si^{\bullet}$) and/or oxygen vacancies [5] (Fig. 6). Both defects are amphoteric centers, which become negatively charged under the near-UV irradiation. They may be positively charged either directly after the ion implantation or, being initially neutral, acquire a positive charge by capturing holes that appear when the Ar ions interact with the electronic subsystem of the SiO_2 matrix. The fact that the charge state of the ion-processed structures does not change under the near-UV irradiation with the field electrode biased negatively indicates that the amphoteric centers become negative after the near-UV irradiation by capturing electrons optically excited from the Si into the conduction band of the SiO_2. For the oxygen-enriched region, where the centroid of the negative charge formed by the ion implantation is located, defects like nonbridging oxygen atoms ($O_3{\equiv}Si{-}O^{\bullet}$) are the most probable [6] (Fig. 6). They are generated in the SiO_2 during and/or after the ion implantation and initially are negative. Subsequenty, they may serve as Coulomb hole traps, which are filled under the action of the field, thus becoming neutral. The centroid of these defects shifts with increasing RTA temperature as a result of the asymmetric broadening of the $SiO_{x>2}$ region due to the existence of the coesite layer near the interface.

Along with defect formation in the oxide, the ion implantation causes some of the displaced atoms in the

SiO_2 matrix to reach the Si/SiO_2 interface. Having an energy large enough to break loose bonds [1], they produce structure defects contributing to the density of surface states in the forbidden gap of the Si at the interface. A contribution to the density of surface states may also be made by defects formed at the Si/SiO_2 interface as a result of the saturation of dangling bonds in the SiO_2 bulk, as well as other long-range effects that are poorly understood.

The constancy of the concentration of the $O_3{\equiv}Si^{\bullet}$ defects (and/or oxygen vacancies), the noticeable amount of the $O_3{\equiv}Si{-}O^{\bullet}$ defects near the interface, and the reduction of the concentration of the $O_2{=}Si$: defects in the oxide layer in going from $D = 10^{13}$ to 10^{14} cm^{-2} are apparently associated with the restructuring in the SiO_2 at the dose $D = 10^{14}$ cm^{-2}. At $D = 3.2 \times 10^{17}$ cm^{-2}, one more restructuring takes place in the oxide layer with the resulting increase in the intensities of the 2.7- and 4.4-eV EL bands and, hence, in the concentration of the $O_2{=}Si$: defects.

The reasons and mechanisms underlying the restructurings remain yet unclear and call for further study.

REFERENCES

1. A. P. Baraban, V. V. Bulavinov, and P. P. Konorov, *SiO_2-on-Si Electronics* (Leningr. Gos. Univ., Leningrad, 1988).
2. A. P. Baraban, P. P. Konorov, L. V. Malyavka, and A. G. Troshikhin, Zh. Tekh. Fiz. **70** (8), 87 (2000) [Tech. Phys. **45**, 1042 (2000)].
3. A. P. Baraban and L. V. Malyavka, Pis'ma Zh. Tekh. Fiz. **23** (20), 26 (1997) [Tech. Phys. Lett. **23**, 786 (1997)].
4. A. P. Baraban, A. A. Kuznetsova, L. V. Malyavka, *et al.*, Izv. Vyssh. Uchebn. Zaved., Élektron., No. 4, 17 (1998).
5. A. P. Baraban and L. V. Malyavka, Pis'ma Zh. Tekh. Fiz. **26** (4), 53 (2000) [Tech. Phys. Lett. **26**, 159 (2000)].
6. A. P. Baraban, L. V. Miloglyadova, and V. I. Ter-Nersisyants, Pis'ma Zh. Tekh. Fiz. **27** (3), 89 (2001) [Tech. Phys. Lett. **27**, 129 (2001)].
7. L. N. Skuja, A. N. Streletsky, and A. B. Pakovich, Solid State Commun. **50**, 1069 (1984).

Translated by M. Lebedev

Technical Physics, Vol. 47, No. 5, 2002, pp. 574–577. Translated from Zhurnal Tekhnicheskoĭ Fiziki, Vol. 72, No. 5, 2002, pp. 61–64.

SOLID-STATE ELECTRONICS

Role of Masking Oxide on the Silicon Surface on Defect Formation in SIMOX Structures

A. Yu. Askinazi, A. P. Baraban, and L. V. Miloglyadova

Research Institute of Physics, St. Petersburg State University, Ul'yanovskaya ul. 1, St. Petersburg, 198904 Russia

Received May 21, 2001; in final form, October 26, 2001

Abstract—The properties of Si/SiO_2 structures produced by oxygen implantation into silicon (SIMOX technology) are investigated by the high-frequency *C–V* method and by the electroluminescence (EL) method. The existence of electrically active and luminescence centers in the oxide layer near the interface is established. The effect of a SiO_2 masking layer on the silicon surface on defect formation in the SIMOX structure is elucidated. The dependence of the concentration of the electrically active and luminescence centers on the thickness of the masking layer is found. © *2002 MAIK "Nauka/Interperiodica".*

Si/SiO_2 structures and related metal–insulator–semiconductor devices are the building blocks for modern micro- and solid-state electronics. In this connection, the properties of these structures are of both fundamental and applied interest. One way of creating Si/SiO_2 structures is the formation of buried oxide layers in the bulk of silicon by oxygen implantation (the so-called SIMOX technology). The minimization of the defect density in such structures and, as a consequence, the improvement of their stability against an electric field are basic issues of many today's investigations. A method of modifying the properties of the buried oxide layer is the variation of the irradiation parameters during the formation of SIMOX structures, including the implantation of oxygen ions into silicon covered by a masking SiO_2 layer of various thicknesses.

The aim of this study is to discover the effect of masking SiO_2 on defect formation in SIMOX structures, in particular, its effect on the concentration of electrically active and luminescence centers within the buried oxide layer.

We investigated Si/SiO_2 SIMOX structures obtained by implanting oxygen ions directly or through a masking SiO_2 layer of various thicknesses ($d_{m.ox}$ = 46.6, 189.7, and 246.4 nm) at a dose of 1.8×10^{18} cm^{-2}, an energy of 190 keV, and at a temperature of 650°C. In order to form buried SiO_2 layers, we used postimplantation annealing at T = 1320°C for 6 h. After the formation of the buried layers, the layer was chemically removed and we obtained Si/SiO_2 structures with an oxide thickness of 360–425 nm. Subsequent electrical measurements were performed at voltages below the oxide breakdown voltage.

The charge states of the SIMOX structures were studied by taking high-frequency *C–V* curves, using, in particular, the method of depth profiling [1], which makes it possible to find the dependence of the flat-band voltage V_{fb} on the oxide layer thickness d_{ox} (Figs. 1, 2). For the positions of the centroids X of charges localized in the oxide layer, we took the oxide layer thicknesses at which the compared curves $V_{fb}(d_{ox})$ interpolated to zero thickness intersected, and the true values of the charges were found from the slopes of these curves [1, 2]. To simultaneously detect electrically active defects in the buried oxide and measure their relative concentrations, we used the method of field cycles [1] (Fig. 3). The method of electroluminescence (in the spectral range of 250–800 nm) allowed us

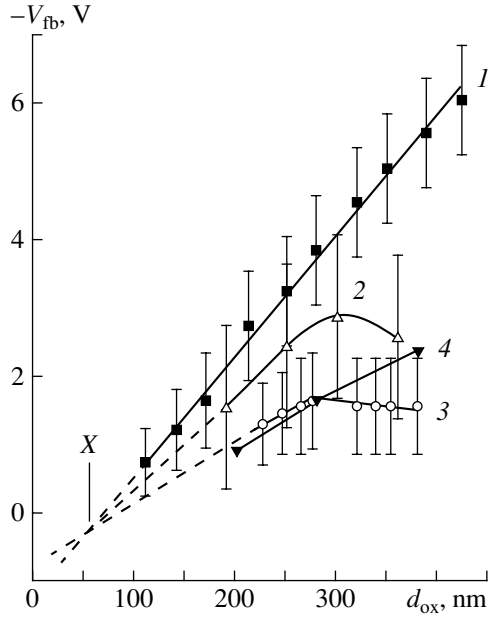

Fig. 1. Flat-band voltage vs. SIMOX oxide thickness. The oxygen ions were implanted (*1*) into Si directly and through a SiO_2 mask of thickness $d_{m.ox}$ = 46.6 (*2*), 189.7 (*3*), and 246.4 nm (*4*).

1063-7842/02/4705-0574$22.00 © 2002 MAIK "Nauka/Interperiodica"

to gain information on the presence, type, and relative concentration of luminescence centers in the SIMOX oxide layer from the EL spectrum and the intensity of characteristic lines (Fig. 4). The measurements were performed in an electrolyte–insulator–semiconductor system at room temperature [1].

Previously, it has been established that, in the SIMOX structures obtained without the masking layer, a positive charge $Q = (0.4 \pm 0.1) \times 10^{12}$ cm^{-2} with a centroid $X = (65 \pm 10)$ nm forms in the SiO_2 near the interface with the Si [2]. The use of the masking oxide decrease the charge, but the value of its centroid remains unchanged (Fig. 1). Subsequent field actions on the SIMOX structures (the method of field cycles) showed the stability of the charge state in the structures in the field range $E_{ox} \le 2.5$ MV/cm (Fig. 3). At the further increase in the electric field intensity, the value of $-V_{fb.}$ sharply rises starting from $E_{ox} = 3$ MV/cm in the case of the structures formed without the masking oxide and from $E_{ox} = 3.5$, 4.5, and 5.5 MV/cm at $d_{m.ox} =$ 46.6, 189.7, and 246.4 nm, respectively (Fig. 3). This indicates that a positive charge forms in the structures. Its centroid, as in the structures formed without the masking oxide [2], was equal to $X = (65 \pm 10)$ nm (Fig. 2). The amount of this positive charge was determined from the electric field intensity and the time of field action.

Taking into account this circumstance and also the fact that the low-temperature annealing had no effect on the amount of this charge [2], we assume that the formation of the positive charge in the SIMOX oxide under the field action is associated with the conversion of electrically inactive centers that arise during the formation of the buried SiO_2 layer to positively charged electrically active ones. The increase in the electric field threshold intensity (at which the fast buildup of the charge is observed) with increasing masking oxide thickness $d_{m.ox}$ is likely to be related to the fact that (1) the concentration of the electrically inactive centers (becoming active under the field action) decreases and/or (2) a greater energy of electrons is required to pass them into the electrically active state (hence, a stronger electric field intensity in the oxide).

Earlier [2], taking into account that the centroid of the positive charge due to the field action coincides with that of the charge appearing in the SIMOX structures and also that the effect of near-UV irradiation on both charges is identical while low-temperature annealing has no effect, we assumed that these charges are caused by defects of the same origin.

The EL spectra of Si/thermal SiO_2 structures contain characteristic lines at 1.9, 2.3, 2.7, 3.3, 3.8, and 4.6 eV, which are associated with the presence of various defects in the oxide layer and at the Si/SiO_2 interface [1]. The 1.9-eV band is excited by thermalized electrons; the others, by electrons heated by the electric field in the oxide layer (in particular, the 2.7-eV band is excited in fields greater than or equal to the critical field E^* at which the impact ionization of the SiO_2 matrix begins) [1].

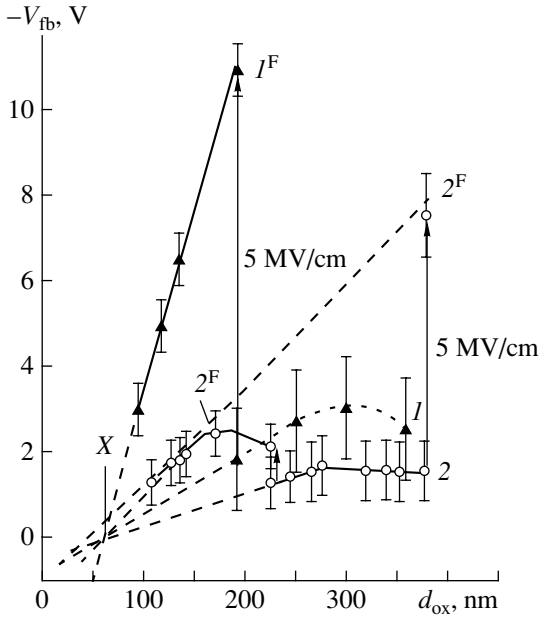

Fig. 2. Effect of the field on the dependences of the flat-band potential on the SIMOX oxide thickness $d_{m.ox} = 46.6$ (*1*) and 189.7 nm (*2*); 1^F and 2^F are field actions.

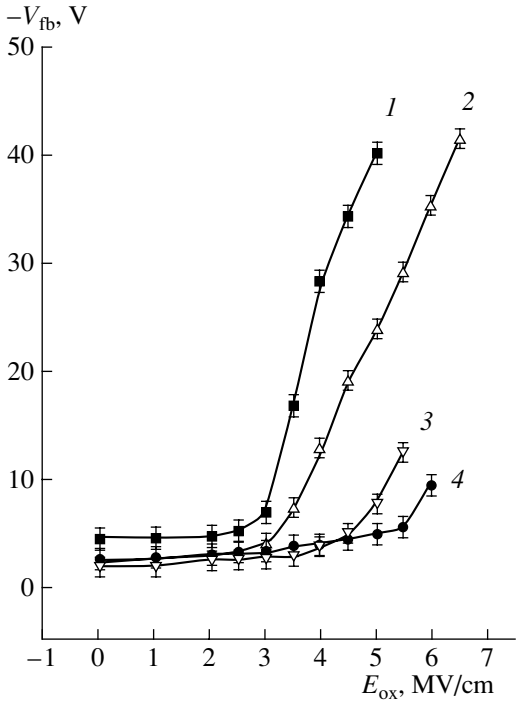

Fig. 3. Flat-band potential vs. electric field intensity in the SIMOX oxide. (*1*) Without a masking oxide; $d_{m.ox} = 46.6$ (*2*), 189.7 (*3*), and 246.4 nm (*4*).

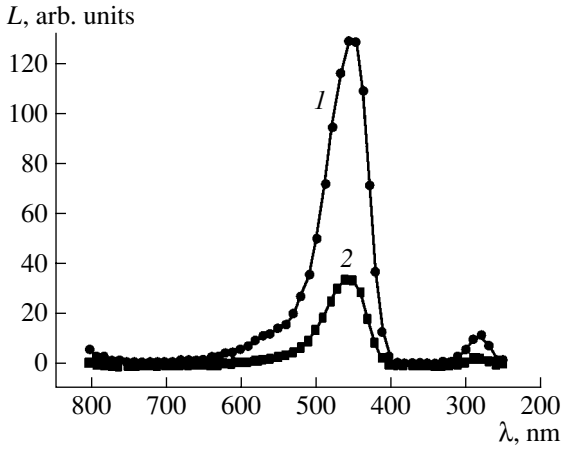

Fig. 4. EL spectra of the SIMOX Si/SiO_2 structures. (*1*) Without a masking oxide layer and (*2*) $d_{m.ox} = 46.6$ nm.

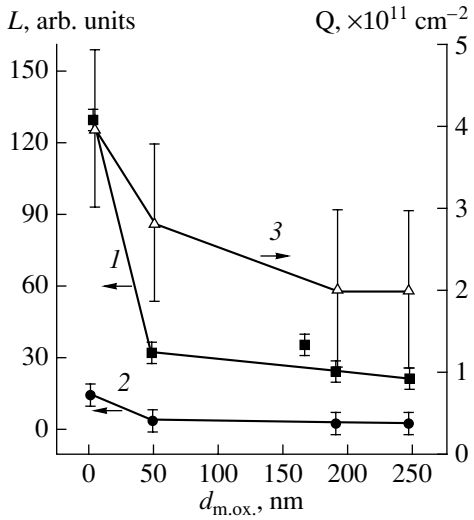

Fig. 5. EL line intensities for the SIMOX Si/SiO_2 structures and the positive charge amount in the buried SiO_2 layer vs. thickness of the masking layer. (*1*) 2.7-eV EL line, (*2*) 4.4-eV EL line, and (*3*) positive charge amount.

The EL spectra of our SIMOX structures contain two characteristic EL lines: at 2.7 eV (460 nm) and at 4.4 eV (280 nm) (Fig. 4) [3]. The 2.7-eV line has the same energy position and is described by the same Gaussian distribution [(0.26 ± 0.07) eV] as in the structures with thermal SiO_2. However, it is excited in fields below E^*, and its intensity is much higher than in the spectra taken from the Si/SiO_2 structures with thermal SiO_2. In the UV range of the EL spectrum, we observed the single well-defined line at 4.4 eV, which is well approximated by a Gaussian distribution with a variance of (0.31 ± 0.11) eV [3].

The intensities of these lines remained unchanged when the SIMOX oxide was thinned by etching down to a thickness of 250 nm. Thus, we conclude that the luminescence centers responsible for these lines are localized in the 250-nm-thick part of the oxide layer at the interface with the silicon.

In this spectrum, the 1.9-eV line was absent, suggesting that the oxide layer does not contain silanol groups (which, as has been previously found [1], are responsible for this line). This is because the SIMOX process prevents the penetration of water fragments (hydrogen and hydroxyl groups) into the oxide layer.

Figure 5 shows the EL line intensities (at 2.7 and 4.4 eV) and the positive charge arising in the SIMOX SiO_2 vs. thickness of the masking layer. With an increase in the masking SiO_2 thickness, the EL intensities and the positive charge amount decrease. The charges become significant even at a mask thickness of 46.6 nm. It should be noted that the intensities diminish by the same factor, which indicates that both bands are caused by identical defects.

To elucidate the effect of implant energy losses in the mask oxide on the EL line intensities and on the amount of the charge, we evaluated the energy losses of 190-keV oxygen atoms having passed the SiO_2 layer [4] (Fig. 6).

Comparing Figs. 5 and 6, we see that the insignificant decrease in the energy of implanted oxygen atoms (in the case of small oxide thicknesses) is accompanied by the considerable decrease in the EL line intensities and the positive charge amount. With the further significant decrease in the energy of oxygen atoms, both the intensities and the charge remain virtually unchanged.

At this stage of investigation, it is believed that impurity-modified defects like triply coordinated silicon atoms are responsible for the positive charge in the oxide [2].

On the strength of our previous results and the analysis of the published data [3, 5], we assume that defects like silicon atoms doubly coordinated by oxygen (O_2=Si:), which are produced by hot electrons with an energy ≈5 eV, are responsible for the 2.7- and 4.4-eV EL.

The appearance of the above two types of defects in the SIMOX structures can be related to microcrystalline silicon inclusions (the existence of which has been established in a number of works [6–8]) arising in the SiO_2 near the Si/SiO_2 interface. The decrease in the intensity of the EL lines considered and in the amount of positive charge with increasing mask thickness correlates with the decrease in the density of silicon islands in the SiO_2 layer at the inner interface [19].

The significant decrease in the concentration of the luminescence centers, electrically active defects, and subdefects in the case of the slight decrease in the energy of the oxygen implant allows us to conclude that this effect is unrelated to a decrease in the oxygen ion energy. We suppose that when passing through the amorphous mask (even of a small thickness), the ion flux spreads, the motion of the ions becomes chaotic, and thus the total momentum of the oxygen ions embedded into the silicon declines. In this case, the

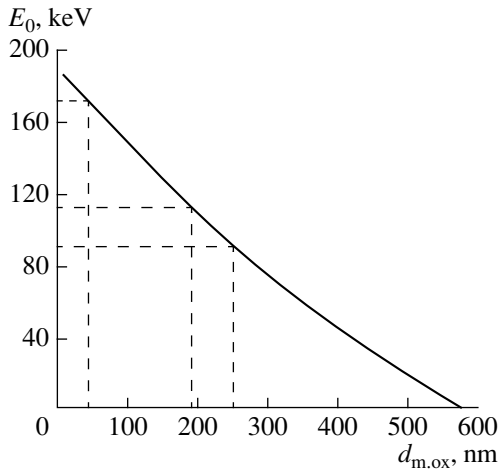

Fig. 6. Energy of implanted oxygen ions vs. thickness of the masking SiO_2 layer.

oxygen ions do not penetrate deep into the silicon and, the subsequent annealing, the resulting SiO_2 does not have a region with a small content of oxygen atoms. Consequently, the concentration of the defects like silicon atoms doubly coordinated by oxygen and triply coordinated silicon atoms is considerably smaller.

The decrease in the defect concentration in the SIMOX oxide produced by the mask process may be related to a reduced contamination level in the silicon, as well as to the redistribution of the energy losses (among the electronic and atomic subsystems of the silicon) of the oxygen atoms when their energy changes slightly, which is the case in our consideration [4].

Thus, the presence of a masking oxide on the silicon surface in fabricating SIMOX Si/SiO_2 structures leads to a significant decrease in the concentration of positively charged defects, predefect states, and luminescence centers causing the 2.7- and 4.4-eV lines in the SIMOX oxide near the Si/SiO_2 interface. The decrease in the concentration of the predefect states improves the stability of the Si/SiO_2 structures against an electric field.

REFERENCES

1. A. P. Baraban, V. V. Bulavinov, and P. P. Konorov, SiO_2-on-Si Electronics (Leningr. Gos. Univ., Leningrad, 1988).
2. A. Yu. Askinazi, A. P. Baraban, V. A. Dmitriev, *et al.*, Pis'ma Zh. Tekh. Fiz. **27** (10), 57 (2001) [Tech. Phys. Lett. **27**, 422 (2001)].
3. A. P. Baraban, P. P. Konorov, L. V. Malyavka, and A. G. Troshikhin, Zh. Tekh. Fiz. **70** (8), 87 (2000) [Tech. Phys. **45**, 1042 (2000)].
4. H. Ryssel and I. Ruge, *Ionenimplantation* (Teubner, Stuttgart, 1978; Nauka, Moscow, 1983).
5. L. N. Skuja, A. N. Streletsky, and A. B. Pakovich, Solid State Commun. **50**, 1069 (1984).
6. V. V. Afanas'ev, A. Stesmans, and A. G. Revesz, J. Appl. Phys. **82**, 2184 (1997).
7. R. E. Stahlbush, G. J. Campisi, *et al.*, IEEE Trans. Nucl. Sci. **NS-39**, 2086 (1992).
8. J. Stoemenos, A. Garcia, *et al.*, J. Electrochem. Soc. **142**, 1248 (1995).
9. S. Bota, A. Perez-Rodriguez, H. R. Morante, *et al.*, in *Proceedings of the VI International Symposium on Silicon-on-Insulator Technology and Devices, San Francisco, 1994*, p. 179.

Translated by Yu. Vishnyakov

Technical Physics, Vol. 47, No. 5, 2002, pp. 578–584. Translated from Zhurnal Tekhnicheskoĭ Fiziki, Vol. 72, No. 5, 2002, pp. 65–71.

SOLID-STATE ELECTRONICS

Formation of Desired Concentration Profiles of Embedded Atoms and Radiation-Induced Defects by Using Monochromatic Fast Ion Beams

G. M. Gusinskiĭ and A. V. Matyukov

Ioffe Physicotechnical Institute, Russian Academy of Sciences, Politekhnicheskaya ul. 26, St. Petersburg, 194021 Russia

Received September 27, 2001

Abstract—A method for the formation of fast ion beams with an energy spectrum providing a desired profile of embedded atoms and radiation-induced defects in the sample is suggested. A rigorous mathematical analysis of the profiles of film energy absorbents that produce light- and heavy-ion beams with a necessary energy spectrum from fast monochromatic beams is performed. *© 2002 MAIK "Nauka/Interperiodica".*

INTRODUCTION

Nuclear methods for modifying electrical, physical, chemical, and mechanical properties of materials are widely used in modern technologies. Specifically, the deep implantation of fast ions and the creation of desired profiles of radiation-induced defects are applied for imparting specific properties to semiconductor structures and associated devices [1, 2]. The concentration profiles of ions implanted depend on the bremsstrahlung losses of the ions in the material, that is, on the type and energy of the ions and also on the properties of the material on the atomic level. The defect density distribution across the sample also depends on the atomic bond strength in the irradiated compound. The ranges of fast ions and the depth distribution of radiation-induced defects in various materials can be simulated with the well-known SRIM program [3]. Naturally, these distributions are a function of the angle between the beam direction and the normal to the sample surface and also (under channeling conditions) between the beam direction and crystallographic directions.

The most efficient way to produce the necessary concentration profiles of ions of a given type and the distributions of radiation-induced defects (RIDs) is the irradiation of the samples by an ion beam with a certain energy spectrum. Since ion accelerators are designed for creating monochromatic beams and their energy tuning is rather difficult (especially in the case of resonant accelerators), it is appropriate to use stopping media in mass production. These media produce beams with a necessary energy spectrum from fast monochromatic beams.

In this work, we for the first time present a method of analysis of profiled energy absorbents (PEAs) in the form of a homogeneous foil arched along one coordinate that is perpendicular to the beam direction. Then, the penetrating depth of the beam in the absorbent will depend on this coordinate. As a result, away from the absorbent, one can form an energy spectrum of the beam that provides the desired depth distributions of the monochromatic beam ions and RIDs produced by the beam.

1. CURVATURE ANALYSIS OF THE ABSORBING FOIL FORMING GIVEN CONCENTRATION PROFILES OF EMBEDDED ATOMS

Let it be necessary to produce some distribution of stopped doping ions in the depth range $0–z_{max}$. The ion density is $n(z)$ [ion/cm^3], and the irradiation dose is N [ion/cm^2]. We approximate a range–energy relation by a power dependence usually used in the case of medium-energy ions [4]. Since at normal incidence the stop depth z of an ion equals its range R, this dependence can be written as

$$R = z = AE^B. \quad (1)$$

In view of (1), the energy spectrum $dN(E)/dE$ of the beam that provides a given concentration profile $n(z)$ can be represented as

$$\frac{dN(E)}{dE} = \frac{dN}{dR}\frac{dR}{dE} = \frac{dN}{dz}\frac{dz}{dE} = C_0 n(z)E^{B-1}, \quad (2)$$

where C_0 is a dimension-adjusting constant.

Let a PEA in the form of a metallic foil be placed in front of the sample irradiated and let the ion range in the absorbent depend on energy as

$$R_f = A_f E^{B_f}. \quad (3)$$

If E_0 is the energy of the incident monochromatic beam, the ion energy at the exit from the foil absorbent of

effective thickness Z_f is given by

$$E(Z_f) = \left(\frac{R_f - Z_f}{A_f}\right)^{1/B_f}, \quad (4)$$

where R_f is the range of ions with the energy E_0 in the foil material.

Figure 1 shows a fragment of the arched foil with a thickness k. Taking into account that $Z_f = k/\cos\alpha(x)$ when the beam direction is aligned with the ordinate axis, we find from (2)–(4) that

$$\frac{dN}{dE} = C_0 n(z)\left(\frac{R_f - k/\cos\alpha(x)}{A_f}\right)^{\frac{B-1}{B_f}}. \quad (5)$$

If the radiation density is uniformly distributed along the X axis, $dN \sim dx$. Then,

$$\frac{dE}{dx} = \frac{C_1}{n(z)}\left(\frac{R_f - k/\cos\alpha(x)}{A_f}\right)^{\frac{1-B}{B_f}}. \quad (6)$$

On the other hand, since Z_f is a function of $\alpha(x)$, differentiating Eq. (4) with respect of x yields

$$\frac{dE}{dx} = \frac{dE}{d\alpha}\frac{d\alpha}{dx} = C_2(R_f - k/\cos\alpha(x))^{\frac{1-B_f}{B_f}}\frac{\sin\alpha}{\cos^2\alpha}\frac{d\alpha}{dx}. \quad (7)$$

From (6) and (7), we find

$$\frac{dx}{d\alpha} = C_3 n(z)(R_f - k/\cos\alpha(x))^{\frac{B}{B_f}-1}\frac{\sin\alpha}{\cos^2\alpha}. \quad (8)$$

Using (8) and the relationship $dy/dx = \tan\alpha$, we come to the expression for the instantaneous coordinates of the PEA profile as a function of parameter α:

$$x(\alpha) = C_3\int_0^\alpha n(z(\alpha))(R_f - k/\cos\alpha)^{\frac{B-B_f}{B_f}}\frac{\sin\alpha}{\cos^2\alpha}d\alpha + C_x,$$
$$y(\alpha) = C_3\int_0^\alpha n(z(\alpha))(R_f - k/\cos\alpha)^{\frac{B-B_f}{B_f}}\frac{\sin^2\alpha}{\cos^3\alpha}d\alpha + C_y. \quad (9)$$

If a desired concentration profile cannot be represented by a functional dependence of z, we represent $n(z)$ as a polynomial expression

$$n(z) = \sum_0^{i_{\max}}\alpha_i z^i,$$

determine α_i, and take into account expression (9) to obtain

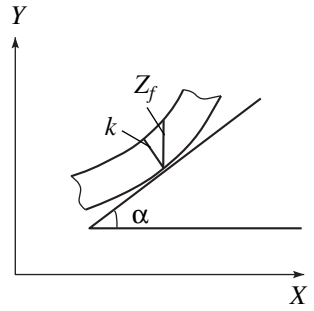

Fig. 1. Fragment of the PEA profile.

$$x(\alpha) = C_4\sum_0^{i_{\max}}\int_0^\alpha \alpha_i\left(R_f - \frac{k}{\cos\alpha}\right)^{\frac{B}{B_f}(1+i)-1}\frac{\sin\alpha}{\cos^2\alpha}d\alpha + C_x,$$
$$y(\alpha) = C_4\sum_0^{i_{\max}}\int_0^\alpha \alpha_i\left(R_f - \frac{k}{\cos\alpha}\right)^{\frac{B}{B_f}(1+i)-1}\frac{\sin^2\alpha}{\cos^3\alpha}d\alpha + C_y. \quad (10)$$

Having put $C_x = C_y = 0$ according to the adopted conditions $x(0) = y(0) = 0$ and having calculated $x(\alpha)$ and $y(\alpha)$ for specific R_f, k, B, and B_f, we find the desired dependence $y(x)$, which specifies the shape of the PEA film.

2. ANALYSIS OF AN ADSORBENT PROVIDING THE UNIFORM DEPTH DISTRIBUTION OF EMBEDDED IONS

The condition $dN/dR = n(z) = \text{const}$ greatly simplifies expressions (9). Moreover, for specific materials, these expressions may be simplified further. Let we form a 50-μm-thick proton-doped region, for example, in a silicon sample with a PEA in the form of an aluminum foil of thickness $k = 40$ μm. For appropriate beam energies and thickness values measured in micrometers, the coefficients in formulas (1) and (3) take the values $A = A_{Si} = 18.56$, $B = B_{Si} = 1.476$, $A_f = A_{Al} = 16.51$, and $B_f = B_{Al} = 1.485$. Hence, for this case, $B \approx B_f$. Replacing the approximate equality by the strict one, assuming that $C_x = C_y = 0$, and taking into account that $y(x)$ is C_3-independent, from (9) we find

$$x(\alpha) = \int_0^\alpha \frac{\sin\alpha}{\cos^2\alpha}d\alpha = \frac{1-\cos\alpha}{\cos\alpha},$$
$$y(\alpha) = \int_0^\alpha \frac{\sin^2\alpha}{\cos^3\alpha}d\alpha = \frac{\sin\alpha}{2\cos^2\alpha} - \frac{1}{4}\ln\left|\frac{1+\sin\alpha}{1-\sin\alpha}\right|. \quad (11)$$

The position of the boundaries of the uniformly doped layer depends on the monochromatic beam energy E_0 and the maximal angle α_{max} of foil inclina-

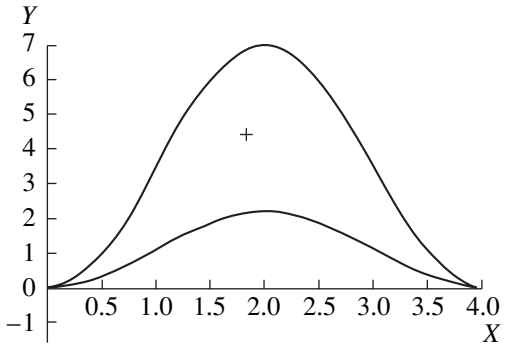

Fig. 2. Period of the PEA profile for proton implantation at $\delta z = 50$ μm (lower curve) and 260 μm (upper curve). $E_0 = 3.01$ MeV.

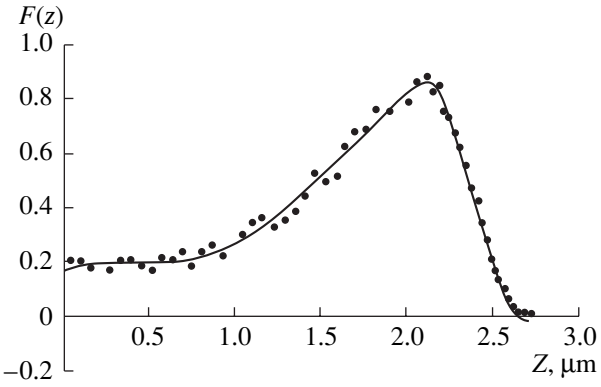

Fig. 3. RID distribution across the Ge sample irradiated by a monochromatic beam of Ar^{40} ions with an energy $E = 4.5$ MeV.

tion. If the outer boundary coincides with the sample surface, α_{max} is determined from the obvious relationship $\cos\alpha_{max} = k/A_{Al}E_0^{B_{Al}}$. Using formulas (1) and (3) with the reduced values of the coefficients and converting the Si layer thickness to the Al thickness equivalent in terms of energy loss, one finds that $E_0 = 3.01$ MeV and $\alpha_{max} = 61.9°$.

If the outer boundary of the layers doped must be at a depth $z_{Si,\,min}$ from the surface, the minimum energy of the ions leaving the PEA is $E_{min} = (z_{Si,\,min}/A_{Si})^{\frac{1}{B_{Si}}}$ and the maximal energy is $E_{max} = (z_{Si,\,max}/A_{Si})^{\frac{1}{B_{Si}}}$. The energy E_0 of the incident beam must meet the condition

$$E_0 = \left(\frac{z_{Al,\,max} + Z_{max}}{A_{Al}}\right)^{\frac{1}{B_{Al}}} = \left(\frac{z_{Al,\,max} + k}{A_{Al}}\right)^{\frac{1}{B_{Al}}}, \quad (12)$$

where $z_{Al,\,min}$ and $z_{Al,\,max}$ are the Al thicknesses that are equivalent (in terms of energy loss) to the Si layers extending to the outer and inner boundaries of the layer doped, respectively, and $Z_{max} = k/\cos\alpha_{max}$.

For $z_{Si,\,min} = 10$ and 100 μm, E_0 was estimated at $E_0 = 3.22$ and 4.84 MeV, respectively. The change in α_{max} for these two values of $z_{Si,\,min}$ does not exceed 1.5°.

The PEA profile given by (11) is depicted in Fig. 2 (lower curve) for $\alpha_{max} \approx 62°$. The calculations were made for the initial quarter-period. The total period was obtained by symmetrizing the segment constructed under the assumption that $y(x)$ is a continuous function. The PEA profile is nearly identical for any depth at which the doped layer of fixed thickness is situated.

A change in the doped layer thickness is related to a substantial change in the PEA profile. By way of example, Fig. 2 demonstrates the PEA profile with $k = 40$ μm and $\alpha_{max} \cong 81°$, which is responsible for the formation of a doped layer of thickness $\delta z \approx 260$ μm (upper curve). The strong dependence of α_{max} on the doped layer thickness and the independence of this angle from the layer position for the materials selected are easy to explain. From (1) and (3), we find $R_{Al} = A_{Al}R_{Si}/A_{Si}$, assuming that $B_{Al} = B_{Si}$. Since $\delta z_{Si} = \delta R_{Si}$, relationship (13) yields

$$\alpha_{max} = \arccos\left[\frac{\delta Z_{Si}A_{Al}}{A_{Si}k} + 1\right]^{-1}.$$

3. FORMATION OF A DESIRED DEPTH DISTRIBUTION OF RADIATION-INDUCED DEFECTS

Since physical processes underlying the formation of proton-induced defects differ from those responsible for the production of the defects by heavy ion (HI) irradiation [5], it seems to be appropriate to analyze the PEA profiles for the two cases separately.

In the case of energetic protons, most defects are produced in narrow final segments of the tracks [5]. Then, the problem of formation of a desired depth distribution of the defects becomes equivalent to the above problem of forming a given hydrogen dopant profile. In particular, the lower PEA profile in Fig. 2 provides the approximately uniform depth distribution of defects from $z = 0$ to $z = 82$ μm in the silicon sample if the energy of an incident proton beam is 3 MeV and $k = 40$ μm.

In the case of HIs, the density of defects is substantially nonzero over the major part of the track. This is because bremsstrahlung losses of HIs grow as E increases to $E(\text{MeV}) \approx A$ of the ion. The reason for this effect is that the equilibrium charge of HIs moving in a stopping medium increases and the "nuclear stopping" component is much higher than for the case of light ions [5]. The relative density function of the defects $F(z)$ vs. penetration depth of Ar^{40} ions with an energy $E_0 = 4.5$ MeV for the germanium sample is shown in Fig. 3. The curve was obtained with the SRIM program.

It is highly asymmetric, having the extended region of monotonic rise and the relatively narrow region of monotonic fall.

The calculation of the PEA desired profile is based on using the density function of HI ranges. This function must satisfy the distribution $F(z)$ of the defects that approximates the desired one as close as possible.

4. DENSITY FUNCTION OF RANGES

The depth distribution of the defects parametrically depends on R. Let $K(z)$ be the density function of the defects that corresponds to a monochromatic beam of HIs having an energy $E_{\max}$ and a range $R_{\max}$. Obviously, the density function of defects produced by ions with lesser energies and lesser ranges shifts parallel to $K(z)$ depthward by a value of $R_{\max} - R$. The shape of the function remains unchanged:

$$\bar{K}(R, z) = K(R_{\max} - R + z).$$

Let $n(R)$ be the density function of the ranges of HIs with an energy spectrum formed by a PEA. The HIs lying at a depth z and having ranges in the interval $(R, R + dR)$ make a contribution $K(R, z)n(R)dR$ to the density function. Integrating over all ranges exceeding z yields the defect distribution

$$F(z) = \int_z^{R_{\max}} K(R_{\max} - R + z)n(R)dR. \qquad (13)$$

For a given $F(z)$, expression (13) can be viewed as an integral equation for a desired function $n(R)$. In this equation, the density function $K(R_{\max} - R + z)$ fulfills the role of a positive kernel.

Equation (13) is a Volterra integral equation of the first kind [6–8] for which a solution should be sought in the class of nonnegative functions from the physical point of view. The right-hand side of this equation is an integral transformation of the convolution type. If an exact solution of Eq. (13) exists, it is usually found by an operational method based on Laplace transforms [6, 7]. Here, we use an iteration solution algorithm for which the existence of an exact solution of Eq. (13) is not necessary. Its essence is that for a given distribution $F(z)$, a kernel $\bar{K}_1(R, z)$ close to $\bar{K}(R, z)$ is selected such that a solution $n_1(R)$ exists *a fortiori* and can be found by any, for example, matrix method [9]. Then, the kernel selected, $n_1(R)$, and true kernel $\bar{K}(R, z) = K(R_{\max} - R + z)$ are substituted into (13) and the free term $F_1(z)$ is refined. The pair of the function $n_1(R)$ and $F_1(z)$ gives the first approximation to the solution desired.

Next, we construct the function $F_1(z)$:

$$\bar{F}_1(z) = \begin{cases} F_1(z_{\max}) \\ F_1(z) \end{cases} \quad \text{for} \quad \begin{cases} 0 \le z \le z_{\max} \\ z > z_{\max}, \end{cases}$$

where $z_{\max}$ is the position of the maximum of $F_1(z)$.

The function $\bar{F}_1(z)$ obtained is substituted into the left-hand side of (13), and the iteration procedure is repeated until the function $F_1(z)$ flattens in the interval $0 \le z \le z_{i_{\max}}$, where i is the number of iteration. Otherwise, the process is terminated.

In the above procedure, the search for the desired distribution $n(R)$ and the refinement of the function $F(z)$ take place simultaneously. Therefore, the procedure can be considered as a solution algorithm for a variational problem with uncertain conditions of extremum. It is also seen that the algorithm is appropriate for the analysis of the density function of ranges if kernel and defect distribution are "fairly close" to each other.

With this method, we simulated the distribution of Ar^{40} tracks in germanium for $E_{\max} = 4.5$ MeV. For this track distribution, the RID distribution was uniform to the greatest extent. The continuous part of the distribution was then approximated by a power polynomial. In analytical form, the solution is given by

$$n(R) = \begin{cases} \sum_{i=0}^{4} \alpha_i R^i + 0.114\delta(R - 2.6) & \text{for } \begin{cases} 0 \le R \le 2.6, \\ R > 2.6, \end{cases} \\ 0 \end{cases} \qquad (14)$$

where $\alpha_0 = 0.04961$, $\alpha_1 = 0.09850$, $\alpha_2 = -0.09165$, $\alpha_3 = 5.259 \times 10^{-2}$, and $\alpha_4 = -1.312 \times 10^{-2}$; R is expressed in micrometers.

Figures 4a and 4b demonstrate the range distribution $n(R)$ obtained and its associated defect distribution $F(z)$, respectively. From Fig. 4b, it follows that the approximate calculation of $n(z)$ corresponds to the fairly flat $F(z)$ at $z \le 2.0$ μm although only three iterations have been made. In the interval $2.0 < z < 2.6$ μm, the distribution $F(z)$ drops to zero monotonically and can be flattened by no means because of the descending part of the kernel $\bar{K}(R, z)$.

In should be noted that distribution (14) has a singularity (at $R = 2.6$ μm) in the form of delta function [10], which affects the PEA profile, as will be shown below.

5. ANALYSIS OF THE PEA PROFILE

As was noted above, the stopping mechanisms for HIs, on one hand, and protons and α particles, on the other, differ. For HIs of mass A that have an energy E(MeV) < A, bremsstrahlung losses per ion grow because of an increase in the equilibrium charge of the ions. In the approximate power dependences of R on E, (1) and (3), the exponents B and B_f become less than unity. However, in a sufficiently wide energy interval, they continue to weakly depend on the stopping medium for a given sort of ions; that is, $B \cong B_f$. Specifically, for Ar^{40} ions with an energy up to 15 MeV, the exponent $B \approx 0.714$ for both aluminum and germanium

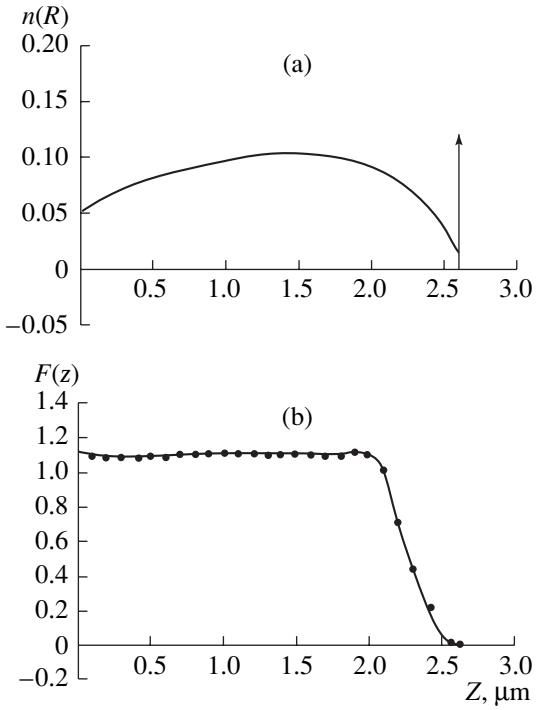

Fig. 4. (a) Range distribution $n(R)$ for Ar^{40} ions in Ge that provides the defect distribution as uniform as possible (E_{max} = 4.5 MeV) and (b) defect distribution over the depth $F(z)$ that corresponds to the range distribution $n(R)$ in Fig. 4a.

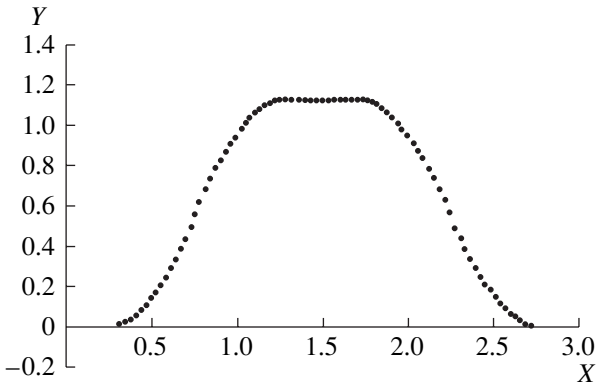

Fig. 5. Period of the PEA profile providing a uniform layer of RIDs with a thickness δz = 24 μm in the germanium sample (striking ions, Ar^{40}; absorbent material, Al; k = 2.4 μm; E_0 = 11.38 MeV; E_{max} = 4.5 MeV; and α_{max} = 62°).

samples. Hence, the profile of an aluminum PEA that provides the uniform distribution of defects in the Ge sample is given by the equations

$$x(\alpha) = A_0\int_0^\alpha \frac{n(R)\sin\alpha}{\cos^2\alpha}d\alpha + C_x,$$
$$y(\alpha) = A_0\int_0^\alpha \frac{n(R)\sin^2\alpha}{\cos^3\alpha}d\alpha + C_y, \quad (9a)$$

which follows from (9) and where R is substituted for z.

Now we express the coordinate z corresponding to the range R in the target material through R_f, k, and α:

$$R = z = A_{Ge}\left[\left(\frac{R_f - k/\cos\alpha}{A_{Al}}\right)^{1/B_{Al}}\right]^{B_{Ge}} = 0.395(R_f - k/\cos\alpha), \quad (15)$$

where A_{Al} = 0.878, A_{Ge} = 0.347, and $B_{Al} = B_{Ge}$ = 0.714.

Substituting (15) into (14) and rejecting the term containing the delta function, we come to

$$n(R_{Al}, k, \alpha) = \sum_{i=0}^{4}\alpha_i[0.395(R_{Al} - k/\cos\alpha)]^i. \quad (16)$$

Formula (16) specifies the depth distribution $n(R_{max}, k, \alpha)$ of tracks in the range of foil inclination $0 < \alpha \le \alpha_{max}$. This distribution corresponds to the condition $F(z)$ = const. Putting $\alpha_{max} = 62°$ and using formulas (1)–(5), we find that, with the aluminum foil thickness k = 2.4 μm and the energy of the Ar^{40} incident monochromatic beam E_0 = 11.38 MeV, the maximal ion path length in the absorbent is $Z_{Al,\,max}$ = 4.99 μm and the maximal energy of the spectrum behind the PEA is E_{max} = 4.5 MeV. Substituting the parameter values into (16) and expression (16) into set (9a), we calculate the parametrically defined PEA profile in the angular range $0° < \alpha \le 62°$. For definiteness, we put A_0 = 1 and $C_x = C_y$ = 0. Eliminating the parameter α, we arrive at the desired dependence $y(x)$. In Fig. 5, this dependence corresponds to the profile in the interval $0.343 \le x \le 1$.

The singularity in the form of the delta function in (14) at R = 2.6 implies that a finite portion of the area under the spectrum concentrates at $E = E_{max}$ (α = 0); in other words, along with the continuous part, the spectrum contains the discrete component. This fraction is given by

$$\xi = \frac{0.114\int_0^\infty \delta(R - 2.6)dR}{\int_0^\infty \rho(R)dR}.$$

Integration using the polynomial representation of $n(R)$ in the interval $0 \le R < 2.6$ and taking into account the properties of the delta function [11] yields ξ = 0.343.

Thus, the extent of the PEA segment to which the angle α = 0 corresponds must account for 34% of the total interval of x considered in the analysis. In Fig. 5, the total interval used in the calculations lies between 0 and 1. From the function $y(x)$ determined in this total interval, one can, by analogy with Fig. 2, construct the

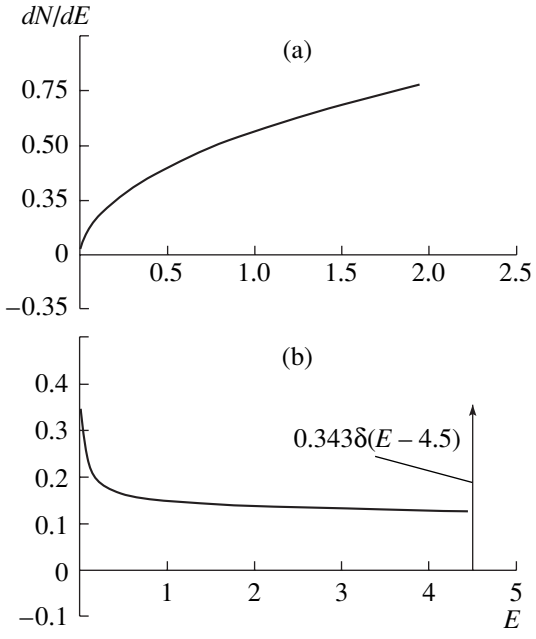

Fig. 6. (a) Energy spectrum of protons producing a constant hydrogen concentration in Si at depths from 0 to 50 μm and (b) energy spectrum of Ar^{40} ions producing the same RID density profile in Ge as shown in Fig. 4a.

PEA profile in the form of a continuous periodic function. The complete period of such a function is represented in Fig. 5.

The presence of plateaus is typical of PEAs for HIs. The plateau appears because the defects generated by a low- or medium-energy heavy particle are distributed along its entire path. As a result, a "wide" kernel $K(R, z)$ appears in integral equation (17) and the delta function arises in the distribution $n(z)$. As the width of the distribution $K(R, z)$ decreases, so does the amplitude of the delta function; therefore, the relative extent of the flat part of the PEA profile shrinks, tending to zero in the limit.

CONCLUSION

In general, a profiled absorbent is an arched foil with the profile meeting expression (9). For dopants to be uniformly distributed over the doping area, the beam usually scans the target in two directions. For the PEA profile not to modulate the surface relief, the PEA can be displaced relative to the sample. However, another simpler approach seems to be more preferable. It uses the effect of angular scattering, which is observed when ions travel in condensed media.

According to calculations carried out with the SRIM program, the transverse straggling of protons passing through a 40-μm-thick Al layer is ≈1.8 μm. This corresponds to a mean scattering angle $\bar{\varphi} = 2.6°$. This angle depends on E_0 only slightly and grows in proportion to the absorbent thickness. Calculations performed in [11] for this case gave a close value: $\bar{\varphi} = 2.37°$. If the period of the arched film is ≈2 mm, the ions having passed through the thinnest part of the absorbent become almost uniformly distributed over the sample even at a distance of several centimeters. As the mass of the ions grow, this distance increases because $\bar{\varphi}$ decreases.

Foil PEAs can be fabricated with a flat extrusion die. The die profile, in turn, can be made with a shaping tool on a planing machine.

With surface barrier detectors, the PEA profile can be tested by comparing the energy spectrum of the ions passing through a PEA with that obtained by formula (2). Figures 6a and 6b demonstrate the analytical energy spectra of protons and Ar^{40} ions that form the uniform depth distribution of hydrogen and RIDs for the cases under study.

It is known that, for given light and heavy ions, the coefficients B are weakly dependent on the stopping medium in a sufficiently wide energy range. Let a material irradiated have a low or medium atomic number and let a PEA be made of aluminum or copper, respectively. Then, for light and heavy ions, $(B - B_f)/B_f < 0.03$. In this case, for real values of R_f, k, and α, the assumption $(R_f - k/\cos\alpha)^{\frac{B-B_f}{B_f}} \approx \text{const}$ changes the results only by several percent, which is quite tolerable.

The basic advantage of doping by ion implantation is the production of doped layers with extremely sharp concentration boundaries, since the longitudinal straggling is <5% of the total range even for light ions.

It should be noted that the above calculations have been carried out under the assumption that the stopping coefficients do not depend on the implantation dose N. However, such a dependence is observed for heavy ions ($A > 10$) at $N > 10^{14}$ ion/cm^2 and for superheavy ions even at $N > 10^{13}$ ion/cm^2. For a doped layer 10 μm thick, these doses correspond to concentrations between 10^{16} and 10^{17} ion/cm^3. In view of the fact that RIDs arise at doses $N < 10^{12}$ ion/cm^2, our calculations also apply to the problem of designing PEAs used for the formation of desired RID distributions.

REFERENCES

1. E. I. Zorin, P. V. Pavlov, and D. I. Tetel'baum, *Ion-Implantation Semiconductor Doping* (Énergiya, Moscow, 1975).
2. V. A. Kozlov and V. V. Kozlovskiĭ, Fiz. Tekh. Poluprovodn. (St. Petersburg) **35**, 769 (2001) [Semiconductors **35**, 735 (2001)].
3. J. F. Zigler, J. P. Biersack, and U. Littmark, *The Stopping and Range of Ions in Solids* (Pergamon, New York, 1985), Vol. 1.

4. H. E. Schiott and P. V. Thomsen, Radiat. Eff. **14**, 39 (1972).
5. N. P. Kalashnikov, V. S. Remizovich, and M. I. Ryazanov, *Collisions of Fast Charged Particles in Solids* (Atomizdat, Moscow, 1980).
6. M. L. Krasnov, *Integral Equations* (Nauka, Moscow, 1975).
7. P. P. Zabreyko, A. I. Koshelev, I. A. Krasnosel'skiĭ, *et al.*, *Integral Equations: A Reference Text* (Nauka, Moscow, 1968; Noordhoff, Leyden, 1975).
8. V. I. Smirnov, *A Course of Higher Mathematics* (Nauka, Moscow, 1974; Addison-Wesley, Reading, 1964), Vol. IV, Part I.
9. V. I. Smirnov, *A Course of Higher Mathematics* (Nauka, Moscow, 1974; Addison-Wesley, Reading, 1964), Vol. III, Part I.
10. V. S. Vladimirov, *Generalized Functions in Mathematical Physics* (Nauka, Moscow, 1979, 2nd ed.; Mir, Moscow, 1979).
11. A. E. Blaugrund, Nucl. Phys. **88**, 501 (1966).

Translated by V. Isaakyan

Technical Physics, Vol. 47, No. 5, 2002, pp. 585–590. Translated from Zhurnal Tekhnicheskoĭ Fiziki, Vol. 72, No. 5, 2002, pp. 72–77.

OPTICS, QUANTUM ELECTRONICS

Phase (Interferometric) Photothermal Method for Separate Measurements of Surface and Volume Absorption

A. Yu. Luk'yanov and A. A. Pogorelko

Institute of Physics of Microstructures, Russian Academy of Sciences, Nizhni Novgorod, 603600 Russia

e-mail: luk@ipm.sci-nnov.ru

Received December 18, 2000; in final form, May 30, 2001

Abstract—The possibility of separately measuring the surface and volume absorption by a phase photothermal method is demonstrated with ZnSe polished samples. A theory developed allows us to directly relate the signal amplitude to the coefficients of surface and volume absorption. From the experimentally found dependence of the temperature oscillation amplitude at the sample surface on the angle of incidence, the position of the absorbing surface layer relative to the interface is determined and a mechanism of interaction between the pumping radiation and the target material is assessed. *© 2002 MAIK "Nauka/Interperiodica".*

The rapid advances in laser technology have lead to a continuous rise in the laser power and, as a consequence, to increasingly stringent requirements for the quality of optics. The absorption coefficient is one of the basic parameters defining optical losses and distortions, as well as the lifetime of optics.

Currently, the absorption coefficient is most frequently measured with the calorimetric method. Its basic advantage is simplicity. However, the interpretation of results obtained by this method is rather difficult, especially if the samples have various shapes. The separate determination of the volume and surface absorption coefficients and finding their distribution over the sample with this method are also a challenge [1, 2].

These problems can be obviated by using photothermal diagnostics methods. Over the last decade, they have gained wide acceptance in microscopy and nondestructive testing, in studying the thermophysical properties of various objects and media, in impurity and pollutant control systems, etc. [3–5]. Of special interest are optical methods of photothermal spectroscopy, which are totally nonintrusive (contactless) and offer high sensitivity and spatial resolution. Among them, the phase (interferometric) method is the most sensitive [6–8]. It was applied for tackling the problem posed.

The setup used in this work is presented in Fig. 1 (for details, see [9, 10]).

We studied absorption in polished plates of polycrystalline ZnSe at a wavelength of 10.6 μm.

Figure 2 shows the experimental dependence of the photothermal signal amplitude A_{ph} on the position of the point where the probing and heating light beams intersect. It follows from this figure that normal heat evolution due to volume adsorption is attended with anomalous heat evolution at the surfaces. Such an effect can be explained by the presence of a thin anomalously absorbing layer at the interfaces.

The nature of this layer calls for special investigation, which is beyond the scope of this work. We only note possible reasons for its occurrence. First, the surface absorbing layer may be formed of contaminants, for example, water molecules adsorbed on the surface from air. Second, the layer may be associated with a polisher left in the cracks. Third, the additional absorption may arise because of a change in the ZnSe band structure in the polishing-damaged layer.

In all the three cases, the thickness of the layer damaged is no higher than several hundred angströms. Since the typical size of the region of interaction

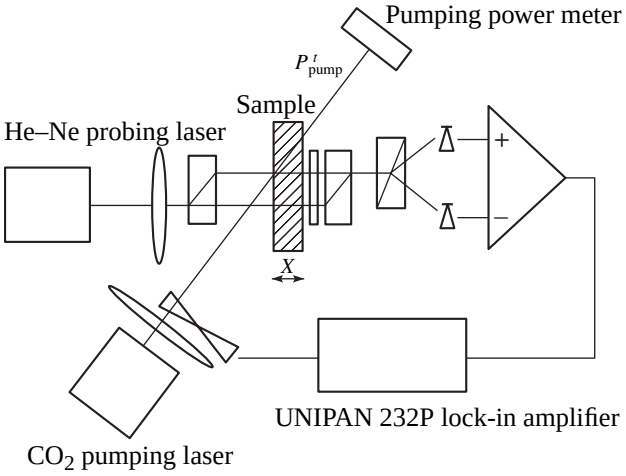

Fig. 1. Experimental setup. The pumping laser power is 1 W. The sensitivity is no worse than 10^{-5} cm^{-1} for volume absorption and 10^{-6} for surface absorption. The measurement accuracy is ±30%.

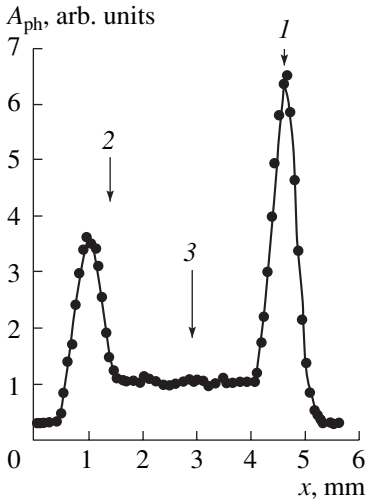

Fig. 2. Amplitude A_{ph} of the signal measured vs. position of the point x, where the probing and heating light beams intersect. The signal peaks at the sample surfaces: the lower peak is at the front (nearer) surface and the higher one, at the rare (farther) surface: (*1*) signal at the rare surface; (*2*) signal at the front surface; and (*3*) signal in the volume.

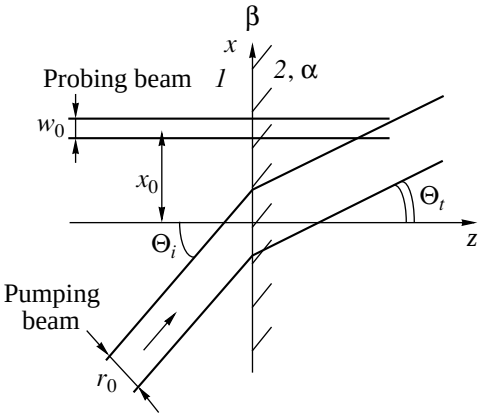

Fig. 3. Geometry of the experiment.

between the probing and heating beams is on the order of several hundreds of micrometers, it is obvious that the presence of the extra layer cannot significantly affect the thermophysical properties of the material. The refractive index also changes only slightly. For a layer thickness of 100 Å and measured losses of about 10^{-2}%, the imaginary part of the refractive index of the anomalous layer does not exceed 10^{-2}.

Thus, the output (recorded) signals can adequately be described within a model of semi-infinite sphere *2* having low coefficients of volume absorption α (cm^{-1}) and surface absorption β (%) (Fig. 3). The sphere is in contact with nonabsorbing air.

We are interested in a variable temperature perturbation arising from the absorption of the pumping radiation. The pumping radiation has a Gaussian distribution of the intensity $I(x, y, z, t)$ and is time-modulated with a mechanical chopper:

$$I(x, y, z, t) = \frac{2}{\pi}\frac{I\cos\Theta}{r_0^2}\exp\left(-\frac{2(x - z\tan\Theta)^2}{r_0^2/\cos^2\Theta_1} - \frac{2y^2}{r_0^2}\right) \times\left(1 + \frac{4}{\pi}\left(\sin(2\pi ft) + \frac{\sin(6\pi ft)}{3} + \ldots\right)\right). \quad (1)$$

Hereafter, $\Theta = \Theta_1$ in the first region (angle of incidence), $\Theta = \Theta_2$ in the second region (angle of refraction), r_0 is the pumping beam radius, f is the modulation frequency, and I is the average pumping intensity. Then, the heat conduction equation for each of the Fourier components has the form

$$\frac{\partial^2 T_m}{\partial x^2} + \frac{\partial^2 T_m}{\partial y^2} + \frac{\partial^2 T_m}{\partial z^2} - \frac{1}{\chi}\frac{\partial T_m}{\partial t} = -\frac{\alpha}{K}I(x, y, z)a_m\mathrm{Im}(e^{im\Omega t}). \quad (2)$$

Here, K is the thermal conductivity, $\chi = K/\rho c$ is the thermal diffusivity, ρ is the density, c is the specific heat, $\Omega = 2\pi f$ is the circular frequency, and a_m is the amplitude of the harmonic with a serial number m (m = 1, 3, 5, …). The temperature distribution $T_m(x, y, z, t)$ is sought in the form

$$T_m(x, y, z, t) = \mathrm{Im}\left(\frac{1}{4\pi^2}\int_{-\infty}^{+\infty}\int_{-\infty}^{+\infty}\tilde{T}_m(\lambda, \delta, z)e^{i\lambda x + i\delta y}d\lambda d\delta e^{im\Omega t}\right), \quad (3)$$

where $\tilde{T}_m(\lambda, \delta, z)$ is the amplitude of the mth harmonic.

For the mth harmonic, Eq. (3) can be recast as

$$\frac{d^2\tilde{T}_m(\lambda, \delta, z)}{dz^2} - \left(\frac{im\Omega}{\chi} + \lambda^2 + \delta^2\right)\tilde{T}_m(\lambda, \delta, z) = -a_m\frac{\alpha}{K}I\exp\left(-\frac{r_0^2}{8}\left(\frac{\lambda^2}{\cos^2\Theta_1} + \delta^2\right) - iz\lambda\tan\Theta\right). \quad (4)$$

Ignoring the air absorption and taking into account that the temperature cannot rise when z approaches $\pm\infty$, we find the solution of (4) in the first and second regions, respectively:

$$\tilde{T}_m^1(\lambda, \delta, z) = A\exp(\xi_1 z), \quad (5)$$

$$\tilde{T}_m^2(\lambda, \delta, z) = B\exp(-\xi_2 z) + a_m\frac{\alpha}{K_2}\frac{I_2}{(\lambda\tan\Theta_2)^2 + \xi_2^2} \times\exp\left(-\frac{r_0^2}{8}\left(\frac{\lambda^2}{\cos^2\Theta_1} + \delta^2\right) - iz\lambda\tan\Theta_2\right). \quad (6)$$

Here, $\xi_{1,2} = \lambda^2 + \delta^2 + im\Theta/\chi_{1,2}$; I_2 is the intensity of the light having crossed the interface; and A and B are constant factors determined from the boundary conditions at $z = 0$:

$$\tilde{T}_m^1(\lambda, \delta, z) = \tilde{T}_m^2(\lambda, \delta, z)|_{z=0}, \tag{7}$$

$$K_1 \frac{d\tilde{T}_m^1(\lambda, \delta, z)}{dz} - K_2 \frac{d\tilde{T}_m^2(\lambda, \delta, z)}{dz} = a_m I^{\text{surf}} \beta \exp\left(-\frac{r_0^2}{8}\left(\frac{\lambda^2}{\cos^2\Theta_1} + \delta^2\right)\right)\Bigg|_{z=0}, \tag{8}$$

where I^{surf} is the pumping intensity in the absorbing layer. The factors A and B are given by

$$A = \frac{a_m}{\Delta}\left[-\beta I^{\text{surf}} \exp\left(-\frac{r_0^2}{8}\left(\frac{\lambda^2}{\cos^2\Theta_1} + \delta^2\right)\right) + \frac{\alpha I_2}{\xi_2^2 + \lambda^2 \tan^2\Theta_2}(i\lambda\tan\Theta_2 + \xi_2) \times \exp\left(-\frac{r_0^2}{8}\left(\frac{\lambda^2}{\cos^2\Theta_1} + \delta^2\right)\right)\right], \tag{9}$$

$$B = \frac{a_m}{\Delta}\left[\beta I^{\text{surf}} \exp\left(-\frac{r_0^2}{8}\left(\frac{\lambda^2}{\cos^2\Theta_1} + \delta^2\right)\right) - \frac{\alpha I_2}{\xi_2^2 + \lambda^2 \tan^2\Theta_2}\left(i\lambda\tan\Theta_2 + \xi_1\frac{K_1}{K_2}\right) \times \exp\left(-\frac{r_0^2}{8}\left(\frac{\lambda^2}{\cos^2\Theta_1} + \delta^2\right)\right)\right], \tag{10}$$

$$\Delta = K_2\xi_2 + K_1\xi_1. \tag{11}$$

Having passed through the thus-heated region perpendicular to the interface, the probing light acquires an additional phase shift (provided that the temperature perturbations and their gradients are small)

$$\tilde{\Phi}_m(\lambda, \delta) = \frac{2\pi}{\lambda_{\text{probe}}}\frac{\partial n}{\partial T}\int_{-\infty}^{+\infty} \tilde{T}_m(\lambda, \delta, z)dz. \tag{12}$$

Periodic variations of the phase difference between the probing beams cause the interference pattern (signal intensity) at the output of the probing interferometer to oscillate. If it is assumed that the probing beam shape does not depend on the temperature oscillations, the complex relative amplitude of the intensity oscillating at a frequency of $2\pi fm$ in the far-field zone can be expressed in terms of the variables x and y as [7, 8]

$$\frac{\Delta I_m}{I} = \int_{-\infty}^{+\infty} dx \int_{-\infty}^{+\infty} dy |U_0(x, y)|^2 \tilde{\Phi}_m(x, y). \tag{13}$$

Here, $|U_0(x, y)|^2$ is the intensity distribution of the probing light in the region heated:

$$|U_0(x, y)|^2 = \frac{2}{\pi\omega_0^2}\exp\left(-2\frac{(x - x_0)^2 + y^2}{\omega_0^2}\right), \tag{14}$$

$$\tilde{\Phi}_m(x, y) = \frac{1}{4\pi^2}\int_{-\infty}^{+\infty}\int_{-\infty}^{+\infty} \tilde{\Phi}_m(\lambda, \delta)e^{i\lambda x + i\delta y}d\lambda d\delta. \tag{15}$$

Substituting (5), (6), (9)–(12), (14), and (15) into (13) eventually yields

$$\frac{\Delta I_m}{I} = \frac{a_m}{2\pi\lambda_{\text{probe}}}\int_{-\infty}^{+\infty}\int_{-\infty}^{+\infty} d\lambda d\delta \exp\left(-\frac{\omega_0^2(\delta^2 + \lambda^2)}{8} + i\lambda x_0\right) \times \left\{\frac{a}{\cos\Theta_2}\frac{I_2}{\xi_2^2 + \lambda^2 2\tan^2\Theta_2}\exp\left(-\frac{r_0^2}{8}\left(\frac{\lambda^2}{\cos^2\Theta_1} + \delta^2\right)\right) \times \left[\left(\frac{\partial n}{\partial T}\right)_2 \frac{1}{K_2}\int_0^{\infty} e^{-i\lambda z\tan\Theta_2}dz - \left(\frac{\partial n}{\partial T}\right)_2 \frac{1}{\Delta\xi_2} \times \left(\xi_1\frac{K_1}{K_2} + i\lambda\tan\Theta_t\right) + \left(\frac{\partial n}{\partial T}\right)_1 \frac{1}{\Delta\xi_1}(\xi_2 - i\lambda\tan\Theta_2)\right] + \frac{\beta I^{\text{surf}}}{\Delta}\exp\left(-\frac{r_0^2}{8}\left(\frac{\lambda^2}{\cos^2\Theta_1} + \delta^2\right)\right) \times \left[\left(\frac{\partial n}{\partial T}\right)_2 \frac{1}{\xi_2} + \left(\frac{\partial n}{\partial T}\right)_1 \frac{1}{\xi_1}\right]\right\}. \tag{16}$$

Taking into account that for the given parameters ($f > 100$ Hz, $r_0 = 270$ μm, $K_2 = 0.18$ W/(cm K), $c_2 = 0.342$ J/(g K), $\rho_2 = 5.265$ g/cm^3, $K_1 = 2.5 \times 10^{-4}$ W/(cm K), $c_1 = 1$ J/(g K), and $\rho_1 = 1.3 \times 10^{-3}$ g/cm^3) $\Omega/\chi_{1,2}$ is larger than λ^2 and δ^2, we expand expression (16) in small parameters $\chi\lambda^2/\Omega$ and $\chi\delta^2/\Omega$. Estimates showed that the first-order corrections in this case are rather small; therefore, we will consider only the zeroth-order terms. Then, integration yields the complex relative amplitude of the photothermal signal at a frequency of $2\pi fm$:

$$\frac{\Delta I_m}{I} = \frac{4a_m}{(\omega_0^2 + r_0^0/\cos^2\Theta_1)^{1/2}(\omega_0^2 + r_0^2)^{1/2}} \times \frac{\alpha}{\sqrt{\rho_1 c_1 K_1}} + \sqrt{\rho_2 c_2 K_2}\frac{I_2}{im\Omega\lambda_{\text{probe}}}\exp\left(-\frac{2x_0^2}{\omega_0^2 + r_0^2/\cos^2\Theta_1}\right)$$

$$\times\left\{\frac{\sqrt{\chi_1}\sqrt{\chi_2}}{\sqrt{im\Omega}}\left[\left(\frac{\partial n}{\partial T}\right)_1-\left(\frac{\partial n}{\partial T}\right)_2\frac{\rho_1 c_1}{\rho_2 c_2}\right]\right.$$

$$\left.+\frac{4\chi_2 x_0\tan\Theta_2}{im\Omega(\omega_0^2+r_0^2/\cos^2\Theta_2)}\left[\left(\frac{\partial n}{\partial T}\right)_1\sqrt{\chi_1}-\left(\frac{\partial n}{\partial T}\right)_2\sqrt{\chi_2}\right]\right\}$$

$$+\frac{\sqrt{2\pi}}{\lambda_{\text{probe}}}\frac{a_m}{(\omega_0^2+r_0^2)^{1/2}}\left(\frac{\partial n}{\partial T}\right)_2\frac{I_2}{im\Omega}\frac{\alpha}{\rho_2 c_2\tan\Theta_2} \qquad (17)$$

$$\times\left(1+\text{Erf}\left(\frac{\sqrt{2}x_0}{(\omega_0^2+r_0^2/\cos^2\Theta_1)^{1/2}}\right)\right)$$

$$+\frac{4}{(\omega_0^2+r_0^2/\cos^2\Theta_2)^{1/2}(\omega_0^2+r_0^2)^{1/2}}\frac{a_m}{\sqrt{\rho_1 c_1 K_1}+\sqrt{\rho_2 c_2 K_2}}$$

$$\times\frac{\beta I^{\text{surf}}}{im\Omega\lambda_{\text{probe}}}\exp\left(-\frac{2x_0^2}{\omega_0^2+r_0^2/\cos^2\Theta_1}\right)$$

$$\times\left[\left(\frac{\partial n}{\partial T}\right)_1\sqrt{\chi_1}+\left(\frac{\partial n}{\partial T}\right)_2\sqrt{\chi_2}\right].$$

Two limiting cases are of interest. For $x_0 \gg \sqrt{\omega_0^2+r_0^2/\cos^2\Theta_1}$, the interface does not influence the amplitude of the signal measured. The first and third terms vanish, so that the coefficient of volume absorption can be measured independently. The signal detected has a sawtooth shape with the effective voltage

$$\left.\frac{\tilde{U}}{\overline{U}}\right|_{x_0\to\infty}=\sqrt{\frac{\pi}{8}}\frac{\alpha I_2}{f\lambda_{\text{probe}}}\frac{1}{\rho_2 c_2\tan\Theta_2}\left(\frac{\partial n}{\partial T}\right)_2\frac{1}{\sqrt{\omega_0^2+r_0^2}}. \qquad (18)$$

At $x = 0$, the absorption surface component dominates in the signal (Fig. 2) and the volume component can be neglected. Then, the effective voltage of the signal is

$$\left.\frac{\tilde{U}}{\overline{U}}\right|_{x_0\to 0}=\frac{\beta I^{\text{surf}}}{2f\lambda_{\text{probe}}}\frac{1}{\sqrt{\omega_0^2+r_0^2}\sqrt{\omega_0^2+r_0^2/\cos^2\Theta_1}} \qquad (19)$$

$$\times\frac{1}{\sqrt{\rho_1 c_1 K_1}+\sqrt{\rho_2 c_2 K_2}}\left(\left(\frac{\partial n}{\partial T}\right)_2\sqrt{\chi_2}+\left(\frac{\partial n}{\partial T}\right)_1\sqrt{\chi_1}\right).$$

As has been shown [11], when measuring the surface absorption, one should consider the interference between the incident pumping radiation and its part reflected from the interface. The situation varies according to the pumping polarization, angle of incidence, and position of the absorbing layer relative to the interface (inside or outside of the sample, as well as above or under the reflecting surface). Also, it depends on the type of interaction between the pumping radiation and the sample (whether it is electric dipole–dipole or magnetic dipole–dipole). This is because in the former case, the electric field strength plays a major role. Therefore, here the interference can be taken into account by adding up the electric field strengths of the incident wave and the wave reflected from the interface. For magnetic dipole–dipole interaction, the magnetic field is of major concern; accordingly, the magnetic fields of the incident and reflected waves are added. If the absorbing layer is above the reflecting surface (i.e., outside) of a plate of finite thickness, the interference effects influence the signal amplitude at the surface that is nearer to the pumping source. Conversely, if the absorbing layer is under the reflecting surface (i.e., inside) of a plate of finite thickness, the interference effects influence the signal amplitude at the surface that is farther from the pumping source.

Thus, for a sufficiently thick plane-parallel (for multiply reflected beams not to intersect inside) plate, the coefficients of volume and surface absorption under the above conditions are given by

$$\alpha=\frac{\tilde{U}}{\overline{U}}\frac{f}{P'_{\text{pump}}}\sqrt{\frac{8}{\pi}}\frac{\lambda_{\text{probe}}\rho_2 c_2\tan\Theta_2}{(\partial n/\partial T)_2}k_t^2\sqrt{\omega_0^2+r_0^2},$$

$$\beta=\frac{\tilde{U}}{\overline{U}}\frac{f}{P'_{\text{pump}}}\frac{2\lambda_{\text{probe}}(\sqrt{\rho_1 c_1 K_1}+\sqrt{\rho_2 c_2 K_2})}{(\partial n/\partial T)_1\sqrt{\chi_1}+(\partial n/\partial T)_2\sqrt{\chi_2}}$$

$$\times\sqrt{\omega_0^2+r_0^2}\frac{\sqrt{\omega_0^2\cos^2\Theta_1+r_0^2}}{\cos\Theta_1}k_{\text{int}}.$$

Here, P'_{pump} is the average power of the pumping radiation having passed through the plane-parallel plate; k_t is the Fresnel transmission coefficient, which is expressed as

$$k_t^2=\left(\frac{2n_2\cos\Theta_2}{n_2\cos\Theta_2+n_1\cos\Theta_1}\right)^2\frac{n_1\cos\Theta_1}{n_2\cos\Theta_2}$$

and

$$k_t^2=\left(\frac{2n_2\cos\Theta_2}{n_2\cos\Theta_1+n_1\cos\Theta_2}\right)^2\frac{n_1\cos\Theta_1}{n_2\cos\Theta_2}$$

for *s*- and *p*-polarized pumping radiations, respectively; and k_{int} is the "interference" coefficient, which includes optical losses due to reflection from the interface and interference effects near it. Under specific experimental conditions, the interference coefficient is expressed as follows:

$$k_{\text{int}}=\left(\frac{2n_2\cos\Theta_2}{n_1\cos\Theta_1+n_2\cos\Theta_2}\right)^2$$

(nearer peak, *s*-polarization of pumping radiation, electric dipole–dipole interaction, absorbing layer outside),

$$k_{\text{int}}=\frac{4n_2\cos^2\Theta_2}{(n_1\cos\Theta_1+n_2\cos\Theta_2)^2}$$

(nearer peak, *s*-polarization of pumping radiation, electric dipole–dipole interaction, absorbing layer inside),

$$k_{\text{int}} = \left(\frac{2\cos\Theta_2}{n_1\cos\Theta_1 + n_2\cos\Theta_2}\right)^2$$

(nearer peak, *s*-polarization of pumping radiation, magnetic dipole–dipole interaction, absorbing layer outside),

$$k_{\text{int}} = \frac{4n_2\cos^2\Theta_2}{(n_1\cos\Theta_1 + n_2\cos\Theta_2)^2}$$

(nearer peak, *s*-polarization of pumping radiation, magnetic dipole–dipole interaction, absorbing layer inside),

$$k_{\text{int}} = 1$$

(farther peak, *s*-polarization of pumping radiation, electric dipole–dipole interaction, absorbing layer outside),

$$k_{\text{int}} = 1/n_2$$

(farther peak, *s*-polarization of pumping radiation, electric dipole–dipole interaction, absorbing layer inside),

$$k_{\text{int}} = 1$$

(farther peak, *s*-polarization of pumping radiation, magnetic dipole–dipole interaction, absorbing layer outside),

$$k_{\text{int}} = n_2$$

(farther peak, *s*-polarization of pumping radiation, magnetic dipole–dipole interaction, absorbing layer inside),

$$k_{\text{int}} = \left(\frac{2n_2\cos\Theta_1}{n_1\cos\Theta_2 + n_2\cos\Theta_1}\right)^2 \frac{1}{\cos^2\Theta_2 + n_2^2\sin^2\Theta_2}$$

(nearer peak, *p*-polarization of pumping radiation, electric dipole–dipole interaction, absorbing layer outside),

$$k_{\text{int}} = \frac{4n_2\cos^2\Theta_2}{(n_1\cos\Theta_2 + n_2\cos\Theta_1)^2}$$

(nearer peak, *p*-polarization of pumping radiation, electric dipole–dipole interaction, absorbing layer inside),

$$k_{\text{int}} = \left(\frac{2\cos\Theta_2}{n_2\cos\Theta_1 + n_1\cos\Theta_2}\right)^2$$

(nearer peak, *p*-polarization of pumping radiation, magnetic dipole–dipole interaction, absorbing layer outside),

$$k_{\text{int}} = \frac{4n_2\cos^2\Theta_2}{(n_1\cos\Theta_1 + n_2\cos\Theta_2)^2}$$

(nearer peak, *p*-polarization of pumping radiation, magnetic dipole–dipole interaction, absorbing layer inside),

$$k_{\text{int}} = 1$$

(farther peak, *p*-polarization of pumping radiation, electric dipole–dipole interaction, absorbing layer outside),

$$k_{\text{int}} = \frac{n_2}{n_2^2\cos^2\Theta_1 + \sin^2\Theta_1}$$

(farther peak, *p*-polarization of pumping radiation, electric dipole–dipole interaction, absorbing layer inside),

$$k_{\text{int}} = 1$$

(farther peak, *p*-polarization of pumping radiation, magnetic dipole–dipole interaction, absorbing layer outside), and

$$k_{\text{int}} = n_2$$

(farther peak, *p*-polarization of pumping radiation, magnetic dipole–dipole interaction, absorbing layer inside).

Figure 4 shows the experimental and theoretical dependences of the volume absorption signal on the angle of incidence for the *p*-polarized pumping radiation. At $\alpha = 2.66 \times 10^{-4}$ cm^{-1}, the theory fits the experimental data well.

Figure 5 demonstrates the experimental and theoretical ratios of the temperature oscillation amplitudes at

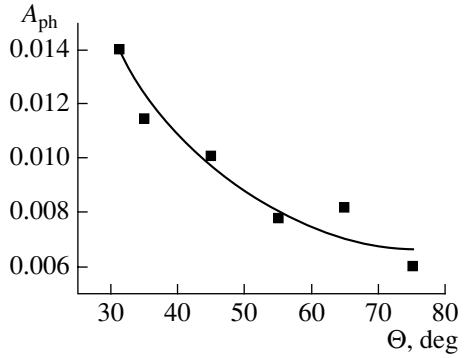

Fig. 4. Experimental (■, mean values) and theoretical dependences (continuous curve, $\alpha = 2.66 \times 10^{-4}$ cm^{-1}) of the amplitude A_{ph} of the volume absorption signal on the angle of incidence of the *p*-polarized pumping radiation Θ.

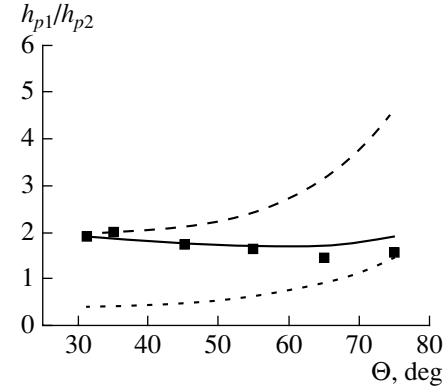

Fig. 5. Experimental (■) and theoretical (curves) dependences of the ratio of the photothermal signal amplitudes A_{ph} at the farther and nearer (relative to the pumping laser) samples surfaces vs. angle of incidence of the *p*-polarized pumping radiation. Continuous and dashed curves, electric dipole–dipole interaction for the cases of internal absorbing layer and external absorbing layer, respectively; dotted curves, magnetic dipole–dipole interaction. h_{p1}/h_{p2} is the ratio of the first and second peak heights.

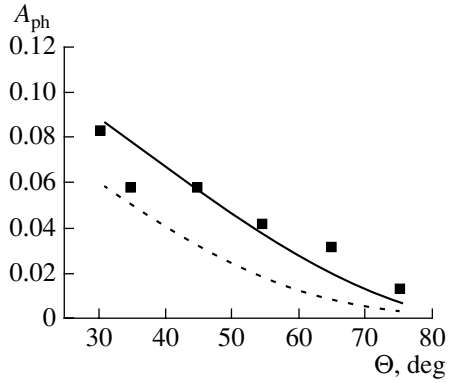

Fig. 6. Mean amplitude of the photothermal signal amplitude A_{ph} at the nearer sample surface vs. angle of incidence of the *p*-polarized pumping radiation Θ, and theoretical dependences of A_{ph} calculated for the two positions of the absorbing layer. ■, measured values; continuous curve, internal absorbing layer ($\beta = 1.65 \times 10^{-2}$%); dotted curve, external absorbing layer ($\beta = 3.5 \times 10^{-2}$%).

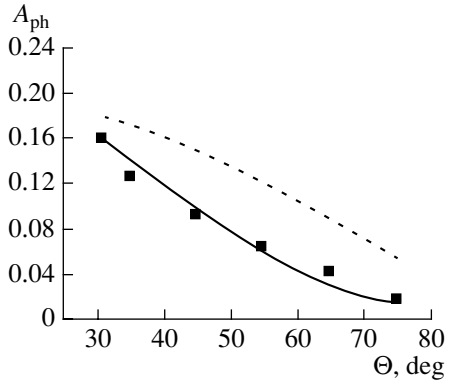

Fig. 7. Mean amplitude of the photothermal signal amplitude A_{ph} at the farther sample surface vs. angle of incidence of the *p*-polarized pumping radiation Θ, and theoretical dependences of A_{ph} calculated for the two positions of the absorbing layer. Designations are the same as in Fig. 6.

the farther and nearer (with respect to the pumping laser) sample surfaces vs. angle of incidence of the *p*-polarized pumping radiation. As was expected, the experimental data are best fitted by the model of electric dipole–dipole interaction between the pumping radiation and the material. Moreover, form these curves, one can determine the position of the absorbing layer relative to the air–sample interface. In this case, the layer lies underneath the reflecting surface.

This conclusion is corroborated by the experimental and theoretical curves (Figs. 6, 7) showing the temperature oscillation amplitudes at the nearer and farther surfaces vs. angle of incidence of the *p*-polarized pumping radiation. It is seen that the model of internal absorption (the absorbing layer under the reflecting surface) adequately describes the experimental data. The coefficient of surface absorption in this case varies between 2.4×10^{-2} and 3.4×10^{-2}%.

Thus, using the phase photothermal method, we succeeded in separately measuring low coefficients of surface and volume absorption in relatively thick polished plates of optical materials. The theory developed makes it possible to directly relate the signal amplitude to the coefficients of volume and surface absorption. In the CVD polycrystalline polished ZnSe sample used in the experiments, the coefficients vary from 2.2×10^{-4} to 3.6×10^{-4} cm^{-1} and from 2.4×10^{-2} to 3.4×10^{-2}%, respectively.

From the experimental dependence of the temperature oscillation amplitude at the surface on the angle of incidence of the *p*-polarized pumping radiation, one can judge the nature of radiation–material interaction. In polycrystalline CVD ZnSe, this is electric dipole–dipole interaction, as was expected.

In addition, the possibility of locating the surface absorbing layer relative to the interface was shown. In the samples studied, it lies under the reflecting surface (i.e., inside the sample). This layer may be associated with a change in the band structure because of polishing-induced damage or a polisher left in the cracks.

REFERENCES

1. M. Hass, J. W. Davisson, P. H. Kleyn, and L. L. Boyer, J. Appl. Phys. **45**, 3959 (1974).
2. V. G. Plotnichenko, V. K. Sysoev, and I. G. Firsov, Zh. Tekh. Fiz. **51**, 1903 (1981) [Sov. Phys. Tech. Phys. **26**, 1105 (1981)].
3. D. Bicanic, *Photoacoustic and Photothermal Phenomena III* (Springer-Verlag, Berlin, 1992).
4. A. Mandelis, *Principles and Perspectives of Photothermal and Photoacoustic Phenomena* (Elsevier, New York, 1992).
5. *Proceedings of the 9th International Conference on Photoacoustic and Photothermal Phenomena* (Taylor & Francis, Washington, DC, 1996), Progress in National Science, Supplement to Vol. 6.
6. P. K. Brazhnik and M. A. Novikov, Opt. Spektrosk. **70**, 453 (1991) [Opt. Spectrosc. **70**, 264 (1991)].
7. A. L. Glazov and K. L. Muratikov, Zh. Tekh. Fiz. **61** (11), 187 (1991) [Sov. Phys. Tech. Phys. **36**, 1302 (1991)].
8. A. Yu. Luk'yanov and M. A. Novikov, Zh. Tekh. Fiz. **70** (11), 99 (2000) [Tech. Phys. **45**, 1470 (2000)].
9. A. Yu. Luk'yanov, G. B. Vladykin, A. A. Aratskova, *et al.*, Zh. Fiz. Khim. **71**, 1497 (1997).
10. O. L. Antipov, A. S. Kuzhelev, A. Yu. Luk'yanov, and A. P. Zinov'ev, Kvantovaya Élektron. (Moscow) **25**, 891 (1998).
11. V. I. Plekhanov, A. Yu. Luk'yanov, and M. A. Novikov, Pis'ma Zh. Tekh. Fiz. **18** (2), 57 (1992) [Sov. Tech. Phys. Lett. **18**, 47 (1992)].

Translated by V. Isaakyan

Technical Physics, Vol. 47, No. 5, 2002, pp. 591–594. Translated from Zhurnal Tekhnicheskoĭ Fiziki, Vol. 72, No. 5, 2002, pp. 78–81.

OPTICS, QUANTUM ELECTRONICS

Pulse Dynamics in an Optical Fiber with Linear Intermode Coupling and Kerr Nonlinearity Dispersion

I. O. Zolotovskiĭ and D. I. Sementsov

Ul'yanovsk State University, Ul'yanovsk, 432970 Russia

Received June 14, 2001

Abstract—The effect of Kerr nonlinearity dispersion on the envelope duration and the velocity of the envelope maximum for a wave packet propagating in an optical fiber and formed by two coupled copropagating waves is studied. The critical (threshold) energy of wave packet collapse can substantially be diminished and the supraluminal mode of propagation of the pulse envelope maximum in a nonamplifying medium can be realized owing to a significantly higher nonlinearity dispersion in such systems in comparison with "single-wave" ones.

INTRODUCTION

In recent years, special attention has been paid to the area of nonlinear fiber optics that investigates distributed-coupled waves, which are of great interest for applications. Usually, such waves emerge in tunnel-coupled, anisotropic, or periodic optical fibers (OFs) [1, 2]. That is why analysis of the short pulse dynamics in such fibers with allowance for various nonlinear effects is topical [3–6]. In OFs with strong linear coupling, these effects can be more diversified and pronounced than in single-mode fibers, because mode coupling and phase cross modulation contribute markedly to the effective dispersion and nonlinearity. Maĭmistov [7] demonstrated the possibility of pulse collapse (the pulse duration tends to zero) in a single-mode fiber with nonlinearity dispersion in the case when the energy density delivered to the fiber reaches a critical value W_{cr}. The strong dependence of the effective parameters of the two-mode fibers considered on the type of their excitation makes it possible to substantially diminish the energy threshold for an optical pulse. In this work, based on the method of partial pulses and the variational approach, which were successfully applied in the analysis of short pulse propagation in nonlinear OFs [5–9], we study the dynamics of a wave packet consisting of two strongly interacting waves copropagating in a Kerr medium. Emphasis will be on the effect of nonlinearity dispersion on the wave packet duration and on the maximum velocity of the wave packet envelope. It is demonstrated that in these systems, the pulses can propagate with supraluminal velocities.

GENERAL RELATIONS

With allowance for a mode mismatch of the group velocities, nonlinear effects of phase self-modulation and phase cross modulation, and nonlinearity dispersion, a system of equations for the time envelopes of two coupled waves forming a wave packet is represented as

$$\frac{\partial A_j}{\partial z} + \frac{(-1)^j}{v}\frac{\partial A_j}{\partial \tau} - i\frac{d_j}{2}\frac{\partial^2 A_j}{\partial \tau^2}$$

$$= -i\sigma A_{3-j} - iR(\gamma_s|A_j|^2 + \gamma_c|A_{3-j}|^2)A_j \qquad (1)$$

$$-\frac{2R}{\omega_0}\frac{\partial}{\partial \tau}[(\gamma_s|A_j|^2 + \gamma_c|A_{3-j}|^2)A_j]; \quad j = 1, 2.$$

Here $\tau = t - z/u$ is running time, u is the group velocity of the wave packet, $v^{-1} = (u_1 - u_2)/2u^2$, $u_j = (\partial\beta_j/\partial\omega)^{-1}_{\omega_0}$ is the group velocity of the jth mode, $d_j = (\partial^2\beta_j/\partial\omega^2)_{\omega_0}$ is the group velocity dispersion for the jth mode, $2u = u_1 + u_2$, R is the parameter of fiber nonlinearity, ω_0 is the carrier frequency of the wave packet, σ is the mode coupling coefficient, and γ_s and γ_c are the self-modulation and cross modulation parameters [3]. Equations (1) must be complemented by initial conditions for the time envelopes of the modes A_j: $A_2(\tau, 0) = \psi A_1(\tau, 0)$, where the parameter ψ defines the type of fiber excitation. The excitation is symmetric (antisymmetric) if $\psi = \pm 1$. For strong mode interaction, one can represent the solution to system (1) as the sum of two partial pulses (PPs):

$$A_j = (-1)^{j+1}a_1(\tau, z)\exp(i|\sigma|z) + a_2(\tau, z)\exp(-i|\sigma|z), \qquad (2)$$

where a_f are the amplitudes slowly varying with the coordinate z in the fiber. The initial conditions for these amplitudes are given by

$$a_f(\tau; 0) = 0.5[A_1(\tau; 0) + (-1)^f A_2(\tau; 0)]; \quad f = 1, 2. \qquad (3)$$

1063-7842/02/4705-0591$22.00

Substituting Eq. (2) into system (1), we obtain a system of equations for PP amplitudes:

$$\frac{\partial a_f}{\partial z} - i\frac{D_f}{2}\frac{\partial^2 a_f}{\partial \tau^2} + iR(\gamma_c + \gamma_s)(|a_f|^2 + s|a_{3-f}|^2)a_f + \chi_1\frac{\partial}{\partial \tau}(|a_f|^2 + s|a_{3-f}|^2)a_f + (-1)^f\chi_2 a_f\frac{\partial}{\partial \tau}(|a_f|^2 + |a_{3-f}|^2) = 0, \quad (4)$$

where $D_f = (d_1 + d_2)/2 + (-1)^f/v^2|\sigma|$ is the effective dispersion of the partial pulse, $s = 2\gamma_s/(\gamma_c + \gamma_s)$, $\chi_1 = 2R(\gamma_c + \gamma_s)/\omega_0$, and $\chi_2 = R(\gamma_c + \gamma_s)/2v|\sigma$.

If the initial conditions of OF excitation are symmetric or antisymmetric, the amplitude of one of the PPs equals zero: $a_1 = 0$ for symmetric excitation and $a_2 = 0$ for antisymmetric excitation [9]. The system of two equations for PPs can then be reduced to a single equation

$$\frac{\partial a_f}{\partial z} - i\frac{D_f}{2}\frac{\partial^2 a_f}{\partial \tau^2} + iR(\gamma_c + \gamma_s)|a_f|^2 a_f + \chi_f\frac{\partial}{\partial \tau}(|a_f|^2 a_f) + \rho_f|a_f|^2\frac{\partial a_f}{\partial \tau} = 0, \quad (5)$$

where $\delta_f = \chi_1 + (-1)^f\chi_2$ and $\rho_f = (-1)^{f+1}\chi_2$.

Let us solve this equation by the variational method. It involves the construction of a trial solution with z-dependent parameters that, following the variational procedure, are determined from a system of appropriate equations.

As a trial solution to Eq. (5), we take the function widely used for describing soliton-like pulses:

$$\tilde{a}_f = G_f\,\mathrm{sech}(\theta_f/\tau_f)\exp[i(\varphi_f + g_f\theta_f + \alpha_f\theta_f^2)], \quad (6)$$

where the amplitude G_f, phase φ_f, correction g_f to the phase velocity of the pulse, the rate of frequency modulation (chirp) α_f, pulse duration τ_f, and parameter $\theta_f = \tau - T_{vf}$ depend on the coordinate z. The parameter T_{vf} takes into account the variation of the group velocity of the pulse. These parameters specify the pulse dynamics. Following the formalism described in detail in [6, 7], we can derive the system of equations

$$\frac{d(G_f^2\tau_f)}{dz} = 0, \quad (7.1)$$

$$\frac{d\tau_f}{dz} = 2D_f\alpha_f\tau_f, \quad (7.2)$$

$$\frac{dg_f}{dz} = \frac{4}{3}\delta_f\alpha_f G_f^2, \quad (7.3)$$

$$\frac{dT_v}{dz} = D_f g + (\delta_f + \rho_f/3)G_f^2, \quad (7.4)$$

$$\frac{\pi^2}{2}\frac{d\alpha}{dz} = D_f\left(\frac{1}{\tau_f^4} - \pi^2\alpha_f^2\right) + ((\delta_f + \rho_f)g_f R(\gamma_c + \gamma_s))\frac{G_f^2}{\tau_f^2}. \quad (7.5)$$

From Eqs. (3) and (7.1), we find $2G_f^2\tau_f = W_0$, where W_0 is the pulse energy at entrance to the fiber. For the symmetric and antisymmetric excitations, $W_0 = 2|A_{j0}|^2\tau_0$, where τ_0 is the pulse duration at $z = 0$. Solving Eqs. (7.1)–(7.3), we come to

$$g_f = g_0 - \delta_f W_0/3D_f\tau_f. \quad (8)$$

Eliminating the variables α_f and g_f from Eqs. (7.3) and (7.5) and taking into account Eq. (8), we arrive at the equation for the pulse duration τ_f:

$$\frac{d^2\tau_f}{dz^2} - p\tau_f^{-2} - q\tau_f^{-3} = 0, \quad (9)$$

where

$$p = \frac{2D_f W_0}{\pi^2}(g_0(\delta_f + \rho_f) + R(\gamma_c + \gamma_s)),$$

$$q = \frac{4}{\pi^2}\left(D_f^2 - \frac{1}{6}(\delta_f + \rho_f)\delta_f W_0^2\right).$$

The expression for the first integral in (9),

$$\left(\frac{d\tau_f}{dz}\right)^2 = f_0 + 2p\tau_f^{-1} - q\tau_f^2, \quad (10)$$

where $f_0 = 4D_f^2\tau_0^2\alpha^2(0) + 2p/\tau_0 + q/\tau_0^2$ and $\alpha_0 = \alpha(0)$, shows that the problem considered is reduced to the well-known equation in the Kepler problem [10]. According to the general theory, its solution depends considerably on the sign of the constants involved. In particular, the parameter f_0 is responsible for the sign of the "total energy" of a particle in the presence of a "center of force," whose character depends on the sign of the parameter p. In the Kepler problem, the parameter q is always positive, since it accounts for the contribution of the azimuthal motion to the kinetic energy of the particle. The signs of these constants specify the possibility of a finite or infinite motion. For a pulse in a fiber, this is equivalent to either its finite duration (quasi-soliton mode) or infinite broadening at $z \longrightarrow \infty$.

SOLUTIONS AND ANALYSIS

Let us analyze more comprehensively the solutions to Eq. (10), which yields the dependence of the pulse duration τ_f on the traveled distance at $q > 0$ and $p < 0$, when pulse compression is possible.

(i) $f_0 < 0$. In this case, Eq. (10) describes a finite motion or a pulse with a periodically varying duration, which can be considered as a quasi-soliton (strictly speaking, such a wave object is not a soliton, since initial system of equations (1) is not integrable). The solution of Eq. (10) yields the pulse duration in the form

$$\tau_p = k(1 - e\cos\zeta), \quad (11)$$

where the parameter ζ is related to the travel by the formula

$$z = b(\zeta - e\sin\zeta) + C, \quad (12)$$

where $k = |p/f_0|$, $b = |p||f_0|^{-3/2}$, and $e = (1 - 16\pi^2|f_0|/R^2(\gamma_s + \gamma_c)^2 W_0^2)^{1/2}$. The constant of integration in Eq. (12) is determined from the initial conditions and equals $C = b(e\sin\zeta_0 - \zeta_0)$. The variable ζ ranges from ζ_0 to ∞, where

$$\zeta_0 \equiv \zeta(0) = \arccos((k - \tau_0)/de). \quad (13)$$

In the case considered, $e < 1$ and the pulse duration τ_f increases with distance from τ_{min} to τ_{max}. The minimum, $\tau_{min} = k(1 - e)$, and maximum, $\tau_{max} = k(1 + e)$, pulse durations correspond to $\zeta = 2m\pi$ and $\zeta = (2m + 1)\pi$ and to the distances $z_{min} = 2m\pi b + C$ and $z_{max} = (2m + 1)\pi b + C$, respectively. If $D_f\alpha(0) < 0$, then $d\tau_f/dz > 0$, so that the pulse duration first decreases to the minimum value and then starts increasing. If $D_f\alpha(0) > 0$, then $d\tau_f/dz > 0$; that is, the pulse first widens to τ_{max} and then shortens (pulse compression takes place). The compression length can be defined as a fiber segment at which the pulse duration varies from the maximum to the minimum. For the case considered, the compression length is $L_{com} = \pi b$.

(ii) $f_0 > 0$. In this case, $e > 1$ and Eq. (10) describes an infinite motion; that is, $\tau \longrightarrow \infty$ at $z \longrightarrow \infty$. Both above scenarios are possible here. If the quantity $D_f\alpha_0$ is positive, the pulse continuously broadens after having entered the fiber. If $D_f\alpha_0 < 0$, the pulse first contracts and then expands. In both cases, the dependence of the pulse duration on the travel is given by

$$\tau_p = |k|(e\cosh\zeta - 1), \quad z = b(e\sinh\zeta - \zeta) + C', \quad (14)$$

where $C' = b(\zeta_0 - e\sinh\zeta_0))$, $\zeta_0 = \ln(\varphi \pm \sqrt{\varphi^2 - 1})$, and $\varphi = (|k| + \tau_0)/|k|e$. In the second relationship, the sign coincides with that of $D_f\alpha_0$.

If $D_f\alpha_0 < 0$, the minimum pulse duration and the compression length are represented as

$$\tau_{min} = |k|(e - 1),$$
$$I_c = [e\sqrt{\varphi^2 - 1} - \ln(\varphi - \sqrt{\varphi^2 - 1})]. \quad (15)$$

(iii) $q \le 0$. Analysis shows that the sign of the parameter q also affects the pulse dynamics. This parameter depends on the energy W_0 delivered to the fiber and can be negative. If $f_0 < 0$ and $p < 0$, an equation similar to Eq. (10) in the Kepler problem describes a particle falling on a center of attraction. For an OF, this means that the pulse duration tends to zero, or, in other words, the pulse collapses. According to Eqs. (9) and (10), the collapse is possible only upon the symmetric ($f = 2$, $a_2 \neq 0$) excitation of the fiber. In the case of antisymmetric excitation, $q > 0$. The collapse of a wave packet takes place if the energy W_0 delivered to the OF exceeds a certain critical value W_{cr} ($W_0 \ge W_{cr}$)

$$W_{cr} = |D_f|\sqrt{6/\chi_1(\chi_1 + \chi_2)}.$$

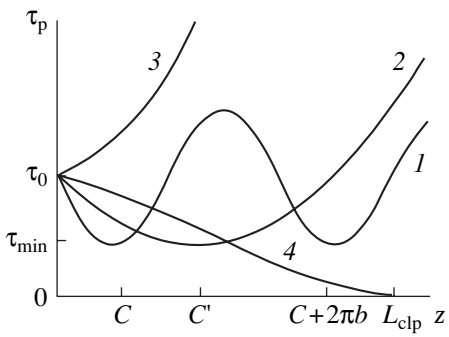

Characteristic curves of the pulse duration versus travel in the OF.

The collapse length is given by $L_{clp} = F(0) - F(\tau_0)$, where

$$F(\tau) = \frac{1}{f_0}\left[\sqrt{f_0\tau^2 + 2p\tau - q} + \frac{1}{\sqrt{-f_0}}\arcsin\frac{f_0\tau + p}{2(p^2 + f_0 q)}\right] \quad (16)$$

and the parameters p, q, and f_0 are negative.

The figure shows characteristic travel dependences of the pulse duration for cases (i)–(iii). Curve *1* corresponds to the "oscillatory" mode of pulse propagation at $f_0 < 0$, curve *2* shows pulse broadening at $f_0 > 0$ and $D_f\alpha_0 > 0$, curve *3* demonstrates the initial stage of compression at $f_0 > 0$ and $D_f\alpha_0 < 0$, and curve *4* reflects optical collapse at $f_0 < 0$ and $p < 0$.

Note that the inequality $w_0/v|\sigma| \gg 1$ holds true in a wide range of parameters of the pulse and the medium. Hence, $\chi_2/\chi_1 \gg 1$. In particular, for a pulse initial duration $\tau_0 \cong 1$ ps, intensity $a_{f0}^2 \cong 10^{10}$ W/cm^2, carrier frequency $w_0 = 10^{15}$ s^{-1}, $v^{-1} = 6 \times 10^{-13}$ s/m, $\sigma = 4.5$ m^{-1}, and $R(\gamma_s + \gamma_c) = 1.5 \times 10^{-14}$ W^{-1} m^{-1}, we obtain $\chi_1 = 3 \times 10^{-29}$ (s m)/W and $\chi_2 = 10^{-27}$ (s m)/W, so that $\chi_2/\chi_1 \cong 30$. This makes it possible to realize optical collapse in a system of coupled waves at energies much lower than those typical of a single-wave system. The strong dependence of the effective dispersion D_f on the OF parameters and energy reduces the critical energy of

optical collapse still further, down to $W_{cr} \cong 1$ J/m^2, whereas the collapse energy for a "conventional" single-wave system is most likely no lower than $W_{cr} = 10$–50 J/m^2.

THE VELOCITY OF THE ENVELOPE MAXIMUM

An important qualitative difference between the systems considered and single-wave ones is that the parameters δ_f and ρ_f may be negative under certain excitation conditions. One of the most interesting consequences of this negativeness is supraluminal velocities, which can be attained in the systems. Consider trial solution (6), which implies that the velocity u_m of the envelope maximum and the group velocity u are related as

$$u_m = \frac{u}{1 + uT_v/z}, \tag{17}$$

where the z dependence of the parameter T_v is given by Eq. (7.4).

It follows from Eq. (17) that $u_m > u$ if $T_v < 0$. Let us analyze conditions for the appearance of a "supraluminal" wave by an example of a quasi-monochromatic wave or a long pulse with a duration $\tau_0 \geq 10^{-9}$ s. For the OF lengths considered, the pulse duration and amplitude are virtually constant ($G_f^2 \cong a_{f0}^2$) because the dispersion length is large ($L_D = \tau_0^2/|d| \geq 10^7$ m). In this case, $\tau_f(z) \cong \tau_0$, $g(z) \cong 0$, and Eq. (7.4) can be reduced to

$$\frac{dT_v}{dz} = \left(\chi_1 + \frac{2}{3}(-1)^f\chi_2\right)a_{f0}^2. \tag{18}$$

Integrating this equation and assuming that $T_v(0) = 0$, we arrive at an expression for $T_v(z)$ in view of which the formula for the velocity of the pulse envelope maximum takes the form

$$u_m = \frac{u}{1 + (\chi_1 + (-1)^f 2\chi_2/3)ua_{f0}^2}. \tag{19}$$

It is seen from (19) that the velocity of the envelope maximum can be greater that the speed of light in the case of OF antisymmetric excitation ($f = 1$) if $3\chi_1 - 2\chi_2 < 0$. Such effects are explained [11] by the energy redistribution in the wave packet due to the fact that the velocity of the envelope maximum exceeds that of its "center of mass." However, this phenomenon was supposed to be related exclusively to the amplifying properties of the medium, which can modify substantially the parameters of the pulse (duration, peak intensity, phase, etc.) propagating in an optical fiber [12, 13]. Note that the above solution is also valid for the case of a soliton-like pulse emerging at $f_0 < 0$, when the conditions $\tau_f \cong$ const and $G_f^2 \cong$ const are satisfied at a certain OF segment $z \gg L_D$.

It should be emphasized that the parameters characterizing the nonlinearity dispersion in systems with a strong mode coupling (when $|\delta_f/\chi_1| = 10$–100) are much greater than those for conventional single-mode systems. Therefore, analysis of the former systems must necessarily include these parameters into consideration. In particular, it seems to be especially important to take into account the nonlinearity dispersion in simulating tunnel-coupled optical fibers which have recently received wide recognition.

REFERENCES

1. A. A. Maĭer, Usp. Fiz. Nauk **165**, 1037 (1995) [Phys. Usp. **38**, 991 (1995)].
2. S. A. Vasil'ev, E. M. Dianov, A. S. Kurkov, *et al.*, Kvantovaya Élektron. (Moscow) **24** (10), 151 (1997).
3. S. A. Akhmanov, V. A. Vysloukh, and A. S. Chirkin, *The Optics of Femtosecond Laser Pulses* (Nauka, Moscow, 1988), p. 312.
4. F. Kh. Abdullaev, R. M. Abramov, V. I. Goncharov, and S. A. Darmanyan, Zh. Tekh. Fiz. **64** (9), 101 (1994) [Tech. Phys. **39**, 916 (1994)].
5. V. A. Vysloukh and L. P. Gevorkyan, Izv. Akad. Nauk SSSR, Ser. Fiz. **35**, 323 (1991).
6. B. A. Malomed, P. L. Skinner, P. L. Chu, and G. D. Peng, Phys. Rev. E **53**, 4084 (1996).
7. A. I. Maĭmistov, Kvantovaya Élektron. (Moscow) **21**, 358 (1994); Kvantovaya Élektron. (Moscow) **22**, 936 (1995).
8. I. O. Zolotovskiĭ and D. I. Sementsov, Kvantovaya Élektron. (Moscow) **27**, 273 (1999).
9. I. O. Zolotovskiĭ and D. I. Sementsov, Opt. Spektrosk. **88**, 620 (2000) [Opt. Spectrosc. **88**, 560 (2000)]; Opt. Spektrosk. **89**, 806 (2000) [Opt. Spectrosc. **89**, 742 (2000)].
10. L. D. Landau and E. M. Lifshitz, (Nauka, Moscow, 1988), p. 51.
11. A. N. Oraevskiĭ, Usp. Fiz. Nauk **168**, 1311 (1998) [Phys. Usp. **41**, 1199 (1998)].
12. A. N. Oraevskiĭ and D. K. Bandy, Kvantovaya Élektron. (Moscow) **21**, 355 (1994).
13. I. O. Zolotovskiĭ and D. I. Sementsov, Zh. Tekh. Fiz. **70** (10), 57 (2000) [Tech. Phys. **45**, 1288 (2000)].

Translated by A. Chikishev

Technical Physics, Vol. 47, No. 5, 2002, pp. 595–603. Translated from Zhurnal Tekhnicheskoĭ Fiziki, Vol. 72, No. 5, 2002, pp. 82–90.

ELECTRON AND ION BEAMS, ACCELERATORS

Vircator with Electron Beam Premodulation Built Around a High-Current Pulsed–Periodic Accelerator

S. A. Kitsanov, A. I. Klimov, S. D. Korovin, I. K. Kurkan, I. V. Pegel, and S. D. Polevin

Institute of High-Current Electronics, Siberian Division, Russian Academy of Sciences, Akademicheskiĭ pr. 4, Tomsk, 634055 Russia

e-mail: pegel@lfe.hcei.tsc.ru

Received May 23, 2001; in final form, September 28, 2001

Abstract—Theoretical, numerical, and experimental studies of a vircator with the premodulation of a dm-wave electron beam are performed. Possible oscillation mechanisms in virtual-cathode systems (modulation of passing current, effect of reflex klystron, and inertial bunching of particles reflected) are analyzed. The microwave efficiency of the vircator using a two-gap electrodynamic system is shown to be significantly higher than that of the vircator with a one-gap system. Based on the results of the numerical experiment, a prototype of a two-stage vircator in the absence of an external magnetic field is designed. In experiments using a high-current pulsed–periodic accelerator, single-mode oscillations with a power of up to 1 GW, a duration of ≈25 ns, and an efficiency of ≈5% are generated in the dm-wave range. The oscillation frequency is demonstrated to be stable during a pulse and from pulse to pulse, which suggests the decisive effect of the electrodynamic system. It is shown that the oscillation frequency can continuously be tuned in a half-power bandwidth of ≈15% by varying the parameters of the resonator. © *2002 MAIK "Nauka/Interperiodica".*

INTRODUCTION

Vircators [1–6] are attracting attention as sources of high-power microwave radiation that operate in the absence of an external magnetic field. Since the length of interaction between the particle flux and the rf field in vircators is comparable to the radiation wavelength, the devices have small sizes, which is of great importance for generating radiation in the long-wave part of the microwave range. In most experiments, however, the vircator efficiency was poor (≈1%) and the radiation frequency was unstable. As a rule, this is a result of a too high injection current and of using overmoded electrodynamic systems with a high density of electromagnetic oscillations. In this work, we study a vircator in which a virtual cathode (VC) forms in a two-stage single-mode resonator and into which an electron beam of a low supercriticality [7, 8] is injected.

OSCILLATION MECHANISMS

As a model of a vircator, we consider a planar gap of length L into which an electron beam with a particle energy $\varepsilon_{in} = mc^2(\gamma_{in} - 1)$ and a current density $j_{in} > j_{cr2}$ (j_{cr2} is the second critical current) is injected. Under such conditions, the two-flow state of the electron beam can be set up with the formation of a VC [9]. The output current and the position z_0 of the VC are given by

$$\frac{1}{j_{out}^{1/2}} + \frac{1}{(2j_{in} - j_{out})^{1/2}} = \frac{2}{j_{cr}^{1/2}},$$

$$z_0/L = 1 - (j_{cr1}/4j_{out})^{1/2},$$

where $j_{cr1} \approx j_{cr2}/2$ is the first critical current.

The probability that a particle will cross the gap is $W_{tr} = j_{out}/j_{in}$. The value of W_{tr} depends on how much the injected current exceeds the critical one. For $j_{in} \approx j_{cr2}$, $W_{tr} \approx 1/4$ and $z_0 \approx L/3$.

Assume for simplicity that the planar gap is an element of a single-mode resonator with a Q factor $\gg 1$, so that the distribution of the rf field in the resonator is invariable. We also assume that the field amplitude is small and a change in the total particle energy for a time of flight over the gap, eEL, is much smaller than ε_{in}; i.e. $eEL \ll \varepsilon_{in}$. Finally, the particle motion is one-dimensional and the particles reflected from the VC do not return to the region of interaction with the rf field.

In the presence of the rf field, the total energy of the particles in the gap becomes time-dependent. Obviously, the energy modulation of the particles causes the modulation of the output current, the current of the electrons reflected, and the VC position. The work done by a field with a frequency ω on the particle flux can be written as

$$P_{\Delta j} \approx \frac{j_{in}S_b}{2e}\mathrm{Re}\{\langle \Delta\tilde{W}_{tr}^*(\Delta\tilde{\varepsilon}_{tr} - \Delta\tilde{\varepsilon}_{ref})\rangle_{Q_0}\},$$

where $\Delta\tilde{\varepsilon}_{tr} = \Delta\tilde{\varepsilon}(L)$ is the change in the transit particle energy in the rf field, $\Delta\tilde{\varepsilon}_{ref} = (1 - e^{i\Theta_{z_0}})\Delta\tilde{\varepsilon}(z_0)$ is the

1063-7842/02/4705-0595$22.00 © 2002 MAIK "Nauka/Interperiodica"

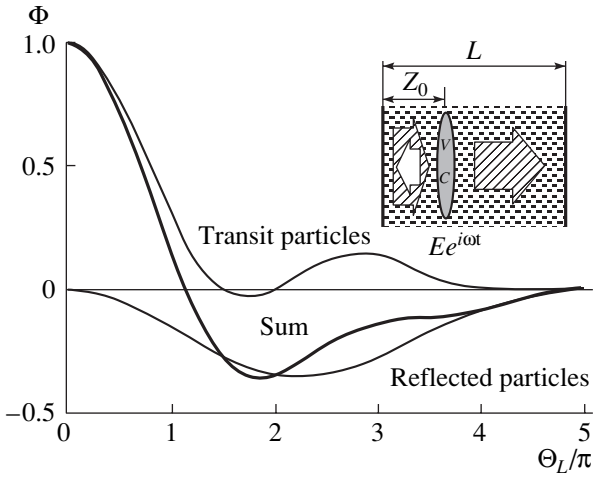

Fig. 1. Transit angle functions for a one-gap vircator.

change in the energy of the particles reflected from the VC,

$$\Delta\tilde{\varepsilon}(z) = e^{i\Theta_0}\int_0^z eEe^{i\Theta}dz,\quad \Theta(z) = \int_0^z \frac{\omega}{V(z')}dz',$$

$V(z)$ is the undisturbed velocity of the particles, S_b is the cross-sectional area of the beam, and Θ_0 is the phase with which the particle enters into the region of interaction with the rf field.

On assumption that $\omega < \omega_{vc}$, where ω_{vc} is the eigenfrequency of VC oscillations, the possibility that the particle will pass through the VC can be represented as

$$\Delta\tilde{W}_{tr} \approx \frac{1}{j_{in}}\frac{j_{out}}{j_{cr1}}\frac{\partial j_{cr1}}{\partial\gamma}\frac{L}{z_0}\frac{\Delta\varepsilon(z_0)}{mc^2}.$$

If the distribution of the rf field in the gap is uniform, the linear interaction efficiency is expressed as

$$\eta_{\Delta j} \approx \frac{1}{2}\frac{j_{out}}{j_{in}j_{cr1}}\frac{\partial j_{cr1}}{\partial\gamma}\frac{|eEL/mc^2|^2}{(\gamma_{in}-1)}\Phi_{\Delta j},$$

where

$$\Phi_{\Delta j} = \mathrm{Re}\left\{f(L)f^*(z_0) - \frac{z_0}{L}(1-e^{i\Theta_{z_0}})|f(z_0)|^2\right\},$$

$$f(z) = \frac{1}{z}\int_0^z e^{i\Theta}dz.$$

At small transit angles, $\Phi_{\Delta j} \approx 1$ and the radiation is absent due to the fact that the energy is absorbed by the transit particles, because the current density of the field-accelerated transit particles is higher than that of the particles decelerated. For finite transit angles and $j_{in} \gg j_{cr2}$, the plane of particle rotation approaches the plane of beam injection. In this case (as before), the particles reflected do not participate in the interaction and we have $\Phi_{\Delta j} \approx \mathrm{Re}\{f(L)\}$. For example, if $\Theta(z) \approx \omega z/\bar{V}$, the transit angle function $\Phi_{\Delta j} \approx \sin\Theta_L/\Theta_L$, where $\Theta_L = \Theta(L)$. Thus, for high values of the injected current, the radiation is observed if $\pi < \Theta_L < 2\pi$. The transit particles make a major contribution to the negative energy exchange with the rf field. Hence, it follows, in particular, that oscillations may be excited in a planar vacuum diode. The transit angle function for $j_{in} \approx j_{cr2}$ at $\Theta(z) \approx \omega z/\bar{V}$ is shown in Fig. 1. Under these conditions, the rf conductivity of the gap becomes negative at $\Theta_L > \pi$ and is minimal at $\Theta_L \approx 2\pi$.

Another mechanism behind oscillation excitation in the vircator is the inertial bunching of the particles under the action of the rf field. For the transit particles, this can occur through the monotronic effect; the particles reflected may exchange energy with the rf oscillations at smaller transit angles as well, $0 < \Theta_L < 2.5\pi$. Taking into account the contribution from both the transit and reflected particles to oscillation excitation and assuming that $L \approx \beta\lambda$ or $\Theta_L \approx \pi$, one finds from the solution of the stationary problem that

$$\frac{\langle\Delta\varepsilon/\varepsilon_{in}\rangle_{\Theta_0,\Delta V}}{\langle\Delta\varepsilon/\varepsilon_{in}\rangle_{\Theta_0,\Delta j}} \approx \frac{\frac{1}{\beta_0}\frac{\partial\beta}{\partial\gamma}}{\frac{1}{j_{cr1}}\frac{\partial j_{cr1}}{\partial\gamma}}$$

$$\approx \begin{cases} \dfrac{1}{(\gamma_0-1)^{1/2}} \gg 1 & \text{for} \quad (\gamma_0-1) \ll -1 \\ \dfrac{1}{\gamma_0^2} \ll 1 & \text{for} \quad \gamma_0 \gg 1. \end{cases}$$

Hence, it follows that the inertial bunching of the particles may be responsible for the excitation of oscillations in a one-gap vircator if the electrons are initially nonrelativistic. For small transit angles ($\Theta_L < 2.5\pi$), the particles reflected from the VC make a major contribution to energy exchange. For relativistic energies, when the particle velocity varies insignificantly because of the interaction with the rf field, the oscillations may occur through current modulation, which in turn is caused by the oscillation of the VC potential. At $j_{in} \approx j_{cr2}$, the particles reflected are responsible for the oscillations in a wide range of transit angles. For $j_{in} \gg j_{cr2}$, the transit particles may cause the oscillations. The oscillations can also be excited through current modulation in the rf field in the case of nonrelativistic electrons, when the VC does not form. An example is a Barkhausen–Kurz oscillator [10], where rf-field-accelerated transit particles are absorbed by the electrode being under the cathode potential and field-decelerated particles oscillate in a potential well near the unbiased grid.

Now let a vircator have two gaps of length L_1 and L_2, respectively, and let $L_1 \ll L_2$. In this case, the VC exists only in the second gap. We also assume, as before, that the gaps are elements of a high-Q resonator in which rf fields with amplitudes E_1 and E_2 coexist. The field in the second gap is out of phase by $\Delta\varphi$ relative to the field in the first gap. It is assumed that the change in the particle velocity due to the rf field is insignificant and transit angles are small. Then, for the particle crossing both gaps, the change in its energy under the action of the field is

$$\Delta\tilde{\varepsilon}_{tr} \approx \Delta\tilde{\varepsilon}_1 + \Delta\tilde{\varepsilon}_2 \approx e^{i\Theta_0}(eE_1L_1 + eE_2L_2e^{i\Delta\varphi}).$$

In this approximation, the change in the reflected particle energy is small compared with that in the transit particle energy; i.e., $\Delta\varepsilon_{ref} \ll \Delta\varepsilon_{tr}$. The probability that the particle will cross the second gap depends on the change in its energy near the VC and also on the energy at the exit from the first (modulating) gap. From the solution of the stationary problem, it follows that

$$\Delta\tilde{W}_{tr} \approx \frac{j^0_{out}}{j_{in}j^0_{cr1}}\frac{\partial j^0_{cr1}}{\partial\gamma}\frac{2(j^0_{out}/j^0_{cr1})^{1/2}\Delta\tilde{\varepsilon}_1 + \Delta\tilde{\varepsilon}_2}{mc^2}.$$

Then,

$$P_{\Delta j} \approx \frac{S_b}{2e}\frac{j^0_{out}}{j^0_{cr1}}\frac{\partial j^0_{cr1}}{\partial\gamma}\frac{|eE_1L_1|^2}{mc^2}\Phi_{\Delta j}(\alpha, \Delta\varphi),$$

where $\Phi_{\Delta j}(\alpha, \Delta\varphi) = 2\sqrt{j^0_{out}/j^0_{cr1}} + \alpha(1 + 2\sqrt{j^0_{out}/j^0_{cr1}})\cos\Delta\varphi + \alpha^2$ and $\alpha = E_2L_2/E_1L_1$.

The function $\Phi_{\Delta j}(\alpha, \Delta\varphi)$ takes negative values at $1 < \alpha < 2\sqrt{j^0_{out}/j^0_{cr}}$ and $\Delta\varphi = \pi$. Its minimal value $\Phi^{min}_{\Delta j}(\alpha, \Delta\varphi) = -(1 - 2\sqrt{j^0_{out}/j^0_{cr1}})^2/4$ is attained at $\alpha \approx (1 + 2\sqrt{j^0_{out}/j^0_{cr1}})/2$. Thus, in a system with two gaps, oscillations may also occur at small transit angles. In this approximation, the transit particles take place in energy exchange. For the emission to arise, it is necessary that the change in the energy in the second gap be larger than in the first one. With this condition met, the particle energy is transferred to the electromagnetic field if the fields in the gap are out of phase by π. In this case, the first gap acts as a modulator of the electron flow. As the current injected grows, the linear efficiency of interaction drops: $\Phi^{min}_{\Delta j} \longrightarrow 0$ at $j^0_{out} \longrightarrow j^0_{cr1}/4$.

The finiteness of transit angles can easily be taken into account for $\alpha \ll 1$. In this case, it is sufficient to ignore the change in the particle energy due to the interaction with the rf field in the gap with the VC. If, in addition, $L_1\omega/\bar{V} \ll \pi$, we have

$$\Delta\tilde{\varepsilon}_{tr} \approx eE_1L_1e^{i\Theta_0}, \quad \Delta\tilde{\varepsilon}_{ref} \approx eE_1L_1e^{i\Theta_0}(1 - e^{i2\Theta_{z0}}).$$

The probability that the particle passes through the VC now depends on its energy at the exit from the first (modulating) gap:

$$\Delta\tilde{W}_{tr} \approx \frac{j^0_{out}}{j_{in}j^0_{cr1}}\frac{\partial j^0_{cr1}}{\partial\gamma}\frac{2\Delta\tilde{\varepsilon}_{tr}(j^0_{out}/j^0_{cr})^{1/2}}{mc^2}.$$

Thus,

$$P_{\Delta j} \approx \frac{S_b}{e}\left(\frac{j^0_{out}}{j^0_{cr1}}\right)^{3/2}\frac{\partial j^0_{cr1}}{\partial\gamma}\frac{1}{mc^2}\mathrm{Re}\{|\Delta\tilde{\varepsilon}_{tr}|^2 - \Delta\tilde{\varepsilon}_{tr}\Delta\tilde{\varepsilon}^*_{ref}\}.$$

In this approximation, the transit particles always absorb the energy of the rf field. The electromagnetic field may gain only the energy of the particles reflected from the VC. The efficiency of interaction is maximal when $2\Theta_{z0} = \pi$. When the value of Θ_{z0} is optimal, the particles accelerated in the modulating gap are further accelerated when being reflected from the VC, while those decelerated lose more energy. On average, the energy exchange is negative because the density of the backward current due to the decelerated particles is higher than the current density of the accelerated ones. It is obvious that for $\alpha \ll 1$, the phase shift of the rf field between the gaps influences the process of energy exchange insignificantly.

Next, in the same approximation, we will include the spatial oscillations of the VC, assuming that they are small. The mechanism of these oscillations is similar to that behind oscillations in a reflex klystron [11]. Then,

$$\Delta\tilde{\varepsilon}_{ref} \approx (eE_1L_1)e^{i\Theta_0}[(1 - e^{i2\Theta_{z0}}) - i2\Delta\Theta_{z0}e^{i2\Theta_{z0}}],$$

where $\Delta\Theta_{z0}$ is the change in the particle transit angle due to the VC spatial oscillations, which result from the energy change in the modulating gap. In this case, we have

$$P_{\Delta z} \approx \frac{S_b(j_{in} - j^0_{out})}{e}\frac{\partial(z_0/L_2)}{\partial\gamma}\frac{(eE_1L_1)^2}{mc^2} \times \frac{L_2}{z_0}\Theta_{z0}\sin(2\Theta_{z0}).$$

As for a reflex klystron, the energy exchange is maximal when $2\Theta_{z0} = 3\pi/2$. The total efficiency of interaction is thus

$$\eta_\Sigma \approx \frac{1}{j_{in}}\left(\frac{j^0_{out}}{j^0_{cr1}}\right)^{3/2}\frac{\partial j^0_{cr1}}{\partial\gamma}\frac{|eE_1L_1/mc^2|^2}{(\gamma_{in} - 1)} \times [\cos(2\Theta_{z0}) + \mu\Theta_{z0}\sin(2\Theta_{z0})].$$

When $j_{in} \approx 2j^0_{cr1}$, the coefficient $\mu \approx 2$. The transit angle function for this case is shown in Fig. 2. It is seen that when $j_{in} \approx j_{cr2}$ and $\alpha \ll 1$, oscillations in the vircator may be due to both the oscillations of the VC potential

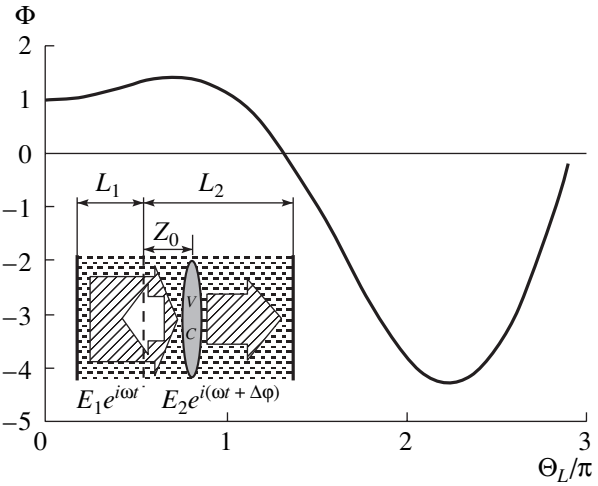

Fig. 2. Transit angle functions for a two-gap vircator at $\alpha \ll 1$ and $j_{in} \approx j_{cr2}$.

and the VC spatial oscillations. When the current injected is high, the oscillations in the vircator may arise only in overmoded systems, where $L_2 \gg \lambda$. In this case, the effect of a reflex klystron dominates in inducing the oscillations, since at $j_{in} \gg j^0_{cr1}$,

$$\mu\Theta_{z0} \approx \sqrt{2}\frac{\Theta_{z0}L_2}{z_0}\left(\frac{j_{in}}{j^0_{cr1}}\right)^{1/2} \gg 1.$$

If $L_2 \approx \lambda$, the transit angle Θ_{z0} decreases as the current injected grows, so that the oscillations cannot be induced.

At $\alpha \approx 1$ and $\alpha z_0/L_2 \ll 1$, the probability that the particle will pass through the VC depends, as in the previous case, on the change in its energy in the modulating gap. Yet, since $\alpha \approx 1$, it is necessary to take into consideration the field–transit particle interaction in both the first and second gaps. In this case, the transit angle function (without considering the effect of a reflex klystron) can be given by

$$\Phi_{\Delta j} \approx \mathrm{Re}\{e^{i2\Theta_{z0}} + \alpha e^{i\Delta\varphi} f(L_2)\}.$$

In particular, for $\Theta(z) = \omega z/\bar{V}$, we have

$$\Phi_{\Delta j} \approx -(1 - \cos 2\Theta_{z0}) + \left[1 + \alpha\cos(\Delta\varphi + \Theta_{L2}/2)\frac{\sin\Theta_{L2}/2}{\Theta_{L2}/2}\right].$$

The first two terms are due to the interaction of the electromagnetic field with the particles reflected; the other two, with the transit particles. The former particles are seen to transfer the energy to the field at any transit angle. The result of the interaction between the transit particles and the rf field depends on the phase shift between the stages (gaps) and on the value of α. For $\Delta\varphi = 0$ and $\alpha < 4.7$, the transit particles absorb the energy at any transit angle. If $\Delta\varphi = \pi - \Theta_{L2}/2$ and

$$\alpha > \alpha_{cr} = \frac{\Theta_{L2}/2}{\sin\Theta_{L2}/2}$$

the transit particles, along with those reflected, can transfer the energy to the field. At $\Theta_{z0} \ll \pi$, the transit particles alone interact with the field.

If $\alpha z_0/L_2 \gg 1$, the modulating gap has a minor effect on the oscillation excitation and the two-gap systems becomes close to the single-gap one in properties.

NUMERICAL SIMULATION WITHIN THE ONE-DIMENSIONAL MODEL: HIGH-EFFICIENCY CONDITIONS

The energy exchange between a VC-containing electron beam and high-strength rf fields in the one- and two-gap systems was simulated with the PIC one-dimensional model, which separately takes into account space-charge and rf fields. The former field was determined self-consistently in the potential approximation. The amplitude and phase of the rf field, as well as the injected electron energy ε_{in} and the injected current density j_{in}, were specified. The microwave efficiency was determined by summing the works done by the rf field on all beam particles over a time interval from the instant of injection to the instant of absorption by the electrodes or a foil. Having compared this sum with the total energy lost by the particles, we arrived at the conclusion that the conservatism of the computational scheme in terms of energy is quite adequate (≈10%).

For the current slightly exceeding the critical value and moderately relativistic electrons injected ($\gamma \approx 2$), the maximal microwave efficiency (≈12%) in the one-gap system with the VC is reached when the accelerating parameter is

$$a = \frac{eEL}{mc^2(\gamma_0 - 1)} \approx 3$$

and the transit angle of the particles passing through the gap in the rf field is undisturbed:

$$\Theta_L = \frac{\omega L}{c\beta_0} \approx 2\pi.$$

This value of the transit angle is close to that observed when the oscillations are excited by modulating the current passing through the VC (Fig. 1). It is nearly twice as large as the transit angle corresponding to the resonance of an electron beam with a relaxation frequency f_r.[1] Under the maximum-efficiency condi-

[1] The frequency of relaxation oscillations arising when the equilibrium current passes in a high-current system, depends on the characteristic time of space charge accumulation. In an ordinary diode, this is the time of electron transit through the gap. In the presence of a VC, the relaxation frequency depends on the time it takes for injected electrons to transit to the VC and back.

tions, the positive contribution to the energy exchange comes from reflected particles. Those transmitted make a negative contribution, which is usually small. Mainly particles having started in the latter half of the decelerating phase or in the former half of the accelerating phase of the rf field undergo reflection.

For the two-gap system, one-dimensional calculations were performed for the case when the current was in a slight excess of the second critical value in the second gap with $L_1 = (0.1–0.2)L_2$. Two simple situations for the VC-reflected particles were simulated. In the first case, a gap-separating foil completely transmitted the particles in both directions. In the second one, the particles crossing the foil in the negative direction were excluded from the calculations.

If the partial rf fields in the stages of the two-gap vircator are phase-shifted, the distribution of the composite rf field along the electron path is more favorable to current modulation and energy exchange. The calculations showed that for $\varepsilon_{in} = 500$ keV, the efficiency of the two-gap system may be thrice as high as that of the single-gap one. In addition, the maximal efficiency is observed when the oscillation frequency becomes equal to the frequency of VC relaxation oscillations, unlike the single-gap vircator. In what follows, we will consider just this case. The optimal phase shift $\Delta\varphi_{opt}$ depends on the transit angle of the electrons, decreases with increasing electron energy, and is virtually independent of conditions at the separating foil. For example, for $L_1 = 1$ cm, $L_2 = 5$ cm, and $j_{in} \approx 1.35j_{cr2}$, we have $\Delta\varphi_{opt} \approx 85°$ at $\varepsilon_{in} = 250$ keV, $\Delta\varphi_{opt} \approx 80°$ at $\varepsilon_{in} = 500$ keV, $\Delta\varphi_{opt} \approx 70°$ at $\varepsilon_{in} = 1$ MeV, and $\Delta\varphi_{opt} \approx 65°$ at $\varepsilon_{in} = 5$ MeV (in each of the cases, the field in the second gap leads in phase).

The foil conditions significantly affect the maximal efficiency value and the values of the accelerating parameters in the stages. For example, if $\varepsilon_{in} = 500$ keV, $\Delta\varphi = \Delta\varphi_{opt}$, and the foil-reflected particles are included, we have $\eta_{max} = 29\%$ at $a_1 = 0.45$ and $a_2 = 1.8$. If the foil-reflected particles are rejected, $\eta_{max} = 38\%$ at $a_1 = 1.05$ and $a_2 = 4.6$. In the other case of practical significance when the phase shift between the stages is absent, $\eta_{max} = 20\%$ at $a_1 = 0.4$ and $a_2 = 1.6$ and $\eta_{max} = 13\%$ at $a_1 = 0.55$ and $a_2 = 1.7$. This means that, in this case, the rejection of the foil-reflected particles deteriorates the efficiency. It should be noted that the conditions with the optimal phase shifts feature the narrowest operating range of the ratio a_2/a_1.

When the current is in a fixed excess of the critical value, $f = f_r$, and the foil conditions are the same, the dependence of the efficiency on the accelerating parameters and its absolute value vary insignificantly in a wide range of electron energies (from $\gamma_{in} \approx 1.5$ to $\gamma_{in} \approx 10$).

With the optimal accelerating parameters, the positive values of the efficiency roughly correspond to the phase shift in the range $-\pi/2 < \Delta\varphi < \pi/2$ and are attained

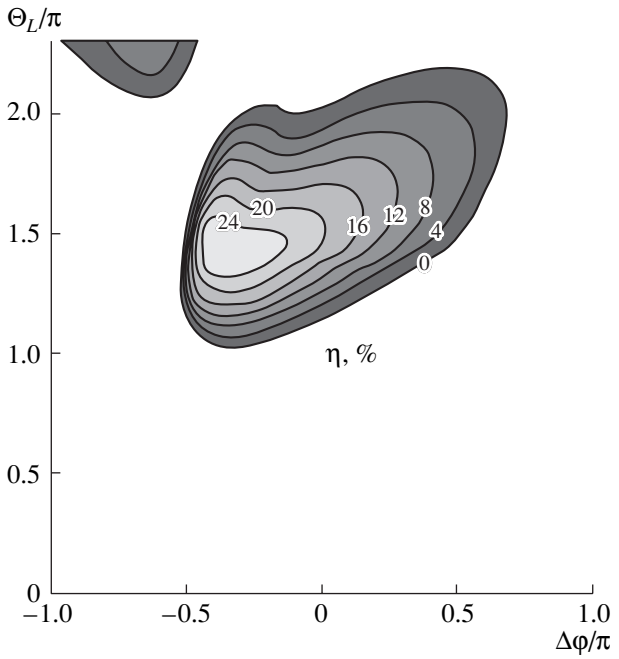

Fig. 3. Microwave efficiency of the two-gap vircator as a function of the phase shift between the rf fields in the stages and the undisturbed transit angle of electrons. $a_1 = 0.4$, $a_2 = 1.6$ (with foil-reflected particles included).

in a relatively wide range of transit angles (Fig. 3). Thus, it is hoped that the oscillation frequency in the real vircator can be varied by appropriately tuning the electrodynamic system with fixed electron beam parameters.

Under the high-efficiency conditions, the rf fields of the space charge of the electron beam have a decisive effect on the energy exchange dynamics. The electrons having lost the energy in the first gap reach the collector for the most part. The positive contribution to the energy exchange with the wave is made largely by the VC-reflected particles, while the efficiency of the particles transmitted is small and can be negative.

THE DESIGN OF THE VIRCATOR

The basic factor specifying the design of a two-stage vircator is the phase shift between the rf fields over the electron path in the stages. The conditions with the optimal phase shift ($\Delta\varphi \approx \pi/2$) can be established by using traveling-wave electrodynamic systems. In resonant electrodynamic systems, the situation with equiphase fields ($\Delta\varphi = 0$) is of interest.

We tried to realize the condition of equiphase fields in the vircator described below. Its electrodynamic system consists of two rectangular waveguides coupled by a rectangular hole (Fig. 4). The operating mode is the lowest TE_{10} mode. The analytical field pattern presented in Fig. 4 arises when the resonator is excited by a linear current source placed across the second gap. In

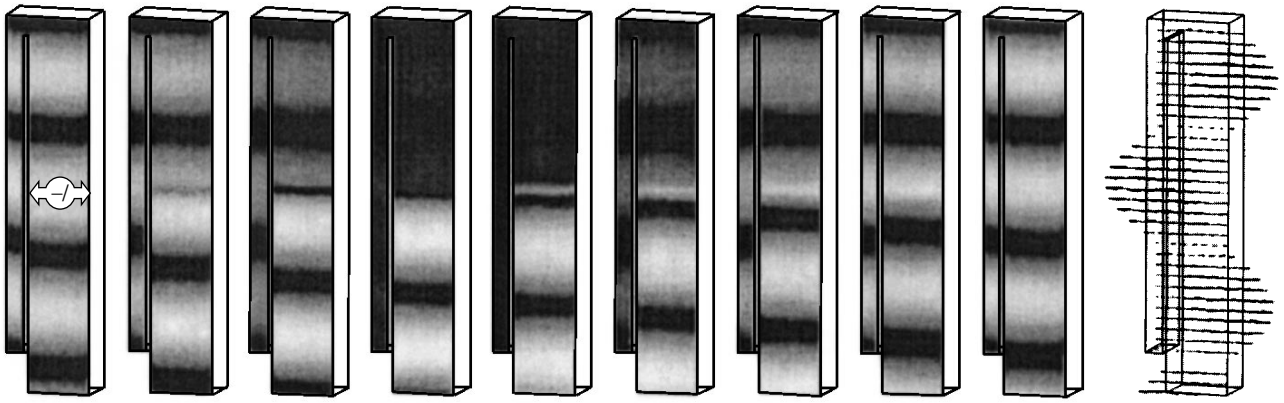

Fig. 4. Analytically derived evolution of the amplitude distribution of the electric field in the cross-sectional midplane of the electrodynamic system during the half-period of rf oscillations (with a step of 20°) under excitation by the given linear current source. The vector map corresponds to the last time instant.

this configuration, the oscillation in the first and second stages behind the current source has the form of a standing wave, and the radiation is extracted from the second stage in the form of a traveling wave (downward in Fig. 4). In the real system, a circular electron beam is passed through the antinodes of the field.

The sizes of the resonator were selected as follows. First, to avoid the formation of a VC in the first gap, its length must be much less than the length of the second gap (≈1/5). Second, to minimize the operating current density (which is desirable for the formation of a high-current beam in a vacuum diode and its transport through a resonator with separating foils or grids) and to make the shape of the electron beam in the gaps of the resonator as close to planar as possible, the diameter of the beam was taken approximately equal to the length of the second gap, $D_b \approx L_2$. This, in turn, limits the transverse dimension of the waveguide stages from below by a value of $\sim 2L_2$. The width of the waveguides ($\sim 0.7\lambda$) was taken such that it coincided with the guide half-wavelength at the operating frequency. Under such conditions, the scale of the transverse nonuniformity of the rf field, which has the sinusoidal distribution in the X and Y directions, was the same along both coordinates. Unfortunately, with all these requirements satisfied, the operating frequency of the vircator was found to be somewhat lower than the undisturbed relaxation frequency of the VC (2.7 GHz against ≈4 GHz) and the microwave efficiency was poor. The width and the position of the coupling hole were selected such that the rf field strengths in the gaps were approximately the same at the operating frequency, $E_1 \approx E_2$.

The preliminary optimization of the vircator parameters was made with the 3D version of the KARAT PIC code [12]. The vircator was simulated in combination with a vacuum diode. In a simplified variant, an electron beam with given parameters was injected into the resonator [7, 8]. The microwave amplitude was shown to resonantly depend on the vacuum diode impedance (the optimal value ≈60 Ω, an excess of ≈30% over the critical current) and adjustable parameters of the resonator (the positions of the pistons, the size and the position of the coupling hole). For the oscillations excited by the rectangular current front, the build-up time was found to be 15 oscillation periods and the radiation had a narrow spectrum. The oscillation frequency depended on the vacuum diode impedance only slightly (it differed by no more than 4% when the impedance was changed by 50%), and the microwave efficiency was kept at 10–12% in a wide range of electron beam powers.

It was demonstrated that the oscillation frequency can continuously be tuned in a half-power bandwidth of ≈20% by varying the geometric dimensions of the resonator with the electron beam parameters remaining unchanged.

EXPERIMENTAL RESULTS

Figure 5 shows the experimental scheme. An electron beam is formed in a planar vacuum diode with the explosive field-emission cathode in the absence of an external focusing magnetic field and is injected into a two-stage resonator with gaps of length $L_1 \approx \lambda/8$ and $L_2 \approx \lambda/2$, respectively. The beam is transported through two highly transparent thin foils or grids. The former separates the diode from the first stage, while the latter is placed between the stages. The TE_{10} operating mode of the vircator is radiated in the form of a quasi-Gaussian beam into open space by means of a horn antenna with an aperture of about 8λ.

In the first stage, the TE_{10} mode has three variations in the transverse direction with respect to the beam axis (along the waveguide). The resonant frequency was varied by varying the waveguide length through changing the positions of the adjustable pistons. Electrodynamic measurements of the resonator parameters were made with a panoramic meter of S parameters. The res-

onator was excited using a short pin located in the first stage along the electron beam axis. The results of tuning the resonant frequency of the TE_{103} mode are depicted in Fig. 6 (curve *b*). The resonant frequencies of the neighboring modes TE_{102} and TE_{104} are offset by approximately 15% from the TE_{103} resonant frequency. The *Q* factor of the TE_{103} mode depended on the size of the coupling hole and was found to be about 40 at the operating frequency for the optimal size of the hole. In this case, the electric field strengths in the stages were nearly the same.

The performance of the vircator was investigated in a SINUS-7 pulsed–periodic accelerator (a pulse half-width of 50 ns, electron energy to 2 MeV, beam current to 20 kA, and pulse repetition rate to 100 Hz) [13]. The electron beam was generated with the use of a metal-covered insulating cathode having a screening electrode and a diameter of the emitting area of $\approx\lambda/2$.

The parameters of the microwave pulses (power, shape, and spectrum) were measured by several dipole antennas with different effective areas. The antennas were calibrated with an HP8510 meter of *S* parameters. Microwave signals from the antennas were either detected or applied directly to an HP5472D wide-band oscilloscope. The radiation total power was determined by summing over the radiation pattern. The energy of a microwave pulse was measured with a calorimeter similar to that described in [14]. The calorimeter was integrated into a 20 × 30-cm rectangular overmoded waveguide, filled with ethyl alcohol. In view of the calibration accuracy, the error in measuring the radiation power was no more than ±20%.

In the experiments, the vircator was tuned to a maximal power and a desired oscillation frequency by varying the gap width in the diode and resonator parameters. When the gap was wide (the diode impedance high), the current was insufficient for the formation of a VC and the radiation was absent. The optimal width of the gap was observed when the current exceeded the critical value for the second stage by 30%. This is consistent with the results of numerical simulation. When the current injected was too high, the radiation power decreased considerably and the spectrum broadened. In this case, regular microwave oscillations in the vircator were absent. The presence of the optimal current is apparently associated with both the nonuniform distribution of the potential along the beam radius and a change in the VC position in response to that in the vacuum diode impedance.

Under the optimal oscillation conditions (the voltage across the diode 1 MV, the electron beam current 19 kA), the radiation power of the vircator was ≈1GW at an efficiency of about 5%; the oscillation frequency, 2.65 GHz; and the half-power duration of a microwave pulse, 25 ns. The radiation pattern corresponded to the radiation of the TE_{10} mode from the horn antenna. The radiation power density at the peak of the radiation pattern (3 m away from the antenna) was about

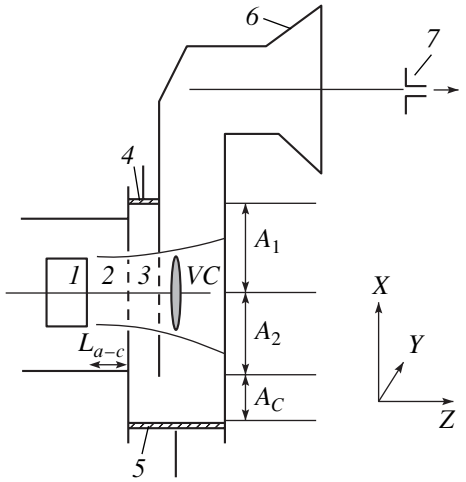

Fig. 5. Vircator design: (*1*) cathode; (*2*) vacuum diode; (*3*) modulating gap; (*4*, *5*) adjustable pistons; (*6*) radiating horn antenna; and (*7*) receiving antenna.

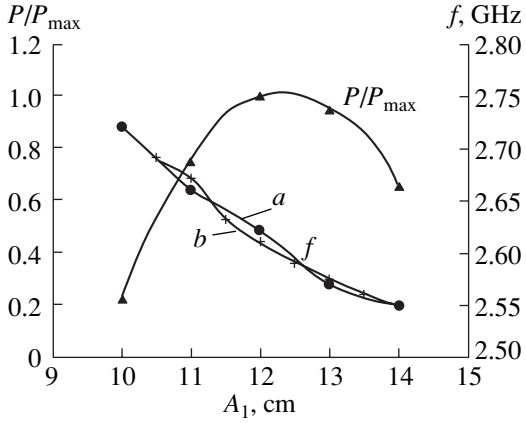

Fig. 6. Power and radiation frequency of the vircator vs. piston position (*a*, experiment; *b*, electrodynamic measurements).

60 kW/cm^2; the energy of a microwave pulse measured with the calorimeter, 20 J.

The experimental microwave efficiency was defined as the ratio of the peak microwave power to the electron beam power calculated with regard for the total current in the vacuum diode. However, as follows from the measurements, from 30 to 50% of the current through the diode is accounted for by the stray current, which passes from the stainless steel focusing electrode surrounding the working area of the cathode. This current was picked up by the collimating diaphragm at the entrance to the vircator and did not contribute to the microwave oscillations. The efficiency calculated in terms of the useful current was found to be 8–10%, which approaches the theoretical value.

The radiation maximal power was reached when the coupling hole width was $A_c \approx \lambda_w/30$ (λ_w is the wavelength in the waveguide). As follows from the electro-

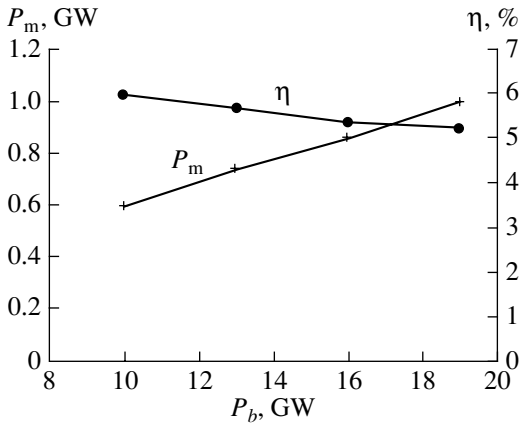

Fig. 7. Experimental dependence of the power and efficiency of the vircator on the electron beam power.

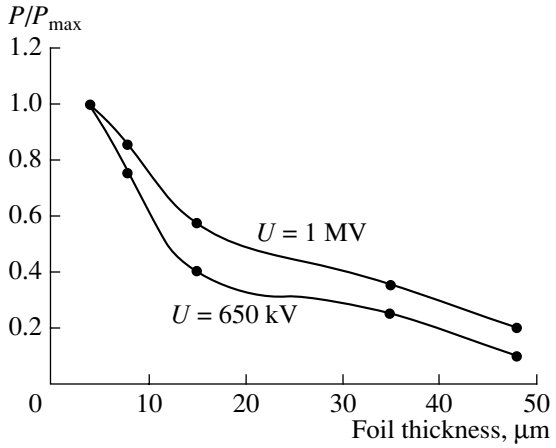

Fig. 8. Radiation power vs. foil thickness for different voltages across the vacuum diode.

dynamic analysis and measurements, under these conditions, the fields in the stages roughly equal each other and $a_2/a_1 \approx 4$. The efficiency of the vircator varied with the electron beam power insignificantly (Fig. 7). The slight increase in the efficiency to 6% as the beam power diminishes to 10 GW was due to the fact that the loss of the current from the screening electrode decreases at lower voltages across the diode. During a radiation pulse, the impedance of the vacuum diode decreased roughly by a factor of 1.5. This is typical of diodes with explosive field-emission cathodes in the absence of an external magnetic field. The increase in the current during a pulse is likely to be associated with the growth of the emission centers on the cathode surface and also with an increase in their number [15]. The expansion of the cathodic plasma into the gap may also be a factor. However, the oscillograms indicate that the radiation frequency remains unchanged during a pulse.

The radiation frequency was varied by varying the position of piston *4* of the modulating stage and the position of the coupling hole. The dependence of the radiation frequency on the spacing A_1 between piston *4* and the beam axis is shown in Fig. 6 (curve *a*). This curve agrees well with the results of electrodynamic measurements (curve *b*). This confirms the fact that the oscillation frequency of the vircator depends on the resonator parameters when the supercriticality of the current is small. The oscillation frequency tuning bandwidth was extended to 15% by simultaneously varying A_1 and A_2 in such a way that the antinode of the electric field was near the beam axis all the time; i.e., $A_1 \approx A_2 \approx 3\lambda_w/4$. The width of the coupling hole remained constant.

Figure 8 shows the dependence of the microwave power on the thickness of the aluminum foil separating the stages for different diode voltages and a fixed diode impedance. At a voltage of 1 MV, the radiated power drops twofold when the foil is 15 μm thick. The relatively rapid drop of the power can be explained by the considerable effect of the foil on the motion of slow electrons existing in the electrodynamic system when they interact with high rf fields. At a lower voltage of 650 kV, the decline of the oscillation power with increasing foil thickness was still faster. Similar experimental dependences were observed in works cited in the review [6]. The dependence of the oscillation power on the thickness of the foil that separates the diode from the modulating stage is much weaker. At the thickness 15 μm and the diode voltage 1 MV, the decrease in the power was about 30%.

The electron beam structure was judged from its print (image) on a polymer film. The transverse distribution of the current at the entrance to the system was fairly uniform, becoming ring-shaped at the collector. We carried out experiments on taking the distribution of the collector current of the beam where some of the electrons having passed through a small hole on the collector struck the central conductor of a coaxial line with a wave impedance of 50 Ω. The signal obtained was attenuated and then applied to the wide-band oscilloscope. The position of the hole could be varied. Both the dc and rf components were detected in the collector current. The frequency of current modulation coincided with the frequency of the microwave radiation. The rf current modulation started 15–20 ns after the beginning of the pulse. This time corresponds to the time of oscillation build-up in the vircator. The distribution of the dc component had the form of a ring diffusing during the pulse. The maximum of the distribution of the relative rf current value was near the beam axis. The maximal depth of electron current modulation was found to be 70–80%.

Using a dm-wave vircator built around the SINUS-7 accelerator, we succeeded in generating trains of pulses in the periodic regime. In this regime, tungsten grids with a mesh size of 0.5 × 0.5 mm and a geometrical transparency of about 0.9 were used instead of the stage-separating aluminum foil. The radiation power in each of the pulses was about 100 MW; the pulse dura-

tion, 20–25 ns. The number of pulses per train was selected so as not to destroy the stage-separating grid and equaled 50 and 400 for pulse repetition rates of 50 and 20 Hz, respectively.

CONCLUSION

Our study makes it possible to draw conclusions about the basic mechanisms behind microwave oscillation in VC-containing devices. At the stage of excitation, these are (i) direct current modulation, associated with VC potential oscillation in the rf field; (ii) electron bunching similar to that in a reflex klystron due to the oscillation of the VC position; and (iii) inertial bunching of reflected particles. For relativistic electrons, the last-named mechanism is of minor importance. At large amplitudes of the rf field, the efficiency is limited by the finite phase width of the modulated electron beam, as in other microwave devices.

Theoretically, the use of a two-gap electrodynamic system in a vircator makes it possible to raise the microwave efficiency to ≈20% (≈40% in the one-dimensional model). This can be achieved by shifting the phases of the rf oscillations in the stages (and, thus, by setting the more favorable distribution of the rf field along the electron path). This value is more than thrice as high as the efficiency of a one-gap system under identical conditions. The considerable (≈20%) bandwidth of electron susceptibility near the relaxation frequency gives a chance to alter the oscillation frequency by appropriately tuning the electrodynamic system.

In experiments, such a high value of efficiency is difficult to reach because of the need for simultaneously satisfying a number of interrelated physical conditions (appropriate gap width, rf field phasing, ratio of the rf amplitudes in the stages, as well as the formation of a high-current electron beam with desired parameters).

Based on the results of numerical simulation performed with the 3D version of the electromagnetic PIC-code KARAT, we developed a prototype of a two-stage vircator for an external magnetic field with equiphase fields in the stages. In the experiments with the high-current dm-wave pulsed–periodic electron accelerator, we realized single-mode oscillation of power up to 1 GW and a duration of ≈25 ns. The associated efficiency was ≈5% and remained almost invariable when the electron beam power was varied. Factors limiting the efficiency were found to be substantial current losses in the vacuum diode and the drift of the beam parameters during a pulse. The oscillation frequency remained constant both during a pulse and from pulse to pulse, suggesting the decisive effect of the electrodynamic system. We succeeded in continuously tuning the oscillation frequency of the vircator in a half-power bandwidth of ≈15% by varying the resonator parameters.

ACKNOWLEDGMENTS

We sincerely thank M. I. Petelin for encouraging discussions.

The fruitful cooperation with V.P. Tarakanov, the author of the KARAT code, is greatly appreciated.

REFERENCES

1. A. N. Didenko, V. P. Grigor'ev, and A. G. Zherlitsyn, *Plasma Electronics* (Naukova Dumka, Kiev, 1989), p. 112.
2. A. A. Rukhadze, S. D. Stolbetsov, and V. P. Tarakanov, Radiotekh. Élektron. (Moscow) **37**, 385 (1992).
3. V. D. Selemir, B. V. Alekhin, V. E. Vatrunin, *et al.*, Fiz. Plazmy **20**, 689 (1994) [Plasma Phys. Rep. **20**, 621 (1994)].
4. N. P. Gadetskiĭ, I. I. Magda, S. I. Naĭsteter, *et al.*, Fiz. Plazmy **19**, 530 (1993) [Plasma Phys. Rep. **19**, 273 (1993)].
5. W. Jiang, K. Woolverton, J. Dickens, and M. Kristiansen, IEEE Trans. Plasma Sci. **27**, 1538 (1999).
6. V. L. Granatstein and I. Alexeff, *High-Power Microwave Sources* (Artech House, Boston, 1989).
7. S. D. Korovin, I. V. Pegel, S. D. Polevin, and V. P. Tarakanov, in *Proceedings of the 11th International Pulsed Power Conference, Baltimore, 1997*, p. 736.
8. S. A. Kitsanov, A. I. Klimov, S. D. Korovin, *et al.*, in *Proceedings of the 1st International Congress on Radiation Physics, High Current Electronics, and Modification of Materials, Tomsk, 2000*, Vol. 2, p. 423.
9. V. S. Voronin, Yu. T. Zozulya, and A. N. Lebedev, Zh. Tekh. Fiz. **42**, 546 (1972) [Sov. Phys. Tech. Phys. **17**, 432 (1972)].
10. E. W. B. Gill and J. H. Morrell, Philos. Mag. Suppl. **44** (259), 161 (1992).
11. V. N. Shevchik and D. I. Trubetskov, *Analytical Methods of Analysis in Microwave Electronics* (Sov. Radio, Moscow, 1970).
12. V. P. Tarakanov, *User's Manual for Code Karat* (BRA, Springfield, 1992).
13. S. D. Korovin and V. V. Rostov, Izv. Vyssh. Uchebn. Zaved., Fiz., No. 12, 21 (1996).
14. A. G. Shkvarunets, Prib. Tekh. Éksp., No. 4, 72 (1996).
15. S. Ya. Belomyttsev, S. D. Korovin, and I. V. Pegel', Zh. Tekh. Fiz. **69** (6), 97 (1999) [Tech. Phys. **44**, 695 (1999)].

Translated by V. Isaakyan

Technical Physics, Vol. 47, No. 5, 2002, pp. 604–607. Translated from Zhurnal Tekhnicheskoĭ Fiziki, Vol. 72, No. 5, 2002, pp. 91–94.

**SURFACES,
ELECTRON AND ION EMISSION**

Low-Temperature Ion Emission

V. I. Batkin* and O. Ya. Savchenko**

** Institute of Solid-State Chemistry and Mineral Processing, Siberian Division, Russian Academy of Sciences, ul. Kutateladze 18, Novosibirsk, 630128 Russia*

*** Institute of Chemical Kinetics and Combustion, Siberian Division, Russian Academy of Sciences, Novosibirsk, 630090 Russia*

e-mail: Batkin@solid.nsc.ru

Received June 21, 2001

Abstract—The kinetics of alkali metal ion emission from metal surfaces heated to temperatures of 800–2500 K is studied. The ion current relaxation is described by the relationship $I = Ae^{-B\sqrt{t}} + C/\sqrt{t} + I_0$. After the relaxation, the ion emission is recovered when the surface is exposed to H_2O at room temperature. The nature of the phenomenon is discussed. © *2002 MAIK "Nauka/Interperiodica".*

The emission of alkali metal ions from a tungsten wire heated in a vacuum was first observed as early as at the beginning of the 20th century [1]. Later, this phenomenon was repeatedly described in the 1960s [2, 3] but has not been studied in detail because of the poor reproducibility of results. Recent works [4, 5] are the only publications concerning the dynamics of thermionic emission. However, they are devoted to ion current noise. The kinetics of ion emission has remained poorly understood. This process can form the basis for sensitive methods of surface investigation and deserves more attention. This paper is an attempt to fill the gap. We quantitatively describe the ion current response to emitter heating and discuss a mechanism of ion emission. The emission of impurity alkali ions from Pt, W, and Mo in a vacuum and from Nichrome alloy in air at emitter temperatures of 800–2500 K was studied. It has been found that preliminary moistening of the metal surface at room temperature and rapid cooling of samples are necessary to provide reproducible observations.

The experimental setup consisted of a locked vacuum chamber evacuated by magnetic-discharge pumps and an rf mass spectrometer with a resolution of 1 u. A metallic filament was used as an ion emitter. The temperature at the filament center was estimated from the filament current and voltage drop across the filament by numerically solving the thermal physical problem. References data from [6] were used. The emissivity taken from [6] was multiplied by a factor $k > 1$, which takes into account the surface contamination. For the primary annealing of the W filament, the factor k was taken to be equal to 1.1 and then was varied in the range 1.0–1.2.

Upon heating the unannealed filament to a temperature of about 1000 K, the current density of alkali metal ion emission lies between 10^{-7} and 10^{-6} A/cm^2. With time, the ion current I drops first rapidly and then slowly, reaching a level $I_0 = 10^{-3}$–10^{-4} of the initial value. Our experiments showed that the current decrease follows the time dependence

$$I = Ae^{-B\sqrt{t}} + C/\sqrt{t} + I_0. \quad (1)$$

The oscillograms of the K^+ current from the W filament at temperatures 1530 and 1760 K (represented by curves *1* and *2*, respectively) and from the Pt filament at 1430 K (curve *3*) are shown in Fig. 1. The curves are seen to be well approximated by Eq. (1). Note that the parameter B in the exponent may take two values (see, e.g., *2* and *3*); i.e., the relaxation with a higher B changes to a slower relaxation. The parameter C remained constant. The disadvantage of such experiments is that each time we had to deal with a new sample with the properties inevitably differing from those of the previous one. Moreover, the initially contaminated surface became clean at the end of the experiment. The regular current relaxation was sometimes disturbed by random current spikes. It was therefore necessary to devise a method providing reproducible ion emission from the surface.

It was noticed that the emissivity of metals increases after long-term exposure to air at room temperature. We examined the effect of air, dry N_2, H_2, and water vapor on a tungsten filament annealed in a vacuum at 2500 K and arrived at the conclusion that the influence of air is due to moisture. The effect is the highest for a single contact of the surface with H_2O in the liquid phase. The effect of surface wetting is retained after keeping the emitter at a pressure of 10^{-3} Pa for 1000 s. The adsorption of N_2 and H_2 by the emitter results in a short ion current peak with an amplitude ≈1/30 of that in the case of H_2O vapor.

1063-7842/02/4705-0604$22.00

The relaxation of the K^+ ion current from the activated surfaces of Nichrome (*1*), Pt (*2*), Mo (*3*), and W (*4*, *5*) is presented in Fig. 2. The emitters were first annealed up to the total relaxation of the ion current. After having been brought into contact with water at room temperature, they were heated to annealing temperatures of 1000, 1400, 1400, 1650, and 850 K, respectively. The experiments with the Nichrome alloy were carried out in air; with the metals (except for activation), at a pressure of 10^{-3}–10^{-4} Pa. The solid curves are the approximation of the data points by Eq. (1). The approximation parameters are listed in the table. The curve for the Nichrome has two portions with different parameters A and B. The emission of K^+ ions was observed at temperatures higher than 800 K. At very low temperatures, the stage of ion current growth (*5*) lasts $t > 1$ h (against $t < 1$ s at very high temperatures). This phase is followed by the current relaxation described by Eq. (1). Zero time in Eq. (1) coincides with the start of heating rather than with the onset of ion current. This indicates that the ion emission occurs in several stages. First, a heating product with a concentration specified by Eq. (1) forms; then, the ion emission limited by this product occurs. The effect of sample hardening observed by us confirmed indirectly that the ion emission is a multistage process. When the filament is rapidly cooled, ion emission is also observed, with the ion current relaxing in the same way as upon heating. The K^+ current as a response to the rapid cooling of the tungsten filament from 2300 to 1830 K (*1*) and from 2140 to 1830 K (*2*) is shown in Fig. 3. The ion current increases, reaches the approximation curve, and then follows it. The curve is described by Eq. (1) with the parameters $A = 13$, $B = 0.41$, $C = 0.297$, and $I_0 = 0.0055$. Time is measured from the start of cooling. The ion emission upon cooling is observed only if the initial emission takes place.

When the temperature varies rapidly, the ion current follows the Arrhenius law. The energy of activation E_a is high and takes several values for different samples of the same metal. For tungsten, the values of E_a were found to be $E_a = 2.27$, 3.33, and 4.58 eV. These values far exceed the energy of ion desorption, ≈1 eV [5, 7, 8], and remained constant after the sublimation of the oxide film during vacuum annealing and after the recovery of the ion emission by water. The ion source is apparently located at grain boundaries rather than on the sample surface. In this case, the value of E_a is the energy of ion emergence on the surface, while the observed kinetics of ion emission reflects the grain boundary relaxation after sample heating.

Numerical experiments show that function (1) is typical of the ion emission kinetics for various alkali metals. Kinetics (1) was observed under various changes in experimental conditions, for example, after a slight, by 30 K, increase in the temperature and after sharp cooling. In (1), the instant the conditions change is taken for the starting time. A number of factors (high

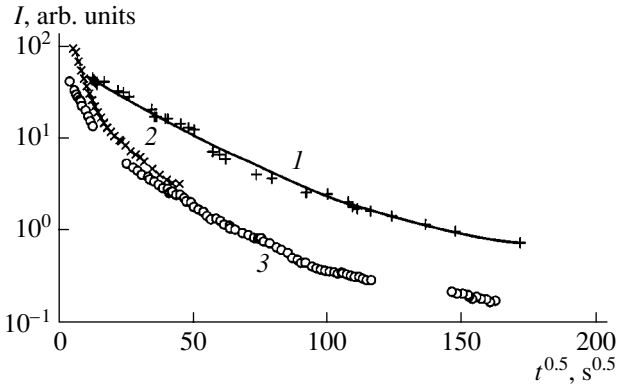

Fig. 1. Relaxation of the K^+ current from the heated filament: (*1*) W at 1530 K, (*2*) W at 1760 K, and (*3*) Pt at 1430 K.

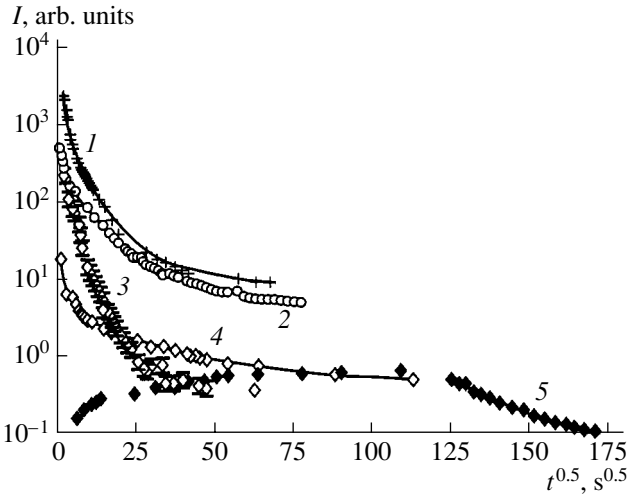

Fig. 2. Relaxation of the K^+ current from the heated filament annealed in a vacuum and brought in contact with H_2O: (*1*) Nichrome at 1000 K, (*2*) Pt at 1400 K, (*3*) Mo at 1400 K, and (*4*, *5*) W at 1650 and 850 K.

activation energy and insensitivity to the surface condition) allow us to consider kinetics (1) as a grain boundary phenomenon. The complexity of such phenomena under unsteady conditions and the lack of experimental data make it difficult to identify mechanisms responsible for the ion current relaxation observed. We will discuss possible explanations of our observations below.

The early stage of the ion emission occurs irrespective of whether the ions are present at the final stage of the process or not and specifies basic quantitative characteristics of the process. It is the early stage that is related with models discussed below. The term $C/\sqrt{t}$ in Eq. (1) is usually associated with diffusion. For platinum, the contribution of this term is shown by the thick curve in Fig. 4, while the total dependence $I(t)$ taken from Fig. 2 is shown by the thin line. The minor amount of the ions adsorbed on the surface and the regenerability of the emitter suggest that the ions come to the metal surface from localized sources. The ions are apparently

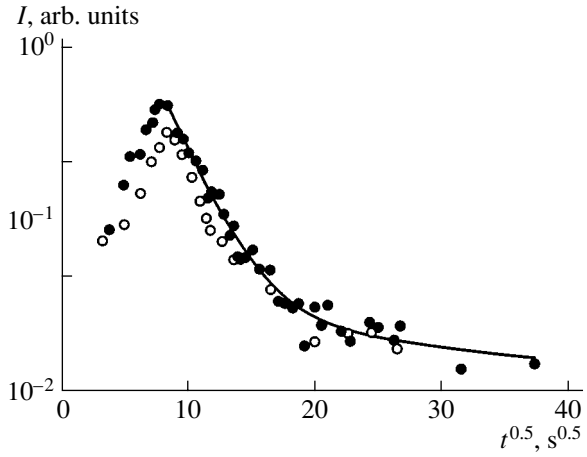

Fig. 3. Relaxation of the K^+ current from the W filament upon cooling (●) from 2300 to 1830 K and (○) from 2140 to 1830 K. Solid line, approximating curve.

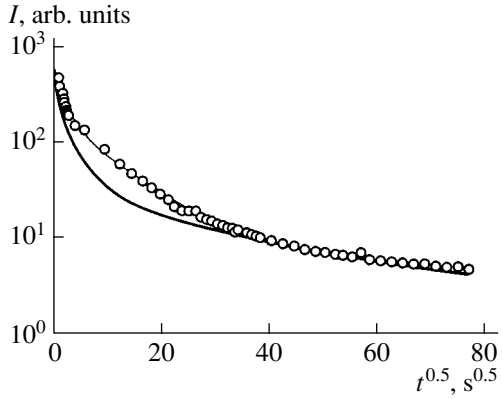

Fig. 4. Kinetics of the K^+ emission from platinum: thick curve, $\sim 1/\sqrt{t}$ component; thin curve, total current.

transported along the grain boundaries. The time dependence of the ion current, $\sim 1/\sqrt{t}$, may be associated with the behavior of vacancies, since the vacancy mechanism of grain-boundary diffusion is typical of metals [9]. After the emission peak, the vacancies concentrate at the grain boundaries and then diffuse into the grains. The origin of the term $\exp(-B\sqrt{t})$ is more difficult to explain.

The exponential term may be related to the differential equation

$$\frac{dn}{dt} = -\frac{a}{\sqrt{t}}n, \qquad (2)$$

which describes the reaction of particles with vacancies or another diffusant. To distinguish the process described by Eq. (2) from that yielding the diffusion term $C/\sqrt{t}$ in Eq. (1), we must assume that there are two kinds of particles near the surface that limit the ion flux to the surface. These particles are produced when the process conditions change rapidly. The first, predominant, kind diffuses into the material, while the second becomes inactive, having reacted with the first one. Under this assumption, the factor B in Eq. (1) is proportional to the amplitude C. This comes into conflict with the experimental results, whereby the higher C, the smaller B. The situation with three kinds of particles is too complicated. A model assuming the linearity of the process space seems to be more adequate. In such a space, a group of particles executes the Brownian motion. This may occur along a dislocation line or at a step on a crystal face. If the interaction between the particles removes them, their number decreases as $\sim 1/\sqrt{t + t_0}$. If the particles disappear, reacting with unsaturated absorption centers, their number relaxes as $\exp(-B\sqrt{t})$. For a chain of sites, the factor B equals $1.64n\sqrt{\nu}$, where n is the fraction of the sites occupied by the centers and ν is the frequency of jumps between the sites. Let us consider an example demonstrating both ways of relaxation. Let there be a set of vacancies where single vacancies coalesce to form extended steps. The number of single vacancies first decreases as $\sim 1/\sqrt{t + t_0}$, when the vacancies coalesce largely by pairs, and then as $\sim\exp(-B\sqrt{t})$. The superposition of the two kinetics leads us to the assumption that two kinds of particles forcing alkali metal ions to move toward the surface are responsible for them.

To conclude, we note that Eq. (1) is valid not only for the kinetics of alkali metal ion emission. It applies to more complicated processes as well. Work [10] considered the scattering of slow hydrogen and nitrogen

Table

No.	Metal	T, K	A	B	C	I_0
1	Nichrome	1000	1120 (7050)	0.212 (0.644)	465	2.11
2	Pt	1400	133	0.123	350	0
3	Mo	1400	249	0.284	17	0
4	W	1650	1.62	0.0347	16	0.33
5	W	850	944	0.0617	13.3	0

ions by a tantalum target and studied the relaxation of the scattering rate after pulsed heating of the target. It was found that relationship (1) approximates the data better than the dependence ~exp(–*kt*) accepted in [10].

ACKNOWLEDGMENTS

This work was supported by the Russian Foundation for Basic Research (grant no. 01-02-17535).

REFERENCES

1. W. Richardson, Proc. R. Soc. London **89**, 507 (1913).
2. M. Kaminsky, in *Advances in Mass Spectrometry*, Ed. by J. Waldron (Heydon and Son, New York, 1959; Inostrannaya Literatura, Moscow, 1963).
3. G. M. Pantsenkov and A. M. Koltsin, Dokl. Akad. Nauk SSSR **131**, 357 (1960).
4. L. Gladiszevwski, Int. J. Mass. Spectrom. Ion Processes **144**, 123 (1994).
5. L. Gladiszevwski and M. Wiertel, Electron Technol. **30**, 228 (1997).
6. *Handbook of Physical Quantities*, Ed. by I. S. Grigoriev and E. Z. Meilikhov (Énergoatomizdat, Moscow, 1991; CRC Press, Boca Raton, 1997).
7. H. Kawaro, K. Funato, S. Matsuc, *et al.*, Thermochim. Acta **299**, 67 (1997).
8. A. W. Adamson, *The Physical Chemistry of Surfaces* (Wiley, New York, 1976; Mir, Moscow, 1979).
9. I. Kaur and W. Gust, *Fundamentals of Grain and Interphase Boundary Diffusion* (Stuttgart, 1989; Mashinostroenie, Moscow, 1991).
10. V. I. Batkin, Zh. Tekh. Fiz. **70** (2), 106 (2000) [Tech. Phys. **45**, 247 (2000)].

Translated by M. Astrov

Technical Physics, Vol. 47, No. 5, 2002, pp. 608–614. Translated from Zhurnal Tekhnicheskoĭ Fiziki, Vol. 72, No. 5, 2002, pp. 95–101.

SURFACES, ELECTRON AND ION EMISSION

Effects of the Emission Charge Saturation in Photocathodes under Nonuniform Illumination

B. I. Reznikov* and A. V. Subashiev**

** Physicotechnical Institute, Russian Academy of Sciences, Politekhnicheskaya ul. 26, St. Petersburg, 194021 Russia*

e-mail: Boris.Reznikov@pop.ioffe.rssi.ru

*** St. Petersburg State Technical University, Politekhnicheskaya ul. 29, St. Petersburg, 195251 Russia*

e-mail: arsen@spes.stu.neva.ru

Received June 27, 2001

Abstract—Photoemission from a semiconductor having a negative electron affinity under nonuniform illumination is investigated theoretically for stationary and pulsed excitation regimes. The maximum emission current is shown to grow exponentially with increasing ratio of the negative electron affinity Δ_0 to a characteristic tunneling energy E_0, and the excitation intensity I_{opt} corresponding to the maximum current has been determined. Excitation nonuniformity results in a weakening of the dependence of the emission current on illumination intensity near the current maximum. The quantum efficiency recovery time measured in a two-pulse excitation mode depends weakly on the illumination intensity and on its nonuniformity over the illuminated spot and is close to the relaxation time of low photovoltages. © *2002 MAIK "Nauka/Interperiodica".*

INTRODUCTION

High-density electron beams obtained from GaAs photocathodes having negative electron affinity (NEA) are used in high-energy electron accelerators [1] and in semiconductor electron lithography [2]. Under intense optical excitation, saturation of the charge emission is observed caused by accumulation of electrons in a near-surface potential well in the space-charge region (SCR) and emergence of a photovoltage that decreases the NEA and impedes emission [3–5]. In earlier studies of the basic mechanisms of the effect of charge saturation, by means of numerical simulation [4, 6–8] and analytically [8], different assumptions concerning the restoring hole flux toward the surface were used; however, only uniform excitation was considered.

If the size of the illuminated spot is less than or close to the activated area of the photocathode, transverse distribution of the light intensity over the spot becomes substantial. In experiments on charge emission from photocathodes known to us, the light intensity distribution varied from an "incorrect" function, asymmetric relative to the beam axis [9], to a Π-shaped curve with 30% intensity variation over the beam cross section [10].

Also, nonuniform illumination intensity is used in the case where local excitation is utilized for preventing deactivation of the cathode by the backward flow of ions [11] and in measurements of the surface distribution of quantum yield [12]. The intensity nonuniformity should also be taken into account when the saturation effect is used in order to determine from experimental data such parameters of photoemitters as the surface barrier permeability and the magnitude of the NEA.

In the present paper, the emission problem is considered in the case of a nonuniformly distributed and intense excitation. Dependence of the emission current on the intensity of local excitation is studied in both stationary and pulsed regimes, and conditions are found for achieving a maximum current for excitation by a Gaussian beam typical of single-mode lasers [13].

1. A MODEL OF PHOTOEMISSION

1. Consider the photoemission from a working layer of thickness d of a semiconducting material with a surface SCR layer of thickness w activated to the NEA state. We assume that the illumination intensity I is nonuniformly distributed over the semiconductor surface and varies with distance from the illuminated spot center, $I = I(\rho)$, where ρ is the radial coordinate. The local density of emitted electrons q_{emi} and the total emission flux q_{tot} are equal, respectively, to

$$q_{emi} = q_w B_n, \quad q_{tot} = 2\pi \int_0^{\rho_{max}} q_{emi}(\rho)\rho d\rho, \qquad (1)$$

where q_w is the density of the electron flux toward the surface at the interface between the working region and the near-surface SCR layer and B_n is the probability of electron escape into vacuum from the near-surface potential well in the SCR.

1063-7842/02/4705-0608$22.00

In the experiment, the distance over which the radial distribution of the excitation intensity changes appreciably is much larger than the working region thickness ($d \le 1$ μm), and the electron flux q_{nz} in the direction of the external normal z to the working layer surface predominates over the radial flux $q_{n\rho}$, namely, $q_{nz} \gg q_{n\rho}$. Therefore, the coordinate ρ enters the one-dimensional transport equation as a parameter in the distribution $I(\rho)$. The electron flux q_w toward the boundary between the SCR and the quasi-neutral region $z = w$ ($w \ll d$) can be found by solving a diffusion equation for the working region under boundary conditions describing the surface recombination with a velocity s_1 at the heteroboundary at $z = d$ and fast capture of electrons in the SCR at $z = w$ at a rate $\bar{v}$. Consequently,

$$q_w = D_n \frac{dn}{dz}(w) = I(\rho)\delta\gamma, \quad \delta = \alpha(d-w). \qquad (2)$$

Here α is the light absorption coefficient; γ is a parameter depending on the magnitudes of δ; $\kappa = (d-w)/L_{dif}$; and $S_1 = s_1(d-w)/D_n$, where L_{dif} and D_n are the diffusion length and diffusion coefficient of electrons in the working layer, respectively. In the limit of weak bulk recombination $\kappa \longrightarrow 0$ and at $\delta < 1$, we arrive at

$$\gamma = (1 - \delta/2 + S_1/2)(1 + S_1 + s_1/\bar{v})^{-1}. \qquad (3)$$

An expression for the diffusion flux toward the surface at arbitrary κ and δ is given in [8]. Note that the flux q_w through the quantity γ and the capture rate $\bar{v}$ in the SCR depends on the SCR width and the arising photovoltage δV ($\delta V = V_b - V_{b0}$, eV_{b0} being the depth of the potential well in the SCR in the dark, and $e\delta V$, its change under illumination); however, for small values of the ratio $s_1/\bar{v}$, this dependence is insignificant.

2. If permeability of the surface potential barrier at the interface with a vacuum is low and the energy relaxation of electrons in the potential well in the SCR has a quasi-elastic character, then B_n is proportional to the NEA, that is, to the energy interval between the edge of the conduction band and the level corresponding to the vacuum, $\Delta = E_c - E_{vl}$, decreasing linearly with photovoltage δV. In this case [5],

$$B_n = B_{n0}\left(1 - \frac{y}{r}\right), \quad r = \frac{\Delta_0}{eV_{b0}}, \quad y = \frac{\delta V}{V_{b0}}. \qquad (4)$$

Here B_{n0} and Δ_0 are the emission probability and the NEA value, respectively, in the case of no illumination.

3. The local decrease in the band bending $\delta V(\rho)$ in the SCR under illumination is determined by the kinetics of capture by the surface centers of photoelectrons from the working zone and holes tunneling through the energy barrier in the SCR, as well as by spreading of the nonequilibrium carriers in the SCR potential well. The characteristic size δl of the charge spreading region associated with the radial drift of electrons on the SCR surface can be evaluated as $\delta l \approx \tau_\varepsilon v_s$, where v_s is the radial drift velocity of electrons in the transverse field created by photovoltage, $v_s \approx (eD/kT)\delta V/\delta l$, and $\tau_\varepsilon \approx (eV_{b0}/\hbar\omega_0)\tau_{opt}$ is the electron energy relaxation time down to the level of the mobility threshold in the SCR potential well, τ_{opt} being the emission time of an optical phonon of energy $\hbar\omega_{opt}$ [5]. For GaAs ($\hbar\omega_0 = 39$ meV, $\tau_{opt} \approx 0.1$ ps) up to a photovoltage of $\delta V \approx 0.2$ V (which is close to the NEA and corresponds to the cease of photoemission), this characteristic size is $\delta l \lesssim 0.1$ μm; for beam radii in excess of 1–2 μm, the electron spreading over the SCR is insignificant.

4. Variation of the surface charge density N_s is determined by the difference between the local fluxes of electrons and holes toward the surface as follows:

$$\frac{dN_s}{dt} = q_{ps} - q_{ns}. \qquad (5)$$

The flow of recombining electrons is found as the difference between the electron flux from the working region and the emission flux of electrons penetrating the surface potential barrier, $q_{ns} = q_w(1 - B_n) \sim I$. Because of the fast capture of electrons by attracting surface centers, the concentration of nonequilibrium carriers in the SCR is low.

The flux of holes restoring the equilibrium is determined by hole capture by neutral surface centers. The flux density of recombining holes is equal to $q_{ps} = p_w\langle v_p\sigma_p\rangle N_{ns}$, where p_w is the concentration of holes at the interface between the SCR and the quasi-neutral region; N_{ns} is the surface density of neutral centers; σ_p is the capture cross section; and v_p is the velocity of the holes. The angle brackets denote averaging over the distributions of holes and the levels of the surface states. The density N_{ns} of neutral centers depends on the surface layer structure. Experimental data on GaAs surface activation prove that no pinning of the Fermi level on activated surfaces takes place, thus indicating the presence of a wide band of partially occupied surface states. When this takes place, the dark density of capture centers for holes is close to the concentration of surface states and is weakly changed by illumination [6, 7].

The hole capture cross section for the surface states is proportional to the probability of tunneling through the repelling SCR potential and is, therefore, exponentially small. Temperature and concentration dependences of the nonlinear effects in photoemission are evidence that a predominant contribution to the hole flux toward the surface comes from the thermal-field component (that is, thermoactivated tunneling). In this case, the recombination flux can be written in the form

$$q_{ps} = q_{s0}[\exp(\lambda_0 y) - 1],$$
$$q_{s0} = 1/4\, v_T p_w \sigma_0 N_{ns} e^{-\lambda_0}, \qquad (6)$$

$$\lambda_0 = eV_{b0}/E_0, \quad E_0 = E_{00}\coth(E_{00}/kT),$$
$$E_{00} = \frac{\hbar}{2}\left[\frac{e^2 N_a}{m_p^* \varepsilon_s}\right]^{1/2}. \tag{7}$$

Here, v_T is the thermal velocity of holes and σ_0 is the effective capture cross section for the tunneling holes. The second terms in brackets in (6) allow for processes holes being ejected back into the semiconductor bulk in the approximation of high density of the surface states.

The main difference between the flux q_{ps} of recombining holes and the flux of holes tunneling to the surface layer (the latter determines the restoring current in a model corresponding to the Schottky diode [5–7]) is given by the factor $\sigma_0 N_{ns}$. The magnitude of σ_0 depends on the capture mechanism. If the thermal velocity of holes is 10^7 cm/s, the surface concentration of the centers $N_{ns} = 10^{12}$–10^{13} cm^{-2}, and a typical value of the capture cross section by a neutral center is $\sigma_0 = 10^{-15}$ cm^2 [14], then this factor is $N_{ns}\sigma_0 \ll 1$. In this case, the recombination flux q_{ps} is appreciably less than the flux of holes tunneling to the surface. Hereinafter, the value q_{s0} is considered as a parameter of the model.

PHOTOVOLTAIC KINETICS: RESULTS FOR UNIFORM ILLUMINATION

1. In a depletion layer approximation, we have $N_s = N_{s0}\sqrt{1-y}$ and Eq. (5) can be written in terms of photovoltage y as follows,

$$\frac{\tau_s}{2\sqrt{1-y}}\frac{dy}{dt} = q_w/q_{s0}(1-B_n) + 1 - e^{\lambda_0 y},$$
$$\tau_s = N_{s0}/q_{s0} \tag{8}$$

and it then can be integrated by quadratures. For a low electron escape probability $B_n \ll 1$, the dependence $y(t)$ has the form

$$y = \frac{1}{\lambda_0} \times \ln\frac{a}{1 + [a\exp(-\lambda_0 y_0) - 1]\exp[-2\lambda_0 a\tau(1-y)^{1/2}]}, \tag{9}$$
$$\tau = \frac{t}{\tau_s}, \quad a = \frac{q_w}{q_{s0}} + 1.$$

Here, $y(t=0) = y_0 = 0$ at the moment when illumination is turned on and $y = y_0 \neq 0$ when illumination is turned off. At low intensities, $q_w/q_{s0} \ll 1$, the stationary photovoltage δV_{st} increases in proportion to the intensity and $y_{st} = 1/\lambda_0(q_w/q_{s0})$. At high intensities, $q_w/q_{s0} \gg 1$, the photovoltage grows logarithmically. Note that the boundary between the low and high intensities is given by the condition $q_w \simeq q_{s0}$, the corresponding intensity being $I_b \simeq q_{s0}/\delta$.

From (9) it follows that the photovoltage relaxation time is

$$t_{rel} = k_t(I)\frac{\tau_{s0}}{(1 + q_w/q_{s0})}, \quad \tau_{s0} = \tau_s/\lambda_0,$$
$$1 < k_t(I) \lesssim 3. \tag{10}$$

At low intensities, $q_w \ll q_{s0}$, $k_t \approx 1$, and the relaxation time is independent of the illumination intensity and equal to $t_{rel} = \tau_{s0}$. At high intensities, $q_w \gg q_{s0}$, $k_t \approx 3$, and the photovoltage relaxation time decreases in inverse proportion to the illumination intensity, $t_{rel} \sim q_w^{-1}$. After the illumination is turned off, electrons escape the working region in a short time, $\tau_{ext} \approx \max(d^2/D_n, d/v)$. Measurement of the relaxation time of the photovoltage in the SCR by the method of two-pulse excitation with the use of formulas (8) and (10) gives an estimate of q_{s0}.

2. According to (4), at a photovoltage of $y = r$, the barrier permeability is $B_n = 0$ and emission Òeases. The corresponding critical illumination intensity I_{cr} can be determined using the stationary state condition: $q_{ns} = q_{ps}$

$$I_{cr} \approx \frac{q_{s0}}{\delta\gamma}e^{\lambda_0 r}. \tag{11}$$

From (11) it follows that the critical intensity increases exponentially with growth of $\lambda_0 r = \Delta_0/E_0$. The intensity I_{opt}, at which the stationary emission current density is maximum, can be found (taking into account (9) at $\tau \longrightarrow \infty$) from an extremum condition for the expression

$$q_{emi} = B_{n0}q_w\left[1 - \frac{1}{\lambda_0 r}\ln\left(1 + \frac{q_w}{q_{s0}}\right)\right]. \tag{12}$$

The emission current is maximum when $q_w/q_{s0} = e^{\lambda_0 r - 1} - 1$. At $q_w \gg q_{s0}$, the intensity I_{opt}, the photovoltage, and the maximum emission current density q_{opt} are, respectively,

$$I_{opt} = \frac{q_{s0}}{\delta\gamma}e^{\lambda_0 r - 1}, \quad y = y_{opt} = r - \lambda_0^{-1},$$
$$q_{opt} = q_{s0}e^{\lambda_0 r - 1}\frac{B_{n0}}{\lambda_0 r}. \tag{13}$$

Using (13) and an expression for the emission quantum yield Y at low intensities, $Y_0 = (q_{emi}/I)_{I\to 0} = B_{n0}\delta\gamma$, we get

$$\frac{I_{opt}}{I_{cr}} = e^{-1}, \quad q_{opt} = I_{opt}\frac{Y_0}{\lambda_0 r}. \tag{14}$$

From (13) it follows that the maximum emission current is proportional to the restoring hole current and the probability B_{n0}, its growth with an increasing Δ_0/E_0 ratio being close to exponential.

3. The formulas given above relate the basic characteristics of a photocathode (Δ_0, eV_{b0}, B_{n0}, q_{s0}, and E_0) with the experimentally measured values, in particular, Y_0, I_{opt}, $Y_{opt} = q_{opt}/I_{opt}$, and $\delta V_{st}(I_{opt})$, as follows:

$$B_{n0} = \frac{Y_0}{\delta\gamma}, \quad \frac{\Delta_0}{E_0} = \frac{Y_0}{Y_{opt}},$$
$$q_{s0} = I_{opt}\delta\gamma e^{-(\lambda_0 r - 1)}, \quad E_0 = \frac{e\delta V_{st}(I_{opt})}{\lambda_0 r - 1}. \tag{15}$$

Let us evaluate the characteristics of GaAs photocathodes investigated experimentally in studies [9, 10] (for a working layer thickness of $d = 2$ μm, an acceptor concentration of $N_a = 6 \times 10^{18}$ cm^{-3}, and a light absorption coefficient of $\alpha = 10^4$ cm^{-1}). Using experimental data for the quantum efficiency, emission current, and photovoltage at corresponding excitation intensities, namely, $Y_0 = 0.219$, $j_{opt} = 1$ A/cm^2 ($q_{opt} = 6.25 \times 10^{18}$ cm^{-2} s^{-1}), $I_{opt} = 30$ W/cm^2 ($I_{opt} = 1.3 \times 10^{20}$ cm^{-2} s^{-1}), $Y_{opt} = 0.049$, and $\delta V_{st} = 152$ mV, we obtain $B_{n0} = 0.384$, $\lambda_0 r = 4.47$, $E_0 = 44$ meV, and $\Delta_0 = 0.2$ eV. E_0 is close to 47 meV, as given by (7), and the preexponential factor q_{s0} (see (6)) is equal to 2.3×10^{18} cm^{-2} s^{-1}. Close values of the two parameters, E_0 and q_{s0}, were obtained in similar experiments with thin GaAs layers [5], which confirms the model's adequacy.

3. NONUNIFORM ILLUMINATION INTENSITY

1. Consider the photovoltage distribution, quantum efficiency, and emission flux under nonuniform illumination of the photocathode $I(\rho) = I_m\Phi(\rho)$ assuming that the size of the illuminated spot $\rho_{max} \gg d$. In a stationary regime, the photovoltage distribution $y(\rho) = \delta V/V_{b0}$ can be found from the equation

$$y = \frac{1}{\lambda_0}\ln\left\{1 + \frac{q_w[I(\rho), y][1 - B_n(y)]}{q_{s0}}\right\}, \tag{16}$$

which, in the case where $B_n < 1$, is effectively solved by the iteration technique. The total emission flux q_{tot} is found by integration over the excitation spot.

Numerical calculations were carried out for a GaAs photoemitter at the parameter values given in Section 2. It was assumed that the intensity $I(\rho)$ drops with distance from the center according to the Gaussian distribution, which is displayed by the principal mode amplitudes in various modifications of single-mode lasers [13]

$$I(\rho) = I_m\exp(-\beta R^2), \quad R = \rho/\rho_{max}. \tag{17}$$

2. As the illumination intensity falls off with distance from the center of the excitation spot, the photovoltage y decreases and the quantum efficiency grows. The emission flux distribution $q_{emi}(\rho)$ along the dimensionless distance from the spot center is given in Fig. 1. In the range of intensities $I_m < I_{opt}$, where the effective permeability of the SCR varies relatively weakly and is not too low ($\Delta = E_c - E_{vl} \approx \Delta_0$), q_{emi} drops with distance from the spot center as does the intensity (curves *1* and *2*). Close to a critical intensity value, at which the effective barrier permeability near the beam axis is close to zero, the distribution $q_{emi}(\rho)$ is nonmonotonic and has a maximum shifted from the spot center. In the range $I_{opt} < I_m < I_{cr}$, as the intensity approaches the critical value, the differences $q_{emi}^{max} - q_{emi}(0)$ and $q_{emi}^{max} - q_{emi}(1)$ increase and the maximum position moves away from the spot center. The maximal emission is not affected by the illumination intensity and is a function of the maximum barrier permeability and the parameters affecting the restoring hole current. Accuracy of the maximum current value q_{opt} with the use of formula (13) depends on B_{n0} and amounts to a few percent.

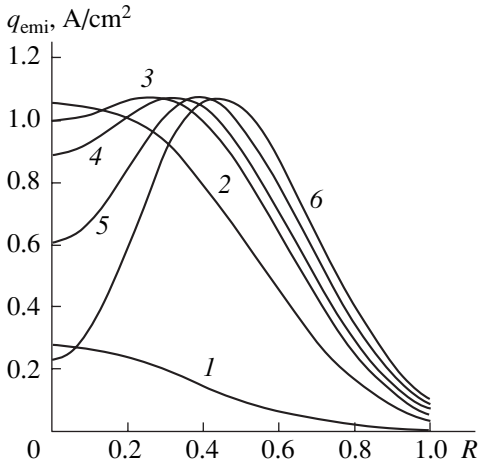

Fig. 1. Variation of the emission current $q_{emi}(R)$ over the illuminated surface ($I_{max}/I_{min} = 100$) for different illumination intensities. I_{max}, 10^{20} cm^{-2} s^{-1}: (*1*) 0.1; (*2*) 1; (*3*) 1.7; (*4*) 2; (*5*) 2.5; and (*6*) 3.

3. Let us determine the illumination intensity at the center of a spot of area S corresponding to the maximum collected charge. This maximum is achieved at an intensity value slightly higher than I_{opt} and less than I_{cr} because the area where $I(\rho) \geq I_{cr}$ corresponds to $B_n \approx 0$ and is inactive. For $I(\rho)$ having the Gaussian distribution given by (17) and using (16), at $B_n \ll 1$ and $q_w = I(\rho)\delta\gamma$ we obtain

$$q_{tot} = Sq_{s0}B_{n0}\Phi(H, \beta),$$
$$\Phi(H, \beta) = \frac{[P - \exp(-\beta)]}{\beta}H - \frac{1}{\lambda_0 r\beta}[\phi(H') - \phi(He^{-\beta})]. \tag{18}$$

Here $H = I_m\delta\gamma/q_{s0}$, $\phi(x) = (x + 1)\ln(x + 1) - x$, and the values P and H' are defined by the relations

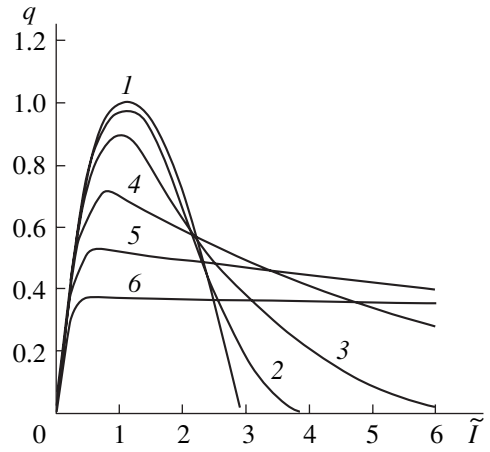

Fig. 2. Dependence of the normalized total emission current $q = q_{tot}/q_{opt}$ on the average dimensionless illumination intensity $\tilde{I} = \bar{I}/I_{opt}$ for various nonuniformity degrees of the illumination distribution over the light spot. I_{max}/I_{min}: (*1*) 1; (*2*) 2; (*3*) 5; (*4*) 20; (*5*) 100; and (*6*) 1000.

$$\begin{aligned} I_m \le I_{cr} \quad P = 1, \quad H' = H, \\ I_m > I_{cr} \quad P = I_{cr}/I_m, \quad H' = I_{cr}\delta\gamma/q_{s0}. \end{aligned} \tag{19}$$

At $H \ll 1$, the total flux is practically independent of β and increases in proportion to the intensity $\bar{I}$ averaged over the spot area as follows:

$$\begin{aligned} q_{tot} = S\bar{I}Y, \quad \bar{I} = I_m\frac{1-e^{-\beta}}{\beta}, \\ Y = Y_0\left[1-\frac{H}{\lambda_0 r}\frac{1+e^{-\beta}}{2}\right]. \end{aligned} \tag{20}$$

At high intensities, $H \gg 1$, the function $\Phi(H, \beta)$ is nonmonotonic. At close to uniform illumination intensity distributions ($\beta \ll 1$), the maximum and average intensities corresponding to the maximum total emission flux and the magnitude of the latter are given by the formulas

$$\begin{aligned} I_m = I_{opt}e^{\beta/2-\beta^2/12}, \quad \bar{I}_{opt} = I_{opt}\left(1-\frac{\beta^2}{24}\right), \\ q_{tot}^{max}/S = q_{tot}\left(1-\frac{\beta^2}{24}\right). \end{aligned} \tag{21}$$

From (21) it follows that as the illumination becomes less uniform, I_m increases and becomes more sensitive to illumination nonuniformity than the emission flux. The maximum flux, same as the average intensity, deviated not much from its highest values up to $I_m/I(\rho_{max}) \lesssim 2$. From (18) and (19) it follows that, for a Gaussian beam, the emission ceases when $I(\rho_{max}) = I_{cr}$, which is achieved at $I_m = I_{sup}$, where

$$I_{sup} = I_{cr}e^{\beta} = I_{cr}\frac{I_m}{I(\rho_{max})}, \quad \bar{I}_{sup} = I_{sup}\frac{1-e^{-\beta}}{\beta}. \tag{22}$$

For strongly nonuniform distributions ($e^{-\beta} \ll 1$) at high intensities, $H \gg 1$, the average and maximum intensities of the incident radiation corresponding to the maximum total emission flux are given by

$$\begin{aligned} H_m = \exp[\lambda_0 r(1-e^{-\beta})], \\ \bar{I}_{opt} \approx q_{s0}\frac{\exp[\lambda_0 r(1-e^{-\beta})]}{\delta\gamma\beta}. \end{aligned} \tag{23}$$

The maximum flux q_{tot}^{max} (same as the quantity $\bar{I}_{opt}$ varies in inverse proportion to β:

$$\begin{aligned} q_{tot}^{max}/S = q_{s0}B_{n0}\frac{\exp[\lambda_0 r(1-\exp(-\beta))]}{\lambda_0 r\beta} \\ \approx \frac{e}{\beta}(1-\lambda_0 r e^{-\beta})q_{opt}. \end{aligned} \tag{24}$$

Variation of the total emission flux q_{tot} (normalized by q_{opt}) with the average illumination intensity for different values of β are presented in Fig. 2. As β grows, the current maximum position shifts towards lower average intensities, the maximum current decreases, and at $\beta \gg 1$ the current near the maximum exhibits distinct "saturation" due to an appreciable increase in the ultimate intensity I_{sup}. The function $q(\bar{I})$ derived theoretically reproduces specific qualitative features of the experimental dependence $j(I)$ [10]: the rather fast drop of the emission current at $\bar{I} < \bar{I}_{opt}$ and practically constant current at $\bar{I} \gtrsim \bar{I}_{opt}$. The smooth variation of $q_{tot}(\bar{I})$ in the vicinity of $\bar{I}_{opt}$ is associated with the integral character of this value. The region around the beam axis where the energy interval adequate for the emission is narrow has a small area, and the basic contribution to the emission comes from the area where the illumination intensity is close to optimal. Because of the sharp exponential variation of the restoring current at high excitation intensities, exact knowledge of the barrier permeability variation in the vicinity of I_{opt} at low values of B_n is not essential.

4. TRANSIENT PROCESSES AND CHARGE RECOVERY

1. For studying the relaxation processes and the quantum efficiency recovery time, the emission current is measured as a function of time after abrupt exposure to light and or in a two-pulse excitation regime. In the latter case the ratio of the charges emitted after the first, probing, pulse and the second, excitation, pulse is measured as a function of time difference between the two pulses.

The results of numerical calculations of transient processes for the case of instantaneous turning on (off) of constant-intensity illumination $I(\rho)$ in one-pulse and two-pulse regimes are as follows. Duration of the illumination pulses is t_i; the time delay of the second pulse is t_p. The parameters of photocathodes were given in Section 2. The photovoltage $y(R, t)$ was determined by numerical integration of Eq. (8) under corresponding initial conditions: at the time moment when the illumination is first turned on the photovoltage is $y_0(R, 0) = 0$; at the moment when the illumination is abruptly turned off the photovoltage is $y(R, t_i)$; and at then moment when the illumination is turned on again it is $y(R, t_i + t_p)$. The total emission flux was determined by integration over the sample area. The magnitude of the accumulated charge is

$$Q = \int_0^{t_i} q_{tot}(t)dt. \qquad (25)$$

2. Shown in Figs. 3–5 are calculation curves of variation with time of the photovoltage and the emission flux for an intensity of $I_m \approx 2 \times 10^{20}$ cm^{-2} s^{-1} and strongly nonuniform distribution of the light intensity $I_m/I(\rho_{max}) = 100$. The illumination time $t_i = 0.1\tau_s$ was close to that required for the photovoltage at the light spot periphery to set in. In Fig. 3 the following is seen. The photovoltage relaxation time after illumination being turned on τ_+ increases considerably with distance from the center toward the spot periphery, that is, $\tau_+(0) \ll \tau_+(\rho_{max})$. The relaxation time after illumination is turned off τ_- is appreciably longer than the time τ_+ for high light intensities and coincides with the latter at low intensities.

The appreciably higher photovoltage relaxation rate at the spot center in the dark results in smoothing out of the photovoltage along the radius in a short time ($\lambda_0\tau \ll 1$). Consequently, in the dark over most of the time period, the relaxation proceeds in a linear regime and, therefore, the charge recovery time is equal to τ_{s0} (see (10)).

The relaxation time of the local emission flux in the dark (Fig. 4) is equal to the relaxation time of the effective barrier permeability (that is, to the photovoltage relaxation time) and rises considerably with distance from the spot center toward its periphery as the ratio $q_w/q_{s0}(\rho)$ decreases (see (10)). The total emission flux q_{tot} relaxes over an intermediate relaxation time close to the relaxation time $t_{rel} \approx \tau_{s0}e^{1-\lambda_0 r}$ in the surface area where the emission flux is maximum.

Influence of the delay time t_p on variation of the total flux with time is demonstrated in Fig. 5, where dependences $q_{tot}(t)$ are shown after the first and the second illumination pulses. As t_p is decreased, the initial magnitude of the total emission flux decreases because of the higher photovoltage encountered by the second pulse.

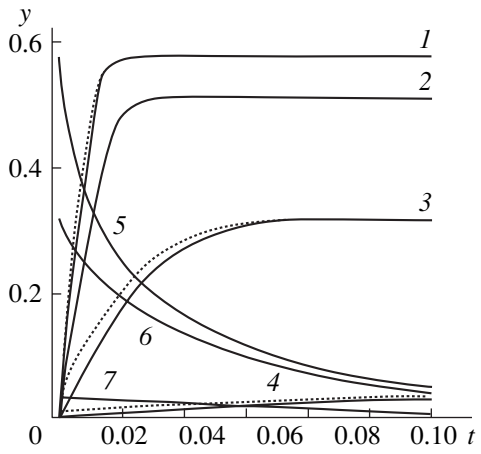

Fig. 3. Variation with time of the dimensionless photovoltage y (normalized by $\tau_s = N_{s0}/q_{s0}$ after switching the illumination on (*1–4*) and off (*5–7*). The dashed line is the dependence $y(t)$ after application of the second light pulse, delayed by $0.1\tau_s$. The time is measured from the moments of switching the illumination on or off and application of the second illumination pulse; ρ/ρ_{max}: (*1*, *5*) 0; (*2*) 0.3; (*3*, *6*) 0.6; and (*4*, *7*) 1.

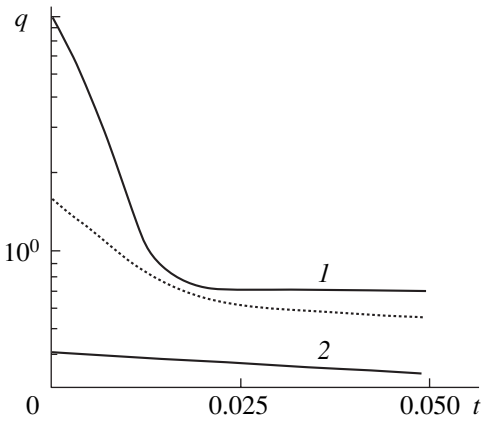

Fig. 4. Variation with time of the normalized emission flux $q = q_{emi}(t, \rho)/q_{opt}$ at the center (*1*) and at the periphery (*2*) of the illuminated spot; ρ/ρ_{max}: (*1*) 0 and (*2*) 0.8. The dotted line corresponds to variation with time of the normalized total emission current $\tilde{q}_{tot} = q_{tot}(t)/q_{opt}$.

3. The most important dependences $\eta = Q_2/Q_1(\tau_p)$ characterizing charge recovery as a function of the delay time for various intensities I_m and different $I_m/I(\rho_{max})$ are shown in Fig. 6. The illumination pulse duration $t_i = 0.02\tau_s$ is nearly as long as the relaxation time of the total emission flux (Figs. 4, 5). It is seen in Fig. 6 that in cases where the charge saturation effects are strongly pronounced (at $I_{opt} \lesssim I_m \lesssim I_{cr}$ and $I_m/I(\rho_{max}) \simeq 1$), the ratio $\eta = Q_2/Q_1(\tau_p)$ depends on the illumination intensity and its nonuniformity over the spot area at short delay times $\lambda_0\tau_\rho \ll 1$ (compare solid and dashed lines *3* or solid lines *1–4*). Because of this

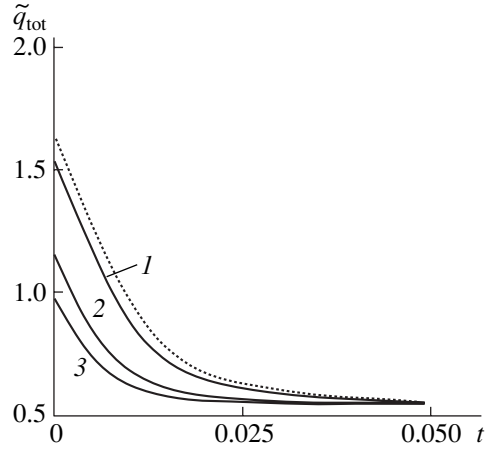

Fig. 5. Variation with time of the normalized total emission current $\tilde{q}_{tot}(t) = q_{tot}(t)/q_{opt}$ for different time delays of the second light pulse. The dashed line corresponds to the relaxation of $\tilde{q}_{tot}(t)$ following the initial illumination; the solid lines show the relaxation during the second illumination pulse; τ_p (normalized by τ_s): (*1*) 0.1, (*2*) 0.02, and (*3*) 0.01.

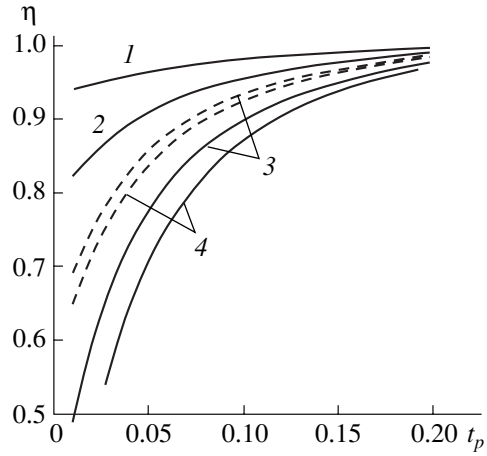

Fig. 6. Variation with time of $\eta = Q_2/Q_1(\tau_p)$ at different illumination intensities and nonuniformities; I_m, 10^{20} cm^{-2} s^{-1}: (*1*) 0.1, (*2*) 0.3, (*3*) 2, and (*4*) 2.8. The solid lines correspond to a uniform illumination $I_m/I(\rho_{max}) = 1$, and the dashed lines correspond to nonuniformity of $I_m/I(\rho_{max}) = 100$.

the charge recovery time, as well as the flux q_{s0} (corresponding to the charge recovery level of $\lesssim$90%), become dependent on the light beam parameters. In those cases where the main contribution to the charge comes from a spot area illuminated below the optimum level, sensitivity of the function $\eta(\tau_p)$ to the light beam parameters diminishes (compare dashed curves *3* and *4*). Complete charge restoration ($\eta = Q_2/Q_1(t_r) \approx 0.99$) is achieved at $t_r \approx \tau_{s0}$. When this takes place, the time t_r, corresponding to restoration of the charge accumulation, depends weakly on the illumination intensity and nonuniformity of its distribution over the light spot. This is due to the fact that, at η values close to 1, the recovery rate is determined by the longest relaxation time corresponding to the light-spot periphery.

CONCLUSION

Calculation results show an exponentially high sensitivity of the maximum emission current to the negative electron affinity. Under nonuniform excitation, the maximum emission current noticeably decreases and its dependence on the illumination intensity in the vicinity of the maximum becomes less steep. Fast photovoltage relaxation in the area of high illumination intensity results in low sensitivity of the charge recovery time to the excitation intensity and nonuniformity of the illumination distribution over the light spot. Therefore, making allowance for nonuniformity of the illumination turns out to be necessary both when determining the photocathode parameters from experiment and choosing an optimum photoemission regime.

The work was supported by INTAS (grant no. 99-00125) and the Russian Foundation for Basic Research (project no. 00-02-16775).

REFERENCES

1. R. Alley, H. Aoyagi, J. Clendenin, *et al.*, Nucl. Instrum. Methods Phys. Res. A **365**, 1 (1995).
2. J. E. Schneider, A. W. Baum, G. I. Winograd, *et al.*, J. Vac. Sci. Technol. B **14**, 3782 (1996).
3. M. Woods *et al.*, J. Appl. Phys. **73**, 8531 (1993).
4. A. Herrera-Gómez, G. Vergara, and W. E. Spicer, J. Appl. Phys. **79**, 7318 (1996).
5. G. A. Mulhollan, A. V. Subashiev, J. E. Clendenin, *et al.*, Phys. Lett. A **282**, 309 (2001).
6. M. H. Hecht, Phys. Rev. B **41**, 7918 (1990).
7. A. Bauer, M. Prietsch, S. Molodtsov, *et al.*, Phys. Rev. B **44**, 4002 (1991).
8. B. I. Reznikov and A. V. Subashiev, Fiz. Tekh. Poluprovodn. (St. Petersburg) **32**, 1125 (1998) [Semiconductors **32**, 1006 (1998)]; Fiz. Tekh. Poluprovodn. (St. Petersburg) **32**, 1467 (1998) [Semiconductors **32**, 1309 (1998)].
9. A. S. Jaroshevich, M. A. Kirillov, D. A. Orlow, *et al.*, in *Proceedings of the 7th International Workshop on Polarized Gas Targets and Polarized Beams, Urbana, 1997*, p. 132.
10. M. A. Kirillov, D. A. Orlov, and A. S. Terekhov, in *Proceedings of the Low Energy Polarized Electron Workshop, St. Petersburg, 1998*, p. 30.
11. C. Sinclair, in *Polarized Sources and Targets,* Ed. by A. Gute *et al.* (Erlangen-Nurnberg, 1999), p. 222.
12. G. A. Mulhollan *et al.*, in *Polarized Sources and Targets*, Ed. by A. Gute *et al.* (Erlangen-Nurnberg, 1999), p. 322.
13. E. F. Ishchenko, *Open Optical Resonators* (Sov. Radio, Moscow, 1980).
14. A. G. Milnes, *Deep Impurities in Semiconductors* (Wiley, New York, 1973; Mir, Moscow, 1977).

Translated by N. Mende

Technical Physics, Vol. 47, No. 5, 2002, pp. 615–620. Translated from Zhurnal Tekhnicheskoĭ Fiziki, Vol. 72, No. 5, 2002, pp. 102–107.

EXPERIMENTAL INSTRUMENTS AND TECHNIQUES

Sulfur and Nitrogen Oxide Conversion in Air by Microsecond Electron Beams

G. V. Denisov, D. L. Kuznetsov, Yu. N. Novoselov, and R. M. Tkachenko

Institute of Electrophysics, Ural Division, Russian Academy of Sciences, Komsomol'skaya ul. 34, Yekaterinburg, 620016 Russia

e-mail: nov@iep.uran.ru

Received July 19, 2001

Abstract—Sulfur and nitrogen oxide conversion in an ionized gaseous mixture modeling the composition of flue gases from thermal power plants is studied experimentally. A pulsed microsecond beam of electrons is used as an ionization source. Oxides of both elements are shown to influence the conversion process. Possible kinetic mechanisms for removing the oxides from the gaseous mixture are discussed. © *2002 MAIK "Nauka/Interperiodica".*

INTRODUCTION

Flue gases from thermal power plants, which contain sulfur and nitrogen oxides in large amounts, are a basic source of environmental pollution. Combining with water vapor and accumulating in the atmosphere, they cause acid rain. To reduce environmental damage due to SO_2 and NO_x, it is necessary to purify flue gases immediately at the site of their outflow into the atmosphere, i.e., at thermal power stations. There are several ways of attacking this problem, one of them being the processing of flue gases by electron beams.

To this end, continuous-mode electron accelerators generating beams of moderate current density (10^{-5}–10^{-9} A/cm^2) are usually used (see, e.g., [1, 2]). In this case, flue gases are removed in several steps. First, fast electrons act on flue gases, which contain water vapor (along with the oxides to be removed), to generate free radicals like O, OH, O_2H, etc. Then, SO_2 and NO_x oxidize to related acids, H_2SO_4 and HNO_3, via chemical reactions involving these free radicals. Further, the acids react with ammonia added to flue gases to form powdered ammonia sulfates and nitrates. At the final step, these powders are trapped by various filters.

The theoretical groundwork for the first two steps has been developed to the point where analytical and experimental data are in good agreement [4, 5]. The refinement of the free-radical mechanism of impurity oxidation when flue gases are processed by electron beams will include the study of heterogeneous processes and aerosol formation [6, 7].

Using the electron beams, one can attain a high degree of purification: up to 95% for SO_2 and 80% for NO_x [1–3]. The energy spent on the removal of one molecule amounts up to 12–30 eV or higher. Clearly, the energy consumption for gas purification, which makes up 3–5% of the rated power of thermal power stations, must be reduced. This is the central problem in developing electron-beam purification technologies.

Earlier, it has been demonstrated with sulfur dioxide [8, 9] that the use of pulsed electron beams makes it possible to considerably (by several times) decrease the energy loss per toxic molecule. The reason is that with the parameters of the beams optimized, the conversion of SO_2 proceeds by the chain plasma-chemical mechanism. Pulsed electron beams also reduce the energy needed to remove NO_x oxides [10, 11]. However, in the works cited, either SO_2 or NO_x nitrogen oxides were removed. In this work, we study the combined effect of SO_2 and NO_x oxides on their conversion.

EXPERIMENTAL EQUIPMENT AND METHODS

Experiments were carried out with the setup built around a plasma-cathode pulsed electron accelerator designed similarly to that described in [12]. The cross-sectional dimensions of the output electron beam were 10×100 cm. The beam energy, half-width, and current density were 200 keV, $\tau \approx 5 \times 10^{-6}$ s, and $j = (4.5–12.5) \times 10^{-3}$ A/cm^2, respectively. The beam was injected to the gas chamber of volume 12 l through a 20-μm-thick titanium foil. The beam energy absorbed by the gas was defined as $W = j\tau D$, where D is the dose of the gas-absorbed energy per unit length. The product $j\tau$ was determined by integrating the current and voltage waveforms, and D was measured with TsDP-F-2 film detectors by the standard technique [13].

A model gaseous mixture prepared in a special mixer was delivered to a pre-evacuated plasma chemical chamber doubly purged by pure nitrogen. The mixture was forced to circulate in the chamber throughout the experiment. The mixture was composed of nitrogen

1063-7842/02/4705-0615$22.00

(90%), oxygen (10%), as well as SO_2 and NO_x impurities from 0 to 5000 ppm.

The qualitative and quantitative analysis of the gas mixture was performed by chromatographic and electrochemical methods with a Tsvet 500M gas chromatograph and a Testo-350 flue gas analyzer. The chromatograph was applied to measure the oxygen and nitrogen concentrations, and the Testo-350 analyzer measured the concentrations of SO_2 and NO_x. The partial concentrations of NO and NO_2 (their sum gives the total concentration of the NO_x impurity) were measured conductometrically with and without cryogenic separation of NO from NO_2 [14]. In the former case, the concentration of nitrogen monoxide [NO] was determined. Without the separation, the total concentration of the nitrogen oxides $[NO_x] = [NO] + [NO_2]$ was measured. Then, the concentration of NO was found from the calibration curve of [NO] vs. absorbing solution conductivity, which was found independently in experiments with $(NO + N_2)$ standard gaseous mixtures with NO concentrations from 200 to 5500 ppm. The mean statistical measurement error was no more 0.03. The methods used cannot monitor the partial concentrations of sulfur and nitrogen oxides simultaneously. Therefore, we determined the initial composition of the mixture and then monitored the concentration of only one sort of the oxides: either sulfur dioxide or nitrogen oxides.

The gaseous mixture studied was irradiated by individual shots. In each of the runs, the number of shots was 300–500. The amount of the sulfur or nitrogen oxides was determined in 50 shot intervals. We measured the absolute change in the oxide concentration, the degree of conversion, and the energy needed to remove one molecule. The degree of conversion η and the energy loss ε were calculated for each of the oxides as

$$\eta = \Delta[C]/[C]_0, \quad \varepsilon = WN/e\Delta[C] \text{ (eV/molecule)}.$$

Here, $\Delta[C]$ is the change in the concentration of SO_2 or NO_x after a series of shots (cm^{-3}), $[C]_0$ is the initial impurity concentration in the mixture (cm^{-3}), W is the beam energy absorbed by the gas per shot (J/cm^3), N is the number of shots, and e is the charge of an electron (C). The total error in measuring ε was no higher than 0.3 (with the error in the absorbed energy W included).

SULFUR DIOXIDE CONVERSION

Earlier [9], it has been shown that in flue gases containing only sulfur dioxide, the SO_2 conversion induced by microsecond electron beams follows the chain mechanism. The chain is initiated by the three-body attachment of thermalized beam electrons and electrons underwent the degradation cascade to oxygen molecules with the formation of O_2^- negative ions:

$$e + O_2 + M \longrightarrow O_2^- + M, \quad (1)$$

where M is a third particle (a nitrogen, oxygen, or water molecule).

The O_2^- active ions disappear in chain propagation reactions and in competing reactions of recombination with N_2^+ positive ions. The chain oxidation reactions are as follows [15]:

$$O_2^- + SO_2 \longrightarrow SO_2^- + O_2, \quad (2)$$

$$SO_2^- + O_2^* \longrightarrow SO_4^-, \quad (3)$$

$$SO_4^- + O_2^* \longrightarrow SO_3 + O_3^-, \quad (4)$$

$$SO_2 + O_3^- \longrightarrow SO_3^- + O_2, \quad (5)$$

$$SO_3^- + H_2O \longrightarrow H_2SO_4 + e. \quad (6)$$

The free electron produced by reaction (6) may take part in reaction (1), closing the chain. In addition, mechanism (1)–(6) involves negative ozone ions, which can form by the reactions

$$e + O_2 \longrightarrow O + O, \quad (7)$$

$$O_2^- + O + M \longrightarrow O_3^- + M \quad (8)$$

and other reactions with the participation of atomic oxygen and O_2^- ions [16].

The characteristic time of the recombination reaction

$$O_2^- + N_2^+ \longrightarrow O_2 + N_2 \quad (9)$$

which involves nitrogen and oxygen ions and competes with (2) and (8), is 10–20 μs at atmospheric pressure, moderate humidity, and beam parameters used in the experiments [17]. Therefore, as time passes, the amount of the O_2^- ions in reaction (9) sharply decreases and the probability of the chain reaction drastically drops. Thus, the use of a pulsed electron beam with an optimal current density $j \sim 10^{-3}$ A/cm^2 and a shot duration $\tau \sim 10$ μs makes it possible to realize the chain mechanism of SO_2 oxidation with low energy losses (~1 eV/molecule) [9].

Figure 1 shows the variation of the SO_2 concentration with the number of shots N for various concentrations of NO_2. The model mixture consisted of N_2 (≈88.5%), O_2 (≈10%), H_2O (≈1%), and NO (≈0–0.1%). The initial concentration of SO_2 equals the ordinate intercept at $N = 0$. It is seen that the SO_2 concentration decreases with an increase in the number of shots, the decrease being the most pronounced in the absence of the NO_2 impurity (curve *1*). Under such conditions, the conversion is $\eta \approx 98\%$ and the energy loss, $\varepsilon \approx 4$ eV/molecule. Apparently, SO_2 oxidizes by the chain mechanism in this case. The energy loss is somewhat

higher than that reported in [9], since in [9] the electron beam was optimized.

With small amounts of NO_2 ($[NO_2] \approx 500$ ppm) added, the efficiency of SO_2 removal drops (curve *3*, Fig. 1) and the conversion η decreased to 60%. The further increase in the NO_2 amount ($[NO_2] \sim 1000$ ppm) improves the process: the conversion rises to ≈65%.

The energy ε needed to remove an SO_2 molecule is an energy characteristic of SO_2 removal. Figure 2 shows the dependences of ε and η on the NO_2 initial concentration in the mixture (curves *1* and *2*, respectively). For each of the experimental points, the number of shots was 300. As the NO_2 initial concentration grows, the conversion of SO_2 declines while the energy loss per SO_2 molecule rises. With a further increase in the NO_2 concentration, the energy loss is slightly reduced.

Let us consider possible reasons for the effect of the nitrogen oxides on the SO_2 conversion process. The presence of NO_2 molecules in the SO_2-containing gas may initiate competing processes that lead to a reduction of the concentration of O_2^-, O_3^-, and SO_2^- negative ions, which participate in the chain mechanism. Such a process can be the attachment of thermalized beam electrons to an electronegative NO_2 molecule, which has an electron affinity of 2.42 eV:

$$e + NO_2 \longrightarrow NO_2^-. \qquad (10)$$

Another process that competes with reaction (2) is the charge exchange reaction

$$O_2^- + NO_2 \longrightarrow O_2^* + NO_2^-. \qquad (11)$$

The rate constant of (11) is much larger than that of (2) ($k_2 \approx 4.5 \times 10^{-10}$ cm^3/s against $k_{11} \approx 12 \times 10^{-10}$ cm^3/s [18]). The loss of SO_2^- negative ions in the charge exchange reaction

$$SO_2^- + NO_2 \longrightarrow SO_2 + NO_2^- \qquad (12)$$

may considerably decrease the probability of the chain mechanism. This reaction proceeds vigorously in mixtures enriched with impurity oxides, and its rate constant is $k_{12} \approx 4.3 \times 10^{-10}$ cm^3/s [18].

The effect of the nitrogen oxides was estimated for the mixture with $[SO_2] = 700$ ppm and $[NO_2]$ varying from 0 to 500 ppm. The mixture was irradiated by an electron beam with a current density of 5×10^{-3} A/cm^2. The duration of rectangular shorts was 5×10^{-6} s. Reactions (2) and (10)–(12) were considered. The analysis shows that the quasi-steady-state free electron concentration in the ionization chamber is established within a characteristic time of ~10^{-7} s and equals ~10^{-11} cm^{-3}. With the nitrogen oxides added into the mixture, the concentration remains virtually unchanged. In our experimental conditions, the rate of production of the negative ions by reaction (1) was shown to be 40 times higher than by reaction (10). Thus, the loss of the electrons due to attachment in reaction (10) cannot significantly affect the initiation of the chain mechanism of SO_2 oxidation.

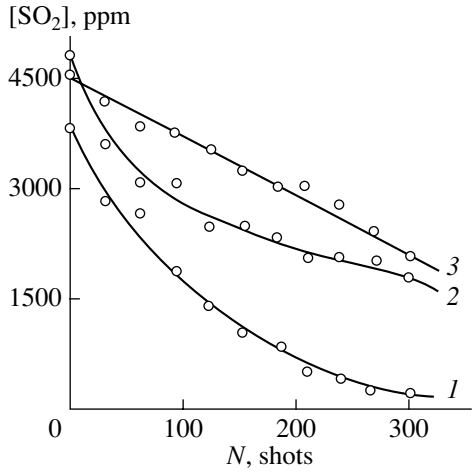

Fig. 1. SO_2 concentration vs. number of shorts. The NO_2 concentration is (*1*) 0, (*2*) 1000, and (*3*) 500 ppm.

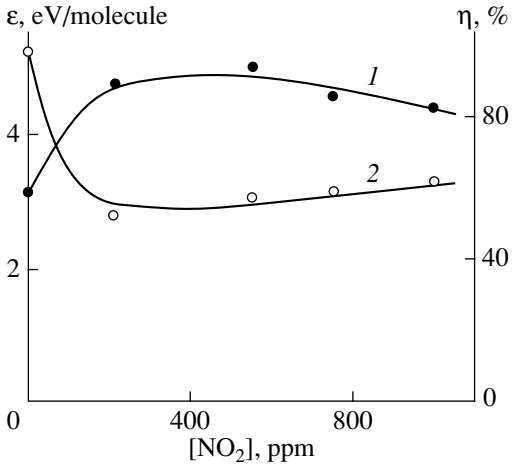

Fig. 2. Energy loss (curve *1*) and conversion efficiency (curve *2*) vs. NO_2 initial concentration upon removing sulfur dioxide. The SO_2 initial concentration is 3600 ppm.

Figure 3a shows the analytical time dependences of the negative oxygen ion concentration. The presence of the nitrogen oxides reduces the O_2^- concentration only slightly; that is, the competition between charge exchange reactions (2) and (11) has a minor effect on the efficiency of chain mechanism (2)–(6).

In the presence of the nitrogen oxides, charge exchange reaction (12) reduces the SO_2 removal efficiency to the greatest extent. Simplified calculations demonstrate that the addition of NO_2 in an amount of 500 ppm drastically reduces the SO_2^- ion concentration

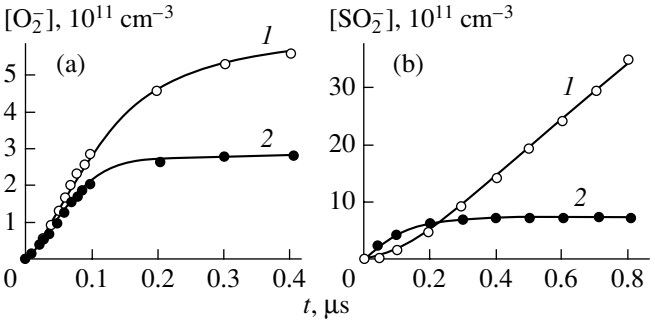

Fig. 3. Results of simplified calculation: time dependences of the (a) O_2^- and (b) SO_2^- concentrations in the (*1*) absence and (*2*) presence of NO_2.

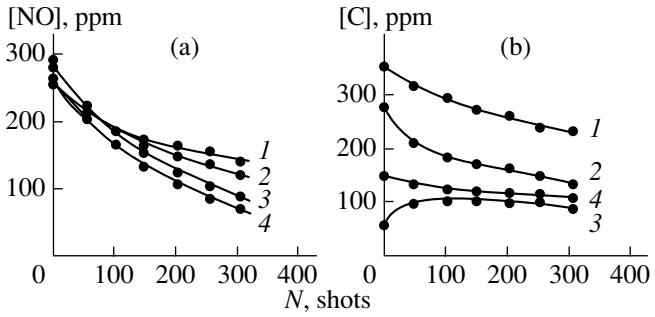

Fig. 4. Impurity concentrations vs. number of shots. (a) Nitrogen monoxide NO for [SO_2] = (*1*) 100, (*2*) 300, (*3*) 500, and (*4*) 0 ppm; (b) (*1*) sum of the nitrogen oxides NO_x, (*2*) NO, (*3*) NO_2, and (*4*) SO_2.

(Fig. 3b). Accordingly, the probability of the chain oxidation mechanism also decreases. Eventually, the SO_2 conversion drops and the energy spent on the removal of a SO_2 molecule rises (Fig. 2).

On the other hand, the nitrogen oxides added in sufficiently large amounts intensify the chemical mechanism of SO_2 conversion. This becomes possible when SO_2 oxidizes to SO_3 in the presence of NO_2 [19, 20] and SO_3 combines with water molecules to form sulfuric acid:

$$SO_2 + NO_2 \longrightarrow NO + SO_3, \quad (13)$$

$$SO_3 + H_2O \longrightarrow H_2SO_4. \quad (14)$$

Quantitative estimates made for our experimental conditions (for example, for curve *2* in Fig. 1 when N = 300) show that with the rate constant of reaction (13) $k_{13} = 4.1 \times 10^{-21}$ cm^3/s [20], the concentration of SO_2 molecules converted by reactions (13) and (14) is $\sim 10^{16}$ cm^{-3}. The value found experimentally (curve *2* in Fig. 1) is $\Delta[SO_2] \approx 6 \times 10^{16}$ cm^{-3}. The fairly good agreement between the calculated and experimental values indicates that reaction mechanism (13), (14) may indeed raise the degree of purification and reduce the energy consumption.

NITROGEN OXIDE CONVERSION

When the gaseous mixture is subjected to an electron beam, nitrogen oxides are removed primarily by the gas-phase oxidation of NO_x following the free-radical mechanism [1, 2]. As was noted in the Introduction, fast electrons of the beam generate free atoms and radicals, which interact with NO_2 molecules:

$$NO_2 + N \longrightarrow 2NO, \quad (15)$$

$$NO_2 + N \longrightarrow N_2 + 2O, \quad (16)$$

$$NO_2 + N \longrightarrow N_2 + O_2, \quad (17)$$

$$NO_2 + O \longrightarrow NO + 2O, \quad (18)$$

$$O + NO_2 \longrightarrow O_2 + NO, \quad (19)$$

$$NO_2 + OH \longrightarrow HNO_3. \quad (20)$$

Nitrogen monoxide rapidly oxidizes to dioxide by the reaction

$$2NO + O_2 \longrightarrow 2NO_2. \quad (21)$$

It has been shown [21] that in flue gases with a low oxygen content, NO_2 conversion is not necessarily accompanied by the formation of the acid as a final product. Atomic nitrogen may interact with NO_x oxides by reactions (15)–(17) to form atomic and molecular oxygen and nitrogen [reactions (16), (17), and (19)].

The reduction of the NO_x concentration in the $N_2 : O_2 : H_2O \approx 89 : 10 : 1$ mixture subjected to electron shots is shown in Fig. 4. In these runs, the initial concentration of NO_x was 260–295 ppm. As the number of shots grows, the nitrogen oxide concentration decreases, the decrease being the most pronounced in the absence of SO_2 (curve *4*). The addition of SO_2 in small amounts (100–200 ppm) retards the process of nitrogen oxide removal substantially. Figure 4b illustrates the concentrations of NO_x, NO, and NO_2, as well as of SO_2, vs. number of shots in the mixture with 150 ppm SO_2. The curves for NO, NO_2, and NO_x = NO + NO_2 run similarly to those in the absence of SO_2 [10]. The concentration of SO_2 smoothly declines, which also agrees qualitatively with the previous results [9].

Figure 5 depicts the dependences of ε and η on the initial concentration of SO_2 in the mixture (curves *1* and *2*, respectively). The number of shots was 300 for each of the experimental curves. The presence of SO_2 is seen to increase the energy loss per NO_2 molecule. The conversion η declines when the amount of SO_2 rises to 100–300 ppm and then varies insignificantly with SO_2 amount. These experiments were carried out for the mixture having water vapor in amounts insufficient for

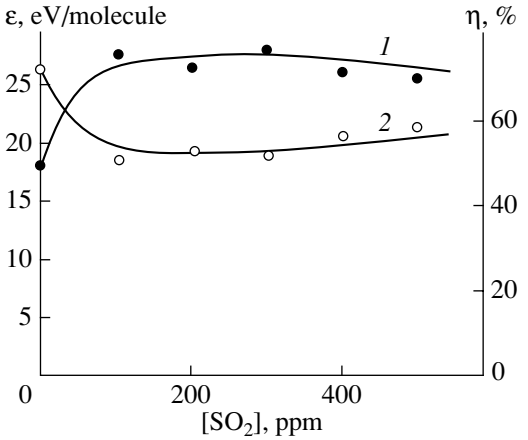

Fig. 5. (*1*) Energy loss and (*2*) degree of purification upon removing NO_x vs. initial concentration of SO_2. The initial concentration of NO_x is 280 ppm.

aerosols to form and NO_x heterogeneous oxidation [6, 7] to proceed. With aerosols formed by liquid-phase reactions in the mixture, the addition of SO_2 improves the NO_x conversion and favors the removal of SO_2 [22].

For our experiments, it seems unlikely that the attachment of thermalized electrons to SO_2 molecules adversely affects the conversion of NO_2. Appropriate estimates show, as before, that the free electron concentration changes insignificantly. Moreover, the energy of the thermalized electrons, which effectively take place in attachment reactions (10) and (22), is insufficient for the mixture molecules to dissociate and free radials to form in detectable amounts. Hence, the loss of the electrons in reactions (10) and (22) is of minor importance for the NO_2 conversion.

The above ionic and molecular reactions involving impurity oxides can also hardly influence the process of NO_2 removal, since charged particles do not participate in nitrogen oxide conversion reactions (15)–(21). The analysis based on the approximate solution of the basic kinetic equations does not allow the elucidation of a kinetic mechanism behind the conversion efficiency variation observed in our experiments. The clarification of this mechanism calls for special experiments in which the variation of the reactive particle concentration both during and after irradiation in a wide time interval can be traced.

CONCLUSION

The conversion of sulfur and nitrogen oxides in the model gaseous mixture irradiated by pulsed electron beams was studied. Our experimental data suggest that the presence of both in flue gases reduces the conversion efficiency in comparison with the case when one of the oxides is present.

In the absence of NO_x in the beam-ionized mixture, SO_2 is removed according to the chain mechanism producing SO_2 negative ions. The presence of the nitrogen oxides in the gaseous mixture initiates the competing charge exchange reaction, which decreases the probability of the SO_2^- negative ions participating in the chain process. In this case, the degree of SO_2 removal declines. As the concentration of NO_x in the mixture rises to 1000 ppm or higher, the chain mechanism of SO_2 conversion fails and SO_2 molecules are removed via SO_2 oxidation reactions involving free radicals and NO_2 molecules. In this case, the purification efficiency somewhat rises.

The effect of SO_2 on the conversion of NO_x oxides under electron beam radiation shows up in a similar way at first glance: the conversion of NO_x decreases with SO_2 added in small amounts but somewhat rises when the SO_2 concentration exceeds some critical value. However, the kinetic mechanism behind this effect remains unclear and calls for further investigation.

ACKNOWLEDGMENTS

This work was financially supported by the International Science and Technology Center (project no. 271).

REFERENCES

1. A. A. Valuev, A. S. Kaklyugin, G. É. Norman, *et al.*, Teplofiz. Vys. Temp. **28**, 995 (1990).
2. *Non-Thermal Plasma Techniques for Pollution Control*, Ed. by B. M. Penetrante and S. E. Schultheis (Springer-Verlag, Berlin, 1993), NATO ASI Series, Vol. G34, Parts A, B.
3. S. Jordan, Radiat. Phys. Chem. **34**, 21 (1988).
4. H. Matzing, *Non-Thermal Plasma Techniques for Pollution Control*, Ed. B. M. Penetrante and S. E. Schultheis (Springer-Verlag, Berlin, 1993), NATO ASI Series, Vol. G34, Part A, p. 59.
5. G. Ya. Gerasimov, T. S. Gerasimova, V. N. Makarov, and S. A. Fadeev, Khim. Vys. Énerg. **30**, 34 (1996).
6. B. V. Potapkin, M. A. Deminsky, A. A. Fridman, and V. D. Rusanov, Radiat. Phys. Chem. **45**, 1081 (1995).
7. G. Ya. Gerasimov, T. S. Gerasimova, and S. A. Fadeev, Khim. Vys. Énerg. **30**, 410 (1996).
8. D. L. Kuznetsov, G. A. Mesyats, and Yu. N. Novoselov, in *Novel Applications of Lasers and Pulsed Power,* Ed. by R. D. Curry; Proc. SPIE **2374**, 142 (1995).
9. D. L. Kuznetsov, G. A. Mesyats, and Yu. N. Novoselov, Teplofiz. Vys. Temp. **34**, 845 (1996).
10. G. V. Denisov, Yu. N. Novoselov, and R. M. Tkachenko, Pis'ma Zh. Tekh. Fiz. **24** (4), 52 (1998) [Tech. Phys. Lett. **24**, 146 (1998)].
11. Y. Nakagawa and H. Kawauchi, Jpn. J. Appl. Phys. **37**, 91 (1998).

12. K. A. Garusov, D. L. Kuznetsov, Yu. N. Novoselov, and V. V. Uvarin, Prib. Tekh. Éksp., No. 3, 180 (1992).
13. V. V. Generalova and M. N. Gurskiĭ, *Dosimetry in Radiation Technology* (Izd. Standartov, Moscow, 1981).
14. E. A. Khudyakova and A. P. Kreshkov, *Theory and Practice of Conductometric Analysis* (Khimiya, Moscow, 1976).
15. E. I. Baranchikov, G. S. Belen'kiĭ, V. P. Denisenko, *et al.*, Dokl. Akad. Nauk SSSR **315**, 120 (1990).
16. V. V. Lunin, M. P. Popovich, and S. N. Tkachenko, *Physical Chemistry of Ozone* (Mosk. Gos. Univ., Moscow, 1998).
17. B. M. Smirnov, *Negative Ions* (Atomizdat, Moscow, 1978; McGraw-Hill, New York, 1982).
18. L. I. Virin, R. V. Dzhagatspanyan, G. V. Karachevtsev, *et al.*, *Ion-Molecule Reactions in Gases* (Nauka, Moscow, 1979).
19. V. N. Kondrat'ev and E. E. Nikitin, *Kinetics and Mechanism of Gas-Phase Reactions* (Nauka, Moscow, 1974).
20. V. N. Kondrat'ev, *Gas-Phase Reaction Rate Constants* (Nauka, Moscow, 1970).
21. G. V. Denisov, Yu. N. Novoselov, and R. M. Tkachenko, Pis'ma Zh. Tekh. Fiz. **26** (16), 30 (2000) [Tech. Phys. Lett. **26**, 710 (2000)].
22. M. A. Deminskiĭ, A. N. Ermakov, G. A. Poskrebyshev, *et al.*, Khim. Vys. Énerg. **33**, 44 (1999).

Translated by V. Isaakyan

Technical Physics, Vol. 47, No. 5, 2002, pp. 621–627. Translated from Zhurnal Tekhnicheskoĭ Fiziki, Vol. 72, No. 5, 2002, pp. 108–114.

EXPERIMENTAL INSTRUMENTS AND TECHNIQUES

Momenta of the Particles Emitted by a Target Heavily Irradiated with Low-Energy Ions

V. G. Beshenkov, A. B. Grigor'ev, and V. A. Marchenko

Institute of Microelectronic Technology and High-Purity Materials, Russian Academy of Sciences, Chernogolovka, Moscow oblast, 142432 Russia

e-mail: marchenk@ipmt-hpm.ac.ru

Received July 30, 2001; in final form, December 7, 2001

Abstract—The total momenta of the particles emitted by a target intensely sputtered with heavy noble-gas ions with an energy of $E_0 \approx 0.5$ keV are measured. For liquid Ga targets and Ga targets at the premelting temperature, the measured momenta are close to the expected values for the sputtered metal atoms and reflected ions, whereas for Cu and Zr targets, the measured momenta are significantly higher. It is assumed that these excessive momenta are related to the sputtering of the noble gas atoms implanted into the target. The average energy of these atoms is estimated as $\langle E \rangle \approx 20$ eV. When gallium is irradiated, the implanted atoms diffuse predominantly to the surface and then are desorbed. © *2002 MAIK "Nauka/Interperiodica".*

INTRODUCTION

Ion sputtering techniques (including ion–plasma sputtering) are widely used for film deposition. The nature and energy of the particles emitted by the target and affecting the condensation surface determine the growth process and the final film parameters. It is known that the bombardment of the deposited film with high-energy particles enhances the mobility of the surface atoms (which allows one to decrease the temperature of epitaxial growth), stimulates the dissociation of molecules and the desorption of the surface atoms, modifies the film structure, and can even lead to resputtering, which, in many cases, changes the film composition. The threshold energies for these processes are close to the corresponding binding energies, whose values, in solids, amount to a few electronvolts.

In the course of ion–plasma sputtering, the growing surface is irradiated with the particles emitted from the target, as well as with the ions and electrons of the plasma adjacent to the film, which are not taken into account here.

In the steady-state phase of sputtering, the irradiation of the target with an ion beam with the current density j results in the emission of atoms and electrons from the target with the flux densities Yj and γj, respectively. Because of the steady-state condition, the flux of the gas atoms leaving the target is equal to the ion flux. The fraction Rj of this flux consists of the reflected former ions, and the rest fraction of the flux, $(1 - R)j$, consists of the ions previously absorbed (implanted) in the target surface layer. Here, Y, γ, and R are the sputtering yield, the coefficient of ion–electron emission, and the ion reflection coefficient, respectively.

The energy spectra of the sputtered metal atoms were measured with various techniques [1–5]. The characteristic average energies are on the order of 10 eV. The energies of the reflected metal ions were measured in [6, 7]. For the gas ions, the data were obtained mainly via computer simulations [8]. The implanted gas ions can escape from the target due to either the diffusion of ions toward the surface and their subsequent desorption or the sputtering by the incident ions. In the former case, the ion energy should be on the order of 0.1 eV. In the latter case, the ion energy should be on the order of the characteristic energy of the sputtered atoms. The measurements of the energy released in a target irradiated with noble gas ions [9, 10] showed that, at $j \sim 1$ μA cm^{-2}, the former case is realized. At $j \sim$ 1–10 mA cm^{-2}, which is characteristic of magnetron sputtering, we could not find any published data on mechanism for the escape of the implanted gas ions, as well as on the energy of escaping ions.

Under the conditions of intense ion bombardment, the outer sputtered target layer constitutes a solution of the implanted atoms of a reaction gas in the initial target material [11]. The fraction of the sputtered gas atoms must be proportional to their concentration in the sputtered layer. By solving the diffusion equation, it was shown that the gas atom concentration increases with increasing j/D ratio, where D is the coefficient of gas diffusion in the target material. Thus, we can assume that, the higher j, the higher the fraction of the sputtered gas atoms and the smaller the fraction of the desorbed atoms in the flux of gas atoms emitted from the target.

In this study, the total momenta of the particles emitted from the target under the conditions of magnetron sputtering with Ar^+, Kr^+, and Xe^+ ions, which have different masses and, consequently, different reflection coefficients R, were measured using a force probe. For targets made from Cu or Zr + 15%Y alloy, the total

Table 1. Sputtering regimes

Target	P, Pa	U_c, V	I_c, mA	$v_d(0)$, 10^{16} at/s cm^2	$F_{meas}(0)$, dyn/cm^2	γ	α_n	Y
Ar/Cu	0.66	447	205	2.5	1.93	0.1	0.65	1.9
Kr/Cu	0.38	550	168	2.3	1.50	0.05	0.8	2.1
Xe/Cu	0.16	635	142	2.1	1.42	0.02	0.88	2.25
Ar/Ga	0.66	473	197	2.2/2.8*	1.18/1.3		0.64	
Kr/Ga	0.47	604	152	2.33/n.d.	1.03/n.d.		0.78	
Xe/Ga	0.23	705	124	2.6/2.7	0.93/0.92		0.86	

* Solid/liquid targets.

momenta turn out to be much higher than the sputtered metal atom momenta calculated based on the energy spectra (including those for Kr^+ and Xe^+ ions, whose reflection coefficients are small) taken from the literature. For liquid Ga targets and Ga targets at the premelting temperature, the measured momenta are close to the expected momenta of the sputtered metal atoms. It is assumed that the excessive momentum observed in sputtering Cu and Zr–Y targets is related to the sputtering of the implanted gas atoms that were captured by the radiative lattice defects. In Ga targets, due to the fast diffusion and thermal annealing of the lattice defects (both provoked by the high temperature close to the melting temperature), the major part of the implanted atoms have time to escape to the surface and then to be desorbed.

Since the energy spectra of the sputtered metal atoms are studied most comprehensively for copper, the calculations of different contributions to the measured force turn out to be more exact for a Cu target than for a Zr–Y target. In the latter case, the results will only be briefly discussed.

EXPERIMENTAL

The data presented in Table 1 were obtained under the conditions of dc magnetron sputtering of targets 76 mm in diameter. The calculated heating of a Cu target soldered to a water-cooled cathode is no more than 1°C. The Ga targets were either solid (T_{sol} = 20°C = $0.97T_{melt}$, where T_{melt} is the melting temperature) or melted (T_{liq} = 50°C). The sputtering rates, as well as the measured forces, turned out to be nearly the same for all Ga targets (Table 1). The ion (I_i) and electron (I_e) components of the cathode current I_c were calculated taking into account the relation $I_e/I_i = \gamma$. The γ value for copper was assumed to be equal to that for tungsten (taken from [12]), because their electron work functions are close to each other. For a Cu target in argon, krypton, and xenon, the ion current density j averaged over the erosion zone is 7.8, 6.4, and 5.4 mA/cm^2, respectively; in the center of the erosion zone, the corresponding values are twice as high.

The distance from the target to the substrates and the measuring plate of the force probe was H = 22 mm, which provided the high sensitivity of the calculated radial profiles of the thickness to the model angular dependences of the escape probability. The radial profiles of the deposition rate $v_d(R)$ were obtained from the profilometric measurements of the film thickness.

A permanent-magnet microamperemeter with a measuring plate attached to a pointer tip [13] was used as a force probe. When the discharge was switched on, the plate underwent a force determined by the change in the momenta of the particles colliding with the plate, including those not emitted from the target. An analysis of the forces acting on the measuring plate due to the desorption of atoms from its surface, impacts by the ions and electrons from the adjacent plasma, and the light pressure showed that, under the experimental conditions, either their values were negligible or the forces acting on the lower and upper (facing the magnetron) plate sides balanced each other. The force induced by the heating of the reaction gas in the space between the magnetron and the probe will be discussed below.

To minimize the scattering of the particles emitted from the target by the reaction gas atoms, the pressure P was kept near the lower threshold for stable discharge operation. The probe measurements of the plasma floating potential near the target surface showed that, at the pressures employed, the thickness of cathode sheath ($d \approx 0.5$ mm) was 6–10 times shorter than the charge-exchange mean free path for Ar^+ ions [14]. Thus, the spectrum of the ions incident onto the target was close to monoenergetic with $E_i \approx E_0 = eU_c$, where U_c is the cathode potential.

The measurements showed that, at $P < 2$ Pa, the normalized radial distributions of the force and the film thickness did not depend on the pressure, which indicated that the scattering processes in the gas only slightly affected the trajectories of the sputtered particles. The transport regime for sputtered atoms was close to the ballistic one, which was confirmed by the estimates of their mean free path l. At incident ion energies of $E_0 \geq 400$ eV, the average energy of sputtered Cu atoms is $\langle E \rangle \approx 10$ eV (see below). At this energy, the

effective cross sections for momentum scattering are 6 times lower than the thermal ones [14]. In argon at $P = 0.66$ Pa, we have $l \approx 6$ cm, which is nearly three times longer than the distance to the magnetron.

Before the film deposition and the measurements with a force probe, the target was treated with ions at an average dose over the erosion zone of no less than 10^{20} cm^{-2}, which, according to optical microscopy measurements, enabled the steady-state level of the target surface microroughness.

ESTIMATION OF THE CONTRIBUTIONS TO THE MEASURED FORCE

1. The radial profile of the force $F_{me}(R)$, induced by the sputtered metal atoms, was determined by using the ballistic transport approach:

$$F_{me}(R) = (2-\alpha_n)\int A(r) f(\Theta) \times \cos\Theta \langle p(\Theta)\rangle \cos\Theta \rho^{-2} r d\varphi dr. \quad (1)$$

Under these conditions, the film deposition rate is

$$v_d(R) = \int A(r) f(\Theta) \cos\Theta \rho^{-2} r d\varphi dr, \quad (2)$$

where φ and r are the running target coordinates; $\Theta = \arccos(H/\rho)$ is the angle between the normal to the target and the escape direction; $\rho^2 = H^2 + R^2 + r^2 - 2rR\cos\varphi$; $f(\Theta)$ is the probability of escape at the angle Θ; $A(r)$ is the sputtering rate at the running point on the target (this rate was assumed to be proportional to the measured depth of the erosion zone); $\langle p(\Theta)\rangle\cos\Theta = p_\perp$ is the vertical component of the average momentum of the particles escaped from the target at the angle Θ; $\langle p\rangle = (2M)^{0.5}\langle E^{0.5}\rangle = (2M)^{0.5}\int E^{0.5} N(E) dE$, where $N(E)$ is the sputtered atom energy distribution function (AEDF); and $\alpha_n = (p_{\perp inc} - p_{\perp refl})/p_{\perp inc}$ is the accommodation coefficient for the vertical component of the momentum [15] (for metal atoms, $\alpha_n = 1$).

The angular distribution of the sputtered copper atoms,

$$f(\Theta) = 0.12\{\cos^{0.5}\Theta + 0.04/[(\cos\Theta - 0.735)^2 + 0.02]\},$$

was determined by fitting the results of the numerical integration of expression (2) with different trial functions $f(\Theta)$ to the measured values of $v_d(R)$. The angular dependence with a maximum at $\Theta \approx 42°$ seems to be a result of the target surface microroughness caused by intense ion etching [16, 17].

The sputtering yield Y (Table 1) was obtained by integrating $v_d(R)$ over the entire surface and the subsequent division of the result by I_i.

Most AEDFs available in the literature [1–4] were measured within the energy range up to 27–40 eV. An analysis of these AEDFs shows that, for various ions, targets, and escape directions, in the ion energy range

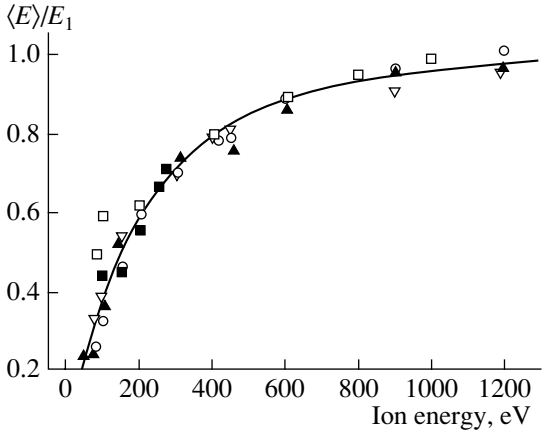

Fig. 1. Average energy of the sputtered atoms vs. ion energy: (squares) Cu–Ar$^+$, E_1 = 8.4 eV [3]; (circles) Cu[110]–Kr$^+$, $\Theta = 0$, E_1 = 9.8 eV [1]; (open triangles) Cu[110]–Kr$^+$, $\Theta = 60°$, E_1 = 15.4 eV [1]; (closed triangles) Ag[110]–Hg$^+$, $\Theta = 60°$, E_1 = 8.0 eV [2]; and (closed squares) Au$^-$–Ar$^+$, E_1 = 10.4 eV [4]. The solid curve shows the fitting function (3).

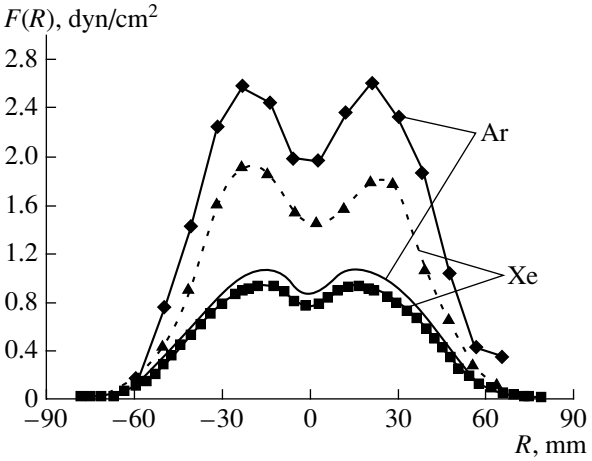

Fig. 2. Measured (symbols) and calculated (solid line) profiles of the forces induced by Cu atoms.

characteristic of magnetron sputtering, the average energy $\langle E_{me}\rangle$ of the target atoms can be satisfactorily described by the dependence

$$\langle E_{me}\rangle = E_1[1 - 1/(0.0017E_0 + 1)^3], \quad (3)$$

where E_1 is determined by the target material and the ion species (Fig. 1). By analyzing the AEDFs from [1–5], it was also shown that all the energy spectra are characterized by nearly the same ratio $\langle E\rangle^{0.5}/\langle p\rangle = (1.08 - 1.16)/(2M)^{0.5}$, where M is the metal atomic mass. We took this into account when calculating F_{me} by formula (1). According to the data from [1], the average momenta of the sputtered atoms depend slightly on the escape angle. In our calculations, we used the fitting expression $\langle p(\Theta)\rangle = \langle p(0)\rangle[1 - 0.1\cos(1.6\Theta)^2]$.

Table 2. Calculated contributions to the force measured

	$\langle E_{me}\rangle$, eV	$F_{me}(0)$, dyn/cm^2	$F_{refl}(0)$, dyn/cm^2	$F_{t1}(0)$, dyn/cm^2	$F_{t2}(0)$, dyn/cm^2	$F_{meas} - F_{me} - F_{refl}$, dyn/cm^2	$\langle E_g\rangle$, eV
Ar/Cu	9.57	0.85	0.2	≤0.04	<1.0	0.86	24
Kr/Cu	10.1	0.82	0.02		<0.68	0.66	29
Xe/Cu	10.4	0.75	<0.01	≤0.01	<0.08	0.67	16
Kr/Ga		1.0				<0.03	<0.07

The energy spectra at high energies (although with a lower resolution in the low-energy range) were measured in [5]. A comparison of the data from [3, 5] on copper sputtering at close energies of Ar^+ ions (400 and 410 eV) shows that taking into account the high-energy part of the distribution function increases the average energy and average momentum of Cu atoms by 40 and 13%, respectively, and that about 7% of the sputtered copper atoms have energies higher than 27 eV. The column $\langle E_{me}\rangle$ of Table 2 presents the calculated average energies of the Cu atoms (with allowance for the 40% addition) sputtered normally to the target surface for the cathode voltages employed. The contribution of the Cu atoms to the measured force is shown in Fig. 2. The values in the column $F_{me}(0)$ of Table 2 correspond to $R = 0$. Taking into account a slight scatter in the literature data on the AEDF for copper, we estimated the error in determining this force component as 5%. The radial force profiles obtained when sputtering in krypton are not shown in Fig. 2; they are similar to those in xenon, the force amplitude being slightly higher (see the corresponding values of $F_{meas}(0)$ and $F_{me}(0)$). For a Ga target, the force and the deposition rate were only measured in front of the magnetron center. To calculate the force induced by Ga atoms, the data from [2] on the average velocity of the atoms knocked out by Kr^+ ions from various targets were used. The average velocity of Ga atoms $\langle v_{Ga}\rangle$ was assumed to be equal to that for Ge (the next element in the periodic table for which, together with Cu, the measurements were carried out in [2]); i.e., $F_{Ga} = F_{Cu}(v_{d,Ga}/v_{d,Cu})(M_{Ga}/M_{Cu})(\langle v_{Ge}\rangle/\langle v_{Cu}\rangle)$.

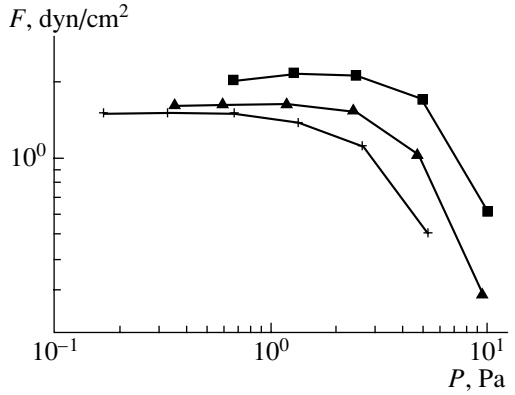

Fig. 3. Force vs. pressure for Ar^+ (squares), Kr^+ (triangles), and Xe^+ (crosses) ions.

2. Reflected ions. Computer simulations based on the molecular dynamics method (the quasi-stable model) with the ZBL interatomic potential [18] used to simulate the reflection of the ions with energies corresponding to the cathode potentials employed shows that, for a Cu target, the ion reflection coefficients R and the average energies of the reflected ions $\langle E_{refl}\rangle$ (in parentheses) are 0.14 (30eV), 0.02 (10eV), and 0.001 (1.7 eV) for argon, krypton, and xenon, respectively. Simulations of the ion reflection with the help of the TRIM 96 (SRIM variation, version 96.xx) numerical code [19] results in nearly two times lower values of R and $\langle E_{refl}\rangle$. The extrapolation of the simulation results for the reflection of Ar^+ ions with $E_0 = 500$ eV from various metals [8] to Cu gives $\langle E_{refl}\rangle = 51$ eV. In front of the magnetron center, the calculated forces induced by the reflected ions are shown in the column $F_{refl}(0)$ of Table 2 (these values were calculated by Eq. (1) using the maximum R_i and $\langle R_{refl}\rangle$ values listed above). The α_n values shown in Table 1 were taken from [15]. In calculations, it was assumed that the angular distribution of the ions reflected from copper was the same as $f(\Theta)$ for the sputtered atoms. The use of another dependence ($f(\Theta) = a\cos\Theta$ or $b\cos^2\Theta$) changes $\langle E_{refl}\rangle(0)$ by no more than 10%. At $M_i/M_{me} > 1$, a significant decrease in R and $\langle E_{refl}\rangle$ with increasing ion mass agrees with both the experimental data for alkali ions [6] and simulation results for noble gas ions [20].

3. The reaction gas atoms in the gap between the magnetron and the force transducer can be heated due to the interaction with high-energy particles. As a result, the flux of gas particles incident onto the measuring plate side facing the magnetron contains high-energy atoms. Hence, the pressures on the opposite sides of the plate will be different. One of the reasons for gas heating is collisions with the atoms emitted from the target. Since the collision frequency is proportional to the gas density, the corresponding force F_{t1} acting on the measuring plate should be proportional to the pressure.

For a Cu target, the pressure dependences of the force are shown in Fig. 3. In argon, the decrease in the force with increasing pressure is accompanied by a decrease in the deposition rate [21]. Separating the term

linear in the pressure from these dependences (with allowance for the decrease in the deposition rate) shows that it does not exceed the F_{t1} values presented in Table 2.

The reaction gas is also heated due to the interaction with the electrons magnetized in the plasma torus near the cathode. Because of the complexity of the plasma processes, it is hardly possible to exactly calculate the corresponding force. An overestimated value can be obtained from the electron power balance in the discharge.

The parts W_i and W_{gh} of the total energy W_e of the electrons escaped from the target are spent on gas ionization and heating, respectively. The rest energy W_{other} is released at an anode and other components of the chamber (this term also includes the radiation of the gas atoms excited by electron impact):

$$W_e = I_e U_c = \gamma I_c U_c/(1+\gamma) = W_i + W_{gh} + W_{other}.$$

Since the discharge is self-sustained, each electron should ionize, on the average, no less than $n_{eff} = 1/\gamma$ gas atoms in order to compensate for the ion loss at the cathode; i.e., $W_i \geq I_e n_{eff} U_i$, where U_i is the ionization energy. The rest energy, which is spent on the heating of the gas and the chamber wall, amounts to

$$W_{gh} + W_{other} = W_e - W_i \leq I_c(\gamma U_c - U_i)/(1+\gamma).$$

The values of the F_{t2} force acting on the upper side of the measuring plate are given in Table 2. These values are certainly overestimated because they are calculated under the assumption that all the rest energy is spent on increasing the kinetic energy of gas atoms in the plasma torus.

For xenon, the F_{t2} values estimated in this way are significantly lower than the quantity $F_{meas} - F_{me} - F_{refl}$ (Table 2). For krypton, the contribution from gas heating to the measured force should also be significantly lower than the calculated value F_{t2}. At nearly the same discharge parameters, the sputtering of Ga in krypton is characterized by the F_{meas} and F_{me} values close to each other (Tables 1 and 2). For the sputtering of Ga in argon and krypton, the contribution from the reflected argon ions is sufficient to account for the different F_{meas} values. Presumably, the replacement of the noble gas species results in a similar change in F_{me} for Ga and Cu targets. Hence, for Cu sputtering in argon, the contribution from gas heating is expected to be no higher than 0.1 dyn/cm^2.

DISCUSSION OF THE RESULTS

The above estimates show that, when copper is sputtered with an ion beam at a current density of $j \approx 5$–8 mA/cm^2, nearly one-half of the momentum measured is brought by the metal atoms, whereas the contributions from the reflected ions are significantly lower. For xenon, the thermal contribution is low; the above qualitative considerations allow us to assume that it is also low for argon and krypton. It is natural to suggest that the rest force $F_{meas} - F_{me} - F_{refl} - F_t$ is related to the momenta of the ions implanted into the target and then escaping from it. The outward flux of these ions is equal to the ion current minus the reflected one. The average kinetic energy of these ions $\langle E_g \rangle = \langle p \rangle^2/2M$, shown in Table 2, is comparable to the characteristic energies of the sputtered atoms ($\langle E_g \rangle$ was estimated neglecting the thermal contribution). A close value of $\langle E_g \rangle$ was obtained when sputtering Zr–Y alloys. Thus, it is reasonable to assume that, under intense irradiation of these targets, the implanted ions are predominantly sputtered. Then, in the sputtered flux, their fraction with respect to the fraction of Cu atoms is $\approx(1 - R)/Y$. Provided that difference between the partial sputtering coefficients is not too high, the concentration of the implanted atoms near the surface should be comparable to this value, because it is the atoms from the outer monolayers of the target that are knocked out. However, the measurements of the surface concentration of argon in copper carried out with the help of Auger spectroscopy (the effective thickness of the layer under study is $t \approx 0.5$ nm) during ion sputtering showed that the concentration is no higher than 1%. The acting ion current density is ~1 μA/cm^2, and, due to the apparatus limitations, it cannot be significantly increased. At this ion current density, the low Ar concentration presumably points in favor of the desorption mechanism. The measurements of the energy absorbed in a Cu target irradiated with a noble-gas ion beam with a current density of $j \sim 1$ μA/cm^2 also indicate the predominant desorption of the implanted atoms [9].

In the magnetron sputtering of gallium, the estimated momentum of metal atoms is close to the measured one. This indicates that the energy of the escaped implanted ions is low (Table 2) and, within the considered mechanisms for the escape of gas atoms from the target, suggests their rapid diffusion to the surface and the subsequent desorption. More rapid diffusion in Ga as compared to Cu and Zr–Y targets can be related to the fact that the Ga melting temperature is close to the cathode temperature.

It is known from the literature on implantation (see, e.g., [11]) that the implanted atoms, after being irradiated, are captured by the radiative defects. Under the action of persistent ion bombardment, the formerly captured gas atoms can be activated, leave the places of location, and diffuse toward other free trapping centers or the surface. Under continuous irradiation, the steady-state gas concentration in the target will be determined by the condition for the rate of ion supply (ion current density j) to be equal to the rate of ion escape. Assuming that the gas atoms move due to diffusion and ignoring the atoms sputtering, one can easily determine the dependence of the gas atom concentration in the surface layers of the target on j.

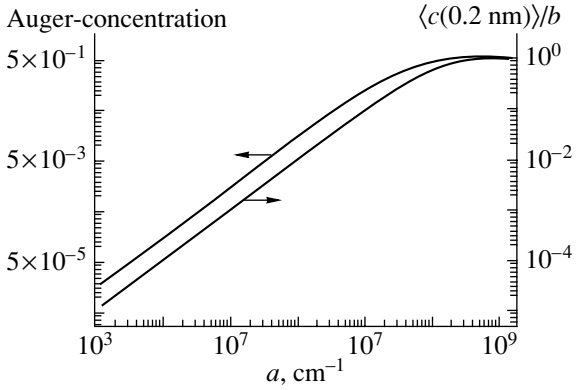

Fig. 4. Average calculated concentration of Ar atoms in the outer monolayer in copper during irradiation and the concentration measured with an Auger spectrometer.

Let $f(z)$ be the distribution of the projective ranges, $\int f(z)dz = 1$, $v = jY/N$ be the velocity at which the outer target boundary is displaced due to sputtering, and N be the target atom density (atom/cm^3). The concentration c of the noble gas in the target is described by the equation

$$dc/dt = Dd^2c/dx^2 + j(1 - R)f(x - vt),$$

where the first term on the right-hand side is responsible for diffusion and the second one is responsible for implantation.

Under the assumption that all the noble gas atoms arriving at the surface are immediately desorbed, the first boundary condition is $c(x = vt) = 0$. Perhaps, this assumption is too strict for materials with a high density of defects (e.g., the lifetime of the noble gas atom on the surface is not known). The second boundary condition, $-Ddc/dx(x = vt) = j(1 - R)$, means that the flux of the ions entering the target surface is equal to the flux of the gas atoms escaping from the target. We introduce the $z = x - vt$ coordinate reckoned from the running target surface. Then, for the relative concentration $c = c/N$ in the steady-state phase of sputtering ($dc/dt = 0$), we have

$$\begin{aligned} d^2c/dz^2 + adc/dz &= -abf(z); \\ a = jY/DN, \quad b &= (1 - R)/Y, \\ c(0) = 0; \quad -Ddc/dz(0) - vc(0) &= j(1 - R). \end{aligned} \tag{4}$$

To simplify calculations, the function $f(z)$ was taken in the form

$$f(z) = 0, \quad z \le 0, \quad z \ge 2R_p,$$

$$f(z) = z/R_p^2, \quad 0 \le z \le R_p,$$

$$f(z) = (2R_p - z)/R_p^2, \quad R_p \le z \le 2R_p,$$

where R_p is the mean projective range.

Solving Eq. (4) by the Green's function method, we obtain the steady-state concentration of the gas atoms in the target,

$$c(z) = b[1 - \exp(-az)] + c_n(z),$$

$$c_n(z) = (b/a^2R_p^2)[\exp(-az) + az - 1 - (az)^2/2],$$

$$0 \le z \le R_p,$$

$$c_n(z) = (b/a^2R_p^2)[a^2R_p^2 - 2\exp(aR_p - az) + \exp(-az)$$

$$- 2a^2R_pz + a^2z^2/2 + 2aR_p - az + 1], \quad R_p \le z \le 2R_p.$$

To give an idea of the gas atom concentration in the outer monolayer, which mainly supplies the sputtered particles, Fig. 4 shows the dependences of both the $\langle c(0.2\text{ nm})\rangle$ average concentration (calculated from $\int c(z)\exp(-z/t)dz/t$ in the 0.2-nm-thick surface layer and the Auger concentration on the parameter $a = jY/DN$ (computer simulations by the TRIM code show that, for copper in the ion energy range under study, $R_p \approx 0.8$ nm). At large a values, both concentrations saturate, so that $\langle c(0.2\text{ nm})\rangle = (1 - R)/Y \approx 0.5$. As the parameter aR_p decreases, the concentration in the outer monolayer decreases linearly with $a \sim j/D$. In order that the concentration measured with an Auger spectrometer be no higher than 1%, we should have $a \le 0.75 \times 10^6$ cm^{-1}. Assuming that, during the magnetron sputtering of copper, $\langle c(0.2\text{ nm})\rangle$ is no lower than 90% of the limiting value and taking into account the current densities in the magnetron and the ion gun of an Auger spectrometer, we estimate the effective coefficient of argon diffusion as $2 \times 10^{-16} < D < 3 \times 10^{-15}$ cm^2/s.

CONCLUSION

When irradiating a target with noble gas ions, the implanted noble gas atoms can escape due to both desorption and sputtering. The average energy of the sputtered noble gas atoms is $\langle E_g\rangle \approx 20$ eV. At low ion current densities and the high coefficients of implanted atom diffusion (the low-melting targets), the desorption mechanism prevails; otherwise, the sputtering occurs.

ACKNOWLEDGMENTS

We are grateful to V.N. Mordkovich and M.Yu. Barabanenkov for continuous interest in this work and the discussion of the results. This study was supported by the Russian Foundation for Basic Research, project no. 99-03-32755.

REFERENCES

1. R. V. Stuart and G. K. Wehner, J. Appl. Phys. **35**, 1819 (1964).
2. R. V. Stuart, G. K. Wehner, and G. S. Anderson, J. Appl. Phys. **40**, 803 (1969).

3. R. A. Brizzolara, C. B. Cooper, and T. K. Olson, Nucl. Instrum. Methods Phys. Res. B **35**, 36 (1988).
4. Y. Okabe, M. Sasao, M. Wada, *et al.*, Jpn. J. Appl. Phys. **30**, L1428 (1991).
5. T. Mousel, W. Eckstein, and H. Gnaser, Nucl. Instrum. Methods Phys. Res. B **152**, 36 (1999).
6. U. A. Arifov, *Interaction of Atomic Particles with Solid Surfaces* (Nauka, Moscow, 1968; Consultants Bureau, New York, 1969).
7. V. V. Evstigneev, I. V. Ivanov, N. M. Krylov, *et al.*, Poverkhnost, No. 3, 35 (1993).
8. Y. Yamamura, T. Kenmotsu, K. Yorizane, *et al.*, in *Proceedings of the International Conference on Ion Implantation Technology, Kyoto, 1998*, Ed. by J. Matsuo, G. Takaoka, and I. Yamaida, p. 672.
9. H. Coufal, H. F. Winter, and H. L. Bay, Phys. Rev. B **44**, 4747 (1991).
10. H. L. Bay, H. F. Winter, H. Coufal, *et al.*, Appl. Phys. A **55**, 274 (1992).
11. *Sputtering by Particle Bombardment*, Ed. by R. Behrisch (Springer-Verlag, New York, 1983; Mir, Moscow, 1986), Vol. II, Chap. 7.
12. Yu. P. Raizer, *Gas Discharge Physics* (Nauka, Moscow, 1987; Springer-Verlag, Berlin, 1991).
13. A. B. Grigor'ev and V. A. Marchenko, Prib. Tekh. Éksp., No. 5, 146 (1999).
14. R. S. Robinson, J. Vac. Sci. Technol. **16**, 185 (1979).
15. S. F. Borisov, N. F. Balakhonov, and V. A. Gubanov, *Interaction of Gases with Solid Surfaces* (Nauka, Moscow, 1988).
16. J. L. Whitton, *Erosion and Growth of Solids Stimulated by Atom and Ion Beams*, Ed. by G. Kiriakidis, G. Garter, and J. L. Whitton (Martinus Nijhoff, Dordrecht, 1986).
17. A. I. Dodonov, E. A. Krylova, E. S. Mashkova, *et al.*, Poverkhnost, No. 6, 133 (1988).
18. W. Eckstein, *Computer Simulations of Ion–Solid Interactions* (Springer-Verlag, Berlinh, 1991; Mir, Moscow, 1995).
19. J. F. Ziegler, J. P. Biersack, and V. Littmark, *The Stopping and Range of Ions in Solids* (Pergamon, New York, 1985).
20. E. Kay, F. Parmigiani, and W. Parrish, J. Vac. Sci. Technol. A **5**, 44 (1987).
21. A. G. Znamenskiĭ and V. A. Marchenko, Zh. Tekh. Fiz. **68** (7), 24 (1998) [Tech. Phys. **43**, 766 (1998)].

Translated by N. Ustinovskiĭ

Technical Physics, Vol. 47, No. 5, 2002, pp. 628–633. Translated from Zhurnal Tekhnicheskoĭ Fiziki, Vol. 72, No. 5, 2002, pp. 115–120.

EXPERIMENTAL INSTRUMENTS AND TECHNIQUES

Electrical Explosion of a Wire by Microsecond Pulses in a Longitudinal Magnetic Field

A. A. Volkov, E. V. Grebenev, P. S. Dydykin, V. F. Ermolovich, M. M. Ivanov, A. V. Ivanovskiĭ, V. I. Karelin, A. P. Orlov, P. B. Repin, R. V. Savchenko, V. D. Selemir, and V. T. Selyavskiĭ

e-mail: selemir@vniief.ru

Received September 10, 2001

Abstract—The explosion of a tungsten wire in a weak longitudinal magnetic field is studied. The longitudinal magnetic field is shown to decrease the rate of rise of initial perturbations and to stabilize the process. This makes it possible to calibrate analytical models of conduction, equations of state, and radiation paths. Good agreement between observed and analytical electrical and optical patterns of the wire explosion and expansion is obtained. *© 2002 MAIK "Nauka/Interperiodica".*

INTRODUCTION

The electrical explosion of a single wire in a longitudinal magnetic field has been studied in [1, 2]. It was noted that the magnetic field stabilizes the process and makes it possible to significantly heat and accelerate the plasma by generating azimuth currents. Emphasis has been placed on the effect of a strong magnetic field on the current in and the voltage across the wire, as well as on the wire resistance as a function of the energy applied. The magnetic fields were as high as 0.5–0.7 MG with the current in the wire ranging from 30 to 35 kA [2].

In this paper, we report experimental and numerical studies of the electrical explosion of a single tungsten wire in a weak (slightly affecting the expansion dynamics) longitudinal magnetic field B_z = 1–50 kG under the action of a ≈70-kA pulse with a ≈1.1-μs rise time. We concentrated on the stabilizing effect of the longitudinal magnetic field.

Such a study is of both scientific and applied interest. Stable conditions of the explosion and plasma expansion may be used for testing physical models of conduction, equations of state, and radiation ranges in a material that are used in simulations. A possible application of this study may be, for example, the magnetic field compression in the *Z*–Θ-pinch geometry, where a high, δ = 15–22, stable radial compression by a plasma sheath formed from a gas jet has been reached [3, 4] (cf. with the theoretically achievable value δ ≤ 30 [5]). High-power explosive sources of microsecond current pulses (built around disk magnetic explosion generators [6]) for feeding *Z*–Θ pinch allow the generation of ultrastrong magnetic fields [3, 4, 7, 8], quasi-adiabatic compression of a *DT* mixture to provide an intense source of neutrons and, perhaps, thermonuclear ignition [5, 9], and generation of soft X-rays [7, 8]. Such high-power current sources offer a possibility for using plasma sheaths generated by wire arrays exploding in a longitudinal magnetic field.

EXPERIMENT

The setup for studying the electrical explosion of wires due to microsecond current pulses in a longitudinal magnetic field is schematically shown in Fig. 1. Tungsten wire *1* of diameter 70 μm and length l = 15 mm is placed between two graphite electrodes *2* on the axis of a stainless steel thin-walled (0.3 mm) cylindrical (diameter 60 mm, length 200 mm) evacuated (10^{-4} torr) chamber *3*. The chamber has a 20-mm-diam window *4* sealed with a Lavsan film. A quasi-stationary (the characteristic time of variation is 170 μs) longitudinal magnetic field (B_z = 1–50 kG) is created around the wire by Helmholtz coils *5*, placed coaxially with the chamber and spaced at 30 mm. The coils were arranged symmetrically about the electrodes *2*. The axial field

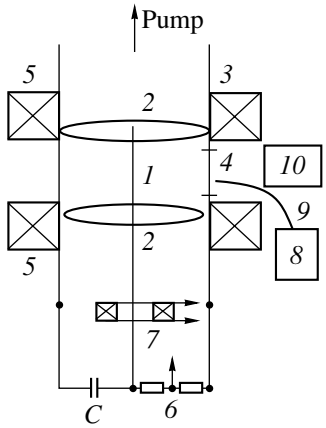

Fig. 1. Setup for studying the electrical explosion of a single wire.

nonuniformity between the electrodes is no higher than 5%. Before explosion, the wire is heated in a vacuum. It explodes at the instant the longitudinal magnetic field pronounced by the 1.2 μ*F* capacitor *C* charged to 40 kV reaches maximum.

In the experiments, we measured the voltage across the wire by divider *6* and the derivative of the current through the wire, by Rogowski loop *7*. The light pulse produced by the explosion and its space–time evolution were recorded with a SNFT-3 photoelectric multiplier *8* equipped with an optical fiber *9* and a streak camera *10*, operating in the frame and slit scan modes. The space and time resolutions of the entire detecting system, built around an electron–optical image converter, are ≈0.13 mm and ≈10 ns, respectively.

EXPERIMENTAL RESULTS

Figure 2 plots typical time waveforms of the derivative *dJ*/*dt*, current *J*, voltage *U* across the wire, and total radiation flux *F* of the process. The electrical characteristics are independent of B_z. The maximum voltage ≈25 kV is achieved ≈70 ns after the pulse has been initiated (i.e., at the instant the wire explodes). The explosion is accompanied by an abrupt increase in the luminance. At the instant of the explosion, the waveform of the current shows a weak singularity (no pause in the current is observed), which is typical of refractory metals [10]. Unlike the electrical characteristics, the integrated (over the length of the wire) luminance depends on B_z significantly (Fig. 3). With increasing B_z, the integrated luminance decreases and irregular spikes observed at small times for $B_z \le 10$ kG disappear.

The space–time evolution of the luminance shows that the value of B_z does not affect the process for $t \gg 1$ μs. At the initial stage, the effect of the magnetic field is however significant. At $B_z = 0$, the process is nonreproducible and irregular along the wire, as indicated by the streak photographs of the glow (Figs. 4, 5a). The photographs were taken with the slit of the streak camera being perpendicular and parallel to the wire, respectively. The inhomogeneities arising during the wire explosion and expansion in a zero magnetic field are clearly seen in the photographs (frame scan mode) shown in Fig. 6a. The expansion of the plasma sheath is accompanied by the development of magnetohydrodynamic (MHD) instability of the Rayleigh–Taylor (RT) type with $m = 0$ and a characteristic wavelength of 1–3 mm. Such phenomena have been observed in many experiments [11, 12] and can be simulated numerically [13, 14].

When a longitudinal magnetic field $B_z \ge B_{cr} \approx 10$ kG is applied, glow appears over the entire wire almost simultaneously and its time behavior is nearly the same in every section (Fig. 5b). The "sausage" structure of the expanding plasma corona, which is typical for $B_z = 0$, is not observed. With $B_z \ge B_{cr}$, the streak photographs become reproducible from run to run (Fig. 7a). The

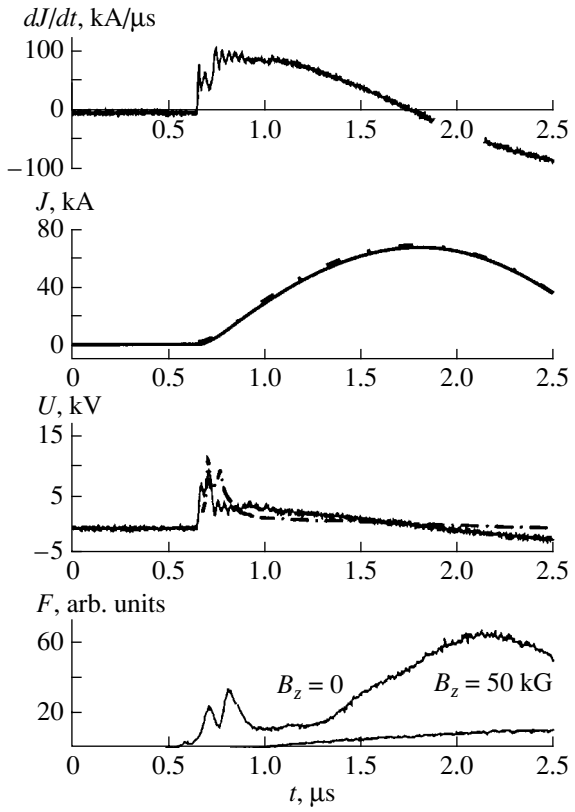

Fig. 2. Time waveforms of derivative of current, voltage, and total radiation flux, solid lines, experiment; dashed lines, simulation.

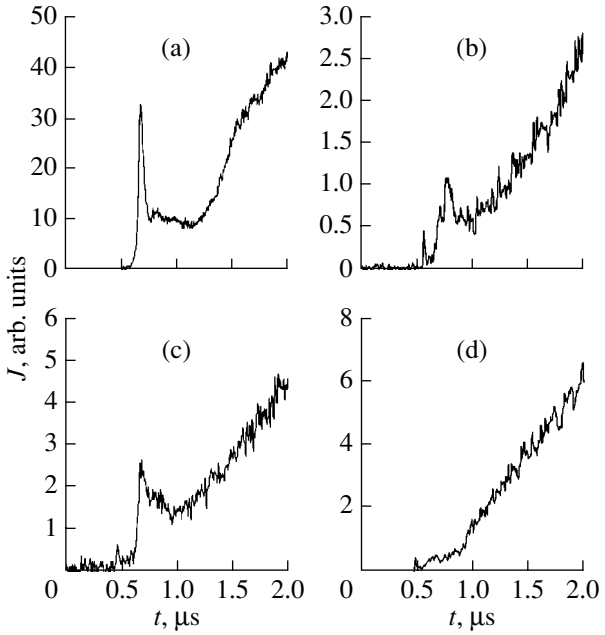

Fig. 3. Time evolution of the integrated (over the wire length) luminance with increasing magnetic field induction: B_z = 1.2 (a), 10 (b), 5 (c), and 20 kG (d).

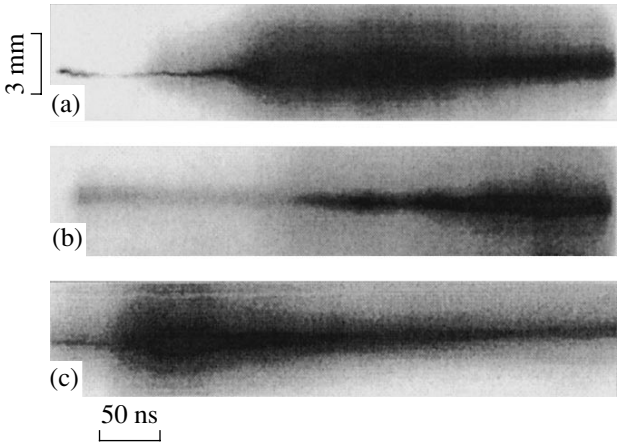

Fig. 4. Streak photographs of the explosion luminance at $B_z = 0$. (a, b) 0–500 and (c) 500–1000 ns (the slit is perpendicular to the wire).

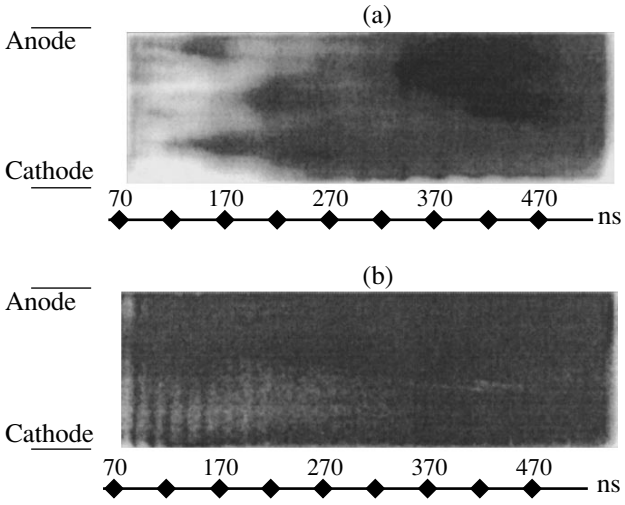

Fig. 5. Streak photographs of the process at $B_z = 0$ (a) and 40 kG (b) (the slit is parallel to the wire).

optical pattern of the expanding plasma exhibits two luminance maxima (at ≈170 and >450 ns). A specific feature of the pattern is a faintly glowing core at the wire axis, which is observed in both the slit and frame scan modes (Fig. 6b). The radius of the core is almost constant in time. The reproducibility of the experimental data at $B_z \geq B_{cr}$ allows for a correct comparison between experimental and analytical patterns of the wire explosion and plasma expansion, making it possible to study the process in greater detail and calibrate models of conduction, equations of state, and radiation paths used in simulations.

NUMERICAL MODEL

In the one-dimensional cylindrical geometry, equations of single-fluid two-temperature magnetohydrodynamics in the Lagrange coordinates have the form

$$\frac{\partial}{\partial t}\left(\frac{1}{\rho}\right) = \frac{\partial}{\partial s}(rv); \quad \frac{\partial r}{\partial t} = v;$$

$$\frac{\partial v}{\partial t} = -r\frac{\partial (P_e + P_i + G)}{\partial s} - r\frac{\partial}{\partial s}\frac{B_z^2}{2\mu_0} - \frac{1}{r}\frac{\partial}{\partial s}\frac{r^2 B_\varphi^2}{2\mu_0};$$

$$\left(\frac{\partial \varepsilon_e}{\partial T_e}\right)_\rho \frac{\partial T_e}{\partial t} = \left(\rho^2\left(\frac{\partial \varepsilon_e}{\partial \rho}\right)_{T_e} - P_e\right)\frac{\partial}{\partial t}\left(\frac{1}{\rho}\right) - \frac{\partial r S_{th}^e}{\partial s} + \frac{cU_r - 4\sigma_{SB}T_e^4}{\rho l_{pl}} + Q_J - Q_{ei};$$

$$\left(\frac{\partial \varepsilon_i}{\partial T_i}\right)_\rho \frac{\partial T_i}{\partial t} = \left(\rho^2\left(\frac{\partial \varepsilon_i}{\partial \rho}\right)_{T_i} - (P_i + G)\right)\frac{\partial}{\partial t}\left(\frac{1}{\rho}\right) + Q_{ei}; \quad (1)$$

$$S_{th}^e = -\rho\chi_e r\frac{\partial T_e}{\partial s}; \quad Q_J = \frac{\sigma(E_\varphi^2 + E_z^2)}{\rho};$$

$$P_{e,i} = P_{e,i}(\rho, T_{e,i}); \quad \varepsilon_{e,i} = \varepsilon_{e,i}(\rho, T_{e,i});$$

$$\frac{\partial}{\partial t}\left(\frac{B_\varphi}{\rho r}\right) = \frac{\partial E_z}{\partial s}; \quad \frac{\partial}{\partial t}\left(\frac{B_z}{\rho}\right) = -\frac{\partial r E_\varphi}{\partial s};$$

$$E_z = \frac{\rho}{\mu_0\sigma}\frac{\partial r B_\varphi}{\partial s}; \quad E_\varphi = -\frac{\rho r}{\mu_0\sigma}\frac{\partial B_z}{\partial s};$$

$$\sigma = \sigma(\rho, T_e, \omega_e\tau_e); \quad \chi_e = \chi_e(\rho, T_e, \omega_e\tau_e),$$

where G is the Neumann quadratic viscosity.

The pressure, $P_{e,i}$, and the internal energy, $\varepsilon_{e,i}$, of the electron and ionic components are calculated within the averaged ion model using the equation of state [15]. In the energy equation for electrons, the ionization loss term is included into the internal energy of the electron component. The energy exchange Q_{ei} between the electrons and the ions allows for the electron degeneration effect [16]. The electrical conductivity σ and the electron thermal conductivity χ_e in the plasma state are chosen in accordance with [17], where both electron degeneration and plasma magnetization were taken into account. The electrical conductivity of tungsten in the condensed (solid and liquid) states is determined in accordance with [18] and the thermal conductivity is found from the Wiedemann–Franz law. The electrical conduction models were matched in such a way as to provide the best agreement with the experiment.

Radiation transport was calculated within the one-group diffusion approximation:

$$\frac{\partial U_r}{\partial t} + \frac{1}{r}\frac{\partial}{\partial r}(rS_r) = \frac{4\sigma_{SB}T_e^4 - cU_r}{l_p}, \quad (2)$$

$$S_r = -\frac{cl_r}{3}\frac{\partial U_r}{\partial r}, \quad l_p = l_p(\rho, T_e), \quad l_r = l_r(\rho, T_e).$$

The averaged Rosseland, l_r, and Planck, l_p, lengths were calculated consistently with the averaged ion

model [19]. At the axis of symmetry, the boundary conditions are

$$v|_{r=0} = 0, \quad H_\varphi|_{r=0} = 0, \quad \left.\frac{\partial B_z}{\partial s}\right| = 0, \qquad S^{\mathrm{e}}_{\mathrm{th}}\big|_{r=0} = 0, \quad S_{\mathrm{r}}|_{r=0} = 0. \tag{3}$$

At the exterior boundary of the plasma $r = r_{\mathrm{ext}}(t)$,

$$P_{\mathrm{e,i}}, S^{\mathrm{e}}_{\mathrm{th}}\big|_{r_{\mathrm{ext}}} = 0, \quad S_{\mathrm{r}}|_{r_{\mathrm{ext}}} = \frac{c}{2}U_{\mathrm{r}}|_{r_{\mathrm{ext}}}, \quad B_z|_{r_{\mathrm{ext}}} = B_0, \qquad B_\varphi|_{r=r_{\mathrm{ext}}} = \frac{\mu_0 J}{2\pi r_{\mathrm{ext}}}. \tag{4}$$

The current J is determined as a solution to the circuit equation

$$L\frac{dJ}{dt} + RJ - U + lE_z|_{r_{\mathrm{ext}}} = -\frac{\mu_0 l}{2\pi}\frac{d}{dt}\left(J\ln\left(\frac{r_{\mathrm{out}}}{r_{\mathrm{ext}}}\right)\right), \qquad \frac{dU}{dt} = -\frac{J}{C}, \tag{5}$$

where C, L, and R are, respectively, the capacitance, inductance, and resistance of the circuit and r_{out} is the radius of the output conductor.

At the initial time instant, we specified the voltage across the capacitor bank, $U|_{t=0} = U_0$, and assumed that the current in the circuit is zero, $J|_{t=0} = 0$.

RESULTS OF SIMULATIONS

As follows from Fig. 2, the analytical curves of the wire voltage and current agree well with experimental electrical parameters of the wire explosion. The luminance curves constructed in the one-dimensional MHD approximation (Fig. 8) differ qualitatively from the experimental curves presented in Fig. 2. At the zero magnetic field, the luminance calculated is lower than that when the field is other than zero. This can be explained by the fact that at $B_z = 0$, the real electrical explosion process is essentially non-one-dimensional and the energy release per unit wire length is highly nonuniform.

When the current rises at a rate of ≈70 kA/μs, the explosion is intermediate between homogeneous vaporization (≈170 kA/μs) and current surface shunting up to tungsten melting (≈20 kA/μs) [20]. This is illustrated in Fig. 9, which shows the electron temperature versus density curves for two extreme Lagrange zones (located near $r = 0$ and $r = r_{\mathrm{ext}}(t)$).

At the linear stage of the development of MHD instability with $m = 0$, the integral increments were estimated using the energy model [21]. The spatial distributions of the mass velocity, acceleration, density, and temperature of the expanding plasma at a particular time instant were numerically simulated in the framework of the one-dimensional MHD approximation.

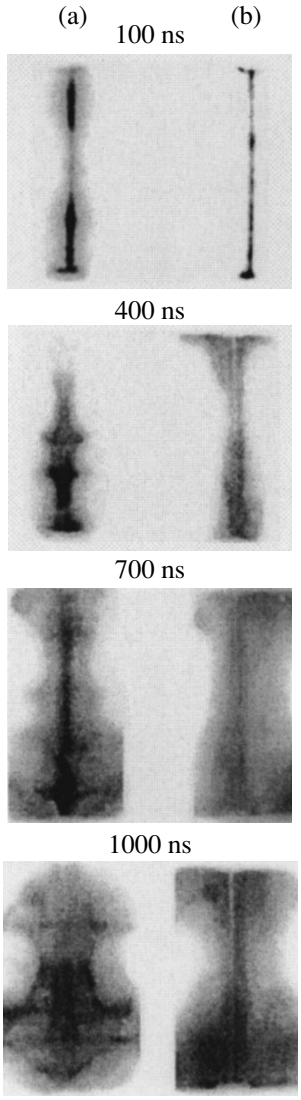

Fig. 6. Frame photographs of the exploding wire at different times after the pulse application at $B_z = 0$ (a) and 30 kG (b).

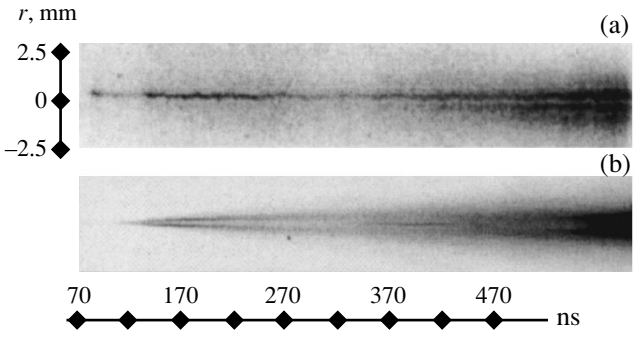

Fig. 7. (a) Streak photograph and (b) calculated optical image of the process at $B_z = 50$ kG.

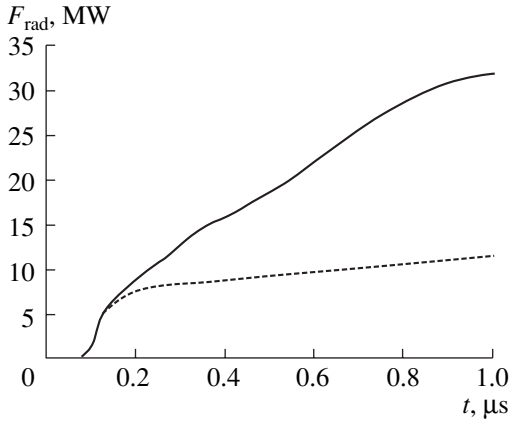

Fig. 8. Total radiation flux versus time at $B_z = 0$ (dashed line) and 50 kG (solid line).

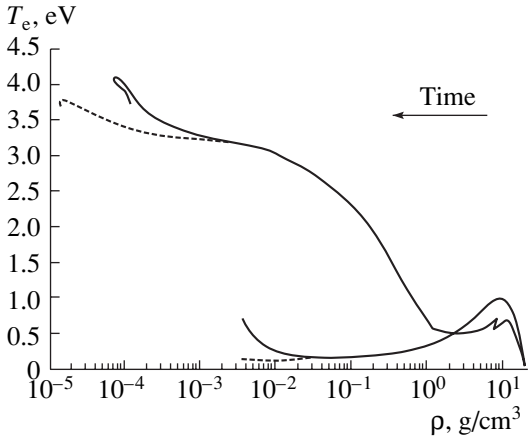

Fig. 9. Electron temperature versus density for the (*1*) innermost and (*2*) outmost Lagrange zones at $B_z = 0$ (dashed line) and 50 kG (solid line).

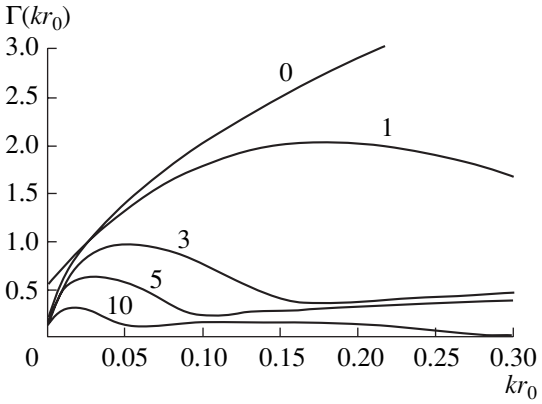

Fig. 10. Integral increments of instability with $m = 0$ versus kr_0 at a wavelength $\lambda \approx 0.22/kr_0$ mm. Figures at the curves are the values of B_z (kG).

Figure 10 shows the integral increments

$$\Gamma(kr_0) = \int_{t_{in}}^{t_f} \sigma_k(t')dt'$$

as a function of dimensionless wave number kr_0 (r_0 = 35 μm) for the mode $m = 0$ at different longitudinal magnetic fields B_z. Integration was performed from $t_{in} \cong 80$ ns (the entire wire passes into the plasma state) to $t_f \cong 500$ ns. It is seen that the rate of instability development with a wavelength of 1–3 mm, which is typical of our experiments, decreases with increasing longitudinal magnetic field. At $B_z \geq B_{cr} \sim 10$ kG, MHD instability with wavelengths ≤0.8 mm is suppressed almost completely. This is in good agreement with the experimental data. Note that, in the presence of the longitudinal magnetic field, the asymptotical spectrum of the mode $m = 0$ is no longer a purely RT spectrum of form $\sigma_k \sim \sqrt{k}$ because of the shear of the total magnetic field.

To analyze the image of the exploding wire, we used the formal solution to the radiation transfer equation [22]:

$$I_\nu(s) = \int_{s_0}^{s} \mathcal{N}'_\nu I_{\nu p} \exp\left[-\int_{s'}^{s} \mathcal{N}'_\nu ds''\right] ds', \qquad (6)$$

where $I_\nu(s)$ is the spectral intensity as a function of the coordinate s along the path of observation, $\mathcal{N}'_\nu$ is the spectral absorption coefficient with allowance for induced radiation [19], and $I_{\nu p} = 2h\nu^3/c^2[\exp(h\nu/kT_e) - 1]^{-1}$ is the spectral intensity of the equilibrium radiation.

Figure 11 illustrates the cross section of the exploding wire and parallel paths of observation along which the integration from s_0 to s_f was performed. We used the approximation of a photodetector placed at infinity and having a narrow entrance slit running perpendicular to the wire.

Figure 7b is the analytical optical image of the explosion and plasma expansion. It was obtained by integrating expression (6):

$$I(s) = \int_{\nu_{min}}^{\nu_{max}} I_\nu(s)d\nu, \qquad (7)$$

where the lower, ν_{min}, and upper, ν_{max}, limits of integration correspond to the boundary frequencies of the visible spectrum.

The streak photograph (Fig. 7a) and the image calculated (Fig. 7b) are seen to be in qualitative agreement.

Our calculations have shown that the faintly glowing core at the wire axis that is observed in both the slit (Fig. 7) and frame (Fig. 6b) scan modes is an optical effect. It is due to the blooming of the outer higher temperature (T = 3–4 eV) low-density (ρ = 10^{-3}–10^{-4} g/cm^3) products of the explosion. As a result,

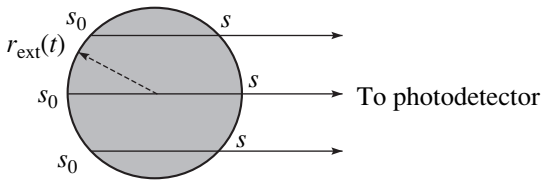

Fig. 11. Cross section of the exploding wire and paths of observation.

colder (T = 0.2–0.5 eV) and denser ($\rho = 10^{-1}$–10^{-2} g/cm^3) inner regions are visible better.

CONCLUSION

With a combination of experimental and theoretical numerical methods, we gained a better insight into the explosion and expansion of a single tungsten wire in a low longitudinal magnetic field.

The effect of stabilization by a weak longitudinal magnetic field (affecting the expansion dynamics only slightly) found experimentally allowed us to improve the reproducibility of experimental data. This offers possibilities for correctly comparing experimental and theoretical patterns of the plasma expansion due the explosion. Also, based on optical observations, one can calibrate models of conduction, equations of state, and radiation paths used in simulations.

The reproducibility of experimental data paves the way to further investigations into the processes of wire explosion, plasma expansion, and plasma sheath generation from wire arrays. Finally, reproducible data make it possible to verify analytical models of conduction, equations of state, and radiation paths under different experimental conditions by invoking a variety of diagnostic methods.

REFERENCES

1. Yu. É. Adam'yan, V. M. Vasilevskiĭ, G. A. Shneerson, *et al.*, Pis'ma Zh. Tekh. Fiz. **21** (23), 43 (1995) [Tech. Phys. Lett. **21**, 968 (1995)].
2. Yu. É. Adam'yan, V. M. Vasilevskiĭ, S. N. Kolgatin, and G. A. Shneerson, in *Proceedings of the Conference on Physics of Low-Temperature Plasma, Petrozavodsk, 1998*, Vol. 1, p. 53.
3. F. S. Felber, F. J. Wessell, N. C. Wild, *et al.*, J. Appl. Phys. **64**, 3831 (1988).
4. F. S. Felber, M. M. Malley, F. J. Wessel, *et al.*, Phys. Fluids **31**, 2053 (1988).
5. S. M. Golberg, M. A. Liberman, and A. L. Velikovich, Plasma Phys. Controlled Fusion **32** (5), 319 (1990).
6. V. D. Selemir, V. A. Demidov, A. V. Ivanovskiĭ, *et al.*, Fiz. Plazmy **25**, 1085 (1999) [Plasma Phys. Rep. **25**, 1000 (1999)].
7. S. A. Sorokin, A. V. Khachaturyan, and S. A. Chaĭkovskiĭ, Fiz. Plazmy **17**, 1453 (1991) [Sov. J. Plasma Phys. **17**, 841 (1991)].
8. S. A. Sorokin and S. A. Chaĭkovskiĭ, Fiz. Plazmy **19**, 856 (1993) [Plasma Phys. Rep. **19**, 444 (1993)].
9. V. F. Ermolovich, A. V. Ivanovskiĭ, A. P. Orlov, and V. D. Selemir, Zh. Tekh. Fiz. **70** (10), 11 (2000) [Tech. Phys. **45**, 1241 (2000)].
10. V. A. Burtsev, N. V. Kalinin, and A. V. Luchinskiĭ, *Electrical Explosion of Semiconductors and Its Application in Electrophysical Installations* (Énergoatomizdat, Moscow, 1990).
11. J. Ruiz-Camacho, F. N. Beg, A. E. Dangor, and M. G. Haines, Phys. Plasmas **6**, 2579 (1999).
12. S. Yu. Gus'kov, G. V. Ivanenkov, A. R. Mingaleev, *et al.*, Fiz. Plazmy **26**, 797 (2000) [Plasma Phys. Rep. **26**, 745 (2000)].
13. J. P. Chittenden, R. Aliaga-Rossel, S. V. Lebedev, *et al.*, Phys. Plasmas **4**, 4309 (1997).
14. G. V. Ivanenkov and W. Stepniewski, Fiz. Plazmy **26**, 24 (2000) [Plasma Phys. Rep. **26**, 21 (2000)].
15. M. M. Basko, Teplofiz. Vys. Temp. **23**, 483 (1985).
16. H. Brysk, Plasma Phys. **16**, 927 (1974).
17. Y. T. Lee and R. M. More, Phys. Fluids **27**, 1273 (1984).
18. T. J. Burgess, in *Megagauss Technology and Pulsed Power Applications*, Ed. by C. M. Fowler, R. S. Caird, and D. J. Erickson (Plenum, New York, 1987), p. 307.
19. M. M. Basko, Preprint of the Institute of Theoretical and Experimental Physics, Moscow, 1985, No. 145.
20. G. S. Sarkisov, B. S. Bauer, and J. S. De Groot, Pis'ma Zh. Éksp. Teor. Fiz. **73**, 74 (2001) [JETP Lett. **73**, 69 (2001)].
21. A. B. Bud'ko, M. A. Liberman, A. L. Velikovich, and F. S. Felber, Phys. Fluids B **2**, 1159 (1990).
22. Ya. B. Zel'dovich and Yu. P. Raizer, *Physics of Shock Waves and High-Temperature Hydrodynamic Phenomena* (Nauka, Moscow, 1966, 2nd ed.; Academic, New York, 1966).

Translated by A. Khzmalyan

Technical Physics, Vol. 47, No. 5, 2002, pp. 634–642. Translated from Zhurnal Tekhnicheskoĭ Fiziki, Vol. 72, No. 5, 2002, pp. 121–129.

EXPERIMENTAL INSTRUMENTS AND TECHNIQUES

Evolution of Carbon from Atomic Clusters to Fullerenes in an Arc Discharge

N. I. Alekseev and G. A. Dyuzhev

Ioffe Physicotechnical Institute, Russian Academy of Sciences, Politekhnicheskaya ul. 26, St. Petersburg, 194021 Russia

e-mail: dgan@hm.csa.ru

Received September 21, 2001

Abstract—The formation of fullerenes from an arc-produced turbulent jet of carbon vapor is described. Both direct and backward mono- and bimolecular reactions are analyzed. Initial characteristics of the jet are used as the input parameters of the problem. The analytical dependences of the fullerene yield on the initial velocity of the jet and carbon vapor concentration explain experimental relationships between the fullerene yield, current, pressure, and buffer gas sort. *© 2002 MAIK "Nauka/Interperiodica".*

This work completes a series of publications [1–5] concerned with the intriguing transformation of the chaotic carbon vapor into fullerene under the action of an arc. The fact that carbon is present in the form of atoms and ions in the arc channel is beyond question. This follows both from experiments with the ^{13}C isotope [6] and from the analysis of a fullerene arc [4] (the analytical results for the arc voltage and the rate of anode erosion agree well with experimental data [7]).

One can assume that the evolution of carbon away from the arc resembles that observed in drift-tube experiments [8]: as the gas cools, chains (for a cluster size of less than ten atoms), rings (for a larger number of atoms), and finally more complex objects (direct precursors of fullerenes) appear successively. Such an assumption, as applied to the arc conditions, seems to be quite reasonable in view of recent experiments [9] and their theoretical substantiation [10]. Namely, the amount of carbon deposited on probes located at different distances from the arc axis can be explained on assumption that, with small distances, carbon is deposited on the probes in the form of atoms and ions (at well-defined jet velocity and temperature), while with large distances, as fullerene associates and soot particles [11].

In [2], we applied the methods of quantum chemistry to show that clusters of two single-bonded rings are the most probable precursors of fullerenes. All possible ways of the transformation of multiring clusters into fullerenes were described in [1, 3]. The next step should be a kinetic analysis of preceding carbon vapor clustering and the determination of the actual concentration of the two-ring cluster.

Carbon vapor undergoes the transformations in an expanding gas–plasma jet originating from an arc source [12]. The existence of such a jet is confirmed by experiments with carbon-collecting probes [9] and those where $^{13}CO_2$ was added to helium [13]. Experimental mass spectra taken from ^{13}C-containing fullerenes were explained in terms of a simple physical model considering gas circulation around the arc.

The condensation of carbon in the jet was considered in [12]. Bimolecular reactions due to cluster collisions and monomolecular reactions introduced arbitrarily were considered to be involved in the transformation. Backward reactions between clusters already formed were rejected. The reaction cross sections and probabilities were calculated numerically with the methods of molecular dynamics [14], where a real three-dimensional problem was subjected only to time simulation. Backward reactions were not considered, as in [12]. However, conditions in the jet vary from nearly equilibrium at its origin to extremely nonequilibrium in the fullerene formation area, which is rather narrow [10, 15].

The aim of this work is to construct an approximate analytical model of carbon condensation in a gas–plasma jet with allowance for backward reactions and also to set a correlation between the fullerene yield and three jet parameters at the exit from the source: flow velocity, carbon concentration, and temperature.

EQUILIBRIUM CONCENTRATION OF CLUSTERS

To take into account backward reactions, it is necessary to know the equilibrium concentration of the carbon clusters at different temperatures and different total carbon concentrations.

When the clusters are in equilibrium, their concentration is conveniently expressed through the concentration of atoms N_1. Then, the equilibrium concentrations of C_2 and C_3 molecules, as well as clusters of n atoms C_n, are given by

$$N_n^{(0)} = \frac{Z_n}{Z_1^n} N_1^n, \quad (1)$$

1063-7842/02/4705-0634$22.00 © 2002 MAIK "Nauka/Interperiodica"

where Z_n is the partition function for a cluster of n atoms, which includes the translational, rotational, and vibrational components.

After substituting the total partition functions for the chains, rings, and two-ring clusters into (1), expressions for the equilibrium concentration of the clusters take the following form:

chains,

$$N_n^{(c)} = A^{\frac{5-3n}{2}} \frac{\pi q_n n^{3/2}}{g_1^n} \left(\frac{T}{h\nu_n}\right)^{3n-5} \exp\left(\frac{E_n^{(c)}}{T}\right) a^{3n-3} N_1^n; \quad (2)$$

rings with even n,

$$N_n^{(r)} = A^{\frac{6-3n}{2}} \frac{n^5}{2\pi g_1^n} \left(\frac{T}{h\nu_n}\right)^{3n-6} \exp\left(\frac{E_n^{(r)}}{T}\right) a^{3n-3} N_1^n; \quad (3)$$

rings with odd n,

$$N_n^{(r)} = A^{\frac{6-3n}{2}} \frac{n^6}{4\pi g_1^n} \left(\frac{T}{h\nu_n}\right)^{3n-6} \exp\left(\frac{E_n^{(r)}}{T}\right) a^{3n-3} N_1^n; \quad (4)$$

and two-ring clusters,

$$B_n^{(0)} \cong A^{\frac{6-3n}{2}} \frac{n^6}{4\pi g_1^n} \left(\frac{T}{h\nu_n}\right)^{3n-6} \exp\left(\frac{E_n^{(0)}}{T}\right) a^{3n-3} \times \frac{1}{2}\left(\frac{1}{2} + \left(1 + \frac{2\pi}{n}\right)^2\right)\left(1 + \left(1 + \frac{2\pi}{n}\right)^2\right) N_1^n. \quad (5)$$

Here, $q_n = I_n/I_2$, I_2 and I_n are the moments of inertia for a diatomic molecule and an n-atomic chain, respectively, about the central axis ($I_2 = ma^2/2$; m is the mass of a carbon atom; and $a \approx 1.4$ Å is the bond length in a carbon molecule, which is taken to be fixed); $E_n^{(c)}$ and $E_n^{(r)}$ are the absolute binding energies for the chains and rings, respectively; and ν_n is the mean geometrical frequency of oscillators involved in a given cluster; the exponents $(3n - 5)$ for the chains and $(3n - 6)$ for the rings and two-ring clusters characterize the vibrational partition function when the condition $h\nu_i/T \ll 1$ is met for all the oscillators;

$$A = \frac{2\pi mT}{h^2} a^2;$$

and g_1 is the orbital moment of the atomic nucleus. The binding energies of the clusters calculated with the AM1 quantum-mechanical method are presented in Fig. 1. The binding energy of the chains is seen to grow almost linearly with the chain size, $E_n^{(c)} \approx (n-1)\varepsilon_0$, in the same manner as the binding energy of the rings at $n > 10$. The value of ε_0 is roughly equal to 5.5–6.0 eV.

The mean vibrational frequency of the chains somewhat decreases with increasing length (within an even–odd accuracy) and remains constant at $\nu_n \approx 2.7 \times 10^{12}$ s^{-1} for $n \approx 10$. The vibrational frequency of the rings is nearly the same.

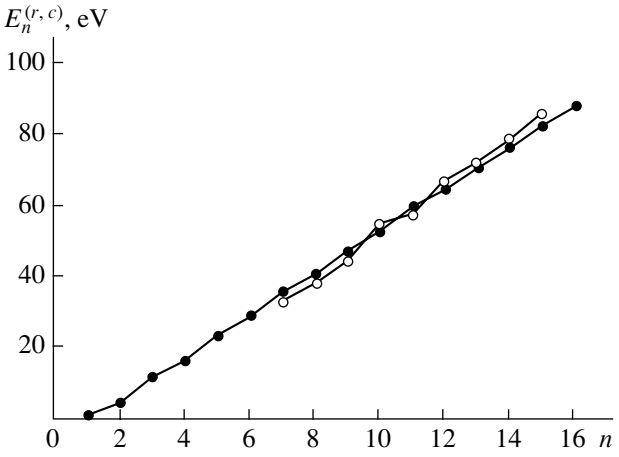

Fig. 1. Binding energy for the (●) chains and (○) rings vs. number of atoms n in the cluster. The AM1 method.

TURBULENT GAS JET

The evolution of the carbon clusters takes place in the turbulent gas jet coming from the arc source. The spatial variation of the jet parameters under the conditions of fully developed turbulence is well known. The total concentration N of carbon atoms in any of the clusters and the jet velocity V vary as [16]

$$(N, V) \cong \frac{(N_0, V_0)\vartheta r_0}{x}. \quad (6)$$

The difference between the temperature in the gas jet, T, and that outside the jet, T_∞ ($T \gg T_\infty$) varies in a similar way:

$$T - T_\infty \cong \frac{(T_0 - T_\infty)\vartheta r_0}{x}. \quad (7)$$

Here, x is the distance to the source axis, r_0 is the electrode radius, $2d$ is the interelectrode spacing, ϑ is a model turbulent constant that depends on r_0 and d. In our geometry, $r_0 = 0.3$ cm, $2d = 0.6$ cm, and $\vartheta \approx 3.5$. Formulas (6) and (7) apply when $x \geq x_1 = \vartheta r_0 = 1.05$ cm, i.e., at distances where the behavior of the plasma parameters in the jet is self-similar [16]. At the point x_1, the initial jet parameters N_0 (carbon concentration), V_0 (jet velocity), and T_0 (jet temperature) are specified.

Figure 2 shows a typical variation of the chain spectrum with distance to the source. The curve was constructed under the assumption that the total concentration of the atoms, C_2 and C_3 molecules, chains, and two-ring clusters is calculated by formula (6) and the temperature varies according to (7).

At a small distance from the source, i.e., at a high gas temperature (curve *1*), the concentration of chains

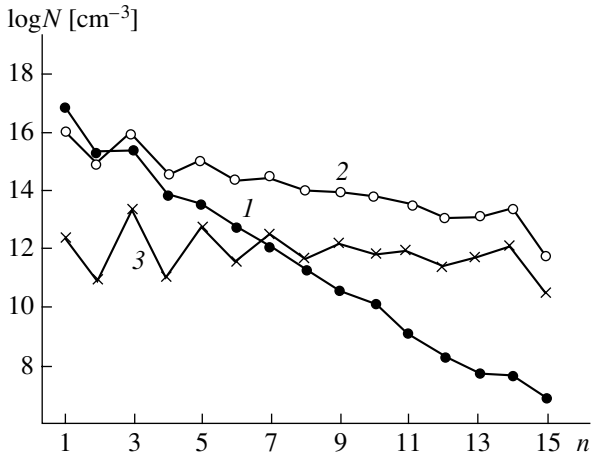

Fig. 2. Variation of the equilibrium spectrum of the chain sizes for distances to the source x = 1.3 (*1*), 1.7 (*2*), and 2.9 (*3*) cm.

decreases on any scale, starting from the atomic scale. At lower temperatures, the C_3 molecules dominate over the C_2 and even C_1 molecules (curve *3*); at $n > 3$, the curve declines monotonically.

QUALITATIVE CONSIDERATION OF THE EQUILIBRIUM BETWEEN CARBON CLUSTERS IN VARIOUS DISCHARGE AREAS

In analyzing the evolution of carbon clusters, it is necessary to consider equilibrium conditions between the clusters on various length scales. The equilibrium is set through the coagulation reactions upon cluster collisions and the reactions of cluster decomposition. Note that in collisions, the coagulation of atoms and small molecules and the attachment of small molecules to large clusters have different probabilities.

In the first case, the probability of the reaction is nearly independent of temperature and is associated with the presence of a third body, a buffer gas (for example, helium) atom. Here, the probability P of the reaction is defined as the probability that the helium atom falls into the region where two carbon atoms collide. Numerically,

$$P_1 \approx 10^{-8}\frac{P_{\mathrm{He}}}{T}, \tag{8}$$

where P_{He} is the helium pressure (torr) and T is the temperature (eV); i.e., $P \sim 10^{-4}$–10^{-5}.

In the second case, the probability of cluster coalescence varies exponentially: $P \sim \exp(-\Delta E/T)$, where ΔE = 0.4–0.6 eV [17]. Here, $P \sim 0.1$.

It has been proposed that the transition from the first to the second type of collisions takes place at $n = 3$, since in C_3 the number of vibrational modes that can be excited (from 1 to 4) is much greater than in C_2, so that the need for the third body, which takes away an excess energy, is eliminated.

In this case, the carbon clusters are in equilibrium on several scale levels.

(1) The scale of equilibrium between small clusters is

$$\lambda_1 = \frac{V}{\sigma_0 V_T N_\Sigma P_1}, \tag{9}$$

where $N_\Sigma \approx N_1 + \sqrt{2}N_2 + \sqrt{3}N_3$ is the total effective concentration of small clusters and atoms; σ_0 is the cross section of atom–atom collisions, which is set equal to $\sigma_0 = 5.3 \times 10^{-16}$ cm^2 [12, 14]; and $V_T = \sqrt{2T/m}$ is the thermal velocity of carbon atoms.

(2) The scale of equilibrium between large clusters (starting from C_3) is

$$\lambda = \frac{V}{\sigma_0 V_T N_\Sigma P}. \tag{10}$$

(3) The scale where equilibrium between larger clusters is disturbed because of a decrease in the number of collisions, i.e., a decrease in the number of small clusters.

For carbon concentrations near the jet source, λ is on the order of several tenths of a millimeter. Hence, large clusters come into equilibrium virtually instantaneously. The value of λ_1 is 1–10 cm or even greater. Therefore, it is not impossible that the atoms and the C_2 and C_3 molecules do not come into equilibrium at all within the arc chamber and the spectrum of large sizes becomes totally depleted [5]. On the other hand, expression (8) for P_1, which yields the lower estimate of the probability [5], assumes that the time of interaction between carbon atoms is of the same order of magnitude as $2a/V_T$. However, this time is actually defined by the lifetime of the metastable complex C_2^* and may be much higher than $2a/V_T$ and λ_1, much less than 1–10 cm.

In this work, the length λ_1 was assumed to be small enough for tiny clusters to have time to come into equilibrium at least in the region where the fullerene precursors and fullerenes themselves form.

A SET OF EQUATIONS FOR CLUSTER EVOLUTION

The curves in Figs. 1 and 2, formulas (1)–(5), and the above considerations provide the basis for considering the problem of cluster spectrum in the three-dimensional statement. The calculation was performed under the following conditions.

(1) For the balance of clusters of each of the types (chains, rings, two-ring clusters, and fullerenes), the kinetics of only their associated precursors is essential. Namely, the formation of two-ring clusters and their decomposition into separate rings have a minor effect on the kinetics of the rings, and the decomposition of

fullerenes insignificantly affects the kinetics of two-ring clusters.

(2) An increase in the size of the chains by attaching atoms or the C_2 and C_3 molecules can be considered as diffusion in the space of sizes. Clusters formed by capturing small molecules have a chance to be isomerized into chains or rings by the instant of subsequent collision.

(3) Before the equilibrium in the large cluster spectrum breaks down, the atoms and C_2 and C_3 molecules come into equilibrium between each other.

(4) A change in the properties of small chains and rings when the number of atoms is changed by unity (parity change) has a minor effect on large clusters.

(5) The properties of the chains and rings are similar. The chains smoothly transform into the rings at $n \approx 10$. Therefore, we can consider the unified spectrum of the chains and rings.

Some of these assumptions need additional commentary. The first assumption is fully justified when only a small fraction of the rings transforms into the two-ring clusters and only a small fraction of the two-ring clusters transforms into fullerenes. If the yield of fullerenes is high, such an assumption may give only qualitatively valid results. The second assumption implies that either carbon atoms (at temperatures $\approx$0.3 eV) or the C_3 molecules (at lower temperatures, Fig. 2) dominate under equilibrium conditions. For $n > 3$, the spectrum does not exhibit singularities, as has been noted above.

At the early stage of this work, we solved a set of balance equations for the chains and rings. Being written in the differential form as a single equation, it is given by

$$V\left[\gamma\left(\frac{\partial N_n^{(0)}}{\partial x} + \frac{N_n^{(0)}}{x}\right) + N_n^{(0)}\frac{\partial \gamma}{\partial x}\right] = \frac{\partial}{\partial n}\left(w_n N_n^{(0)}\frac{\partial \gamma}{\partial n}\right). \quad (11)$$

This set was supplemented by an equation for atom concentration variation:

$$V\left(\frac{\partial N_1}{\partial x} + \frac{N_1}{x}\right) = \sigma_0 V_T P N_1 \int_3^\infty dn N_n^{(0)} n \frac{\partial \gamma}{\partial n}. \quad (12)$$

Here, $N_n^{(0)}$ is the equilibrium concentration of the clusters at a given atom concentration N_1 (for a given carbon concentration, N_1 differs from the equilibrium value), $\gamma = N_n/N_n^{(0)}$, and w_n is the effective probability of cluster growth through the coagulation with the atoms and the C_2 and C_3 molecules. With regard for the fact that the cross section of coagulation for two clusters with arbitrary numbers of atoms n and k is $\sigma_{nk} \approx (n + k + \eta)\sigma_0 P$ ($\eta \sim 1$) [12, 14] and the relative thermal velocity of the clusters is

$$V_T^{(n,k)} = \sqrt{\frac{n+k}{nk}} V_T,$$

the expression for w_n at a sufficiently high n has the form $w_n \approx \sigma_0 P_n N_\Sigma V_T$, where N_Σ has been defined above. The second terms on the left-hand sides of (11) and (12) are of turbulent character. They provide the appropriate behavior of the concentration of a given carbon impurity when the right-hand side vanishes, i.e., when the transformations are absent.

The formation of the two-ring clusters is described by the equation

$$V\frac{dB_n}{dx} = \sigma_0 V_T P \frac{n^{3/2}}{\sqrt{n_1 n_2}} \sum_{n_1 + n_2 = n} \left(N_{n_1} N_{n_2} - N_{n_1}^{(0)} N_{n_2}^{(0)} \frac{B_n}{B_n^{(0)}}\right), \quad (13)$$

where B_n and $B_n^{(0)}$ are the actual and equilibrium concentrations of two-ring clusters of size n.

Equation (13) means that a two-ring cluster can be formed through the coagulation of two rings, not by sequentially attaching small molecules. The diffusion term in (13) is rejected. The disappearance of two-ring clusters having transformed into fullerene is also neglected. This is justified by the fact that virtually all possible two-ring clusters already form by the time the optimal transformation temperature is established.

When analyzing the transformation of the two-ring clusters into fullerenes, we assumed that the material forms in a fixed temperature range δT centered at the optimal value 0.25 eV [5, 14, 18]. It is then reasonable to integrate the expression for the fullerene yield,

$$F = \int_0^\infty \frac{dx}{V}\frac{dF}{dt}, \quad (14)$$

with respect to temperature. The result is

$$F \sim \int_0^\infty x(T)\frac{dT}{T}\frac{1}{V}\frac{dF}{dt} \sim \frac{x_F}{V}\frac{\delta T}{T_F}(w_{\text{spont}} + \Phi W_0 \varepsilon^2)B \sim \frac{1}{V_0}(w_{\text{spont}} + \Phi W_0 \varepsilon^2)B. \quad (15)$$

In (15), it is assumed that, at the optimal temperature, the rate of fullerene formation has the "spontaneous" part and that associated with the capture of small clusters (primarily C_3). It was shown [5] that the latter part is expressed as $\Phi W_0 \varepsilon^2$, where $W_0 = \sigma V_T N_\Sigma P$, ε is on the order of the relative change in the partition function when one new polyhedron is formed in a growing cluster, and Φ is a factor on the order of unity. The value of

σ is $\sigma \approx 5\sigma_0$ [1], and the probability w_{spont} of fullerene formation at the optimal temperature was set equal to 10^4 s^{-1} according to [3].

SOLUTION OF THE SET OF EQUATIONS FOR CHAINS AND RINGS

Expressions (2)–(4) for the equilibrium concentrations of the chains and rings have some features that simplify solution (11).

(1) The derivative

$$\frac{\partial}{\partial n}\ln N_n^{(0)}$$

is almost independent of n and depends only on the coordinate x (Fig. 2). Indeed, let us recast (2)–(4) in the form

$$N_n^{(0)} = \Psi\pi\frac{n^{4.5}}{6a^3} \times \exp n\left(\frac{\varepsilon_0}{T} - 1.5\ln A + \ln(a^3N_1) + 3\ln\left(\frac{T}{h\nu_n}\right)\right), \quad (16)$$

where

$$\Psi = A^{5/2}\left(\frac{T}{h\nu}\right)^{-5} = \left(\frac{2\pi ma^2\nu_n^2}{T}\right)^{5/2}.$$

Then, the positive quantity

$$\Theta = -\frac{\partial}{\partial n}\ln N_n^{(0)} \quad (17)$$

equals

$$\Theta = \frac{\varepsilon_0}{T} - 1.5\ln A + \ln(a^3N_1) + 3\ln\left(\frac{T}{h\nu_n}\right) = \frac{\varepsilon_0}{T} - 1.5\ln\left(\frac{2\pi ma^2\nu_n^2}{T}\right) + \ln(a^3N_1).$$

Numerically,

$$\Theta \approx -\left(\frac{\varepsilon_0}{T} - 13.5 + \ln\frac{N_1}{10^{16}} + 1.5\ln T\right) \quad (18)$$

(for N_1 in cm^{-3} and T in eV).

(2) The cross section for the coagulation of large and small clusters is almost proportional to n.

(3) The derivative

$$\frac{\partial}{\partial x}\ln N_n^{(0)} \approx nD$$

is proportional to n; that is, the proportionality coefficient

$$D = \frac{d\ln N_1}{dx} + \left(1.5 - \frac{\varepsilon_0}{T}\right)\frac{d\ln T}{dx} \quad (19)$$

is a function of x alone. As follows from calculations, D = 3–4. Since the equations were used for sufficiently large n and x, the value of $1/x$ is much less than nD and can be ignored.

(4) At carbon concentrations $\geq 10^{14}$ cm^{-3}, the length λ is very small. Moreover, as follows from the approximate solution constructed, of the two terms proportional to this parameter, that involving γ will always dominate. Indeed, the right-hand sides of the equations are small compared with the last terms in the left-hand sides if

$$Dn \gg \frac{\partial B}{\partial x} \sim \frac{\partial}{\partial x}\left(\frac{\lambda D}{\Theta}\right) \sim \frac{\lambda D}{\Theta x}, \quad (20)$$

where $x \sim 1$ cm is the characteristic scale of distance.

In the equilibrium solution, $\Theta \approx 2$ and condition (20) has the form $n \gg \lambda/2x$ even for $n = 3$; that is, the parameter λ must be <6. This is valid even if the concentration of small clusters is at a level of 10^{13} cm^{-3}.

Thus, Eq. (11) takes the form

$$n\frac{\partial^2\gamma}{\partial n^2} - \Theta n\frac{\partial\gamma}{\partial n} - \lambda Dn\gamma = \lambda\frac{\partial\gamma}{\partial x}, \quad (21)$$

where the right-hand side is much less than the last term on the right-hand side. Then, this equation turns into an ordinary differential equation and its solution is given by

$$\gamma^{(0)} = \exp(-B(n-3)), \quad (22)$$

where

$$B = -\frac{1}{2}(\Theta \pm \sqrt{\Theta^2 + 4\lambda D}). \quad (23)$$

Bearing in mind that the spectrum becomes equilibrium in the limit $\lambda \longrightarrow 0$, the minus sign should be taken in (23).

At $x = \vartheta r_0$, $\gamma^{(0)} \approx 1$ for any n; however, the equations for γ apply on large scales.

In the approximation that follows, it is necessary to look for a partial solution to the inhomogeneous equation

$$n\frac{\partial^2\gamma}{\partial n^2} - \Theta n\frac{\partial\gamma}{\partial n} - \lambda Dn\gamma = \lambda\frac{\partial\gamma^{(0)}}{\partial x}.$$

This solution has the form

$$\gamma^{(1)} = \frac{1}{2k}\lambda\frac{dB}{dx}\exp(-3B)\int_n^{n_1}\frac{bn'}{n'} \times \exp\left(n\left(\frac{\Theta}{2} - k\right)\right)(\exp(2k(n-n')) - 1),$$

where

$$k = \sqrt{\frac{\Theta^2}{4} + \lambda D},$$

and the upper limit of integration is arbitrary.

Being very awkward, this correction makes the further solution difficult. It was rejected by virtue of condition (18).

The rigorous solution of Eq. (21) as a partial differential equation by using standard techniques of mathematical physics is possible but will be basically incorrect, because one does not know a distance over which the initial shape of the spectrum ($\gamma = 1$) must be specified.

Therefore, when considering the kinetics of fullerene formation, we used simple solution (22). Substituting it into expression (12) for atom balance, we find

$$\frac{dy}{dx} + \frac{1}{x} = \frac{\sigma_0 V_T P}{V}\int_3^\infty dn N_3^{(0)} \times \exp(-(\Theta + B)(n-3))\left(\frac{n}{3}\right)^{4.5} n(-B), \quad (24)$$

where $y = \ln N_1$.

In this expression for $N_n^{(0)}$ for any n, we used expression (16), which is valid for the chains and applies to the rings up to the preexponential. Although actually the rings dominate at $n > 10$, the relative error in determining the right-hand side is insignificant, since the integrand falls rapidly. It is easy to see that the integral

$$S = -\frac{1}{3^{4.5}}\int_3^\infty dn \exp(-(\Theta + B)(n-3))n^{5.5} \quad (25)$$

equals

$$S \approx \frac{3}{B+\Theta} + \frac{5.5}{(B+\Theta)^2} + \frac{6}{(B+\Theta)^3} + \frac{4}{(B+\Theta)^4} + \frac{3}{(B+\Theta)^5} + \frac{2}{(B+\Theta)^6} \quad (26)$$

at sufficiently large $B + \Theta$.

In terms of the limiting value of B, $B_{\lim} = (\lambda D)/\Theta$ at $(\lambda D)/\Theta \ll 1$, Eq. (24) can be written in the form

$$\frac{dy}{dx} + \frac{1}{x} = -\frac{B}{B_{\lim}}\frac{DS}{\Theta}\frac{N_3^{(0)}}{N_\Sigma}. \quad (27)$$

Formally, this equation looks like an ordinary differential equation; however, the right-hand side itself depends on dy/dx. Therefore, at any point of integration, the equation was first solved numerically as an algebraic equation for dy/dx.

SOLUTIONS FOR THE CHAINS AND RINGS

Figure 3 shows the variation of the atom concentration in the zero jet velocity limit (curve *1*) and for the uniform distribution of the atoms (curve *2*). In the case of the "ideal" solution to the set of balance equations, the curves must coincide. The difference between them indicates that the diffusion approach is not quite adequate. However, all curves shown in the subsequent figures were obtained without correcting the solution. It turned out that any correction changes the results thus presented insignificantly.

Figure 4 plots the atom concentration versus distance for various jet velocities. Up to $x \approx 2.6$ cm, the curves are nearly coincident with the equilibrium curve. At large distances, as the concentration of small clusters decreases and the temperature drops, the entrainment of the clusters by the jet becomes increasingly significant. The concentrations of the large clus-

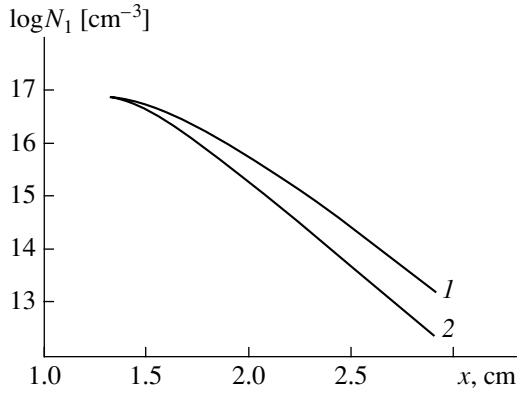

Fig. 3. Radial distribution of the carbon atom concentration (*1*) for the zero gas jet velocity and (*2*) in the presence of the equilibrium distribution of the atoms.

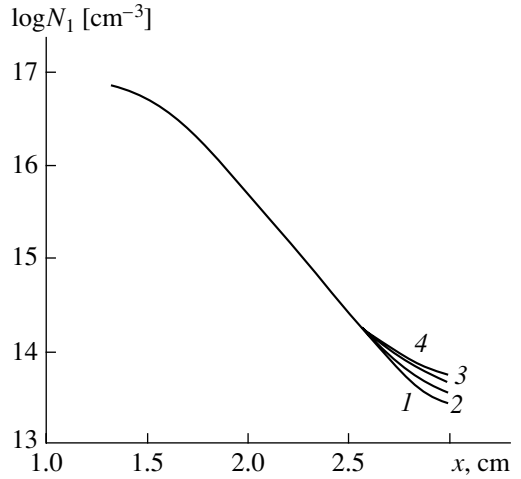

Fig. 4. Radial distribution of the atom concentration for gas jet velocities $V_0 = 2 \times 10^3$ (*1*), 4×10^3 (*2*), 6×10^3 (*3*), and 8×10^3 (*4*) cm/s. $N_0 = 10^{17}$ cm^{-3}, $T_0 = 0.7$ eV.

ters, which are rings almost without exception, become much smaller than the equilibrium values. Accordingly, the spectrum of the two-ring clusters and fullerenes also becomes depleted.

FORMATION OF TWO-RING CLUSTERS AND FULLERENES

The solution to Eq. (13) has the form

$$B_n = \int_{x_0}^{x} d\xi P \frac{n^{3/2}}{\sqrt{n_1 n_2}} \frac{\sigma_0 V_T}{V} N_{n_1} N_{n_2} \exp\left(-\int_{\xi}^{x} d\xi' L\right), \quad (28)$$

where

$$L = \sum \frac{n^{3/2}}{\sqrt{n_1 n_2}} \frac{\sigma_0 V_T}{V} P \frac{N_{n_1}^{(0)} N_{n_2}^{(0)}}{B_n^{(0)}}. \quad (29)$$

Clearly, only those values of x for which L is not too large contribute to the concentration of two-ring clusters of a given size. Therefore, with a reasonable accuracy (as applied to the approach considered), we can assume that

$$\exp\left(-\int_{\xi}^{x} d\xi' L\right) = 1,$$

and integrate over ξ to the point ξ_B where $\ln L = 0$. Since L does not depend on the carbon concentration and is a function solely of the initial velocity and initial temperature, it will suffice to determine ξ_B for one pair of $(V_0^{(0)}, T_0^{(0)})$. Then, one can readily show that for any other pair

$$L(x, V_0, T_0) = \frac{V_0^{(0)}}{V_0} L\left(x \frac{T_0^{(0)}}{T_0}, V_0, T_0\right). \quad (30)$$

Similarly, if the position of the point ξ_B is known for the pair $(V_0^{(0)}, T_0^{(0)})$: $x_B = \xi_B(V_0^{(0)}, T_0^{(0)})$, then

$$\xi_B = \left(x_B + \frac{1}{\alpha} \ln \frac{V_0^{(0)}}{V_0}\right) \frac{T_0}{T_0^{(0)}}, \quad (31)$$

where α is found from the relationship $\ln S(x, V_0^{(0)}, T_0^{(0)}) = -\alpha(x - x_B)$, which holds in a relatively wide range of x.

As the basic pair of the initial values, we took $T_0^{(0)} = 0.8$ eV and $V_0^{(0)} = 5 \times 10^3$ cm/s. Then, $\alpha = -14.81$ and $x_B = 2.222$. Substituting (22) into (28) yields

$$B_n(x_F) \sim \frac{\sigma_0 V_{T_0}}{V_0} \sum \frac{n^{3/2}}{\sqrt{n_1 n_2}} \left(\frac{n_1 n_2}{3}\right)^{4.5} \int_{\xi_B}^{x_F} dx' (N_3^{(0)})^2 \times \sqrt{\frac{x'}{\vartheta r_0}} P \exp(-(\Theta + B)(n-3)), \quad (32)$$

with none of the quantities under the integral sign being dependent on n_1 or n_2 alone.

If we consider only large clusters with $n \approx 60$, the constant factors related to n_1 and n_2 can be omitted:

$$B_n(x_F) \sim \frac{\sigma_0 V_{T_0}}{V_0} \int_{\xi_B}^{x_F} dx' (N_3^{(0)})^2 \times \sqrt{\frac{x'}{\vartheta r_0}} P \exp(-(\Theta + B)(n-3)). \quad (33)$$

Hence, the fullerene concentration is given by

$$F \sim \frac{\sigma_0 V_{T_0} (w_{\text{spont}} + \Phi \varepsilon^2 W_0)}{V_0^2} \int_{\xi_B}^{x_F} dx' (N_3^{(0)})^2 \times \sqrt{\frac{x'}{\vartheta r_0}} P \exp(-(\Theta + B)(n-3)), \quad (34)$$

where V_{T_0} and V_0 are the initial thermal velocity and jet velocity, respectively.

The results of integration of (34) are demonstrated in Figs. 5–7. The fullerene concentration is given in arbitrary units. The fullerene yield (as well as the percentage of fullerenes in soot) is seen to depend on the initial velocity and carbon concentration to the greatest extent. With an increase in the current, both parameters grow but have an opposite effect on α. Therefore, the curve $\alpha(I)$ has a peak, which was observed in experiments [7]. Unfortunately, detailed comparison between the theory and experiment is difficult, because the analytically found anode erosion in a complicated way depends on the flow $N_0 V_0$ toward the chamber walls and the flow toward the cathode. Moreover, for the velocity V_0, we know only estimates of the plasma transfer rate in a self-sustained high-current arc [19] originating from a source of small diameter $2r_0$:

$$V_0 = (I/cr_0)\sqrt{1/\pi\rho}, \quad (35)$$

where ρ is the effective density of the gaseous medium.

Figures 5 and 7 clarify the reason for a decrease in α when helium is replaced by heavy buffer gases. For given current and pressure (P_B) of a buffer gas, the velocity V_0, which varies in proportion with the square root of the density, depends on the type of the gas only slightly even if the atomic weights of buffer gases differ considerably. For light helium, the overall density

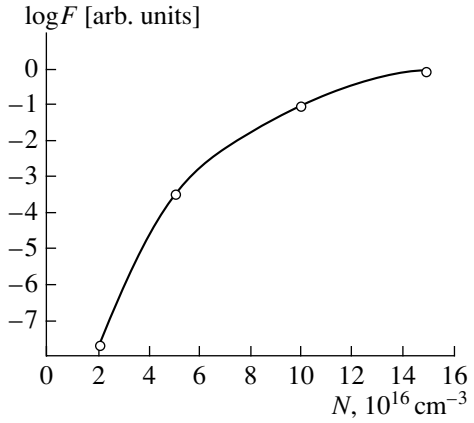

Fig. 5. Fullerene yield vs. carbon concentration at the inlet. $T = 0.7$ eV, $V_0 = 4 \times 10^3$ cm/s.

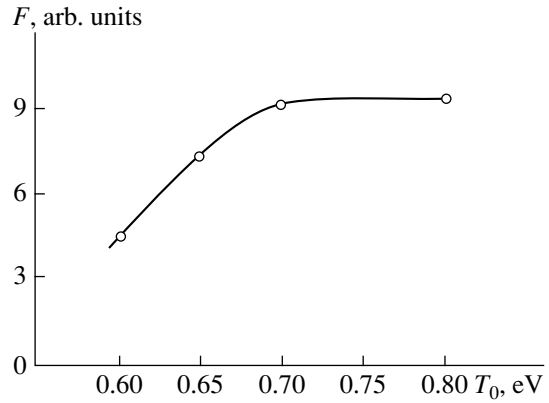

Fig. 6. Fullerene yield vs. gas (helium) temperature at the inlet. $N_0 = 10^{17}$ cm^{-3}, $V_0 = 4 \times 10^3$ cm/s.

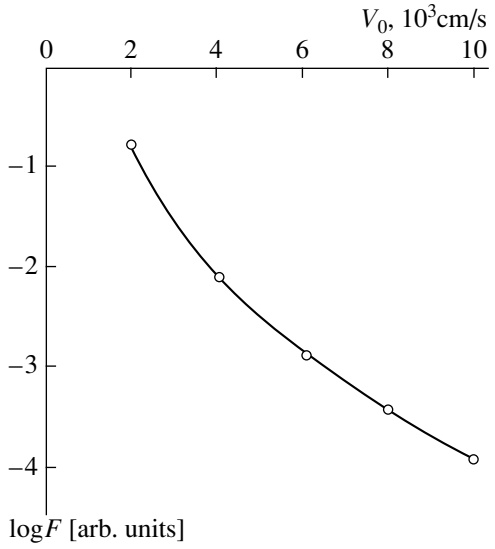

Fig. 7. Fullerene yield vs. initial jet velocity. $T = 0.7$ eV, $N_0 = 10^{17}$ cm^{-3}.

increases because of a minor amount of the heavier carbon present. The effective density of a heavier buffer gas is reduced because the gas is forced out from the gap by lighter atomic carbon and the heavily ionized carbon plasma. Therefore, although the atomic weights of helium and, e.g., argon differ 20 times, the velocity ratio is no more than 2.5–3 rather than $\sqrt{20}$. On the other hand, the degrees of erosion differ by more than one order of magnitude, so that the ratio of the concentration $N_0 \sim q/V_0$ for helium to N_0 for argon exceeds the velocity ratio. Since α depends on N_0 stronger than on V_0, the fullerene yield for helium is much higher. In the case of a heavy gas, a rise in the current elevates the erosion to the same level as in helium but owing to an increase in the velocity and a decrease in the concentration N_0 and not vice versa. The fact is that, in a heavy gas, the velocity given by (35) rises with current supralinearly, since the effective density drops as the heavy gas is forced out by lighter carbon. As a result, with the same erosion, the velocity in a heavy gas turns out to be higher while the carbon concentration lower than in helium although the atomic weight of the former is much larger. Both factors tend to reduce α.

No distinct supporting evidence for the experimentally found variation of α with pressure P_B has been obtained. Velocity (35) varies roughly as $1/\sqrt{P_B}$, and the erosion calculated declines somewhat faster than $1/\sqrt{P_B}$ [4, Fig. 5b]. Accordingly, the concentration $N_0 \sim q/V_0$ also drops with pressure but several times more slowly than the velocity. However, α depends on N_0 stronger and may behave nonmonotonically, of which the major peak in the α vs. pressure curve is an indication [7]. The minor peak is associated with a similar nonmonotonic dependence for the anode erosion. This dependence has not yet found adequate explanation.

ACKNOWLEDGMENTS

This work was supported by the Russian Foundation for Basic Research under the Program “Fullerenes and Atomic Clusters” (project no. 00-02-16928).

REFERENCES

1. N. I. Alekseev and G. A. Dyuzhev, Zh. Tekh. Fiz. **69** (9), 104 (1999) [Tech. Phys. **44**, 1093 (1999)].
2. N. I. Alekseev and G. A. Dyuzhev, Zh. Tekh. Fiz. **71** (5), 67 (2001) [Tech. Phys. **46**, 573 (2001)].
3. N. I. Alekseev and G. A. Dyuzhev, Zh. Tekh. Fiz. **71** (5), 71 (2001) [Tech. Phys. **46**, 577 (2001)].
4. N. I. Alekseev and G. A. Dyuzhev, Zh. Tekh. Fiz. **71** (10), 41 (2001) [Tech. Phys. **46**, 1247 (2001)].
5. N. I. Alekseev and G. A. Dyuzhev, Zh. Tekh. Fiz. **72** (5), 130 (2002) [Tech. Phys. **47**, 643 (2002)].
6. T. W. Ebbesen, J. Tabuchi, and K. Tanigaki, Chem. Phys. Lett. **191**, 336 (1993).

7. D. Afanas'ev, I. Blinov, A. Bogdanov, *et al.*, Zh. Tekh. Fiz. **64** (10), 76 (1994) [Tech. Phys. **39**, 1017 (1994)].

8. J. M. Hunter, J. L. Fye, and M. F. Jarrold, J. Chem. Phys. **99**, 1785 (1993); J. M. Hunter, J. L. Fye, E. J. Roskamp, and M. F. Jarrold, J. Chem. Phys. **98**, 1810 (1994).

9. D. V. Afanas'ev, G. A. Dyuzhev, and A. A. Kruglikov, Zh. Tekh. Fiz. **71** (5), 134 (2001) [Tech. Phys. **46**, 638 (2001)].

10. N. I. Alekseev, F. Chibante, and G. A. Dyuzhev, Zh. Tekh. Fiz. **71** (6), 122 (2001) [Tech. Phys. **46**, 761 (2001)].

11. O. P. Gorelik, G. A. Dyuzhev, D. V. Novikov, *et al.*, Zh. Tekh. Fiz. **70** (11), 118 (2000) [Tech. Phys. **45**, 1489 (2000)].

12. O. Nerushev and G. I. Sukhinin, Zh. Tekh. Fiz. **67** (2), 41 (1997) [Tech. Phys. **42**, 160 (1997)].

13. D. V. Afanas'ev, G. A. Baranov, G. A. Dyuzhev, *et al.*, Pis'ma Zh. Tekh. Fiz. **25** (18), 12 (1999) [Tech. Phys. Lett. **25**, 722 (1999)].

14. V. A. Schweigert, A. L. Alexandrov, Y. N. Morokov, and V. I. Bedanov, Chem. Phys. Lett. **235**, 221 (1995).

15. G. A. Dyuzhev and V. I. Karataev, Fiz. Tverd. Tela (St. Petersburg) **36**, 2795 (1994) [Phys. Solid State **36**, 1528 (1994)].

16. G. N. Abramovich, *Theory of Turbulent Jets* (Nauka, Moscow, 1984).

17. A. L. Aleksandrov, V. M. Bedanov, Yu. N. Morokov, and V. A. Shveĭgert, Zh. Strukt. Khim. **36**, 991 (1995).

18. L. Jing and J. R. Chelikowsky, Phys. Rev. B **46**, 1550 (1992).

19. S. Ramakrishnan, A. Stokes, and J. Lowke, J. Phys. D **11**, 2267 (1978).

Translated by V. Isaakyan

Technical Physics, Vol. 47, No. 5, 2002, pp. 643–647. Translated from Zhurnal Tekhnicheskoĭ Fiziki, Vol. 72, No. 5, 2002, pp. 130–134.

EXPERIMENTAL INSTRUMENTS AND TECHNIQUES

The Role of Small Clusters in the Transformation of Two-Ring Clusters into Fullerenes

N. I. Alekseev and G. A. Dyuzhev

Ioffe Physicotechnical Institute, Russian Academy of Sciences, Politekhnicheskaya ul. 26, St. Petersburg, 194021 Russia

e-mail: dgan@hm.csa.ru

Received September 21, 2001

Abstract—Possible reactions by which small carbon molecules C_2 and C_3 can join a cluster at an intermediate assembly stage from a two-ring cluster to a fullerene are considered. For analysis of the separate stages of this type of reaction, methods of quantum chemistry are used. The generalized reaction probabilities obtained are then included into the general scheme of assembly kinetics alongside monomolecular reactions. It has been shown that at a small cluster concentration of about 10^{14} cm^{-3} the assembly time drops severalfold. Also given are generalized results of the effect on the assembly time of the multiplicity of paths of fullerene assembly from two-ring clusters. © *2002 MAIK "Nauka/Interperiodica".*

This study is a continuation of a series of works [1–5] on transformation of carbon vapor into fullerene under arc discharge conditions. Direct precursors of the fullerenes in this process, as shown in [3], are almost planar two-ring clusters with one bond between the rings. It was considered [4] that transformation of these clusters into fullerenes proceeds only via monomolecular reactions with a buffer gas for thermostatting. An important result obtained in [4] is that the position $N_\Sigma^{(0)}$ of the binding energy maximum as a function of the number of polygons comprising the assembled frameworks of the fullerene surface (number of steps) N_Σ shifts to lower $N_\Sigma^{(0)}$ values. For clusters with $n \geq 62$–65, $N_\Sigma^{(0)} = 5$; thus, the binding energy maximum becomes lower. Therefore, in considering the process, a fairly detailed level of abridged description is possible because all frameworks of clusters with $N_\Sigma \leq 6$ acceptable from the energy considerations can be easily overviewed manually, assuming that different ways of attaching ring fragments to these frameworks are possible and mutually balanced. Vibrational partition functions of such paths within a given framework can be considered equal. In [4] it is considered that "small clusters" (atoms and C_2 and C_3 molecules) do not participate in the transformation process. In this work, calculations are presented of the kinetics of transformation into fullerene (hereinafter referred to as assembly) as a function of small cluster concentration.

TRANSFORMATION INTO FULLERENE OF A TWO-RING CLUSTER WITH A LARGE NUMBER OF ATOMS (60 OR MORE)

Prior to elucidating the role of small clusters in the fullerene assembly kinetics, a calculation was performed of the assembly of clusters having a size of $n = 60$ atoms or more. As in [4], the calculation was carried out taking into account all possible assembly paths and assuming only monomolecular reactions.

In calculating the assembly kinetics, probabilities of the direct reactions for every intermediate configuration were determined by summation over all possible variants μ of this configuration with their relative statistical weights and over all possible reactions for every variant:

$$w_{n_1 \to n_2} = \sum_\mu \frac{\Omega_{n_1,\mu}}{\Omega_{n_1}} \sum_k w_{n_1,\mu}^{(k)}. \quad (1)$$

Here, n_1 and n_2 are the numbers of the framework configurations and $N_\Sigma(n_1) + 1 = N_\Sigma(n_2)$, with superscript k denoting the reaction number, and $\Omega_{n_1,\mu}$ and Ω_{n_1} are the ratios of the statistical weights of variant μ and the complete statistical weight of this configuration to the statistical weight of the initial two-ring cluster. In order to determine the reaction probabilities, it is necessary to specify some set of cluster parameters. This set defines an average number of fragments of the framework edge permitting a given reaction [1]. This number is determined by purely combinatorial relationships and related to the possibility of ring fragments to become attached to the framework in different ways even if a complete set of parameters is specified.

The calculation of the rate of evolution was carried out in a quasi-stationary approximation. As in [4], the solution was obtained from a system of balance equations of all the framework configurations taken into

1063-7842/02/4705-0643$22.00

account,

$$-qy_n\Omega_n = \sum_{N_\Sigma(k) = N_\Sigma(n)-1} w_{kn}\Omega_k(y_k - y_n) + \Omega_n \sum_{N_\Sigma(k) = N_\Sigma(n)-1} w_{kn}(y_k - y_n) \quad (2)$$

at $N_\Sigma^{(0)} - 1 \geq N_\Sigma(n) \geq 2$,

$$-qy_n\Omega_n = \sum_{N_\Sigma^{(k)} = N_\Sigma^{(n)-1}} w_{kn}\Omega_k(y_k - y_n) - \Omega_n w_{N_\Sigma \to F} y_n \quad (3)$$

at $N_\Sigma(n) = N_\Sigma^{(0)}$,

$$-q = \sum_{N_\Sigma(k) = 2} w_{1k}(1 - y_k) \quad (4)$$

for the initial configuration. In formulas (2)–(4), $y_n = N_n/N_n^{(0)}$ is the ratio of the concentration of a given cluster type to the equilibrium concentration for a given concentration of initial two-ring clusters N_1 and q is the decay rate of the initial state, assumed to be exponential $N_1 = N_1^{(0)}\exp(-qt)$.

The calculated variation of the transformation time $\tau_F = q^{-1}$ with temperature T is shown in Fig. 1. Note that at $T = 0.28$ eV, τ_F is close to the result obtained in [4], where the calculation scheme was somewhat different: n and k denoted not a particular framework configuration but some average configuration with specified numbers (N_5, N_6, and the internal summation in (1) was carried out over the numbers of radicals R_5, R_6, ρ_5, and ρ_6).

The role of the path multiplicity factor in determining τ_F can be demonstrated as follows. For a particular path chosen, the total assembly time is determined in the quasi-stationary approximation by

$$\tau_F = 1/w_{12} + \sum_{i=1}^{N_\Sigma^{(0)}-1} 1/\Omega_i w_{i \to i+1} + \frac{n_F^{(0)}}{n_1^{(0)}} \sum_{i = N_\Sigma^{(0)}}^{F-1} \Omega_{i+1}/\Omega_i w_{i \to i+1}. \quad (5)$$

It is seen from (5) that the contribution of the decaying branch of the energy diagram to the assembly time is insignificant.

If all paths are taken into account, τ_F is obtained from a linear system of balance equations of all clusters but can also be estimated by formula (5); for this purpose, it is sufficient to replace each product $w_i\Omega_i$ in (5) with a sum over all possible reactions and variants μ of the configurations i admissible for a given reaction. By way of estimation, it can be assumed that this sum is

$$\sum\nolimits_k w_i^{(k)} \sum\nolimits_{\mu(k)} \Omega_{i,\mu} \approx \sum\nolimits_k w_i^{(k)} \times \sum\nolimits_\mu \Omega_{i,\mu}.$$

So, an increase of every term in (5) due to the multiplicity of paths is determined by two factors. One is the ratio $\Omega_{sum}/\Omega_{max}$ of the total statistical weight $\Omega_{sum}(N_\Sigma)$ of the clusters with a given N_Σ to the maximum possible statistical weight of some configuration $\Omega_{max}(N_\Sigma)$ (as a rule, this configuration is characterized by a minimum binding energy). The other is the ratio of the total probability of all the reactions possible for a given cluster to the maximum probability. In the estimation of both of these ratios, the configuration with a maximum statistical weight does not necessarily coincide with the configuration of the most probable path; therefore, the total estimated increase of the assembly rate by (5) is a lower bound.

In determining the statistical weights necessary for the estimation, the following approximation was used. Because computation of all clusters with $n \sim 60$ requires an enormous amount of computer time, the configuration of minimum energy was determined by looking at clusters of 40 atoms. Then, in the case of $n = 60$, it was sufficient to determine the energies and vibrational spectra of only six clusters ($N_\Sigma = 0\ldots5$). For determination of parameters of all the remaining clusters, parameterization similar to that suggested in [4] was employed.

The estimate was carried out for a temperature of $T = 0.25$ eV. That this temperature is an optimum choice can be seen in Fig. 2, which shows variation with temperature of the ratio of equilibrium concentrations of two-ring clusters and fullerenes. It is seen that at $T > 0.25$ eV the concentration of two-ring clusters is higher despite the fact that the binding energy of the C_{60} fullerene is lower by about 28 eV. This is explained by a gigantic reduction of the vibrational statistical weight of fullerenes as a result of bond formation between atoms. This result is in full agreement with the results of study [6] and earlier studies (for example, [7]).

It has been found that at the optimum temperature $T = 0.25$ eV, the characteristic ratio $\Omega_{sum}/\Omega_{max}$ in the region of the bottleneck is equal to ~ 4–5, the ratio of the total reaction probabilities to the most probable ones being ~ 2. It is thus seen that taking into account the combinatorial factor accelerates the fullerene assembly by about an order of magnitude.

PROBABLE SMALL CLUSTER JOINING REACTIONS

If the assembly time is long, it can be significantly affected by the joining of small carbon molecules: atoms and C_2 and C_3 molecules [1, 8]. A number of possible ways for such joining resulting in the emergence of new polygons has been proposed [1]. It was assumed that the joining molecule is C_2. This assumption was

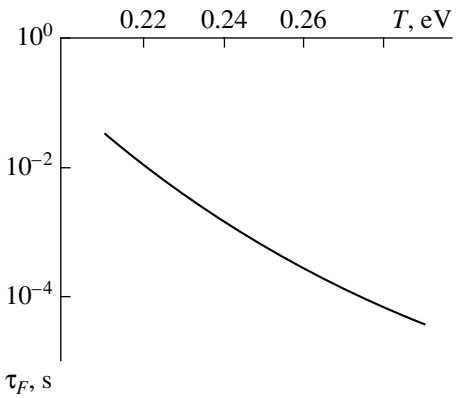

Fig. 1. Temperature dependence of the time it takes a two-ring cluster of $n = 60$ atoms to transform into a fullerene.

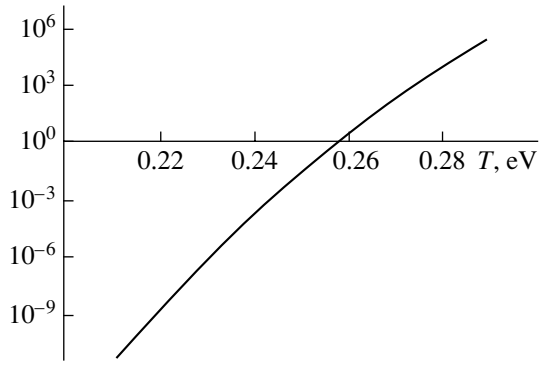

Fig. 2. Temperature dependence of the ratio of the equilibrium concentration of two-ring clusters ($n = 60$) to the concentration of fullerenes (calculation by AM1 method).

based on the fact that such molecules have been reliably registered in emission spectra from a fullerene arc [9].

However, results of the theoretical calculation of the equilibrium spectrum of carbon molecules indicate that over a wide range of carbon concentration at temperatures $T \le 0.4$ eV, the predominant molecules are not C_2 but C_3. A possible reason for this discrepancy between experiment and calculation is the rather long time necessary for the equilibrium between atoms and C_2 and C_3 molecules to be reached.

The equilibrium is established by way of direct and reverse coagulation reactions between atoms and small molecules, $C + C \longrightarrow C_2$, $C + C_2 \longrightarrow C_3$, with the probability of direct reactions being determined by a third particle, which is an atom of the buffer gas. It is estimated as a probability that a buffer gas atom will be found at the collision point of two carbon atoms and is numerically equal to

$$P_1 \approx 10^{-8}\frac{P_{\mathrm{He}}(\mathrm{torr})}{T(\mathrm{eV})} \qquad (6)$$

(where P_{He} is the buffer gas (helium) pressure), i.e., a quantity on the order of 10^{-4}–10^{-5}.

Then the length of establishment of the equilibrium in the range of small clusters is estimated as

$$\lambda_1 = \frac{V}{\sigma_0 V_T N_\Sigma P_1}, \qquad (7)$$

where $N_\Sigma \approx N_1 + \sqrt{2}\,N_2 + \sqrt{3}\,N_3$ is the total effective concentration of atoms and small molecules, σ_0 is a cross section of atom–atom collisions taken equal to $\sigma_0 = 5.3 \times 10^{-16}$ cm^2 [10], $V_T = \sqrt{2T/m}$ is the thermal velocity of carbon atoms, and V is the gas-flow velocity.

At concentrations corresponding to the initial portion of the gas–plasma jet, λ_1 is 1–10 cm or even greater. Therefore, it is possible that within the arc chamber, small clusters never reach equilibrium, the concentration of C_3 molecules is much lower than the equilibrium one, and such molecules are not observed.

However, expression (6) for P_1 is a lower bound of the estimated probability assuming that at the moment when two atoms collide a third particle instantaneously emerges at the collision point, whereas actually the metastable complex C_2^* can exist for quite a long time (its lifetime is not reliably known), so that the probability P_1 can be significantly higher. Therefore, in this

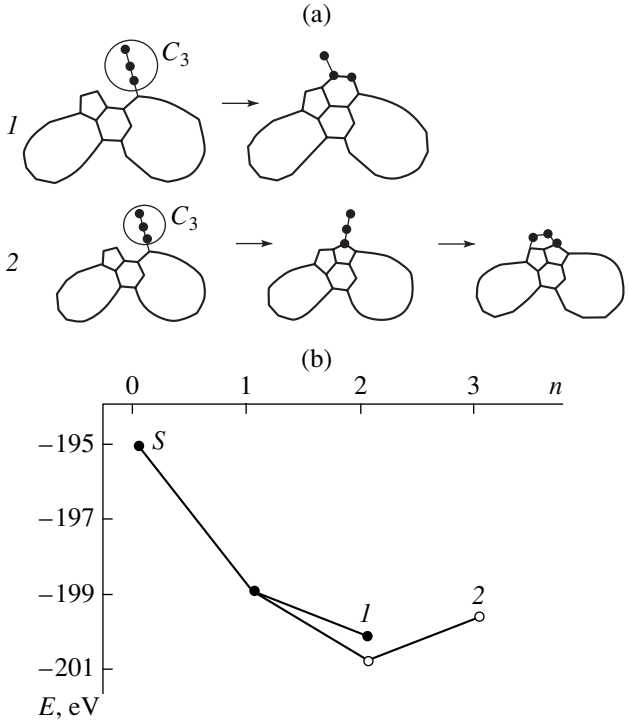

Fig. 3. (a) Two versions of the reaction by which a C_3 molecule (encircled) is added to a two-ring cluster. (b) Variation of the total binding energy of a C_3 molecule-cluster system as new polygons are formed; point *S*: the cluster and the C_3 molecule are not bound together; (*1*, *2*) variants *1*, *2* (a).

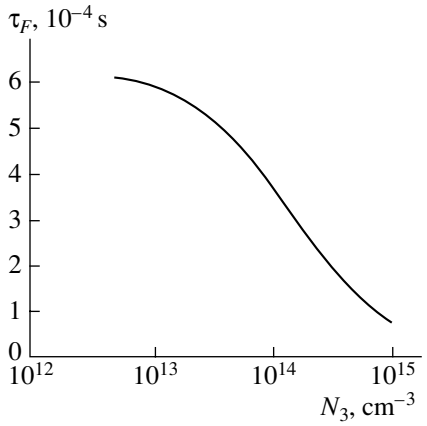

Fig. 4. Transformation time of a two-ring cluster into a fullerene as a function of the concentration of C_3 molecules.

work and in calculations in [4], it was assumed that C_3 molecules are still capable of attaining equilibrium with atoms and become predominant among small carbon molecules, but their concentration level is such that they are hard to observe (on the order of 10^{14} cm^{-3}). The entire region where fullerenes are formed happens to be located in the C_1–C_2–C_3 equilibrium zone and the dominant reaction of molecule capture by a cluster is the capture of a C_3 molecule instead of C_2.

CALCULATION OF THE EFFECT OF SMALL CLUSTERS ON THE FULLERENE FORMATION PROCESS

Figure 3 shows reactions by which C_3 molecules join a two-ring cluster at some assembly stage and the binding energy of the system. The binding energy of an initial state of the system, which is an isolated cluster and molecule, corresponds to point *S* in Fig. 3b. It can be seen that the capture of a C_3 molecule reduces the binding energy. The reason is that the weakly bound end atom is no longer there. Subsequent steps, in which a hexagon (situation *1* in Fig. 3) or two pentagons (situation *2*) are formed, the binding energy changes by a much lesser amount.

It is easy to see that this kind of chain reactions, in which C_3 molecules are "solved," can include one, two, or three reactions and therefore are influenced by the structure of a fairly large vicinity near the joining point. Therefore, in distinction from the case where a C_2 molecule or an atom is added, a reasonable level of detail in the brief description scheme of a cluster cannot be attained. Two possibilities remain.

(1) A cluster is described by one variable, the full number of polygons N_Σ (extremely brief description), and it is assumed that each act of adding a C_3 molecule to any doubly bonded atom of its framework or the first atom of a ring fragment increases the number of polygons by 1 or 2 and is not followed by a reverse reaction because of a large gain in energy. All configurations within a given N_Σ are assumed to be in equilibrium.

(2) Consider all possible configurations of the framework surface until an energy maximum is found at $N_\Sigma = 5$, as was done for an isolated cluster, and take into account all further possible reactions. In this work, the first approach is chosen as being a simpler one.

As in the case of an isolated cluster, a system of balance equations was solved for the number of clusters with a given set of parameters; now this set consists of only one parameter: the full number of polygons N_Σ. Taking into account the additions of small molecules was reduced to adding to the probability of even a single monomolecular reaction producing a new bond and one more polygon in the cluster (in [1] such reactions have been termed "spontaneous") the probability of an "induced" reaction, in the course of which a small carbon molecule is captured and one (W_{10}) or two (W_{20}) polygons emerge. Probabilities of these reactions were assumed to be identical:

$$W_{10} = W_{20} = \sigma N_3 V_T \exp(-\Delta E/T). \qquad (8)$$

In expression (8), the capture probability of a small cluster by a large one as a result of their collision is characterized by an exponential factor $P \sim \exp(-\Delta E/T)$, where $\Delta E \sim 0.4$–0.6 eV [10]. The cross section σ was taken to be equal to the total area of the active belt on the edge of the growing fullerene surface, to which ring fragments are attached, $\sigma \cong 5\sigma_0$ [1].

Solution of the chain of balance equation for $N_\Sigma = 1, 2, 3, 4, 5$ taking into account induced reactions has the form

$$q = \frac{1 + \frac{W_0}{w_1} + W_{20}\left(\frac{1}{w_2\Omega_2} + \frac{\Omega_2}{w_3\Omega_3} + \frac{\Omega_3}{w_4\Omega_4}\right)}{\frac{1}{w_1} + \frac{1}{w_2\Omega_2} + \frac{1}{w_3\Omega_3} + \frac{1}{w_4\Omega_4} + W_{20}\left(\frac{\Omega_3}{w_4\Omega_4}\left(\frac{1}{w_1} + \frac{1}{w_2\Omega_2}\right) + \frac{\Omega_2}{w_1}\frac{1}{w_3\Omega_3}\right)}, \qquad (9)$$

where $w_i \equiv w_{i,\,i+1}$, $W_0 = W_{10} + W_{20}$.

As the probability W_{20} is much less than w_k and has the same order of magnitude as the rate of spontaneous transformation q_{spont} [formulas (2)–(4)], an illustrative estimate of the calculation result can be made assuming

$$w_{12} = w_{23} = w_{34} = w_{45} = w,$$

$$\Omega_2 = \frac{\Omega_3}{\Omega_2} = \frac{\Omega_4}{\Omega_3} = \varepsilon \ll 1.$$

The estimate has the form

$$q = \frac{1 + \frac{W_{20}}{w}\frac{3}{\varepsilon}}{\frac{1}{w\varepsilon^3} + \frac{W_{20}}{w^2\varepsilon^2}} \approx q_{\text{spont}} + 3\varepsilon x^2 W_{20}. \qquad (10)$$

In Fig. 4 the dependence of the assembly time $\tau_F = q^{-1}$ of a two-ring cluster into fullerene obtained using (10) on the concentration of C_3 molecules at the optimum temperature $T = 0.25$ eV. It is seen that acceleration of the assembly on account of small molecules is not that great: for an increase in C_3 concentration of two orders of magnitude, the decrease in the time $\tau_F = q^{-1}$ is only by a factor of several. However, this estimate is in fact a lower bound. The reason is that it is precisely the capture of small molecules that ensures the feasibility of all those framework configurations and variants of the connection of ring fragments that are topologically possible.

ACKNOWLEDGMENTS

This work was supported by the Russian Foundation for Basic Research under the Program "Fullerenes and Atomic Clusters" (project no. 00-02-16928).

REFERENCES

1. N. I. Alekseev and G. A. Dyuzhev, Zh. Tekh. Fiz. **69** (9), 104 (1999) [Tech. Phys. **44**, 1093 (1999)].
2. N. I. Alekseev and G. A. Dyuzhev, Zh. Tekh. Fiz. **69** (12), 42 (1999) [Tech. Phys. **44**, 1435 (1999)].
3. N. I. Alekseev and G. A. Dyuzhev, Zh. Tekh. Fiz. **71** (5), 67 (2001) [Tech. Phys. **46**, 573 (2001)].
4. N. I. Alekseev and G. A. Dyuzhev, Zh. Tekh. Fiz. **71** (5), 71 (2001) [Tech. Phys. **46**, 577 (2001)].
5. N. I. Alekseev and G. A. Dyuzhev, Zh. Tekh. Fiz. **72** (5), 121 (2002) [Tech. Phys. **47**, 634 (2002)].
6. V. A. Schweigert, A. L. Alexandrov, Y. N. Morokov, and V. I. Bedanov, Chem. Phys. Lett. **235**, 221 (1995).
7. L. Jing and J. R. Chelikowsky, Phys. Rev. B **46**, 15503 (1992).
8. A. V. Krestinin, A. P. Moravskiĭ, and A. B. Tesner, Khim. Fiz. **17** (9), 70 (1998).
9. D. Afanas'ev, I. Blinov, A. Bogdanov, *et al.*, Zh. Tekh. Fiz. **64** (10), 76 (1994) [Tech. Phys. **39**, 1017 (1994)].
10. A. L. Aleksandrov, V. I. Bedanov, Yu. N. Morokov, and V. A. Shveĭgert, Zh. Strukt. Khim. **36**, 991 (1995).

Translated by B. Kalinin

Technical Physics, Vol. 47, No. 5, 2002, pp. 648–650. Translated from Zhurnal Tekhnicheskoĭ Fiziki, Vol. 72, No. 5, 2002, pp. 135–137.

BRIEF COMMUNICATIONS

Metastable Ions in the Mass Spectrum of Uranium Hexafluoride

B. A. Kalinin, V. E. Atanov, and O. E. Aleksandrov

Ural State Technical University, ul. Mira 19, Yekaterinburg, 620002 Russia

e-mail: kalinin@dpt.ustu.ru

Received October 15, 2001

Abstract—A high content (about 0.3%) of metastable ions is detected in the mass spectrum of uranium hexafluoride (UF_6). The apparent masses of the metastable ions found from the masses of UF_6 fragment ions, which were taken as references, are close to values predicted (the discrepancy is no more than 0.015 u). It is shown that these ions are responsible for the background current in a wide mass range. The lifetime of a UF_5 metastable ion with a mass of 333 is estimated. © *2002 MAIK "Nauka/Interperiodica".*

Mass spectrometry of metastable ions is extensively used in organic chemistry for gaining extra information on the composition of complex mixtures and the molecule structure [1, 2]. Metastable ions arise when some of the ions (including fracture ions) generated in an ion source are in the excited state with a lifetime comparable to the time of ion transit between the source and the collector. In practice, an ion produced when a truly metastable ion disintegrates on its way between the source and the collector is often also called metastable [2, p. 147]; however, such terms as parent ions and daughter ions are more appropriate here [3]. A parent (metastable) ion with a mass M_1 disintegrates following the reaction

$$M_1^+ \longrightarrow M_2^+ + M_3^0 \qquad (1)$$

to produce a daughter ion M_2^+. In doing so, the parent ion changes its mass, energy, and, as a consequence, trajectory curvature in a magnetic field.

Mass spectra of uranium hexafluoride samples with the natural isotopic composition were taken with an MI-1201 AGM mass spectrometer operating in the ion counting regime.[1] The mass spectrum of ions with masses ranging from 230 to 355 is shown in Fig. 1. The magnified region of the highest peak corresponding to metastable ions with a mass number of 296 is depicted in Fig. 2.

The ion current is plotted on the ordinate in ions/s. The tops of the peaks for ions with mass numbers of 333, 314, 295, and 276 (Fig. 1) are distorted because these peaks go beyond the upper limit of the dynamic range of the ion counter. The mass spectrum was taken for 3.5 h at an ionizing voltage of 50 V, an emission current of 0.1 mA, an accelerating voltage of 5 kV, a sweep pitch over the mass scale of 0.01 u, and an integration time per point of 1 s. A metastable ion peak can easily be distinguished by its width. For instance, the half-height resolutions of the mass-292 and mass-296 peaks are $R_{50} = 1116 \pm 17$ and 586 ± 1.6, respectively.

The peaks associated with masses of 258, 277, 296, and 315 (produced by the parent ions with masses of 295, 314, 333, and 352, respectively) were also identified. For this purpose, the spectrometer mass scale in Fig. 1 was calibrated with the reference masses of UF_6 ion fragments. The corrections ΔM to the peak positions measured by the mass spectrometer are well approximated by a parabola (Fig. 3). The standard error of approximation was 2.7 mu (1 mu = 10^{-3} u).

The corrected masses of the metastable daughter ions were compared with the calculated (apparent) masses (Table 1). The calculation was carried out by the formula

$$M_{\text{cal}} = \frac{M_2^2}{M_1}. \qquad (2)$$

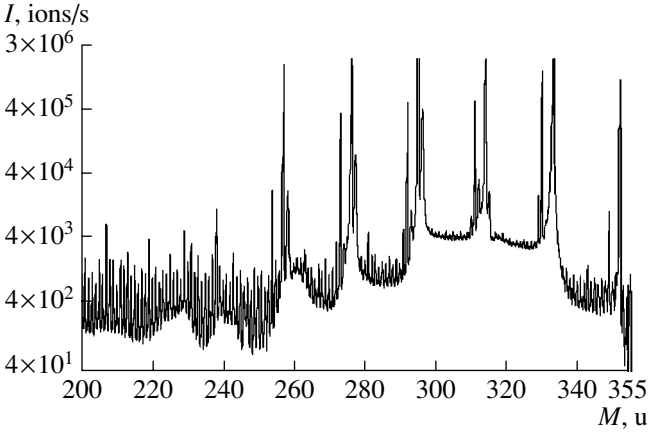

Fig. 1. Mass spectrum of UF_6.

[1] An MI-1201 AGM single-focusing sector mass spectrometer is provided with a secondary emission multiplier (SEM) and a counter of pulses due to ions striking the SEM collector.

1063-7842/02/4705-0648$22.00 © 2002 MAIK "Nauka/Interperiodica"

This formula assumes that disintegration products go on moving with the same velocity as a parent ion and that the parent ion disintegrates on its way between the ion source and the entrance to the magnetic field of the analyzer (field-free space). The values measured exceed those calculated, as has been observed earlier [1, p. 259], possibly because of a strong electric field gradient at the entrance slit of the mass spectrometer, which influences the lifetime of the metastable ions.

On the other hand, the good agreement between the calculated and measured masses of the metastable ions (the discrepancy is ≈0.01 u) means that the lines broadened are correctly identified as belonging to the daughter metastable ions. The elevation of the background ion current near $M = 262$ can be explained by the disintegration $333^+ \longrightarrow 295^+ + 38^0$ with the formation of ions with an apparent mass of 261.4. Similarly, the background ion current near $M = 241$ is related to the disintegration $314^+ \longrightarrow 276^+ + 38^0$ with the formation of ions with an apparent mass of 242.6.

The trajectory of daughter metastable ions and, as a result, the position of the corresponding peaks in the mass spectrum depend on the region of disintegration of a parent metastable ion. This is illustrated with the disintegration $333^+ \longrightarrow 314^+ + 19^0$ (Table 2).

From this table, it follows that the ions disintegrated in the magnetic field are distributed over the mass range between 296 and 333, causing the substantial increase (approximately, five times) in the background ion current for masses higher than 296 (Fig. 1). Also, the height of the metastable ion peaks correlates with the background ion current due to these peaks. This dependence is nearly linear (up to 30%) if we assume that the contribution of the scattered ion current 150 ions/s to the background ion current is constant.

The mass spectrum shows that the background ion current decreases, for instance, in the range between 315 and 329 because of the disintegration of the metastable ions (the decrease in their number) when they move in the magnetic field. A feature of the metastable ion disintegration in the ion source is that the masses of the ions decrease as the site of disintegration shifts toward the exit slit. As a result, the background ion current drops more slowly in the range between 296 and 310.

The dimensions of the ion channel in the mass spectrometer are as follows: the distance from the exit slit of the ion source to the entrance of the magnetic analyzer is 39.5 cm; the ion path length in the magnetic field (with the stray field neglected), 29 cm; and the distance between the exit of the magnetic analyzer and the ion collector, 42 cm. Knowing the dimensions of the ion channel, one can estimate the lifetime of the metastable ions.

With these dimensions and an accelerating voltage of 5 kV, the ion transit time through the channel is 20 μs. The lifetime of a metastable ion is expected to be of the same order of magnitude. This value for the UF_5 metastable ion ($M = 333$) can be estimated more accurately from the background ion current varying from 4×10^3 to 2.9×10^3 ions/s in the mass range between 314 and 326. Since the total channel length in the magnetic field is covered by ions of masses 333–296, the travel of ions with masses of 326–314 is equal to $(29/37) \times 12 = 9.4$ cm and the transit time for this length is $t = 1.7$ μs. Then,

$$\tau = \frac{t}{\ln\frac{N_1}{N_2}} = \frac{1.7}{\ln\frac{4}{2.9}} = 5.3\ \mu\text{s}.$$

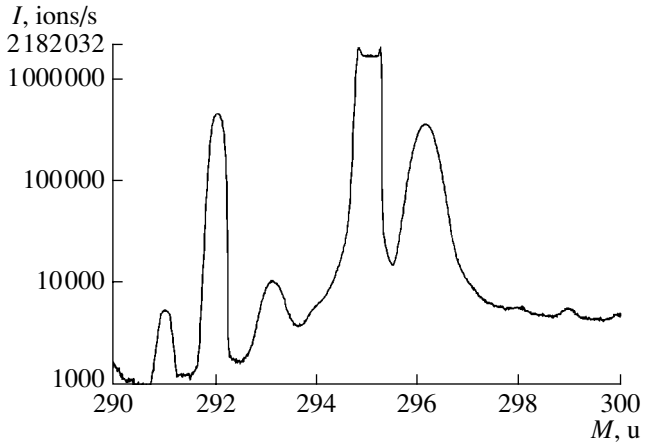

Fig. 2. Fragment of the mass spectrum for UF_6.

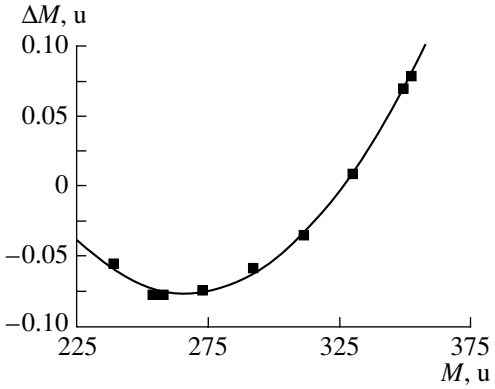

Fig. 3. Correction curve for the mass scale.

Table 1. Comparison between the measured and calculated (apparent) masses of the daughter metastable ions

M_m, u	M_{cal}, u	$M_m - M_{cal}$, mu	Error, mu
258.2846	258.2725	12.0	±1.5
277.2079	277.1969	11.0	±1.6
296.1417	296.1298	11.9	±1.8
315.0728	315.0697	3.1	±1.7

Table 2. Position of the peak for the $^{238}UF_4^+$ daughter ion (M = 314) in the mass spectrum vs. site of disintegration of the $^{238}UF_5^+$ metastable ion

Site of $333^+ \longrightarrow 314^+ + 19^0$ disintegration	Position in mass spectrum
Ionization chamber	314
Between ionization chamber and exit slit of ion source	314–296
Between exit slit of ion source and entrance to magnetic field	296
Magnetic field	296–333
Exit from magnetic field	333

The mass spectra with the starting and corrected mass scales are available from ftp://www.mp.dpt.ustu.ru/spectr (files Spectr 1 and Spectr 2, respectively).

ACKNOWLEDGMENTS

This work was supported by the Ministry of Education of the Russian Federation (grant no. 05.01.038).

REFERENCES

1. J. H. Beynon, *Mass Spectrometry and Its Applications in Organic Chemistry* (Elsevier, Amsterdam, 1960; Khimiya, Moscow, 1964).
2. J. Chapman, *Practical Organic Mass Spectrometry* (Wiley, Chichester, 1985; Mir, Moscow, 1988).
3. A. A. Polyakova, *Molecular Mass Spectrometric Analysis of Organic Compounds* (Khimiya, Moscow, 1983).

Translated by B. Malyukov

Technical Physics, Vol. 47, No. 5, 2002, pp. 651–653. Translated from Zhurnal Tekhnicheskoĭ Fiziki, Vol. 72, No. 5, 2002, pp. 138–140.

BRIEF COMMUNICATIONS

Laser Excitation of Flexural Waves and Their Scattering by Fractal Inhomogeneities in a Thin Plate

M. L. Lyamshev

Center for Wave Research, General Physics Institute, Russian Academy of Sciences, Moscow, 119991 Russia
e-mail: lyamshev@kapella.gpi.ru

Received October 30, 2001

Abstract—The excitation of flexural waves in a thin plate (film) by harmonically modulated laser radiation and their scattering by small fractal inhomogeneities are considered. An expression for the mean fluctuation intensity for the scattered wave field is obtained. A relationship between the intensity, parameters of the laser radiation and the plate, and the fractal dimension of inhomogeneities is found. The expected frequency dependence of the flexural wave attenuation in the plate due to their scattering by fractal inhomogeneities is discussed.

Films of various materials with different physical properties provide the basis for modern electronic and laser devices. To date, considerable progress has been made in film production technology. For example, it is possible today to grow diamond films of large areas (up to several thousands of square centimeters) and thicknesses of 1–2 mm [1]. Diamond films may be used in creating windows for powerful CO_2 lasers.

The surface of any film is rough. This, in particular, is true for films grown by chemical vapor deposition. The film roughness may be as high as 10% of the film thickness. It is worth noting that the surfaces of real bodies are also always rough. Even if they appear to be perfectly smooth, they are actually rough (the difference is only in scale of roughness) [2]. For instance, it has been recently reported that statistical irregularities with fractal properties are always present on the surface of a computer hard disk, along with regular information tracks (grooves) [3]. The internal structure of a film greatly influences its mechanical, electrical, magnetic, etc., properties. The film microstructure is often disordered and fractal. This in especially true for amorphous semiconductor layers [4].

From the acoustical standpoint, films can be considered as thin plates with surface irregularities (asperities) and microinhomogeneities of the internal structure. We will consider the excitation of flexural waves in a thin plate by harmonically modulated laser radiation and their scattering by the plate inhomogeneities. It is assumed that the laser radiation is absorbed in a thin (much thinner than the plate) surface layer. The inhomogneities are taken to be random, statistically uniform, and small (weak). The weak perturbation method is used to solve the problem. The results obtained may be of interest for laser optoacoustic diagnostics of film inhomogeneities as a technique of nondestructive film testing.

The scattering of flexural waves by random inhomogeneities in a plate has been considered earlier. Inhomogeneities were assumed either to be delta-correlated [5] or to have statistical properties described by the Gaussian correlation function [6]. However, inhomogeneities in plates (films) often have fractal properties. Fractal structures are characterized by scale invariance (scaling). As a result, the correlation functions, as well as random fractal spectra, are described by power laws with a fractional exponent [2]. Therefore, the statistical models used in [5, 6] may turn out to be inadequate for real inhomogeneities in plates (films).

Let a laser beam with the harmonically modulated intensity be incident normal to the surface of a thin plate. The displacements $u(x, y)$ of the plate executing forced flexural vibrations obey the equation [7]

$$[\Delta^2 - k^4(x, y)]u(x, y) = \frac{F(x, y)}{g}, \qquad (1)$$

where

$$\Delta \equiv \frac{\partial^2}{\partial x^2} + \frac{\partial^2}{\partial y^2} \text{ is haplocian, } g = \frac{Eh^3}{3(1-\sigma^2)},$$

$$k^4(x, y) = k^4(1 + \mu(x, y))^4,$$

$$k^4 = [3\omega^2\rho(1-\sigma^2)]/Eh^2.$$

Here, g is the flexural rigidity; E, Young's modulus; σ, Poisson's ratio; $2h$, the thickness; ρ, the density of the plate material; ω, the circular frequency of radiation intensity modulation; k, the wave number of the flexural waves propagating in the plate; $\mu(x, y)$, the random statistically uniform function describing plate inhomogeneities $\langle\mu(x, y)\rangle = 0$ and $|\mu(x, y)| \ll 1$; and $F(x, y)$, the function characterizing the external force acting on the plate due to the laser radiation.

1063-7842/02/4705-0651$22.00

We assume that the plate is opaque for the laser radiation, which is absorbed in the thin surface layer. This does not restrict the generality of the problem. The intensity distribution $I_0(x, y)$ on the plate surface usually obeys a Gaussian law. In view of the aforesaid, $F(x, y)$ may be represented in the form [8]

$$F(x, y) = -\frac{E\alpha\mu_1 m}{C_p} I_0 \exp\left[-\frac{x^2 + y^2}{a^2}\right], \quad (2)$$

where a is the radius of the laser beam on the plate surface; α, the volumetric thermal expansion coefficient; C_p, the specific heat of the plate material at constant pressure; m, the modulation factor ($0 \le m \le 1$); and μ_1, the radiation absorption coefficient of the plate.

Let us represent the plate displacement in the form

$$u(x, y) \cong u_0(x, y) + u_1(x, y) + \ldots, \quad (3)$$

where $u_1(x, y)$ are the displacements due to the scattering of the "zero-order" flexural waves with the displacements $u_0(x, y)$.

Substituting (3) into (1) and taking into account (2), we arrive at the following equations for $u_0(x, y)$ and $u_1(x, y)$:

$$(\Delta^2 - k^4)u_0(x, y) = -\frac{E\alpha\mu_1}{C_p g} I_0 \exp\left(-\frac{x^2 + y^2}{a^2}\right), \quad (4)$$

$$(\Delta^2 - k^4)u_1(x, y) = -4k^4\mu(x, y)u_0(x, y). \quad (5)$$

With the Green's function approach applied, the solutions to Eqs. (4) and (5) may be written as

$$u_i(x, y) = \int_S Q_i(x_0, y_0)G(x_0, y_0/x, y)ds(x_0, y_0), \quad (6)$$

where $Q_i(x, y)$ are the functions describing the right side of Eqs. (4) and (5) ($i = 0, 1$) and $G(x_0, y_0/x, y)$ is the Green's function satisfying the equation

$$(\Delta^2 - k^4)G(x_0, y_0/x, y) = \delta(x_0 - x)\delta(y - y_0) \quad (7)$$

and radiation conditions at infinity. Assume that the front curvature of the zero-order flexural wave incident on inhomogeneities does not influence the scattering effects. This means that the wave front can be considered to be plane on scales of inhomogeneity correlation. The field of the waves scattered will be studied in the Fraunhofer zone in terms of the radius of inhomogeneity correlation. In this case, as follows from the reciprocity theorem [8], it is sufficient to know the asymptotics of Green's function in order to find the zero- and first-order plate displacements. This asymptotics has the form [7]

$$G(x_0, y_0/x, y) = -\frac{\exp(ikR)}{\sqrt{32\pi ik^5 R}} \exp(ik_x x_0 + ik_y y_0), \quad (8)$$

where $R = \sqrt{x^2 + y^2}$, (x, y) are the coordinates of the point of observation, (x_0, y_0) are the coordinates of the source point, and $k^2 = k_x^2 + k_y^2$.

Substituting (8) into (6) and integrating, we find the zero-order approximation of $u_0(x, y)$:

$$u_0(x, y) = \frac{E\alpha\mu_1 m I_0 \pi a^2}{C_p g\sqrt{32\pi ik^5}} \frac{\exp(ikR)}{\sqrt{R}} \exp\left(-\frac{k^2 a^2}{4}\right). \quad (9)$$

From (9), it follows that the zero-order flexural wave in the Fraunhofer zone is a diverging cylindrical wave with the amplitude dependent on the laser radiation power $I_0\pi a^2$ and the plate parameters. The factor

$$\exp\left(-\frac{k^2 a^2}{4}\right)$$

means that the amplitude of the zero-order wave depends markedly on the parameter ka, characterizing the size of the laser spot on the plate surface relative to the wavelength. It can be seen that the size of the spot has to satisfy the condition $ka \ll 1$ in order to efficiently excite the zero-order flexural wave in the plate.

Consider fluctuations of the plate displacements in the field of the wave scattered. Under the assumption that the front of the incident zero-order wave is a plane in the region with correlated inhomogeneities, the solution to Eq. (5) can be represented in the form

$$u_1(x_1, y_1) = A_0 \frac{k^2}{\sqrt{2\pi ik}} \frac{\exp(ikR_1)}{\sqrt{R_1}} \times \int_S \mu(x_0, y_0)\exp[ik_x x_0 + ik_y y_0] \times \exp[-ik'_x x_0 - ik'_y y_0]ds(x_0, y_0). \quad (10)$$

Here, $A_0 \equiv u_0(x, y)$ is the amplitude of the incident zero-order wave at a distance $R = \sqrt{x^2 + y^2}$ in the region where the inhomogeneities are located; $\mathbf{r}_0(x_0, y_0)$, coordinates of the inhomogeneities; and $\mathbf{r}_1(x_1, y_1)$, those of the point of observation. Multiplying (10) by its complex conjugate, we find the mean square fluctuation of the plate displacement in the wave scattered:

$$\langle|u_1(x_1, y_1)|^2\rangle = |A_0|^2 \frac{k^3}{2\pi R_1} \iint_S B(x'_0, y'_0, x''_0, y''_0) \times \exp[ik(\mathbf{n} - \mathbf{n}')(\mathbf{r}'_0 - \mathbf{r}''_0)]dx(x'_0, y'_0)dx(x''_0, y''_0), \quad (11)$$

where $B(x'_0, y'_0, x''_0, y''_0) \equiv \langle\mu(x'_0, y'_0)\mu^*(x''_0, y''_0)\rangle$ is the correlation function of random inhomogeneities, and $\mathbf{n}$ and $\mathbf{n}'$ are the direction vectors of the incident (zero-order) and scattered (first-order) waves, respectively.

We introduce differential coordinates $\xi = x'_0 - x''_0$ and $\eta = y'_0 - y''_0$, as well as the center-of-mass coordinates $\rho_1 = 1/2(x'_0 + x''_0)$ and $\rho_2 = 1/2(y'_0 + y''_0)$. Since the correlation function of statistically uniform pro-

cesses depends only on the coordinate difference and integration over the center-of-mass coordinates yields the plate surface area S, we find

$$\langle |u_1(x_1, y_1)|^2 \rangle = |A_0|^2 \frac{k^3}{2\pi R_1} S \int_{-\infty}^{+\infty} B(\mathbf{r}') \exp(i\mathbf{q} \cdot \mathbf{r}') d\mathbf{r}'. \quad (12)$$

In (12), the finite limits of integration defined by the plate size S are replaced by $\pm\infty$, since the correlation function rapidly falls to zero beyond the region of inhomogeneity correlation and

$$\mathbf{q} = k(\mathbf{n} - \mathbf{n}')\mathbf{r}'(x', y').$$

The integral in (12) differs from the spatial energy spectrum of inhomogeneity fluctuations

$$G(\mathbf{q}) = (2\pi)^{-2} \int_{-\infty}^{+\infty} B(\mathbf{r}) \exp(i\mathbf{q} \cdot \mathbf{r}) d\mathbf{r} \quad (13)$$

by the factor $(2\pi)^{-2}$.

As is customary in the statistical wave theory, we find the scattering factor m_S, which depends on the energy flux through the closed loop of radius R. In view of (12) and (13), we obtain

$$m_S \sim 2\pi k^3 G(\mathbf{q}). \quad (14)$$

Of principle importance for fractal models of inhomogeneities is the fluctuation power spectrum

$$G(\mathbf{q}) \sim q^{\gamma}, \quad (15)$$

where the parameter γ is a fractional number. In the case of inhomogeneities with a fractal boundary (fractal surface), this parameter is given by

$$\gamma = D - 2d. \quad (16)$$

Here, D is the fractal dimension and d is the dimension of the nested space. In order to describe random fractal inhomogeneities, we choose the correlation function in the form (see, e.g., [9])

$$B(\mathbf{r}) = \langle \mu^2 \rangle [2^{\nu-1}\Gamma(\nu)]^{-1} (r/r_0)^{\nu} K_{\nu}(r/r_0), \quad (17)$$

where $\Gamma(\nu)$ is the gamma function; $K_{\nu}(u)$, the Macdonald function of the νth order; and r_0, the inhomogeneity correlation radius.

For the energy spectrum, we have

$$G(q) = \langle \mu^2 \rangle \nu r_0^2 [\pi(1 + q^2 r_0^2)^{\nu+1}]^{-1}. \quad (18)$$

Substituting (18) into (14) yields for the scattering factor

$$m_S \sim \langle \mu^2 \rangle 2\pi\nu k^3 r_0^2 [\pi(1 + q^2 r_0^2)^{\nu+1}]^{-1}. \quad (19)$$

From (19), it follows that the fractal properties of inhomogeneities have no effect on wave scattering at $q^2 r_0^2 \ll 1$. In contrast, we get

$$m_S \cong \langle \mu^2 \rangle 2k^3 (qr_0)^{-2-2\nu}. \quad (20)$$

for $qr_0 \gg 1$.

Let us estimate the frequency dependence of the flexural wave attenuation due to scattering by inhomogeneities:

$$\beta(\omega) \sim \oint_{\Gamma} m_S d\Gamma. \quad (21)$$

Consider the case of inhomogeneities for fractal-surface structures. It is well known that the fractal dimension of boundaries varies in the range $D = 1.3$–1.7 (see, e.g., [2]). Inserting this value of fractal dimension in (16) and taking into account that $d = 2$, we find $\gamma = -(2.7$–$2.3)$. Equating γ to the exponent of q in (20), we find the order of the Macdonald function: $\nu = 0.35$–0.15. Since $q \approx k$, the frequency dependence of the attenuation coefficient is

$$\beta(\omega) \sim \omega^{0.3-0.7}.$$

As is seen, the exponent in the frequency dependence of the attenuation is a noninteger number. This is due to the fractal properties of inhomogeneities. The exponent can serve as a measure of the inhomogeneity fractality [10]. Note that the theory of dislocation-induced ultrasonic attenuation in solids gives $\beta(\omega) \sim \omega^{-1}$, i.e., nonfractal dependence (the exponent in the frequency dependence of the attenuation is an integer).

ACKNOWLEDGMENTS

This work was supported by the Russian Foundation for Basic Research (grant no. 99-02-16334) and the INTAS (grant no. 97-31680).

REFERENCES

1. *Handbook of Industrial Diamond Films*, Ed. by M. A. Prulas, L. Popovie, and L. Bigelow (Marcel Dekker, New York, 1997).
2. J. Feder, *Fractals* (Plenum, New York, 1988; Mir, Moscow, 1991).
3. T. Karaback, Y.-P. Zhao, T. Liew, *et al.*, J. Appl. Phys. **88**, 3361 (2000).
4. Z. Chen, S. Zhang, and S. O. Tan, J. Appl. Phys. **89**, 783 (2001).
5. S. A. Rybak, Akust. Zh. **17**, 412 (1971) [Sov. Phys. Acoust. **17**, 345 (1971)].
6. V. N. Krasil'nikov, Akust. Zh. **8**, 183 (1962) [Sov. Phys. Acoust. **8**, 141 (1962)].
7. P. M. Morse and U. K. Ingard, *Theoretical Acoustics* (McGraw-Hill, New York, 1968).
8. L. M. Lyamshev, *Laser Thermooptical Excitation of Sound* (Nauka, Moscow, 1989).
9. Y.-P. Zhao, G.-C. Wang, and T. M. Lu, Phys. Rev. B **58**, 7300 (1998).
10. B. J. West and M. F. Shlesinger, J. Stat. Phys. **36**, 779 (1984).

Translated by M. Fofanov

Technical Physics, Vol. 47, No. 5, 2002, p. 654.

ERRATA

Erratum: "Methods for Calculating the Spectral Properties of Multilayer Anisotropic Structures Based on Crossed Polarized Gratings" [*Technical Physics* 46 (12), 1489 (2001)]

A. V. Arzhannikov and S. A. Kuznetsov

e-mail: sakuzn@inp.nsk.su

Page 1389, left column:
row 10 from below should read as "Conventional multiple-beam microwave interferometers ..."

Technical Physics, Vol. 47, No. 5, 2002, p. 654.

ERRATA

Erratum: "The Effect of High Implant Doses and High Ion Current Densities on Polyimide Film Properties" [*Technical Physics* 47 (4), 459 (2002)]

V. N. Popok, I. I. Azarko, and R. I. Khaibullin

Implant should be replaced by implantation in the title and throughout the text.